Title	Sensing at nanostructures for agri-food and enviromental applications
Authors	Creedon, Niamh
Publication date	2018
Original Citation	Creedon, N. 2018. Sensing at nanostructures for agri-food and enviromental applications. PhD Thesis, University College Cork.
Type of publication	Doctoral thesis
Rights	© 2018, Niamh Creedon. - http://creativecommons.org/licenses/by-nc-nd/3.0/
Download date	2024-05-08 16:35:33
Item downloaded from	https://hdl.handle.net/10468/7014

Ollscoil na hÉireann

NATIONAL UNIVERSITY OF IRELAND

Sensing at Nanostructures for Agri-Food and Environmental Applications

A Thesis Presented to the National University of Ireland

for the degree of Doctor of Philosophy

by

Niamh Creedon

Supervised by Dr Alan O'Riordan

Department of Chemistry
&
Tyndall National Institute

University College Cork, August 2018

Declaration

I hereby declare that this thesis is my own work and certify to the best of my knowledge it contains no materials previously published or written by another person, or substantial proportions of material which have been accepted for the award of any other degree or diploma at University College Cork or any other educational institution, except where due acknowledgement is made in the thesis in accordance with the standard referencing practices. Any contribution made to the research by others, with whom I have worked directly at Tyndall National Institute - University College Cork or elsewhere, is explicitly acknowledged in the thesis. I also declare that the intellectual content of this thesis is the product of my own work, except to the extent that assistance from others in the project's design and conception or in style, presentation and linguistic expression is acknowledged.

I declare that this is a true copy of my thesis, including any final revisions, as approved by my thesis committee and the Graduate Studies office, and that this thesis has not been submitted to any other University or Institution.

_____

Niamh Creedon

August 2018

Abstract

With a predicted population increase of 2.3 billion people, by 2050, agricultural productivity must be vastly improved and made sustainable. Globally, agriculture must deliver a 60% increase in food production to cope with the population demand. Moreover, this needs to be achieved against a changing climate, an exploitation of natural resources, and growing water and land scarcities. New digital technologies can optimise production efficiency and ensure food security and safety while also minimising waste within the production systems and the supply chain. To this end, new sensor technologies are being developed for applications in animal health diagnostics and environmental issues related to the global population, such as food & crop protection, pathogen and toxin detection, and environmental remediation. In this thesis, two new nanosensing diagnostic devices are developed and presented; surface enhanced Raman sensing and electrochemical sensing.

Surface-enhanced Raman spectroscopy (SERS) substrates were fabricated by templating a flexible thermoplastic polymer against an aluminium drinks can followed by coating with a silver film, to produce a rough nanostructured metallic surface. SERS is used for both qualitative (molecular fingerprint) and quantitative detection of dye molecules and food toxins. In addition, the SERS technique is also applied in combination with nanoelectrochemical square wave voltammetry to detect nano-concentrations of neonicotinoid pesticides. The enhanced sensitivity and minimum sample preparation requirements provide tremendous opportunities for food safety and security sectors.

An impedimetric immunosensor device (with a micro SD style pin-out) was also developed for the serological diagnosis of viruses and antibodies associated with bovine respiratory disease and bovine liver fluke. The silicon chip devices consist of six on-chip nanoband electrodes which can be independently modified with a polymer layer for covalent immobilisation of capture and target biomolecules. This electrochemical biosensor technology provides label-free and cost-efficient sensing capability in a compact size, and demonstrates the potential development of immunoassay-based point-of-use devices for on-farm diagnosis or therapeutic monitoring in animal health applications.

Acknowledgments

First and foremost, I would like to express my great appreciation to Dr. Alan O'Riordan, for giving me this incredible opportunity. His guidance and expertise have been invaluable and I wouldn't be here without his patience (lots and lots of that), support and encouragement. I would probably say, I now have a fairly good knowledge of electrochemistry and how to build greenhouses.

I would also like to thank all the other supervisors in the Nanotechnology group, Dr. Aidan Quinn, Dr. Micheal Burke and Dr. Daniela Iacopino, for all their help and advice. In particular, Dr. Mary Manning, for all the brainstorming and discussions we had when I wasn't allowed into the lab, and Dr. Armelle Montrose, who introduced me to the wonderful world of impedance. A huge special thanks to Dr. Pierre Lovera, who was my first supervisor at Tyndall (way back). He has given us some lasagne (once) and quite a few (about 6) football-related laughs. On a serious note, he has always helped me and been available for advice whenever I've needed it. Thanks Pierre and "Paris est Magique!"

A big, huge thanks to all my co-students in NTG; those who have escaped (Darragh, Ethel, Micki, Keith, Daniel, Baby Dan, Alfonso, Carola and Andrea), current NTGers (Fernando, Luiza, Rob and Abeer) and to the people outside of the group, my "Tea Amigos" (Fiona, Julia, Louise, Harry, Catherine, Tomas, Jan, Cian and Cormac) and all the Tyndall Taggers! I'm going to have to give a special mention to Caoimhe, who always made sure I wasn't going to become malnourished. Amélie, for keeping me sane throughout this whole process. Roxane, for all the stimulating Rugby conversation and getting me playing the greatest sport on earth. Ian, for completely encouraging and embracing my lab singing. Sean and Colm, for answering any questions/ concerns I sent your way (you thought you had escaped me). Finally, last and most certainly least, to my neighbour Benjy, who has a trifecta of attributes as my personal calculator, dictionary, and the-a-saurus. Between tea breaks, BBQ's, climbing mountains, horrendous cycles and evenings in our second home, Cavanaghs, you have all made these past 4 (maybe 5) years unforgettable.

I am grateful for all the members of the extended Tyndall community, who I worked and collaborated with, particularly to Donal O'Sullivan, Richard Murphy, Krimo Khalfi and

To my family

x

Table of Contents

Chapter 2:   Transparent Polymer-based SERS Substrates Templated by a Soda Can

Chapter 3: Spectro-electrochemical detection of Neonicotinoid Insecticides

Chapter 4: Bovine Viral Diarrhoea virus (BVDV) and antibody (BVDAb) detection in serum

Chapter 7: Summary, Conclusion and Future Work

Appendices

Chapter 1 Introduction

1.1 Trends and challenges in Agriculture and Food Systems

With the world population at over 7 billion and increasing to over 10 billion by 2050, we are experiencing an unprecedented exploitation of natural resources globally. The Food and Agriculture Organisation (FAO) reports global trends and challenges that will influence food and agriculture in the coming decades. These include population growth, water scarcities, loss of biodiversity, soil depletion and high levels of greenhouse gas emissions. They state that the challenges that need to be addressed in order to make agriculture and food systems sustainable are "the threats posed by climate change, the intensification of natural disasters and upsurges in transboundary pests and diseases, and the need to adjust to major changes taking place in global food systems." [1]

To achieve sustainable growth while reducing impacts on climate change, it is evident there is a requirement to develop robust and achievable mitigation strategies that can lower emissions within this sector, optimise efficiency from the use of natural resources, and ensure food security and safety. New digital technologies such as smart monitoring strategies and processing can deliver increased productivity and enhance the natural resource base while also minimising food losses and waste within the production systems and supply chain.

1.1.1 Control of Agricultural Diseases

The increased global food production required to meet the demand of the rising population amounts to 60% of our current agricultural output. A third of this is already lost due to emerging infectious diseases. Livestock diseases that remain endemics in parts of the world have devastating outcomes on animal health, impact on international trade as well as have a major economic impact on affected countries. [2]

Pathogens can emerge as a result of changes in the environment, in agriculture and in global demography. Farmers and commercial livestock producers need to be concerned about two major types of disease; the production limiting diseases, which include most of the respiratory diseases, Bovine Spongiform Encephalopathy (BSE, mad-cow disease)

and Enteritis, and the catastrophic diseases such as Foot and Mouth disease and the Swine flu.

It is important to understand the severity of the economic impact of these diseases; Bovine Respiratory Disease (BRD) is recognised as the leading natural cause of death in the US and EU beef and dairy herds, contributing to an annual loss of over 1 million animals at a total cost to the US agri-food industry of up to $2 billion.[3-6] It is one of the most devastating cattle diseases caused by a variety of viral pathogens: Bovine Viral Diarrhoea Virus (BVDV), Parainfluenza 3 (BPI3), Infectious Bovine Rhinotracheitis (IBR), Bovine Respiratory Syncytial Virus (BRSV), and Adenovirus.[5, 7, 8] Similarly, the outbreak of BSE in England in the 1990s cost $9 to $14 billion in compensation costs and $2.4 billion in losses of export markets.[9]

Disease outbreaks have detrimental impacts on the cattle industry as diseased animals perform sub-optimally and decrease on-farm efficiency and profitability through waste feed, increased labour and veterinary costs. Control and management of these diseases and maintaining healthy livestock is absolutely crucial for achieving sustainable food production and to reduce production losses. However, stressors predisposing to the severity of infections, like BRD, include animal transportation and mixing, feedlot alterations, and climate variation, all of which are common farming practices.[10, 11] Furthermore, increasing milk yields and herd size, which are a necessary requirement for the growing population, will increase overcrowding and add to this already high-stress environment. Consequently, this demand-driven livestock production will pose a concern to farm animal welfare and inevitably increase the spread of disease. Given the magnitude of this issue, control and eradication strategies must be implemented on a global scale to minimise losses arising from diseases. Rapid identification of disease states is now critical for herd and crop protection and for the prevention of outbreaks.

Technological advancements must be employed to provide farmers with tools and resources to make farming more sustainable. Subsequently, to ensure effective decision making at farm level, farm-side diagnostic devices that permit fast, economical detection of disease-causing pathogens and biomarkers are essential.[12] Screening for these diseases in live animals will enable targeted treatment and more informed herd health

management, reduced therapeutic costs and increased animal performance, and improved use and implementation of vaccination and eradication disease control strategies.

1.1.2 Agricultural and Environmental monitoring

The introduction of modern sensing technologies into the agri-food sector for disease control and eradication can be expanded to provide accurate data for monitoring crops, soil, water and other environmental conditions. Fundamentally, the widespread use of pesticides needs to be monitored and controlled. A pesticide is defined by the Food and Agricultural Organisation (FAO) as "any substance or mixture of substances intended for preventing, destroying, or controlling any pest, including vectors of human or animal disease, unwanted species of plants or animals, causing harm during or otherwise interfering with the production, processing, storage, transport, or marketing of food, agricultural commodities, wood and wood products or animal feedstuffs."[13]

The majority of pesticide usage for crop protection is targeted against pests such as insects, rodents/ birds, weeds and microorganisms. They are classified in groups such as insecticides (organophosphates, pyrethroids and neonicotinoids), herbicides and biopesticides, based on the pests they are intended for. The hazards resulting from pesticide usage are well documented in the literature.[14-17] Their drawbacks include the potential toxicity to humans and other non-target organisms through environmental contaminations in soil, water, and other vegetation.[18, 19] Although, pests and diseases damage up to one-third of crops during growth, harvest or storage; with the growing global concern over food scarcity, pesticide usage is essential in modern agricultural practices, providing the required benefits such as increased food production, improved farm productivity and food quality, extended shelf-life, as well as the obvious economic advantage to farmers.[20, 21] There are exceptions to the predominantly negative view of pesticides; Lomborg *et al.* wrote, "If pesticides were abolished, the lives saved would be outnumbered by a factor of around 1000 by the lives lost due to poorer diets. Secondary penalties would be massive environmental damage due to the land needs of less productive farming, and a financial cost of around 20 billion US Dollars".[22]

Implementation of new technologies for the detection of pesticides can provide monitoring and regulation of pesticide usage in the environment. Sensors can potentially provide real time data on soil nutrients, monitor water run-off and contaminants in water supplies and also detect pesticide residues on food and crops. Another advantage of implementing sensor technologies is to reduce nitrogen emissions by determining the nutrient content of soils prior to fertilisation. Monitoring can, in turn, encourage a reduction in pesticide usage (or introduce insect-specific pesticide use) and better placement of fertilisers to ensure the production of high quality foods and sustainability in the market. Recent technological advancements have encouraged the creation of "point-of-concern" techniques, that provide added advantages such as ultrasensitive detection, faster turnover, *in-situ* sampling, on-site capability and reduced cost.

1.1.3 Food Safety and Security

"Food security exists when all people, at all times, have physical and economic access to sufficient, safe and nutritious food that meets their dietary needs and food preferences for an active and healthy life."[23] Food security has become a primary focus and concern as it directly affects both human and animal lives. Maintaining clean resources and food quality is a key challenge in food sustainability. It is one of the most topical issues, with thousands of recalls globally every year. In 2016, the Food and Safety Authority Ireland issued a total of 67 food alerts. Of this total, 28 were food allergen related for mislabelling the presence of milk, eggs, soybeans and nuts. Whereas the remaining 39 food alerts were either product recalls or withdrawals from the Irish market for the following reasons: presence of a foreign body, presence of pathogens, and chemical contamination. A Category 1 alert is when there is an identified risk to consumers and official action is compulsory. Some Category 1 examples in Ireland include the presence of salmonella in chocolate, a high nicotinic acid content in a pre-workout drink, presence of histamine in tuna fish cans, the presence of *listeria monocytogenes* in hummus and the recall of tofu due to rodent infestations.[24]

The development of sensor technologies in food safety can provide rapid detection of foodborne toxins, allergens, pathogens, toxic chemicals, heavy metals, and other

contaminants. Point-of-use sensors have the added ability and advantage to detect contaminants in food as well as microbes in food packaging, prior to human consumption. In the case of the food adulterant Melamine, which was widely used to falsely increase the protein content of infant formula in China, the discovery of the chemical was post-retail. Subsequently, the delay in discovery affected ~300,000 Chinese infants and young children.[25, 26] Moreover, the economic impact of the product recalls was massive.[27] Another discovery that received heightened scrutiny by the FDA and FAO was imported seafood, mainly from Southeast Asia and China, which tested positive for the presence of harmful substances and unapproved drug residues such as dyes like crystal violet (CV), malachite green (MG), fluoroquinolones (FQs), and other illegal drugs.[28] The majority of imported seafood also contained antibiotic residues.[29] To this end, the use of banned chemical contaminants in food needs to be more strictly controlled. Superior "point-of-care" technologies provide the required sensitivity and selectivity to achieve this.

1.2 Sensing at the Nanoscale

Nanotechnology and nanomaterials have enabled significant advancements in analytical sensor devices within the agri-food, environmental, pharmaceutical and security sectors. They are the most promising tool in dealing with animal health and environmental issues related to the global population, such as food & crop protection, pathogen and toxin detection, water purification and environmental remediation.

Currently, most existing sensors are limited in their ability to sense and discriminate small amounts of analyte with sufficient selectivity, as well as limited in their remote sensing capabilities. The development of new sensing devices based on nanomaterials can be an alternative to overcome these limitations. Nano/micro system technology has the potential to enable significant developments in food production and next generation farming practice through the provision of real time data from point-of-care sensing systems. Nanosensors are therefore expected to lead to innovative applications, providing early disease detection that can result in faster treatments and better outcomes, as well as the early and accurate detection of environmental pollutants, contaminants, and even biological or chemical weapons.

Sensors, by definition, are devices that react to a physical, chemical or biological change in their local environment and convert that change into a measureable, quantifiable signal[30]. They are composed of two parts: the receptor, i.e. sensing element and the transducer (the detector device) which converts the change into an observable response. The main transduction methods generally used are electronic,[31, 32] piezoelectric, thermic, electrochemical[33-35] and optical.[36-38] Due to their unique chemical and physical properties, nanomaterials may be used as a transducing component, as well as receptors. Nanomaterials and nanofabricated devices have many advantages over bulk materials and traditional sensors. One advantage is their ability to be fabricated on the same scale at which many physical phenomena occur e.g. DNA width ~2 nm.[39] Furthermore, advances in nanofabrication approaches, particularly the convergence of 'top-down' and 'bottom-up' fabrication techniques have accelerated the development of functional nanosensing devices that demonstrate improved performances when compared to traditional larger

devices. A second advantage of employing smaller sized sensors is that it enables high densities of sensors to be fabricated in a much smaller footprint at key substrates, such as on silicon chips, thus yielding much higher information-generating capability per device. To this end, there is the potential to achieve enhanced sensitivity at a smaller footprint compared to traditional microsensor devices by increasing the number of sensing elements in the device by fabricating arrays of nanosensors.

The main requirements of sensors, i.e. selectivity, sensitivity, fast response, low fabrication costs, robustness and portability, are fulfilled by the use of nanomaterials and nanotechnology. For example, nanosensors enable the measurement of most molecular interactions in real-time with much faster analysis times.[40] The selectivity and sensitivity of nanosensors can be further improved using a suitable transducer with the receptor according to the targeted application. For example, within the environmental and security sectors, localised surface plasmon resonance excitation provides molecular fingerprinting of molecules of interest[41] due to enhanced properties of nanostructures. These nanosensor devices, providing highly sensitive measurements, can be classified according to their transduction methods.

In this thesis we will focus on the optical transducer, particularly surface enhanced Raman spectroscopy (SERS), as well as the more broadly used electrochemical transducer.

1.3 Optical Transducer – Vibrational Spectroscopy

Molecules are made of atoms which are connected by chemical bonds. The length of the chemical bonds or the distance between atoms is not fixed, so, as a whole, molecules vibrate and rotate. The spectroscopic method for studying these vibrations is vibrational spectroscopy.[42]

A molecular vibration occurs when atoms in a molecule are in periodic motion while the molecule as a whole has constant translational and rotational motion. A molecular vibration is excited when the molecule absorbs a quantum of energy, E, corresponding to the vibration's frequency, v, according to the relation $E = hv$, where h is Planck's constant. This energy comes from different wavelengths of light. Subsequently, each chemical bond in the molecule has a unique vibrational energy which provides a unique fingerprint of the molecule. There are two types of vibrational spectroscopy that can be used to directly measure vibration frequencies: infrared spectroscopy and Raman spectroscopy.[43] In this thesis, Raman spectroscopy is the main focus.

1.3.1 Vibrational Modes

There are three types of motion in a molecule; translational, rotational and vibrational motion. Translational and rotational motions are movements of the molecule as a whole, either in the same direction or spinning on its axis, respectively. The third motion is vibrational motion, which, as discussed previously, is the movement of the covalent bonds between atoms within a molecule. This occurs at specific frequencies corresponding to their vibrational energy level, which is called the vibration frequency ($\sim 10^{13}$ to 10^{14} Hz), and corresponds to wavenumbers (~ 300 to 3000 cm^{-1}) in the Raman or IR spectra.[44, 45]

A diatomic molecule contains only a single motion, while polyatomic molecules exhibit more complex vibrations known as normal modes.[46] The six normal modes of vibration are illustrated in Figure 1.1. The vibrational modes can be either IR or Raman active, which are complimentary to each other. A three atom complex (a central atom and two atoms connected by covalent bonds) is used as an example to describe the vibrational movements:

- Stretching – changing the bond length, either symmetrically or asymmetrically. Symmetric stretching is where both atoms move simultaneously towards and away from the central atom. Asymmetric stretching is where the atoms move in opposite directions towards and away from the central atom.

- Bending – changing the angle between the bonds. Both atoms are moving toward each other or both away from each other, in the same plane, so the bond angle is getting smaller and larger.

- Rocking – changing the angle between groups of atoms. Similar to bending but the atoms move in the same direction, clockwise or anticlockwise, i.e. the bond angle remains the same.

- Wagging – changing the angle between the plane and a group of atoms. Both atoms are moving out of plane simultaneously in the same direction.

- Twisting – changing the angle between the planes of two groups of atoms. Both atoms are moving out of plane in the opposite directions.

Symmetric Stretch	Bending	Twisting
Asymmetric Stretch	Rocking	Wagging
Stretching	**In-plane**	**Out-of-plane**
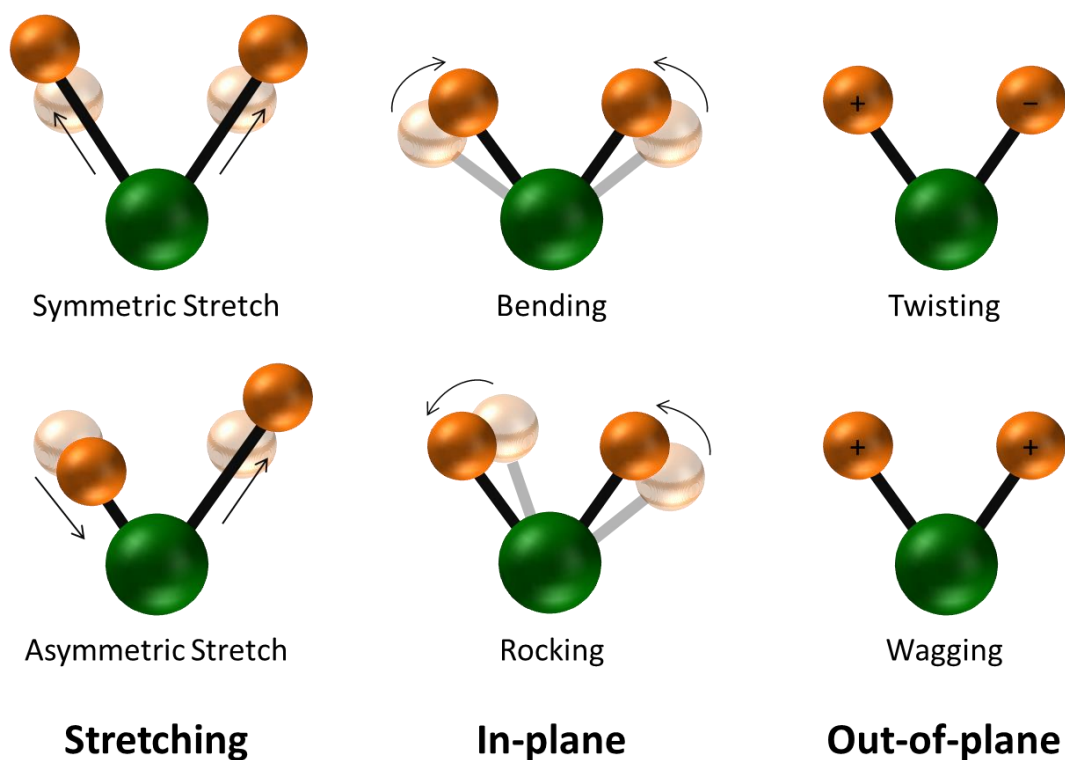
Figure 1.1: Six ways in which molecular bonds can vibrate. The green circle represents the central atom and the orange circles are the vibrating atoms. There are two stretching vibrations (asymmetric and symmetric), and two in plane (bending and rocking) and two out of plane (wagging and twisting) vibrations.

1.3.2 Raman Spectroscopy

Spectroscopy is the study of interaction of electromagnetic radiation with matter. Raman spectroscopy is a spectroscopic technique for studying vibrational, rotational, and other low-frequency modes in a system. It was first discovered in 1928 by Sir Chandrasekhara Venkata Rāman,[47] an Indian physicist. The Raman phenomenon has led to major advancements in spectroscopy, including the detection of Raman active molecules by observing the molecule's vibrational and rotational modes. The Raman technique uses a monochromatic beam or laser source, and occurs in the visible, near-infrared, or near ultraviolet range of the electromagnetic spectrum, see Figure 1.2.
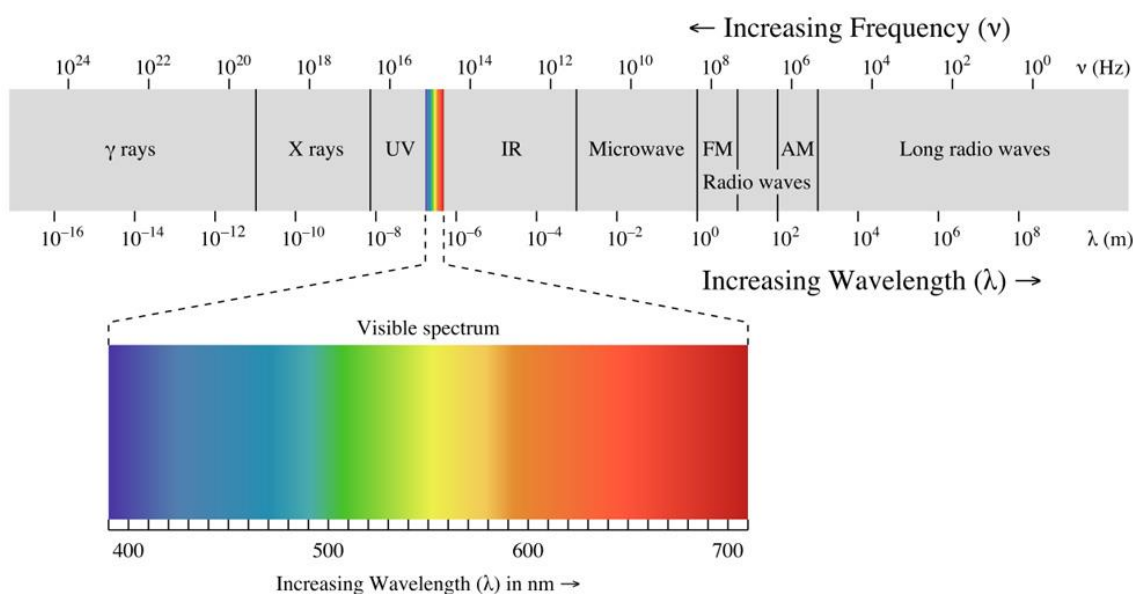
Figure 1.2: The electromagnetic spectrum highlighting the visible region, (reproduced from [48]).

Molecular energy levels are quantised and from this we can develop the concept of scattering cross section, which is an area that contains the probability of photons being scattered after interaction with a molecule. In order to determine if a molecule is Raman active, the classical Raman Effect must be considered. This effect is described by the polarizability, α, of a molecule, which determines its distortion in an electric field, E, and the vibrational cross section.[49] When an electric field is applied to a molecule, it induces a dipole moment in the molecule and is described by:

$$\mu_{ind} = \alpha.E$$

(Equation 1.1)

12

The induced dipole oscillates at a certain frequency, and photons are emitted at that frequency. Whether the frequency is the same as the incident light, or has changed, determines whether the scattering is elastic or inelastic. The polarizability is determined by the size and shape of the electronic cloud and for a molecule to be Raman active, this polarizability must change during the molecular vibration. Therefore vibrational modes that alter the electric cloud are said to be Raman active.[49, 50]

The quantum mechanical theory of light interacting with molecules in air provides an explanation of the scattering process known as Raman scattering.[51] When light interacts with a molecule, it distorts the molecules cloud of electrons to form a "virtual state". This state is not stable and the photon is immediately re-radiated as scattered light. The majority of light is elastically scattered, i.e. the energy of the incident photon and the scattered photon are the same. A small fraction of photons are also scattered inelastically, or Raman scattered, whereby the scattered light has different energy from incident light. Figure 1.3 shows an energy diagram for the two types of scattering. [52]
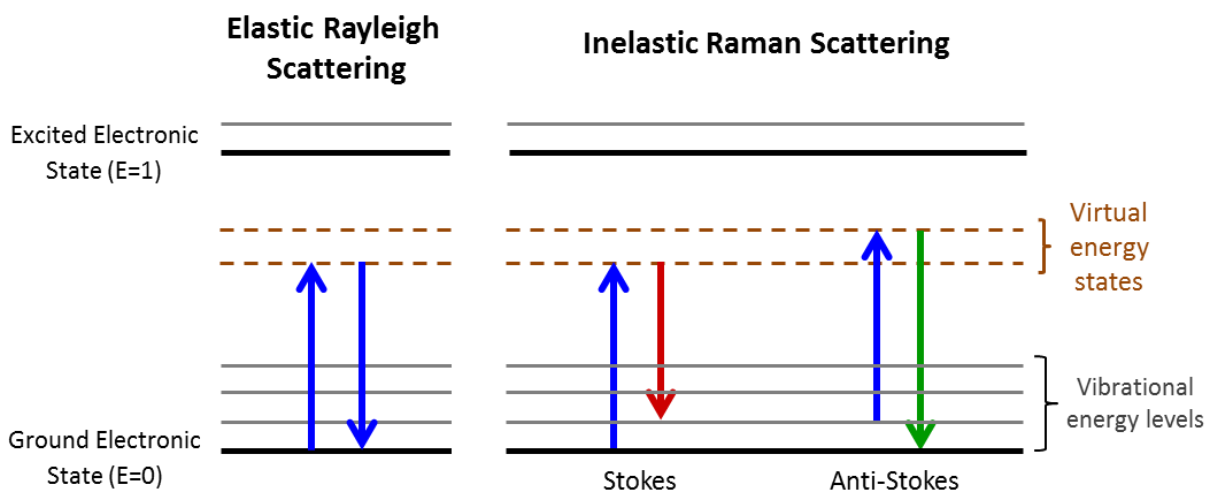
Figure 1.3: The Jablonski diagram[53] of quantum energy transitions for Rayleigh and Raman Scattering (adapted from [54])

Rayleigh scattering is a process in which an electron in the ground level is excited and falls to the original ground level. Because this scattered light is does not involve any energy change from the incident light, both lights have the same wavelength. There are

two types of inelastic scattering whereby the emitted photon either has gained energy or lost energy. These are known as anti-stokes and stokes, respectively.[55] Stokes Raman scattering is a process in which electrons are excited from the ground level and falls to a vibrational level, involving energy absorption by the molecule. Therefore the scattered light has less energy and longer wavelength than incident light. Alternatively, with anti-Stokes scattering, the electron is exited from a vibrational state to the ground level. Energy is therefore transferred to the scattered photon, thus anti-Stokes Raman scattered light has more energy and a shorter wavelength than the incident light.

The energy of each scattered photon corresponds to a vibrational mode in the molecule which has a characteristic spectral peak. A collection of these provides spectral molecular fingerprints of the Raman active molecule of interest. Figure 1.4 illustrates the components of a typical Raman spectrometer. A collimated beam of monochromatic laser light is provided by the excitation source and expanded out by the beam expander. The laser light (photons) is reflected by a series of mirrors and focused onto the sample in the sample holder. The laser light irradiates the sample and the photons interact with the molecules. The light is emitted and scattered as electromagnetic radiation.[56] This scattered light is collected by the microscopes objective lens and passed back through a series of filters which collect the Raman scattered light (Stokes) and filters out the Raleigh and Anti Stokes light. The light is then focused through a diffraction grating, which bends the Raman shifted light according to wavelength. The photons are detected by a charged coupled device, CCD, which counts the number of photons at each wavelength, and the software displays the spectrum.

Raman spectroscopy has its advantages in that is it non-destructive, requires little sample preparation and has a fast analysis time. However, the technique has limitations that hinder its effectiveness. The intensity of Raman scattering is very weak; only 1 in 10^8 incident photons are Raman scattered resulting in its low detection sensitivity which makes it impractical and vulnerable to background interferences.[57] The efficiency of this scattering can be increased by various enhancement methods, particularly surface enhanced Raman spectroscopy (SERS).
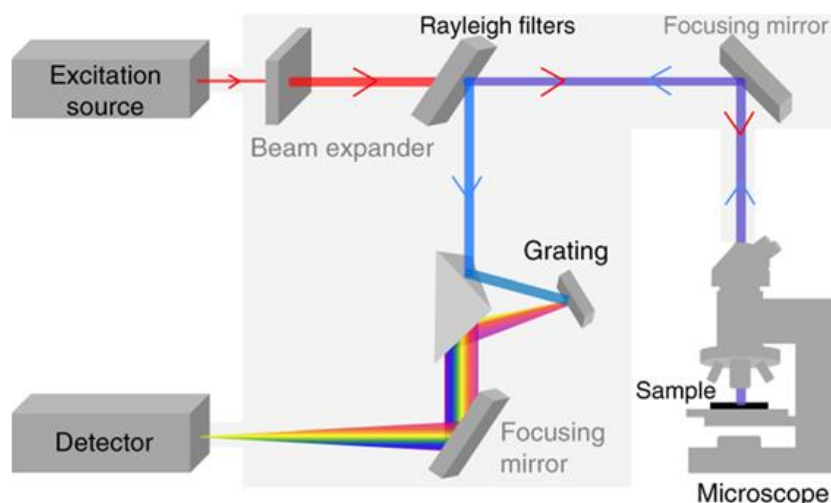
Figure 1.4: Schematic of the laser path in a typical Raman spectrometer, (reproduced from [58]).

1.3.3 Discovery of Surface Enhanced Raman Spectroscopy (SERS)

Surface enhanced Raman spectroscopy is a surface sensitive technique that significantly increases the signal of Raman active molecules adsorbed onto metallic surfaces. This was first observed by Fleischman *et al.* in 1974, when SERS was obtained from pyridine on electrochemically roughened silver.[59] However, he did not acknowledge the intensity increase from the roughened silver, and proposed that the increase was due to a larger amount of pyridine adsorbed onto the surface. The phenomenon was discovered three years later by different groups,[60, 61] when they identified that it was the roughened silver surface that caused the Raman enhancement. In SERS, lasers are used to excite the vibrational transitions of molecules adsorbed onto nanostructured metallic surfaces, which enhances the Raman signal, by factors of up to 10^8. SERS has presented an approach to overcoming the sensitivity problems associated with Raman spectroscopy. The importance of SERS is not only that it improves the sensitivity but also that it is a surface-selective technique.

1.3.4 The Mechanisms of SERS

SERS enhancement occurs at nanostructured plasmonic surfaces following illumination with monochromatic radiation. It is generally accepted that there are two separate

mechanisms that combine to generate the SERS phenomena. The first is responsible for the majority of SERS enhancement and is based on an electromagnetic enhancement due to localised surface plasmons, whereas the second mechanism is a chemical resonant energy charge transfer.[59, 62-64]

1.3.4.1 Electromagnetic Mechanism

The electromagnetic mechanism (EM), proposed by Gersten and Nitzan,[65, 66] is viewed as the more dominant theory as it accounts for physisorbed species on the surface as well as chemically bonded species. The theory suggests that Raman enhancement is due to the excitation of localised surface plasmons (LSP) in the metallic nanostructures by the incident radiation. Briefly, when light impinges on the nanostructure, it causes the free conduction electrons on the surface to oscillate. This collective oscillation is known as localised surface plasmon resonance (LSPR).[67] The excited LSP's make the molecule highly polarisable and forms a large electric field on the surface. This electric field induces dipole moments in the molecule on the nanostructures, and sequentially produces the Raman enhancement. This large localised electromagnetic field present around the nanostructure or gap between the closely-spaced nanostructures, that provides Raman enhancement, is known as the "hot spot",[68] see Figure 1.5. The intensities of the Raman photons are susceptible to enhancement, if their wavelengths are in resonance with the plasmon mode of the nanostructure. LSPR enhancement, therefore, depends on the size and shape of the metal nanostructures, which will be discussed in the next section.

The increase in SERS signal is due to an increase in the cross-section of the molecules, resulting in the concept of the SERS enhancement factor (EF). SERS is generally measured from assemblies of different nanostructures, so the enhancement factor (EF) can therefore be described as the average of a combination of enhancements for many molecules in different situations, i.e. depending on their adsorption states, the roughness and homogeneity of the surface, surface morphology, the laser intensity and wavelength, etc. Experimental values of EFs are typically in the range of 10^4 to 10^6, which is a combination of the above described weak enhancements and strong "hot spots". However, electromagnetic "hotspots" are claimed to have provided massive enhancements of between 10^{11} to 10^{14} orders of magnitude to the SERS signal.[69] This

theory is still being largely researched as it is key to single molecule detection, which may be achieved from selective excitation of single molecules.[70-72]
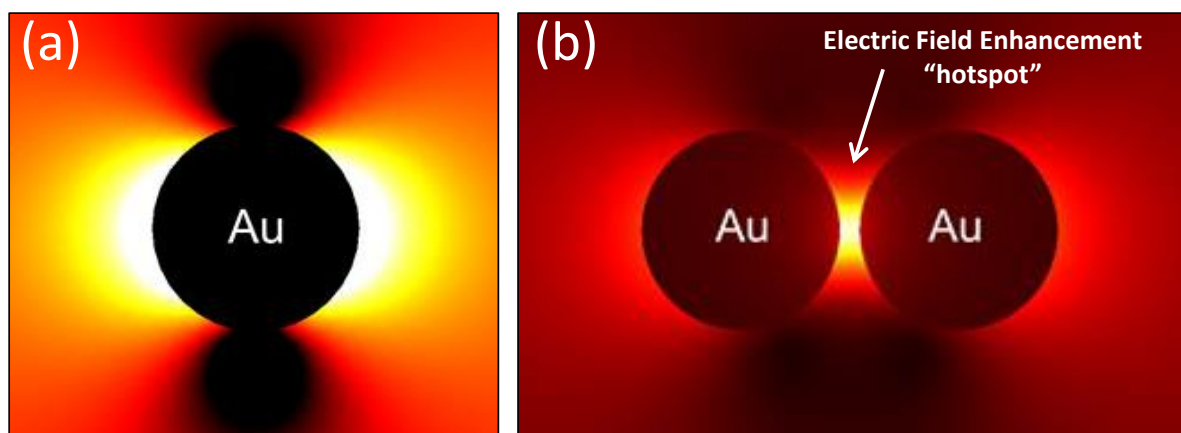
Figure 1.5: Plasmonic effects: (a) Electric field distribution around a nanoparticle and (b) Electric Field around two nanoparticles and the presence of a SERS "hotspot", (reproduced from [73]).

1.3.4.2 Chemical Mechanism

The origins of the chemical mechanism for enhancing SERS are still a topic of discussion.[74-77] Although controversial, the mechanism is based on the change in polarisability of molecule adsorbed to a metal surface. It is estimated that the chemical effect contributes to a factor of 10^2 of the total SERS enhancement.[78] The mechanism arises when an analyte is adsorbed onto a metallic surface; a chemical reaction occurs between the surface and the adsorbate, known as chemisorption. In this reaction, the analytes molecular orbitals broaden into the conductive electron band of the metal therefore overlapping with the Fermi-level for the metal. The Fermi energy level of metal cluster drops between the lowest unoccupied molecular orbital (LUMO) and the highest occupied molecular orbital (HOMO), illustrated in Figure 1.6. Upon absorption of the incident laser light, charge transfer occurs between the molecule and metal.[79] This enhances the polarizability of the molecules (refer to Equation 1.1), and hence enhances the Raman response.[80, 81] The chemical effect is only associated with situations where there is a chemical interaction between a molecule and the metallic surface. Therefore it is unique to the binding site and strongly dependent on the analyte molecule.
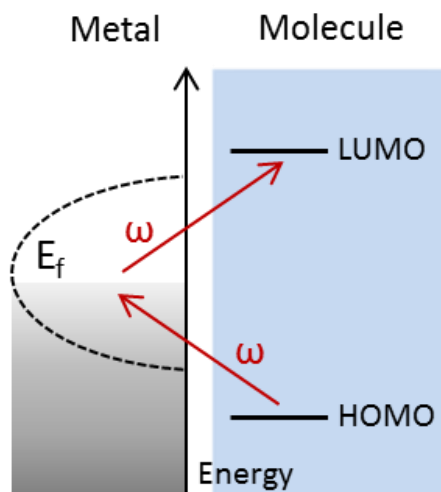
Figure 1.6: Charge transfer model for the SERS chemical enhancement mechanism (adapted from [82]).

1.3.5 Fabrication of SERS-active substrates

The fundamental requirement for SERS fabrication is a substrate that supports a surface plasmon resonance. In general, SERS substrates must have a nanostructured rough surface with well-defined gaps in the region of 10 - 100 nm between metallic clusters in order to amplify scattering.[83] The electromagnetic field strength depends on the polarisation and wavelength of the incident light and thus causes an enhancement. But the main feature that affects the enhancement is the physical parameters of the nanostructures (such as material, geometry and arrangement) of the nanostructures on the surface.[68, 84] The SERS signal intensity will decrease if the surface structures are smaller than ~10 nm or larger than ~100 nm. For example, by decreasing the gap between the nanostructures, the electric field will become more localised and concentrated, and the corresponding SERS intensity signal increases. An example of this is discussed by Lee *et al.* where the nanogap is decreased from 30 nm to 10 nm, and an intensity increase of over 200-fold was observed.[85] There are two fundamentally different approaches to development of SERS-active nanostructures with "hotspots": bottom-up assembly and top-down synthesis.

1.3.5.1 Bottom-up Assembly

Bottom-up approaches refer to the fabrication of nanostructures by chemical synthesis[86], colloid aggregation[87] and self-assembly.[88, 89] These methods have been reported to fabricate a variety of nanoparticles ranging from a few nanometers to a few hundred nanometers in size. Metal nanoparticles can be synthesised chemically at low cost with a tailored geometry such as nanoparticles,[90, 91] nanowires,[32, 92] nanospheres,[90, 93, 94] nanorods,[95-97] nanotubes,[98] nanotriangles,[99] nano-urchins,[100] and/or nanoshells[101] (see Figure 1.7).
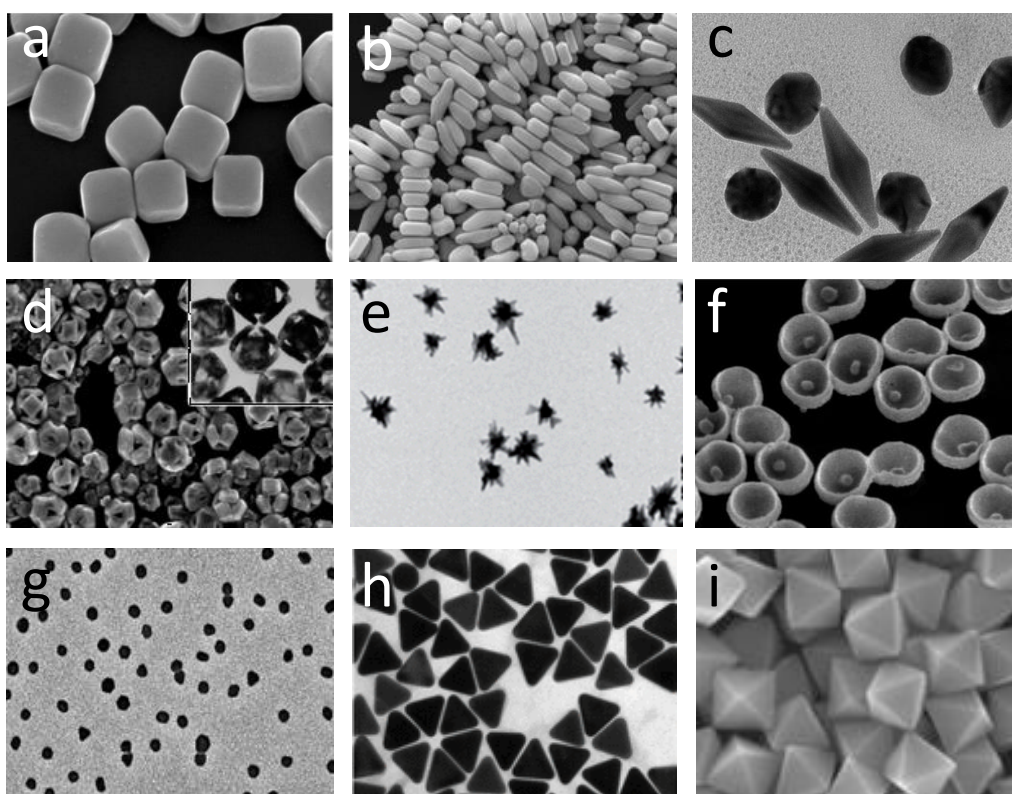
Figure 1.7: TEM and SEM images of (a) Ag/ Au nanocubes, [102] (b) gold nanorods, [103] (c) Au bipyramids,[104] (d) Au nanocages, [105] (e) nanostars,[106] (f) Au nanobowls with Au seed inside,[107] (e) gold nanocages,[105] (g) Au nanotriangles,[108] and (h) gold octahedral colloid[109] (Figure adapted from [110])

Plasmonic nanoparticles of metals such as gold or silver possess great potential for numerous applications due to their unique optical properties.[83, 111] The most common fabrication of SERS substrates are gold (Au) and silver (Ag) colloids in diameters between 10 and 200 nm, as they yield the greatest enhancements at their "hot spots". [112] These nanoparticles

comprise the fundamental SERS "building block" and are easy to isolate. They are generally presented in a suspension or sol-gel in the presence of the analyte of interest.[113-115] They can then be drop-casted onto a substrate where they aggregate, creating the necessary hot spots for Raman enhancement.[116] A disadvantage to this method is that nanoparticle suspensions must be mixed with the analyte solution for SERS applications,[117] which is not ideal for measurements on non-Raman active surfaces. However this drawback was addressed by Yang *et al.* who grew Ag nanoshells on thiol-modified silica NP's, and deposited them directly on apple skin for analysis. [118] Although there is a greater enhancement observed with these substrates, it is hard to obtain a homogeneous surface to produce a uniform enhancement. Additionally, they are not suitable for field analysis, due to their complex preparation steps. In contrast, devices which employ a solid base may be more suited for portable sensing, i.e. NP's that are immobilised on a solid substrate.[119-122] For example, Fan *et al.* fabricated and self-assembled Ag NPs onto glass slides by using 3-mercaptopropyltrimethoxysilane.[122] The transference of the particles to solid supports stabilises them, avoids the usual aggregation process and produces self-sustaining and portable SERS active substrates. Yu *et al,* fabricated silver colloidal nanoparticles for SERS analysis but alternatively injected them through a millipore PVDF filter membrane, thus entrapping them in the filter. The filter therefore was used as the solid portable substrate. It demonstrated 1–2 orders of magnitude better SERS enhancement than the typical approach of drying a sample in silver colloid onto a surface. [123] In addition, Shiohara *et al.* fabricated gold nanostars and deposited them onto a PDMS platform for SERS evaluation. They used back side illumination for detection of selected pesticide on fruit skin [106] These methods are deemed more suited for remote sensing applications.

Optical fiber-based SERS sensors are devices which have generated steady interest as a versatile means of extending SERS for portable field applications.[124-126] Also there is a growing interest in the fabrication of paper-based SERS substrates. These substrates are ultra-low cost, disposable, easy to use and highly suitable for point of care sensing applications. Polavarapu *et al.* fabricated SERS substrates by directly writing on paper using a pen filled with plasmonic nanoparticle inks to detect thiabendazole, which is a fungicide and parasiticide.[127] Lee *et al.* also fabricated SERS paper substrates impregnated with gold nanorods by dip coating. [128] Chen *et al.* combined adhesive tape

and SERS activity of Au nanoparticles to fabricate a "SERS tape" substrate. The Au particles were deposited onto the sticky side of the tape and it was used to extract pesticides from different kinds of fruit and vegetable peels. [129] These paper-based sensors fabricated by different methods dramatically improve the portability and feasibility of SERS detection for pollutants as a promising technique for both laboratory and field-based detection. Bottom up assemblies have shown very high enhancement but they often give inconsistent performance when spot tests are conducted within a substrate or between "identical" substrates. This is mainly because of a lack of structural uniformity over the entire area of the substrate resulting in poor reproducibility and inhomogeneity. Also the arrangements of the aggregates are hard to control with these methods.

1.3.5.2 Top-down Synthesis

The ability to control the shape and orientation of nanoparticles on a surface has reduced many of the complex variables related to SERS and has greatly enhanced our understanding of the phenomenon. In general, top-down approaches for nanofabrication are very common as they are cost effective scalable and highly reproducible. Top-down approaches include lithography techniques (electron-beam (E-beam),[130, 131] focus ion beam milling and nanoimprint lithography[132]), laser etching[133], film deposition (sputtering, metal evaporation, atomic layer deposition)[134, 135] and templating (using anodic aluminium oxide [98], masks[134] or molds[92]).

E-beam and nanoimprint lithography are fabrication methods used in nanotechnology to create patterns with dimension down to 10 nm. In e-beam lithography, a resist is exposed to an electron beam, which induces a change in the chemical structure of polymer resist (cross linking). The exposed polymer can be washed away using a solvent, leaving only the unexposed polymer on the substrate. Metal is then evaporated on the whole substrate and the unexposed polymer is then removed using another solvent. This process results in the metal being deposited only on areas that have been patterned. SERS substrates with various geometries such as nanoparticle dimers have been fabricated using E-beam lithography, see Figure 1.8.
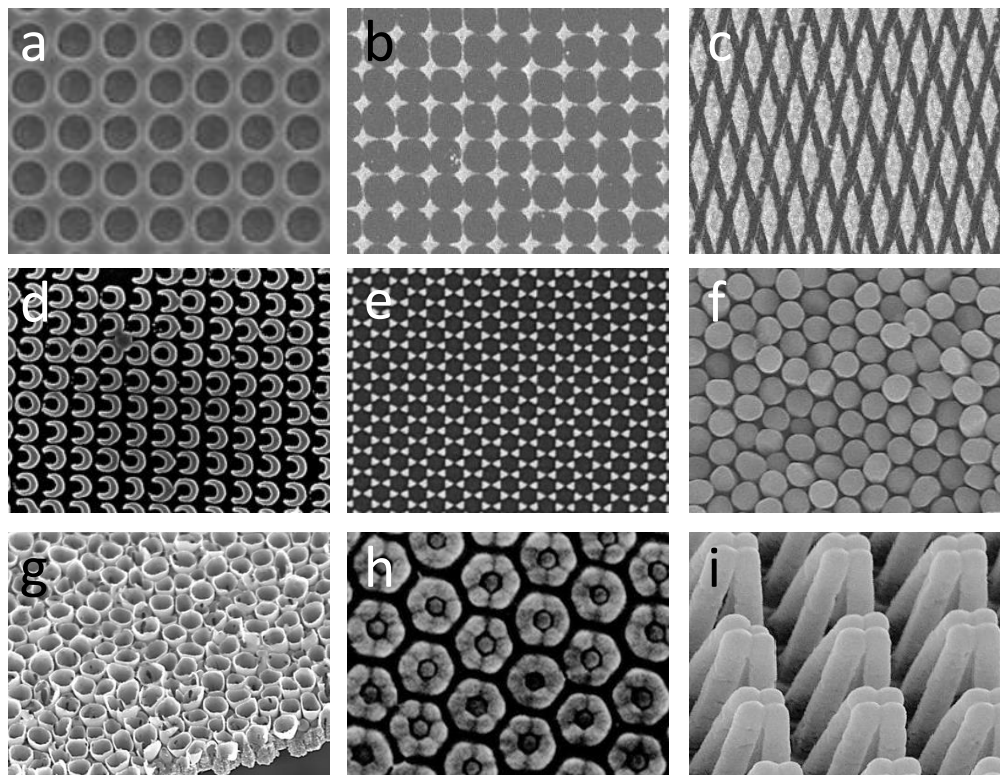
Figure 1.8: TEM and SEM images of top down approaches including E-beam fabricated (a) gold nanodisks,[131] (b) Au star-like arrays,[136] (c) Au diamond shaped structures,[136] (d) Ag nanocrescent structures,[137] (e) Au nanotriangles[138] ; AAO templated structures: (f) Ag-nanorods via metal deposition,[139] (g) Pt nanotubes by E-beam evaporation, [139] (h) Ag "nano-crown" arrays[140] and (i) Au "nanofingers".[141]

Similarly, Hu *et al.*. fabricated polymer nanofinger structures on Si wafers using nanoimprint lithography, and coated the nanofingers with 70 nm of gold by e-beam evaporation, see Figure 1.8 (i). Following fabrication, exposure to solvent induced leaning or self-closing of the nanowires, creating hot spots,[141] and demonstrating how powerful nanofabrication lithography processes are. They fabricated arrays of electromagnetically coupled Ag nanoparticles on Si, and could increase Raman efficiency by controlling the interparticle separation between Ag nanoparticles.[142] These substrates show high SERS enhancement with good control and reproducibility. However, lithography methods, although extremely tuneable and scalable, suffer from a high cost and slow throughput.

SERS substrates fabricated by templating methods is another common approach and have been demonstrated by a number of groups, see Figure 1.8 (f) to (h). Van Duyne *et al*. have studied substrates based on colloidal Polystyrene (PS) capped by silver. These substrates

have shown high enhancement and have been used to demonstrate sensing of analytes such as glucose [143] Another very popular method is using widely employed Anodised Aluminium Oxide (AAO) as a template to produce nanotubes.[144] Aluminium foil is anodised in acid to create nanopores which are then used as a template to create SERS substrates. Metals can be pulsed electrodeposited inside the template channels,[139] [145, 146] or deposited via electron beam evaporation, [147, 148] Alternatively, polymers can be employed to template the AAO. Lovera *et al.* fabricated superhydrophobic PS nanotubes by wetting commercial AAO filters and depositing silver onto the resulting PS nanotube structures.[98] Similarly, Wang *et al.* patterned polymethyl methacrylate (PMMA) on a honeycomb-like AAO template and deposited Ag onto the polymer to create Ag "nano-crown" arrays.[140] Other templates used for the fabrication of nanowires and nanotubes for SERS substrates include Polycarbonate membranes (PCM),[149-151] Polystyrene microspheres (PSM)[152-154] and nano-channel glasses. The above substrates fabricated with "top-down" methods can be manufactured reproducibly with high throughput, but often produce weaker signals and involve the use of expensive equipment and/or complex procedures.

1.3.5.3 Commercially available SERS substrates

There are several commercially available SERS substrates. Klarite[TM] substrates, the most well know commercial SERS substrates, are based on gold coated inverted pyramids. They show a high and homogeneous enhancement of 10^6. A single substrate costs €55, and only 633 nm and 785 nm laser wavelengths are suitable for analysis. Slimco "SERSstrates" are manufactured nanopillars on a silicon chip with gold or silver coatings, costing €70 for a single-use substrate. Integrated Optics substrates are similar in price to the Silmco substrates at €77. They fabricate gold and silver nanostructures on soda-lime glass. Ocean Optics glass slide SERS substrates based on gold (785 nm) or silver (532 nm) nanoparticles on paper, or gold/silver nanosponge technology (638 nm). Other substrate include Q-SERS substrates (Nanova Inc., Columbia, Mo., U.S.A.), StellarNet Inc. substrates and Horiba scientific SERS substrates.

1.3.6 Application of SERS

As described previously, SERS is one of the most powerful techniques for surface science and is emerging as a powerful technique for remote chemical [155] and biological sensing applications[156]. It allows for highly sensitive detection of molecules of low concentration. Its flexibility in regard to the various chemical and biological species it can detect, coupled with the wide range of instruments available for identification, has progressed SERS as one of the most highly sophisticated analytical techniques. It offers many advantages when compared to standard laboratory techniques, such as rapid and easy sample preparation processes, portability of sensors, and the suitability for large-scale screening. It is therefore advantageous within various fields of research including industrial, material, forensic, biological and electrochemical fields.[135, 156-158] Continuing the theme of this study (outlined in section 1.1), the applications of SERS sensing within the agri-food industry are discussed in this section. These primarily consist of contaminants from agriculture and the environment, and chemical adulterants. The most common chemical contaminants in foods that have been studied using SERS are pesticides, melamine, antibiotics and illegal drugs and illegal food dyes.

1.3.6.1 Environment

Environmental pollution has become an increasingly serious problem, mainly due to human interferences. Accordingly, there are growing demands for the development of corresponding analytical techniques for a variety of pollutants affecting crops (pesticides), water (heavy metals) and the air (polycyclic aromatic hydrocarbons). In this study, the SERS publications on environmental pesticides are reviewed. Unfortunately, rapid, chemical analyses of these environmental pollutants are unavailable, and only a very small fraction of foods are inspected. Pesticides are widely used in modern agriculture. The first SERS study of pesticides was the detection of organophosphorus pesticides in 1987 by Alak *et al*.[159] Since then, the potential toxicity to humans, animals, and the environment was discovered, and tolerance levels were introduced for a large number of harmful pesticides. [160] This triggered the investigation, and thus, the publication of numerous articles and reviews on the analysis of different types of pesticides in the environment.[161-163] Moreover, SERS detection methods have also developed considerably, resulting in a large number of the more recent reports employing

in-situ SERS detection methods on the skin of different foods.[164-166] A web of science search combining the topics of "surface enhanced Raman" and "pesticides" revealed 287 publication results. The majority of these demonstrated the detection of organophosphate (OP) insecticides, for example phosmet,[165, 167] parathion-methyl,[129, 168-171] malathion,[123, 172, 173] and chlorpyrifos.[129, 174-176] Other SERS pesticide studies included fungicides (thiram,[118, 129] thiabendazole[106]), herbicides [177], and the insecticide, neonicotinoids (imidacloprid[164, 178], thiacloprid[179], acetamiprid[180]).

Organophosphates are the largest class of pesticide, making up 50% of the neurotoxic agents in chemical pesticides.[181] Most OP use is agricultural, since the Environmental Protection Agency banned their residential use in 2001.[182] However, their human and animal toxicity still make them a societal health and environmental concern.[183-185] Moreover, small amounts can be detected in food and drinking water.[186-189] Hou *et al.* showed an *in situ* SERS method, using commercially available gold nanoparticle colloids to detect the organophosphates, isocarbophos and phorate, and neonicotinoid pesticide, imidacloprid, on different plant surfaces.[164] Similarly, Bianhua Liu *et al.*. reported the use of silver-coated gold bimetallic nanoparticles for *in situ* detection of a range of pesticides on fruit peels without further sample preparation.[190] Both of these techniques demonstrated sufficient limits of detection (LOD) at the pesticides required maximum residue levels (MRL). However, as described above, these colloidal based solutions are not ideal for portable applications and solid SERS substrates that can be prepared in advance, are more suitable. For example, Chen *et al.* used "SERS tape" to extract OP pesticides (thiram, chlorpyrifos, methyl parathion) from different kinds of fruit and vegetable peels. The tape can simply be placed on to the surface of the produce and peeled off for SERS analysis. This is non-invasive and required no sample or substrate preparation. Additionally, Li *et al.* have created a 'smart dust' that can be easily spread over a probed surface for *in-situ* TERS measurements. This method requires no preparation or particle aggregation/concentration on the substrate, like solutions of nanoparticles would need. Their shell-isolated nanoparticles were used to analyse the OP pesticide residue, parathion, on a fresh orange, see Figure 1.9. They presented comparable results between a normal Raman and a portable Raman, demonstrating the substrates potential use in-field.
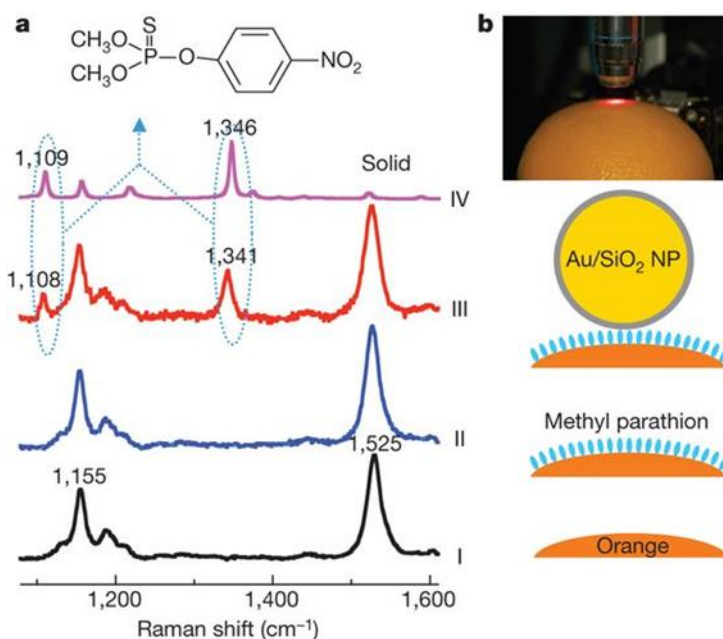
Figure 1.9: Normal Raman spectra of parathion on fresh citrus fruits and a schematic of the "shell-isolated nanoparticle-enhanced Raman spectroscopy" experiment, by Li *et al.*[168]

Some studies use commercially available SERS solid substrates to detect pesticides. Fan *et al.* employed commercially available Klarite substrates to detect the organophosphate phosmet. [165] Whereas Bin Liu *et al.* demonstrated quantitative detection of three types of pesticides (azinphos-methyl, phosmet, and carbaryl) on tomatoes and oranges, using commercial Q-SERS™ substrates.[167] However, their detection limits did not meet the regulatory standards for these pesticides.

Neonicotinoids are a relatively powerful class of insecticide, and since the introduction of imidacloprid in 1991; they have been the fastest-growing class of insecticides in modern crop protection,[191] representing almost 17% of the global insecticide market.[192] Typical detection methods of neonicotinoids are enzyme linked immuno-sorbent assays (ELISA),[193, 194] HPLC- or GC- mass spectrometry,[195-199] surface plasmon resonance,[200] and fluorescence spectroscopy,[201] none of which are suitable for field analysis. Neonicotinoids are extremely effective against herbivorous insects,[202] while having perceived low toxicity to mammals, birds and fish.[203] This led to their widespread uptake for use on a variety of crops. However, concerns were raised about environmental impact in affecting the homing capacity of honey bees, resulting in global colony collapse of the pollinator population.[204, 205] Consequently, the European Union enforced a temporary

ban (Dec 2013)[206] reducing the MRL of neonicotinoids to between 0.01 to 3 mg/kg for many fruits and vegetables.[195, 207] Regarding SERS neonicotinoid detection, all publications are dated post 2013, after the restriction was placed to protect honeybees. Only in these last few years have SERS studies been carried out, with the total number of publications in the field at roughly 15 articles (Web of Science). The compounds most reported on were acetamiprid (7 articles)[208-213] and imidacloprid (3 articles).[164, 213, 214] Other neonicotinoids that have been studied using SERS include thiamethoxam[215, 216] and thiacloprid.[179]

Cao *et al.* synthesised three types of AuNP/MOF (metal–organic framework) composite to investigate the interaction between acetamiprid and the bridging molecules of the MOFs. Acetamiprid in this case was used to evaluate the characteristics of the SERS substrates. LOD's of 0.02 μM, 0.009 μM, and 0.02 μM were achieved for the three composites which could satisfy the requirement of detection according to the MRLs of acetamiprid.[208] Yang *et al.* used SERS to evaluate the penetration behaviours of 4 pesticides (acetamiprid, thiabendazole, ferbam and phosmet) in a variety of fresh produce matrices. They used a pescticide/ AgNP complex to deposit onto the external surfaces of different fresh produce and measured the penetration depth of the complex using SERS.[208] Although the results are promising, this method requires complex sample preparation with the pesticide and AgNP, including washing steps, and is not ideal for farm-side analysis. On the other hand, Wijaya *et al.* employed silver dendrites for the SERS detection of acetamiprid in apple juice and from swabs of the apple surface.[209] In this method, no pre-treatment was undertaken on the apple juice samples and the use of the swab is non-invasive to the fruit. This method therefore has the potential to be used for on-site pesticide detection.

1.3.6.2 *Food security*

Recent incidents regarding the safety of consumer foods have driven the need for highly sensitive, specific and reliable methods to determine potential contaminants.[217] In this section, the SERS methods for chemical contaminants are reviewed, such as dye molecules, melamine, and antibiotics, particularly for use in remote monitoring. Implementation of remote SERS sensing has the potential to limit public exposure to adulterated products and maintain the current stringent levels of food safety. The literature

also presents a considerable number of SERS studies for detecting biological contaminants in food such as bacteria, viruses, parasites, fungi, and toxins from plants, mushrooms, and seafood.[218-223]

1.3.6.2.1 Dye Molecules

The detection of trimethyldiamine dye molecules, namely rhodamine 6G, malachite green, crystal violet and 4-aminobenzenthiol, are the most reported chemical contaminants due to their ease of detection. These dye molecules are highly Raman active and are used indiscriminately as antimicrobials in aquaculture, despite the reports of it causing serious toxic, carcinogenic and mutagenic effects in mammalian cells.[224, 225] Thousands of SERS publications employ these dyes as standard probe molecule to investigate the Raman enhancement of the reported substrate.[106, 123, 226-228] Moreover, the most significant and influential papers in this field have employed these dye molecules to report on single molecular SERS detection,[227, 229, 230] the study of enhancement factors,[74] and the mechanisms of SERS.[231]

1.3.6.2.2 Melamine

The 2008 melamine scandal involved the intentional contamination of milk powder with melamine to give a false appearance of high protein levels. Monitoring the level of residual melamine has become an important issue for industry. During and following the scandal, much research effort has been focussed on the detection of melamine in a wide range of products using a wide variety of analytical methods, including, chromatography and ELISA techniques, which are discussed in chapter 2. Regarding SERS, melamine is probably the most widely documented food adulterant, with Web of Science literature search revealing 181 articles.[123, 154, 232, 233] The majority of these articles employ SERS substrates, for melamine analysis, based on Au and Ag nanoparticle fabrication. Gold substrates include: Au colloids,[233-235] AuNP agglomerates,[236-238] 4-mercaptopyridine-modified AuNP's,[239] and magnetic AuNPs,[240] to name a few. Similarly the silver SERS substrates include: Ag Colloids,[241] AgNP agglomerates,[242] AgNP coated Ag/C nanospheres,[243] AgNP coated polystyrene nanospheres,[154, 244] cyclodextrin-coated AgNP's,[245] AgNP-coated Fe_3O_4/SiO_2 microspheres, [246] graphene oxide AgNP hybrid,[247] functional graphene/ Ag nanocomposite.[248]

The biggest challenge with point-of-use sensing in milk products is that the SERS method must be (i) highly sensitive and specific, (ii) fast and easy to use by untrained personnel (iii) require little or no sample pre-treatment to the milk, and (iv) employ solid SERS substrates (not solution based substrates). Peng *et al.* used self-assembled vertical arrays of nanorods to detect melamine in methanol. [246] and similarly, Hu *et al..* coated Ag nanoparticles on the surfaces of "$Fe_3O_4@SiO_2$" composite microspheres to detect a melamine methanol solution.[246]   Neither of these articles demonstrates melamine detection in real samples. Zhang *et al.* demonstrated melamine detection in milk using silver colloid solution. They report and easy pre-treatment for the milk, which however still requires large instrumentation and, additionally, the colloid NPs required mixing with the diluted and filtered milk.[233] Alternatively, Guo *et al.* developed self-assembled hollow gold nanospheres to detect melamine in milk on a solid chip platform, which is ideal for remote sensing. However, they employ centrifuging as their only method of sample pre-treatment which is complex and not suitable for transporting.

There is only one commercial substrate utilised for melamine detection, Klarite™ substrates (Renishaw Diagnostics Ltd., Glasgow, U.K.). [249, 250] Lin *et al.* used Klarite™ substrates to detect melamine in gluten, chicken feed and other processed foods. [250] They demonstrate detection of the characteristic peaks of melamine; however these commercial substrates are not sensitive enough to detect trace amounts of contaminants, especially in complex media. Another novel method by Betz *at al.* used copper tape and a penny coin to fabricate Ag micro- and nanostructures and analyse infant formula adulterated with melamine.[242] The fact that these substrates can be formed in five minutes on-site without the need for complex equipment, sample pre-treatment or harsh chemicals enables the possibility of remote point-of-sampling. However their LOD (5 ppm) is also not sufficient for remote melamine detection.
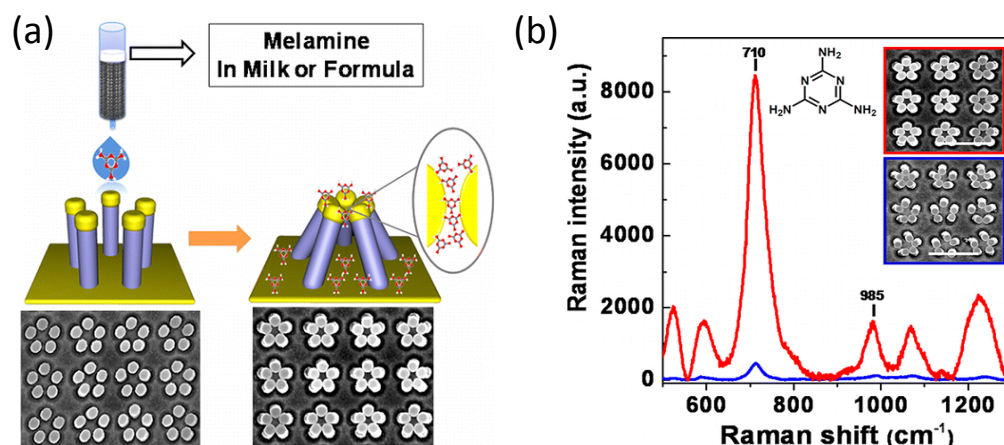
Figure 1.10: (a) The representative SEM images of open (left) and closed (right) pentamer gold nanofingers before and after treatment with the filtered milk. (c) Effect of the nanofingers closing on the melamine sensing performance, by Chen *et al.*. [232]

Finally, Chen *et al*. reported on detection of melamine in egg whites using fabricated ZnO/Au composite nanoneedle arrays, see Figure 1.10. The results showed some background interferences from the egg proteins but the characteristic peak for melamine at ~ 682 cm^{-1} remained detectable and was well resolved. [232] The only sample preparation was a filtering of the egg solution through 4 layers of gauge, which can be easily employed off-site as it required no complex instrumentation. Similarly, Kim *et al*. subjected their previously reported gold nanofingers to melamine detection in milk.[141] Although they also required sample pre-treatment, the authors avoided using centrifugation as it was neither portable nor low cost. Instead they employed a mini dialysis kit and detected characteristic melamine peaks from the dialysis filtered solutions at 1 ppm.[251] They also demonstrated melamine detection at 100 ppb in infant formula using a solution gel filtration chromatography treatment. These are two of very few articles that report SERS substrates and methods of sample pre-treatment, that both are fully compatible for field applications in a limited-resource environment.

1.3.6.3 *Pathogen detection and health applications*

SERS represents a promising technique for the portable detection and identification of pathogens in environmental samples.[252] For example, Wood *et al.* report the coupling of a portable Raman spectrometer to an acoustic levitation device to enable environmental monitoring and identification of microalgae.[253] Zhou *et al.* show SERS detection of living

bacteria in drinking water in 10 minutes using AgNPs. Furthermore, they report the ability to discriminate between three strains of *Escherichia coli* and one strain of *Staphylococcus epidermidis* in a 3 μL solution.[254] Traditional identification and detection methods for microorganisms, mostly viruses and bacteria, are based on culturing of the microorganisms and isolation of single strains. This involves a combination of different tests and relies on determining their phenotypic characteristic and their ability to grow in different media. All of these methods are labor-intensive and very time-consuming. SERS has been utilised to identify microorganisms in complex media, such as anthrax, so single strain isolation is not required, significantly reducing detection time.[255-257] It can be used to assess the quality of natural waters in rivers, where contamination from improperly treated wastewater imposes health problems.[223]

SERS has been utilised for the detection of various pathogens, reported by Li *et al.* such as *Giardia*, *Enterococcus faecalis*, *Streptococcus pyogenes*, *Acinetobacter baumannii*, *Kleb siella pneumonia*, *Salmonella typhimurium*, *Pseudomonas aeruginosa*, *Bacillus megaterium*, *Staphylococcus cohnii*, *Helicobacter pylori*, *Listeria monocytogenes*, *Erwinia amylovara*, and *Escherichia coli*.[161] Furthermore, Granger *et al.* reviewed the use of SERS for pathogen detection in human health/infectious disease and food, water and biosecurity applications. They focus particularly on the potential to develop point-of-use (or point-of-care, POC) sensors exploiting the capability of SERS, such as, improved LODs, multiplexing abilities, ease of use, and cost effective instrumentation.[222] SERS is also used for the detection of numerous different biological species,[258] for example, detection of many different cancer biomarkers,[259] DNA and RNA detection,[260] and also for the detection of glucose.[261] It offers an alternative approach to biosensing, without the limitations found in other analytical techniques; fluorescent dyes are not needed for sensing, there is no interference from water absorption, and plasmon resonances allow for a tuneable sensor. Although SERS is a highly sensitive and selective technique, it remains challenging to maintain these advantages for field analysis.

To conclude this section describing the optical transducer; we can see that SERS is an exciting tool for agricultural and environmental sensing applications. It has many

attributes that make it an excellent method for POC analysis. The sizes of Raman spectral features are 10–100 times narrower than those of fluorescence; this minimizes spectral overlap between different labels that are used in SERS methods for indirect quantification, making more extensive multiplexing possible. Second, the optimum excitation wavelength for SERS is linked to nanoparticle size, shape and composition; as described previously, therefore only one laser excitation wavelength is required for multiplexing. There are many methods for fabricating SERS substrates from the expensive but highly accurate and tuneable lithographic approaches, to the low-cost, disposable substrates fabricated from everyday materials, such as paper, leaves and aluminium cans. Most importantly, SERS has the potential to deliver rapid, sensitive and highly specific detections of a wide range of chemicals, biomolecules and micro-organisms, at the point of concern.

Electrochemistry constitutes another promising group of sensing devices that allows increased sensitivities, low cost and short analysis times with easy miniaturisation for point of use devices. An overview of electrochemistry, particularly at nanoscale, is given in the next section.

1.4 Electrochemical Transducer - Fundamentals

1.4.1 Electron Transfer Mechanism

Electrochemistry is the study of chemical changes that cause electrons to move from one element to another in a reaction known as a redox reaction or oxidation-reduction reaction. Electron transfer governs the pathway of electrochemical reactions and as it is difficult to trace the movement of electrons using spectroscopy methods, electrochemical methods are used.[262]

In an electrochemical system, the application of potential results in chemical reactions occurring at the electrode-solutions interface. This phenomenon, known as electrolysis, involves the transfer of electrons or charge between an electrode and electroactive species in solution,[263] which produces a positive or negative current flow around an electrical circuit. Other common electrochemical reactions include, a change of the electrode surface, e.g., formation of an thin film on the electrode surface or deposition of a metal,[264] or a change of physical state, e.g., from liquid to gas.[265, 266] In all cases, electrochemical reactions are either oxidation (a loss of electron) or reduction (a gain of electron) reactions, represented by the following equation:

$$O + ne^- \rightleftharpoons R$$

<div align="right">(Equation 1.2)</div>

where O is the oxidised form of a redox species in solution, *n* is the number of electrons *e*$^-$ transferred and R is the reduced form of the redox species. The electrode where reduction reactions occur (electrons gained) is known as the cathode and the electrode where oxidation reactions occur (electrons are lost) is called the anode.

For electron transfer reactions to occur at the electrode/solution interface, it is necessary that the energy level of the electron corresponds to the energy level of the donor or acceptor molecular orbital. The energy that is required to move the electron is known as the activation energy and depends on the applied potential. Application of an applied voltage allows us to control the maximum energy in an electrode.

For reduction reactions the formal potential of the redox couple, E^{0}' (the potential that is actually measured in an electrochemical cell) is greater than the applied potential, *E*. In this case, for electrons to be transferred to the lowest unoccupied molecular orbital (LUMO) of a molecule in the solution, the electrodes Fermi-level must be high, as

illustrated in Figure 1.11 (a), thereby forming a reduction current. This is achieved by decreasing the potential applied. Alternatively, for oxidation reactions the applied potential, *E*, is greater than the formal potential of the redox couple, *E⁰'*. So in order for electrons to be transferred from the species in solution to the electrode, the electrode energy must decrease sufficiently (potential is increased) to allow electron transfer from the highest occupied molecular orbital (HOMO) of the molecules in the solution, to the electrode, thus forming an oxidation current. This process is illustrated in Figure 1.11 (b). Figure 1.11 highlights the changes in the electronic states at the solution/electrode interface and the electron transfer for both reduction and oxidation processes.
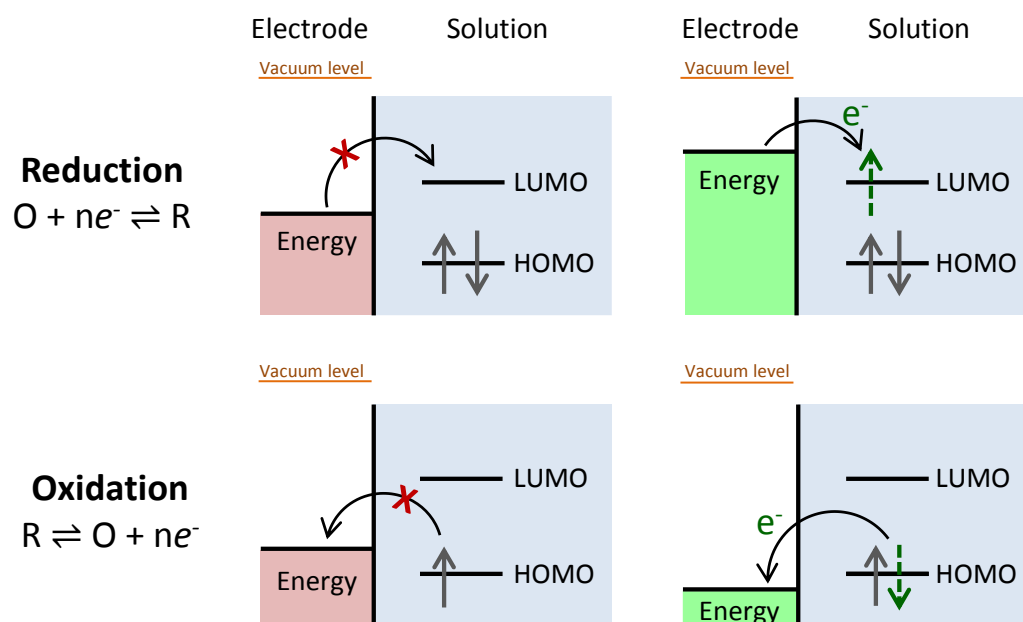
Figure 1.11: Diagram of the electron transfer and energy levels at an electrode-solution interface for reduction and oxidation processes. LUMO is the lowest unoccupied molecular orbital and HOMO is the highest occupied molecular orbital. An applied voltage is required to surmount the energy barriers and allow electron transfer.

The application of a potential to an electrode makes the reaction thermodynamically favourable which can be determined by the change in Gibbs free energy (ΔG):

$$\Delta G = -nFE^0$$

(Equation 1.3)

where, *n* is the number of electrons involved in the reaction, *F* is Faraday's constant (96485 C.mol⁻¹) and *E⁰* is the standard cell potential. *ΔG* is the difference in the energy

between reactants and products in a chemical reaction. Standard thermodynamics says that the actual free energy change is related to ΔG^0, the free energy change under standard conditions (1 atm, 298K), by the relationship:

$$\Delta G = \Delta G^0 + RT \ln Q$$

(Equation 1.4)

where, R is the standard gas constant (8.314 J.mol^{-1}.K^{-1}), T is temperature (K) and Q is the reaction quotient which is the function of the activities or concentrations of the chemical species involved in a chemical reaction. This equation relates Gibbs free energy to the concentration of the oxidised and reduced species and it can be combined with (Equation 1.3 to calculate the cell potential, E, with respect the concentrations of a redox chemical species:

$$E = E^0 - \frac{RT}{nF} \ln \frac{Red}{Ox}$$

(Equation 1.5)

where, *Red* and *Ox* are the concentrations (mol.cm^{-3}) of the reduced and oxidised forms of a redox couple, respectively. This is known as the Nernst equation.

1.4.2 Electrochemical Experimental Set-up

One of the most popular setups for an electrochemical system is a standard three-electrode electrochemical cell. It consists of a working electrode (WE), a reference electrode (RE) and a counter electrode (CE) immersed in an electrolytic solution of interest. To minimise background interferences and electromagnetic noise, the cell can be placed into a faraday cage, which facilitates lower detection limits. A simplified schematic of a potentiostat circuit is illustrated for a standard three-electrode electrochemical experiment, in Figure 1.12. All three electrodes are electrically connected to the potentiostat which is required to maintain the applied potential at the working electrode and measure the current generated by electrochemical reactions occurring at the WE/solution interface. The Signal generator provides the required voltage and applies it to the potentiostat circuit. This voltage is controlled by the control amplifier, which drives current through the system to ensure the desired voltage matches the measured voltage. The I/E convertor used an amplifier to measure the voltage before and after it passes through a resistor (R_m). This

voltage difference is then used to determine the current in the electrochemical cell. The electrometer also used an amplifier to instead determine the potential difference between the WE and RE. Therefore, it is said that the potential is controlled between the WE and RE, whereas the measured current passes between the WE and CE via the analyte solution. The potentiostat is connected to a computer to acquire data.
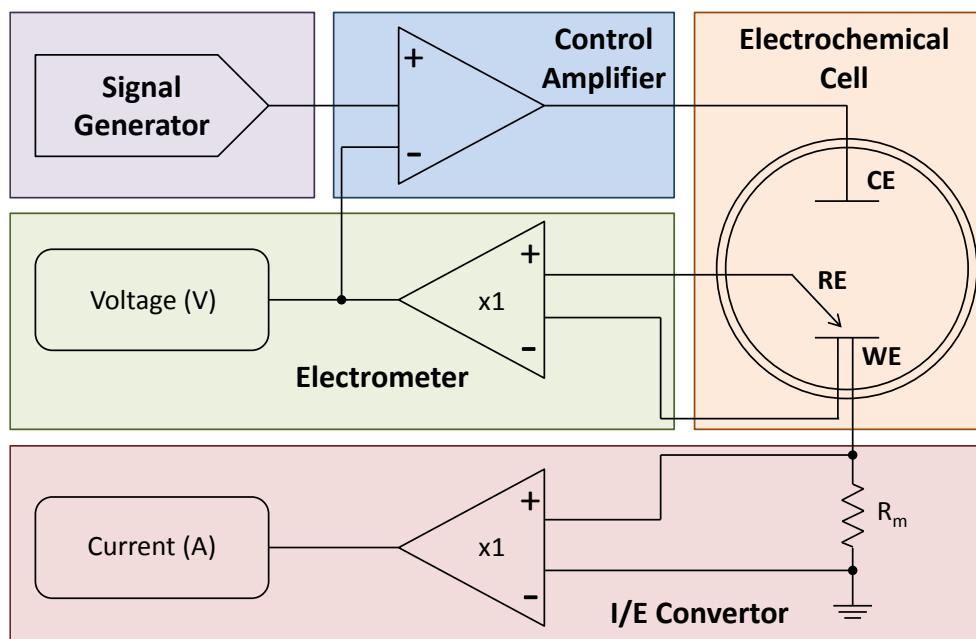
Figure 1.12: A schematic circuit diagram of a potentiostat controlling a three-electrode electrochemical cell. (Reproduced from [267])

1.4.2.1 *Working Electrode*

The working electrode is the electrode in an electrochemical system on which the reaction of interest is occurring. Examples of materials used for working electrodes include gold, carbon, silver and platinum. The material used and the size/ shape of the working electrode depends on its application, i.e. the reactions that take place on the electrode. If the reaction is a reduction, the electrode is cathodic; alternatively, if it is an oxidation reaction the electrode is called anodic.[262] It is essential to have a clean working electrode surface to obtain reliable, reproducible experiments. Therefore, depending on the electrode material and size there are different cleaning protocols obtained. For the on chip experiments carried out in this study (discussed in chapter 3), a gold working electrode is employed.

1.4.2.2 Reference Electrode

The function of a reference electrode is to provide a stable known potential and is used as the point of reference for the control and measurement of potential in the electrochemical cell. It also must be chemically stable so that the system control is maintained. As outlined previously, the measured current passes between the working and counter electrodes via the analyte solution. Little to no current should pass though the reference electrode to prevent polarisation of the electrode and therefore the change of its potential.[262] There are many types of reliable RE, including the saturated calomel electrode, the silver/ silver chloride electrode, standard hydrogen electrode, platinum pseudo-reference and the copper/copper sulfate electrode. One of most widely used of these electrodes is the Ag/AgCl electrode due to its stability, low cost, non-toxicity and easy fabrication. The Ag/AgCl requires a high sample volume due to its size, which limits its use with micro/ nano devices. Consequently, alternative reference electrodes have been developed, such as an on-chip Ag/AgCl reference electrode,[268, 269] which provides a quasi-stable RE but requires modification of the silver after every use with AgCl, which can be time consuming and unreliable. A different option is to use a noble metal pseudo-reference electrode, e.g., platinum or gold,[270, 271] which is the electrode of preference for our experiments. Calibration of these electrodes is required prior to every measurement.

1.4.2.3 Counter Electrode

The counter electrode (or auxillary electrode) provides a circuit with the WE over which the current is either applied or measured. Because the CE acts as a supply of electrons (source/sink of electrons) to the working electrode to balance the reaction occurring, it is common to use a CE that is ten times larger than the WE so that it will not be a limiting factor in the kinetics of the electrochemical process. This also prevents current from flowing through the RE so that the fixed potential can be maintained in the cell. In most electrochemical reactions, the counter and working electrodes are separated so that the alternate redox processes occurring at each electrode will not interfere with each other and electoneutrality is maintained in the solution.

1.4.3 Application of Nanoelectrochemistry

Electroanalytical techniques particularly at the nanoscale provide enhanced sensors compared to commercial micro/macroscale electrodes in terms of sensitivity, response times and real-time signal readout.

In typical electrochemical reactions, electrons are transferred between an electrode and a redox species, resulting in a current flow. Faradaic currents are controlled by this electron transfer and also by mass transport; the transport of material from the bulk solution to the electrode surface. Oxidation or reduction occurs at the electrode-solution interface and the electro-active species at the electrode are consumed, which creates depletion zones. Due to this, redox molecules move from areas of high concentration to low concentration, i.e. from the bulk solution to the electrode/ solution interface. This flux is a type of mass transport known as diffusion and is defined as the number of moles passing through a certain position per unit time and area. Figure 1.13 illustrates the concentration gradient for the diffusion of a redox species over time.
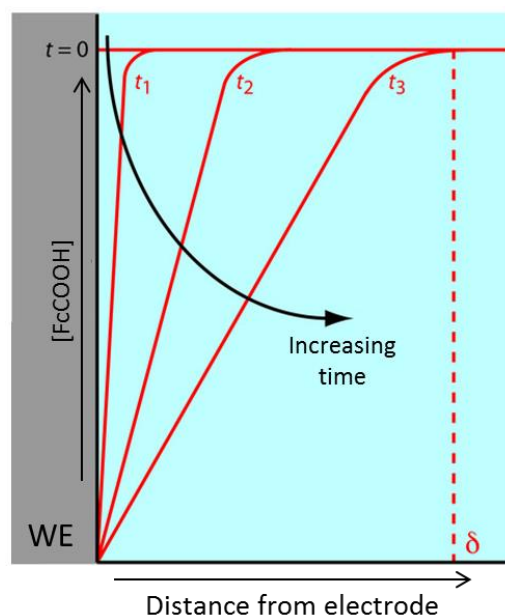
Figure 1.13: Concentration gradients (in red) for the reduction of FcCOOH following the application of a potential. The longer the potential is applied the larger the distance of the diffusion layer.[272] (Image adapted from [273])

At t=0, before applying a potential the concentration of the redox species (Ferrocene monocarboxylic acid - FcCOOH) is the same at all distances from the electrode's surface. Once a potential is applied, the FcCOOH concentration at the electrode's surface is depleted and more FcCOOH diffuses from bulk solution to the electrode. The longer we apply the potential, the greater the distance over which diffusion occurs.

Effectively, nanoelectrodes display enhanced mass transport, over microelectrodes, due to their small critical dimension. At macroelectrodes, cyclic voltammograms are typically peak-shaped, particularly at high scan rates. This time-dependant current arises because the diffusion layer is small compared to the critical dimension of the electrode and mass transport occurs perpendicular to the electrode surface. This is called planar diffusion. Alternatively, nanoelectrodes produce steady-state voltammograms. Mass transport to these electrodes exhibit a hemispherical shape due to their extremely small critical dimension. This is known as radial diffusion. The smaller the electrode size, the faster radial diffusion can be achieved. Moreover the faradaic current can readily reach a time-independent limiting value, even at high scan rates.

Figure 1.14 (a) to (c) demonstrates how the shape of simulated concentration profiles at a microdisk electrode (12.5 μm diameter) varied with the applied scan rate. [274] At 50 mV s^{-1}, Figure 1.14 (a), the diffusion layer thickness appears uniform and larger than the electrode diameter, suggesting the analyte mass transport behaviour is dominated by radial diffusion. As the scan rate was increased to 500 mV s^{-1}, Figure 1.14 (b), planar diffusion becomes more dominant. When a fast scan rate of 5000 mV s^{-1} was employed, Figure 1.14 (c), the extent of the diffusion layer is of similar dimension to the electrode diameter, strongly suggesting that planar diffusion dominates at the electrode surface. The electrode experienced slow mass transport of the analyte, which prevented rapid replenishment of the electrolysed species at the electrode surface. Therefore, the response is time-dependant and diffusion-limited. This behaviour was experimentally confirmed by the emergence of diffusion limited peak shaped cyclic voltammograms at higher scan rates in Figure 1.14 (g). Furthermore, it is observed that the current is also increasing with increasing scan rate. This is because current is the flow of electric charge over time (I =

Q/t). As the scan rate is increasing the charge will remain the same but the scanning time is reduced, therefore a larger current is measured.

When the critical dimension of the electrode is reduced to the nanoscale, radial analyte diffusion to the electrode dominates. This is illustrated in the equivalent simulations for a nanoelectrode (100 nm), Figure 1.14 (d-f). It is clear that the diffusion layer thickness is uniform and much larger than the nanowire electrode width, resulting in increased rates of mass transport. The increased mass transport allows for the rapid regeneration of the analyte at the electrode surface providing time-independent, steady-state current measurements, even at fast scan rates and in low concentrations of analyte,[275] as shown in Figure 1.14 (h).
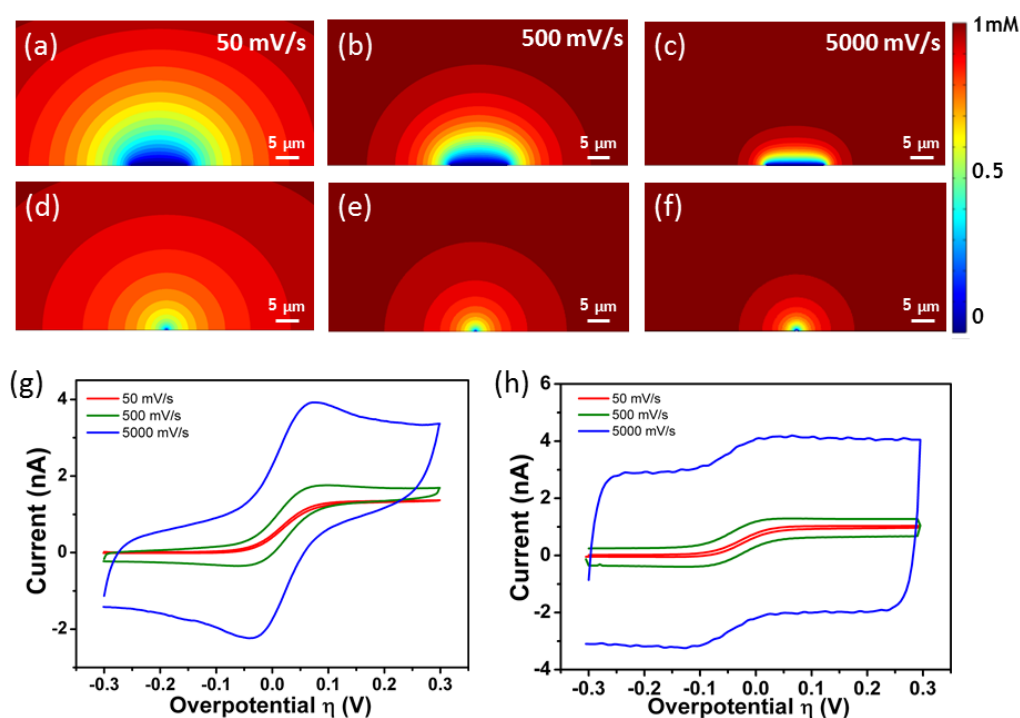
Figure 1.14: Simulated FcCOOH concentration profiles at a plane perpendicular to a single ultramicrodisc electrode, at scan rates of (a) 50 mV.s⁻¹, (b) 500 mV.s⁻¹ and (c) 5000 mV.s⁻¹. The equivalent FcCOOH concentration profile at single nanowire electrodes are (d), (e) and (f), respectively. Cyclic voltammograms obtained for a gold (g) ultramicrodisc electrode and (h) nanowire electrode in 1 mM FcCOOH in 10 mM phosphate buffered saline showing the change in wave shape and peak current with increasing scan rates, 5, 500 and 5000 mV s⁻¹, (reproduced from [274]).

Another important factor that must be considered is that the presence of the double layer is responsible for non-faradaic charging currents, or capacitive currents, i.e., they are not related to any oxidation or reduction reactions. While in most cases capacitive currents are negligible, they can sometimes be a hindrance for monitoring faradaic processes particularly at low concentration levels or at fast scan rates. In the case of nanoelectrode, the charging currents are significantly reduced because of the smaller electrode area. To this end, compared to macroelectrodes, nanoelectrodes exhibit higher sensitivity due to higher current densities, reduced double layer capacitance thus reduced background charging currents, and higher signal to noise ratios. Furthermore, nanoelectrodes enable direct low volume analysis,[276] low supporting electrolyte concentrations and faster response times.[275, 277]

1.5 Electrochemical Techniques

Electrochemical transducers detect changes in the form of electrical signal which is directly proportional to the concentration of analyte in the electrochemical cell. These methods can be broken down into several categories depending on which aspects of the cell are controlled and which are measured. There are four types of techniques: voltammetric, potentiometric, coulometric and impedimetric techniques. Potentiometry measures the potential of a solution between the working and reference electrodes. Coulometry either uses an applied current or potential to measure the number of electrons transferred in the redox reaction.

The main techniques employed frequently in this thesis include, voltammetry in particular electrochemical impedance spectroscopy (EIS) which will be discussed in detail, in the next section. Computer-controlled electrochemical instruments such as potentiostats enable voltammetric techniques to monitor the current generated by the application of a potential wave function to a working electrode for a range of redox species in solution. The current-potential curves obtained are known as voltammograms. The applied potential at which electronic processes occur provides qualitative information, whereas the current can be employed as a quantitative measure for specific redox molecules. The two voltammetric techniques employed in this work and described here are (i) cyclic voltammetry, and (ii) square wave voltammetry. [278]

1.5.1 Cyclic Voltammetry

Cyclic voltammetry is one of the most widely used techniques to investigate an electrochemical system. In CV, a potential is applied to the system and the current is measured. The current response derives from the application of a triangular potential waveform, Figure 1.15 (a), which produces a forward and a reverse scan. The potential is swept linearly from an initial potential, E_{in}, to a final potential, E_{fin}, and reversed from that potential back to generally the initial one. The linear sweep rate is known as scan rate and can vary from 1 mV up to thousands of V. The initial potential is set at a potential where no redox reaction occurs and is swept towards the potential region where the

electrochemical reaction of interest takes place, i.e. swept negatively or positively past the standard potential for a redox couple, E_0'. An oxidation and a reduction reaction will occur on either the forward or the reverse scan, depending on the redox species present. The most useful parameters in a cyclic voltammogram are the cathodic peak potential, E_{pc}, the anodic peak potential, E_{pa}, the cathodic peak current, i_{pc}, and the anodic peak current, i_{pa}, illustrated in Figure 1.15 (b). The reversibility of the reaction can simply be verified by calculating the ratio between the cathodic and anodic peak currents; a result of 1 indicates a reversible reaction. Moreover, for a Nernstian reaction at 25 °C the difference between peak potentials, ΔEp, is expected to be 0.059/n, where n is the number of electrons involved in the half-reaction. Higher ΔEp indicates irreversibility due to slow electron transfer kinetics.
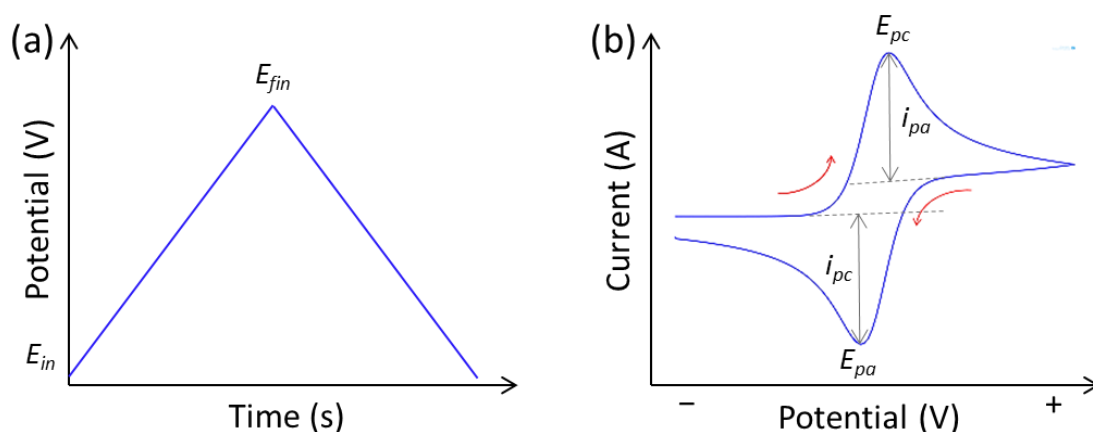
Figure 1.15: (a) Schematic diagram of the potential wave form in cyclic voltammetry. (b) Typical voltammogram of a reversible redox couple.[262]

1.5.2 Square Wave Voltammetry

Square wave voltammetry is a widely used voltammetric technique employed to maximise faradaic to charging current ratio. It is a pulsed technique in which the potential applied to the working electrode is composed of a large symmetrical square wave pulse superimposed on a staircase scan. The staircase waveform is shown in Figure.1.16, starting from a potential E_{in}, where no redox reactions take place, passing through the formal potential Eo' of a redox species, and ending at a potential E_{fin}, once either a reduction or an oxidation reaction occurred. It is swept in a series of cycles consisting of two symmetrical pulses, one forward and the other reverse. Each pulse is characterised

by a pulse height (or amplitude), ΔE_h and a pulse width, *t*. Each cycle is characterised by a frequency f and at the start of each cycle the potential shifts by an incremental potential, ΔEi, such that cycles successively superimposed onto each other. The current is sampled twice during each square wave cycle, one at the end of the forward pulse, and again at the end of the reverse pulse, in order to minimise the contribution of charging current. The difference between the two current measurements is plotted versus the potential and a peak-shaped voltammogram is obtained. Square wave voltammetry yields peaks for faradaic processes, where the peak height is directly proportional to the concentration of the species in solution.
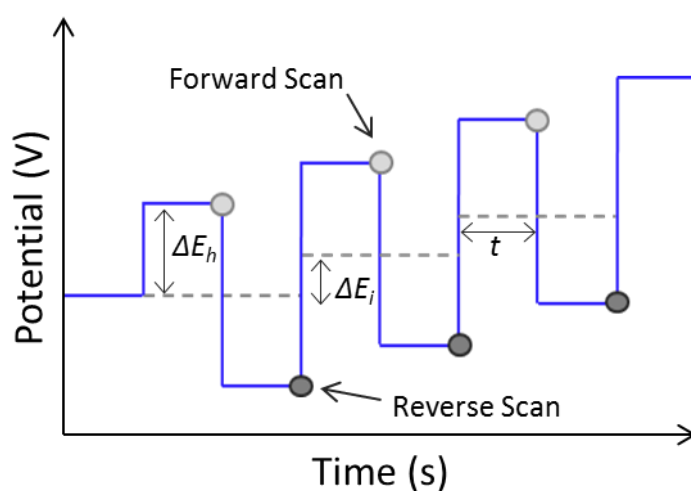
Figure.1.16: Schematic diagram of the potential wave form in square wave voltammetry. Each cycle comprises a forward pulse and a reverse pulse, which are characterised a pulse height (ΔE_h), a pulse increment (ΔE_i) and a pulse width (*t*).[262]

1.5.3 Potentiometric Field Effect Transistors

An ion selective field effect transistor (ISFET) is a transistor that measures ion concentrations in a solution, causing an interface potential on the gate insulator. In general, a field-effect transistor (FET) consists of three terminals; the source, drain, and gate, see Figure.1.17. The voltage between the source and drain of the FET regulates the current flow in the gate voltage. The current-control mechanism is based on an electric field generated by the voltage applied to the gate.[279] The current of the ISFET channel is affected by the potential change on the sensing surface, i.e. the physical gate of the MOSFET. The sensing signal can be obtained by analysing the transfer characteristics of

the sensors. When the charged analytes attached to the sensing surface, the charges will change the potential across the surface, and thus changes the effective gate bias of FETs. In this thesis the extended gate FET (EGFET) is used as a sensing platform, whereby the sensing chip is separated (an extended gate) from the readout transducer (FET). In EGFET configuration, an extended gate (sensing chip) is electrically connected to the gate terminal of a transistor (transducer).[280] This is further described in Chapter 6.
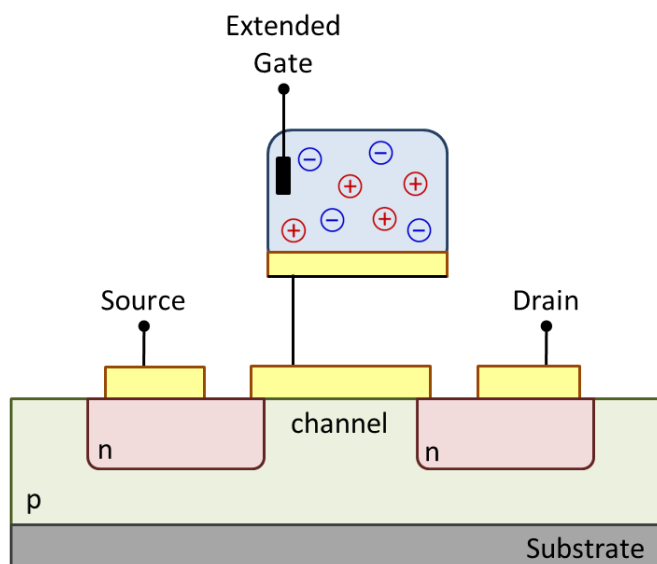
Figure.1.17: Basic schematic of an EGFET. The extended gate (i.e. the active sensing surface) is separated from a MOSFET (i.e. a readout transducer) with electrical interconnection and is immersed in the electrolyte, while the MOSFET is operated in a dry environment. The change of surface potential due to the attachment of charged species onto the sensing chip (extended gap) is transmitted to the MOSFET.[279]

1.6 Fundamentals of Electrochemical Impedance Spectroscopy

Impedance is the measure of a circuit's ability to resist the flow of electrical current and to store electrical energy. Electrochemical impedance spectroscopy is a technique where a sinusoidal potential is applied to an electrochemical system and the responding sinusoidal current signal is measured. Impedance measurements are conducted using small amplitude perturbation signals to create a pseudo-linear system that is free from harmonics of the excitation frequency. The resulting current sine wave oscillates at the same frequency as the applied potential wave but will be shifted in phase (ϕ). The ratio between the change in the applied voltage and the change in the current determines the impedance of the system. A spectrum is generated by sweeping over a range of frequencies and measuring the impedance at each point. To fully understand the fundamentals of the concept of impedance, the basic understanding of how an electronic circuit works is essential.

1.6.1 Ohms Law for DC and AC Currents

The fundamental relationship between voltage, current and resistance in an electrical circuit is called Ohm's Law. Ohm's law states that the electric current that flows through a conductor, I, is directly proportional to the voltage applied to the conductor, V. The ratio of voltage to current is called the resistance, R.

$$I = \frac{V}{R}$$

(Equation 1.6)

The resistance is constant, regardless of the voltage or current applied. Ohm's law only covers circuits containing resistive elements (no capacitances or inductances), whether the circuit driving force is constant DC (direct current) or time-varying AC (alternating current), see Figure 1.18.
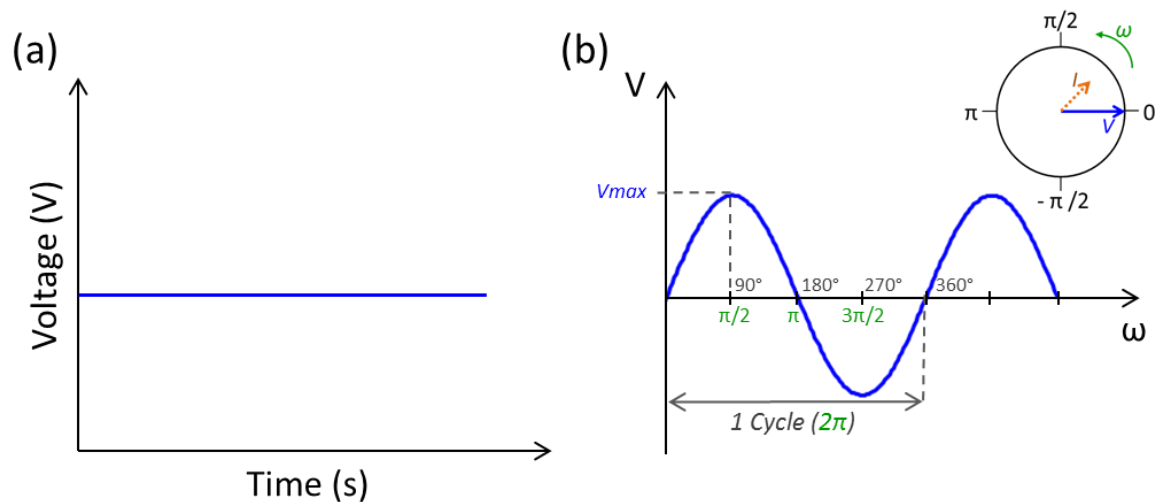
Figure 1.18: Graphs of voltage vs. time for (a) a direct current and (b) an alternating current.

The circuit's ability to resist electrical current in a DC circuit can be described using only resistance. As most AC circuits are not purely resistive, a modification to Ohm's law makes the law applicable to them. The modification considers the effect of capacitive and inductive elements which is known as reactance (X). The combined opposition of all the circuit's reactive and resistive components is called impedance, Z:

$$I = \frac{V}{Z}$$

(Equation 1.7)

where, V and I are the root mean squared (RMS) values of the voltage and current, respectively. To understand the concept of impedance, resistance and reactance are first explained using waveforms and phasor diagrams. Briefly, if a sine wave voltage is applied to a circuit, the resulting sinusoidal current will have the same frequency but may have a phase difference. This is the difference (given in degrees) between the two waves, at the same point in time. Two oscillators that have the same frequency and no phase difference are said to be "in phase". Whereas, two oscillators with the same frequency but have a phase difference, i.e. one lags or leads the other, are said to be "out of phase". This phase shifting is expressed by an angle, θ, which is associated with the impedance of the circuit and can be depicted graphically in a phasor diagram.

1.6.2 Resistance

The electrical resistance of a circuit component or device is defined as the ratio of the voltage applied to the electric current which flows through it; see Equation 1.6. In purely resistive circuits, the current and voltage have the same behaviour, regardless of whether the applied voltage is direct or alternating. This can be illustrated using a waveform, see Figure 1.19. In this scenario, for a purely resistive circuit, the resulting sinusoidal current (orange wave) attains the same frequency and passes through zero at the same time as the voltage. So, although the current value may vary in proportion to the sinusoidal voltage, they remain in-phase with each other i.e. the phase angle is zero ($\theta = 0$).
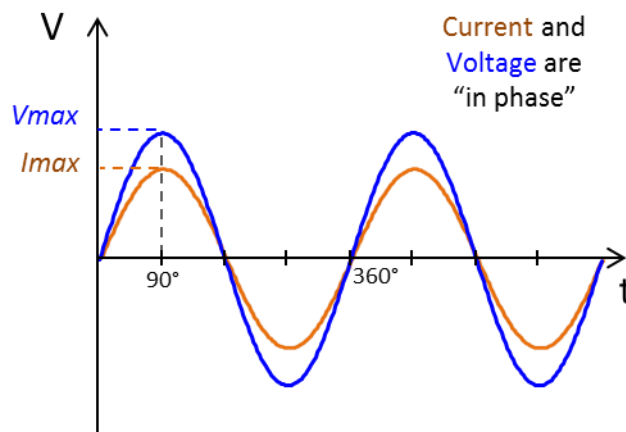
Figure 1.19: Waveform illustrating a purely resistive circuit

This "in-phase" effect is represented in Figure 1.20 as a phasor diagram, which provides information regarding complex impedance. Impedance is a complex number, which consists of a real and an imaginary part. The positive x-axis of the phasor diagram represents the "real part" of the system whereas the y-axis represents the imaginary components (j). This phasor diagram, with an angle of zero, illustrates that pure resistance does not contain an imaginary component (j). Therefore we can say that resistance is the real part of the impedance.

$$Z_R = R \text{ (resistive impedance)}$$
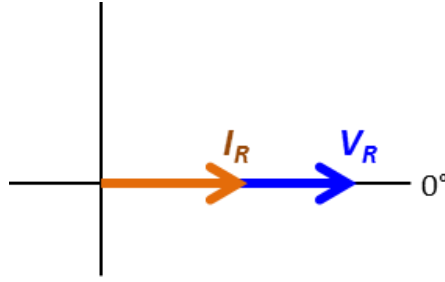
Figure 1.20: Phasor diagram for purely resistive circuit ($\theta = 0$).

1.6.3 Reactance

Electrical reactance is the opposition of a circuit element to a change in current or voltage, due to that element's inductance or capacitance. The total reactance is the sum of the capacitive reactance (X_C) and the inductive reactance ($-X_L$):

$$X = X_C + X_L$$

<div align="right">(Equation 1.8)</div>

Unlike resistors, ideal capacitors and inductors store energy rather than dissipating it, and contribute to the imaginary part of the impedance:

$$Z = R + jX$$

<div align="right">(Equation 1.9)</div>

where, Z is the complex impedance, R is the resistance and X is the circuit reactance (j represents an imaginary unit where $j^2 = -1$). The presence of capacitors or inductors in an AC circuit induces a phase shift between the current and voltage therefore, are considered "out of phase". When an alternating current goes through pure reactance, the phase angle is 90°, representing ideal capacitors or inductors.

1.6.3.1 Capacitors

Capacitors store energy in an electric field between two parallel conducting plates separated by a dielectric insulating layer. When a DC voltage is applied to a capacitor, the plates accumulate charge (negative on one side and positive on the other) forming an electric field. This field is the source of the opposition to the current. When the potential

associated with the charge is equal to the applied voltage the current flow stops and the capacitor maintains or stores that charge. With an AC supply, the capacitor will alternately charge and discharge at a rate determined by the frequency of the voltage supply; the higher the frequency, the less charge will accumulate and the smaller the opposition to the current. In other words, the capacitive reactance is smaller and therefore is inversely proportional to the signal frequency ($\omega = 2\pi$ f):

$$X_C = \frac{1}{\omega C} = \frac{1}{2\pi f C}$$

(Equation 1.10)

1.6.3.2 *Inductors*

An inductor is a wire coil that stores energy in a magnetic field as a result of the current flowing through it, which is formed when a voltage is applied to the inductor. This current produces a self –induced electromotive force (emf) that opposes current change. For a DC supply, an inductor acts as a short circuit because once the storage is complete, current flow becomes stable and there is no longer an emf produced. Therefore, it just acts like an ordinary wire with no resistance.

With an AC supply, the magnetic field is constantly changing as the AC current oscillates back and forth, with respect to the frequency. This change forms an opposing emf which impedes the flow of the current that is generating the magnetic field. Regarding the frequency of the applied voltage, as it increases, so does the inductive reactance value of the coil (or opposition to the current flowing through the coil). Hence, this back emf force is proportional to the rate of change of current flow and its opposition, the inductive reactance, is proportional to the frequency:

$$X_L = \omega L = 2\pi f L$$

(Equation 1.11)

1.6.3.3 *Phase Relationship*

We now know that reactance is made up of capacitive reactance, inversely proportional, and inductive reactance, proportional, to the frequency. Therefore, with increasing AC frequency the capacitive reactance decreases, whereas the inductive reactance increases. Waveforms are again used to explain this relationship.

Firstly, an ideal capacitor is considered. The voltage is proportional to the charge on the capacitor plate and in order to build up this charge, the current must flow. If a large voltage is applied across the capacitor it will charge to its maximum and stop (Vmax). At this point, the current is zero. The current in turn will flow in the opposite direction as the voltage starts to decrease. When the voltage reaches zero, the current is at its maximum (Imax). This movement is illustrated in the waveform diagram, Figure 1.21. Looking at the graph, when both sinusoids are plot together, it is clear that the voltage lags behind the current by a 90° phase shift. It is said that the voltage wave is -90° "out of phase" with the current wave. The reactance of an ideal capacitor (considering ohms law, with no R) is therefore its impedance and is negative for all frequency and capacitance values.

$$Z = X_C = \frac{1}{\omega C}$$

(Equation 1.12)
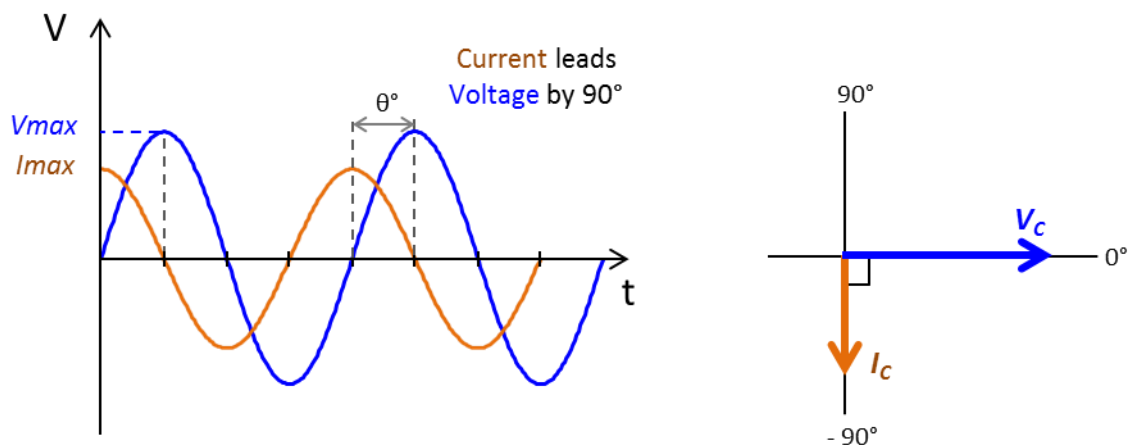
Figure 1.21: (a) sinusoidal waveform and (b) phasor diagram for a pure capacitance, with the voltage as the reference phasor (θ = -90°)

An inductor works in the opposite way to a capacitor. For an ideal inductor in an AC circuit, the effect of impeding a change in the current flow is due to dropping a voltage directly proportional to the rate of change of current. So, the AC sine wave for voltage is at zero whenever the current is at its maximum and vice versa, when the voltage is at its maximum the current is at maximum change. This results in the voltage leading the current by a 90° phase shift, see Figure 1.22. Here it is said that the voltage wave is +90° "out of phase" with the current wave. Similar to the ideal capacitor, the reactance of an

ideal inductor (no R) is therefore its impedance and is positive for all frequency and inductance values.

$$Z = X_L = \omega L$$
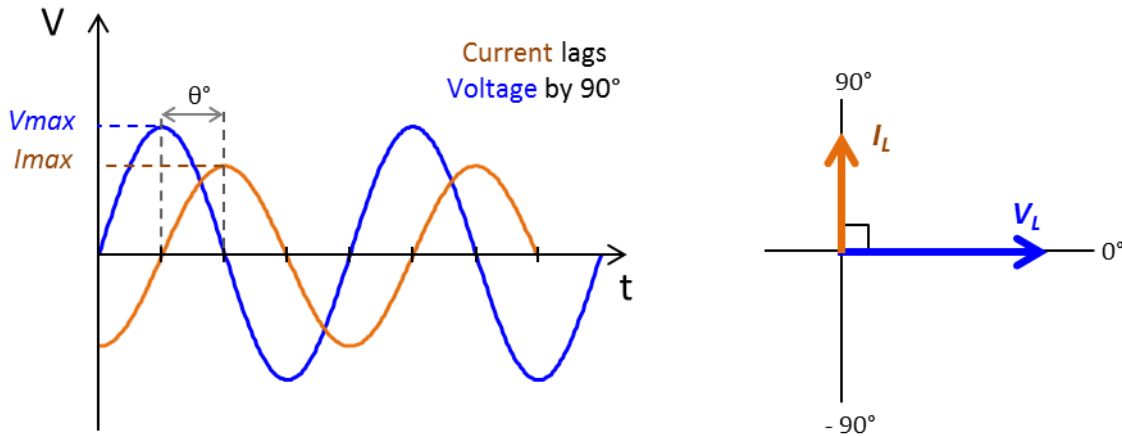
Figure 1.22: (a) sinusoidal waveform and (b) phasor diagram for a pure inductance, with the voltage as the reference phasor ($\theta = 90°$)

The phasor diagrams for both a pure capacitor and inductor illustrates that the impedance of these circuit is purely imaginary and contains no real parts.

1.6.4 Impedance

Theoretically, the concept is understood in ideal elements. However, like pure resistance, pure capacitive or inductive circuits do not exist. In reality, resistors and capacitors (or inductors) will be connected together in a circuit. In this case, the total impedance will have a phase angle somewhere between 0° and 90° depending upon the value of the components used. In this thesis, inductance does not have an effect on the system, so going forward I will only discuss the capacitive and resistive elements.

For components connected in series, the current through each circuit element is the same. A simple circuit composed of two components, a resistor and a capacitor in series, is evaluated. The capacitor will store energy and the resistor will control the rate at which it charges and discharges. For this example, the resistor will provide the circuit resistance

(R) and the capacitor will provide the reactance (-1/ ωC). Both elements are combined into a series RC circuit for analysis, see Figure 1.23 (a).
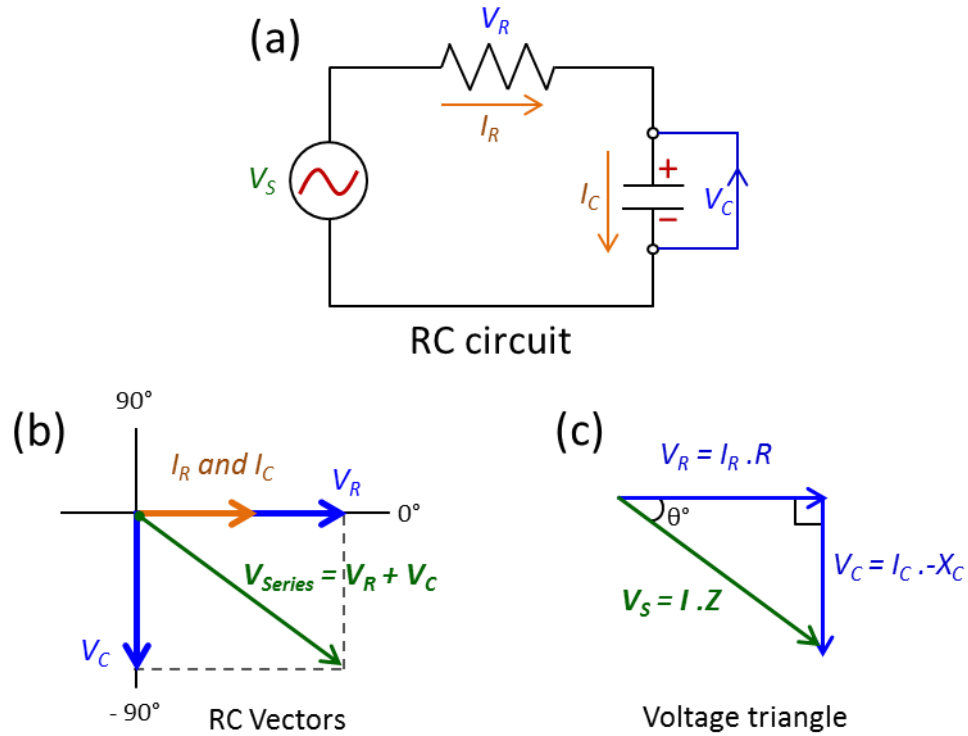
Figure 1.23: (a) RC circuit in series (b) Vectors for an RC circuit, assuming ideal capacitance and resistance. (c) Use of Pythagoras' theorem to calculate the total series voltage.

Referring back to the phasor diagrams, the voltage wave for resistor is "in phase" and the capacitor is "out of phase". The alternating current vectors in the circuit are all equivalent (I_R and I_C) whereas the voltage vector are changing with regard to their phase shift. Therefore, to find the series voltage in the system, the circuit's current is used as the reference vector, and the sum of the two voltage vectors is calculated, see Figure 1.23. The total voltage in the series (V_S) vector is created between the existing voltage vectors, forming a rectangular triangle. Therefore, Pythagoras's theorem, Equation 1.4, can be used to calculate the total voltage.

$$(V_S)^2 = (V_R)^2 + (V_C)^2$$

(Equation 1.14)

$$V_S = \sqrt{(V_R)^2 + (V_C)^2} \qquad \text{where, I = V/R}$$

53

$$V_S = \sqrt{(I_R.R)^2 + (I_C.X_C)^2}$$

$$V_S = Imax \sqrt{(R)^2 + (X_C)^2}$$

As we know, the RMS sum of the reactance and resistance is impedance:

$$Z = \sqrt{(R)^2 + (X_C)^2}$$

therefore, $V_S = I.Z$

Hence, the total impedance is the sum of the component impedances, in series.

$$Z = Z_1 + Z_2 + Z_3$$

(Equation 1.15)

For a circuit in parallel the voltage across each circuit element is the same, but the current is changing through the individual elements as well as their phase. Therefore, the voltage vector is used as the reference vector and the total current can be calculated using a current triangle. Considering a RC circuit in parallel:

$$I_S = \sqrt{(I_R)^2 + (I_C)^2} \qquad \text{where, I = V/R}$$

$$I_S = \sqrt{(\frac{V_R}{R})^2 + (\frac{V_C}{X_C})^2}$$

$$I_S = \frac{V}{Z}$$

The ratio of currents through any two elements is the inverse ratio of their impedances. Hence the inverse total impedance is the sum of the inverses of the component impedances:

$$\frac{1}{Z_{eq}} = \frac{1}{Z_1} + \frac{1}{Z_2} + \frac{1}{Z_3}$$

(Equation 1.16)

1.6.4.1 *Concept of Complex Impedance*

As discussed, electrochemical impedance spectroscopy (Z) is determined by applying a small sinusoidal potential excitation to a system and measuring the AC current response. The system impedance is studied as a function of the frequency of the potential wave. The applied potential excitation is defined by:

$$E_t = E_0 \sin(\omega t)$$

54

(Equation 1.17)

where E_t is the potential at time t, E_0 is the amplitude of the signal and ω is the radial frequency ($\omega = 2\pi f$ where f is the frequency in Hertz). The sinusoidal output current response (I_t) is shifted in phase and has a different amplitude, and is defined as:

$$I_t = I_0 \cos (\omega t - \phi)$$

$$\text{Or } I_t = I_0 \sin (\omega t + \phi)$$

(Equation 1.18)

where I_0 is the current signal amplitude and ϕ is the phase shift of the response signal (It) from the input signal (E_t).

The ratio between the applied potential and current response, according to Ohm's law, can be represented at any frequency (ω) by the complex electrical impedance of the system:

$$Z = \frac{E_t}{I_t} = \frac{E_0 \sin (\omega t)}{I_0 \sin (\omega t + \phi)} = Z_0 \frac{\sin (\omega t)}{\sin (\omega t + \phi)}$$

therefore, the impedance is expressed in terms of a magnitude, Z_0, and the phase shift, ϕ. It accounts for the combined ability of all the components within an electrochemical cell to resist the electron flow in the system.

Complex impedance is represented by real, Z', and imaginary, Z'' impedance terms which mainly originate from the resistance and reactance of the cell, as described in detail above. For circuit analysis purposes, Eulers formula can be used to express impedance as a complex function. It states that:

$$\exp (j\phi) = \cos \phi + \sin \phi$$

(Equation 1.19)

The AC potential is described as,

$$E_t = E_0 \exp (j\omega t)$$

and the resulting current as,

$$I_t = I_0 \exp (j\omega t\text{-}\phi)$$

The impedance can therefore be expressed in terms of its real and imaginary parts,

$$Z(\omega) = \frac{E_t}{I_t} = \frac{E_0 \exp(j\omega t)}{I_0 \exp(j\omega t - \phi)}$$

$$= Z_0 \exp(j\phi) = Z_0(\cos \phi + j\sin \phi)$$

The imaginary component, Z'', is represented by a capacitor or inductor. In an ideal capacitor, the voltage runs always 90° behind the current; this is indicated with -j followed by the impedance value. The voltage always runs 90° ahead of the current with an ideal inductor and is indicated by +j followed by the impedance value.

1.6.5 Equivalent Circuit Modelling

Equivalent circuits in EIS are used to model and fit experimental data using different electronic components. The circuit therefore represents alterations occurring at the electrode/electrolyte interface due to modifications of the electrode surface. To start, we assume the Randles circuit, as shown inset of Figure 1.23. It consists of an active electrolyte resistance (R_S) in series with the parallel combination of the double-layer capacitance (C_{dl}) and an impedance of a faradaic process, i.e. the Warburg element (W) with the charge-transfer resistance (R_{ct}).

1.6.5.1 Electrolyte Resistance (R_s)

All electrochemical cells have a solution resistance controlled by the cell's geometry and the composition of the cell's electrolyte. Current flow through this solution resistance can cause significant errors in the cell's measured potential. However, a modern three-electrode potentiostat compensates for some of the solution resistance through placement of the RE. However, any uncompensated resistance between the RE and the WE must be considered when you model your cell. This uncompensated resistance is inserted in series in the circuit owing to the fact that all current must pass through the electrolyte solution.

1.6.5.2 Warburg Impedance (W)

The Warburg impedance, W, represents the diffusion of the reacting species towards the electrode surface. It depends on the frequency of the potential perturbation. At high

frequencies, W is small since diffusing reactants don't have to move very far. At low frequencies, the reactants have to diffuse farther, increasing the Warburg-impedance. When the nominal size of the working electrode is reduced, such as for the nano-size electrodes employed in this thesis, mass transport increases, and thus the current is no longer dominated by the diffusion of the redox ions toward the WE.[281] As a result, the mass transfer dominated W becomes negligible and the Randles circuit can be simplified to a simple RC circuit.

1.6.5.3 Charge Transfer Resistance (R_{ct})

Electrochemical charge transfer is the transfer of electrons from the solution to the electrode metal, and the diffusion of metal ions in to the electrolyte, via oxidation and reduction processes, refer back to section 1.4.1. R_{ct} reflects the resistance to this charge transfer depending on the dielectric and insulating features at the electrode/electrolyte interface. Moreover, because of the absence of W on our nanoelectrodes, a change of surface properties on the sensing surface is mainly reflected through the change of R_{ct}.

1.6.5.4 Double Layer Capacitance (C_{dl})

An electrical double layer exists on the interface between an electrode and its surrounding electrolyte. This double layer is formed as ions from the solution adsorb onto the electrode surface. The charged electrode is separated from the charged ions by an insulating space, often on the order of angstroms. Charges separated by an insulator form a capacitor so a bare metal immersed in an electrolyte will behave like a capacitor. Capacitors in EIS experiments, however, often do not behave ideally. For example, the surface of the gold electrode will have a roughness factor to it; therefore will never act as a pure capacitor. Instead, they act like a constant phase element (CPE), which reflects the inhomogeneity of the surface and the current and potential distributions associated with electrode geometry.[282]

1.6.6 Data Presentation

The most popular formats for evaluating electrochemical impedance data are the Nyquist and Bode plots. Both data formats have different advantages, discussed below for a simplified Randles cell.

1.6.6.1 Nyquist Plot

The Nyquist Plot for a Simplified Randles cell is always a semicircle. A small sinusoidal potential (or current) is applied of fixed frequency. The system response is measured and the impedance is computed for that frequency. That is then repeated for a range of frequencies. The nyquist plot consists of the real component of impedance (Z') plotted against the imaginary component ($-Z''$) at these predetermined excitation frequencies. The plot goes from high to low frequency and each point is the total impedance (Z_{tot}) at that frequency value, see Figure 1.24.
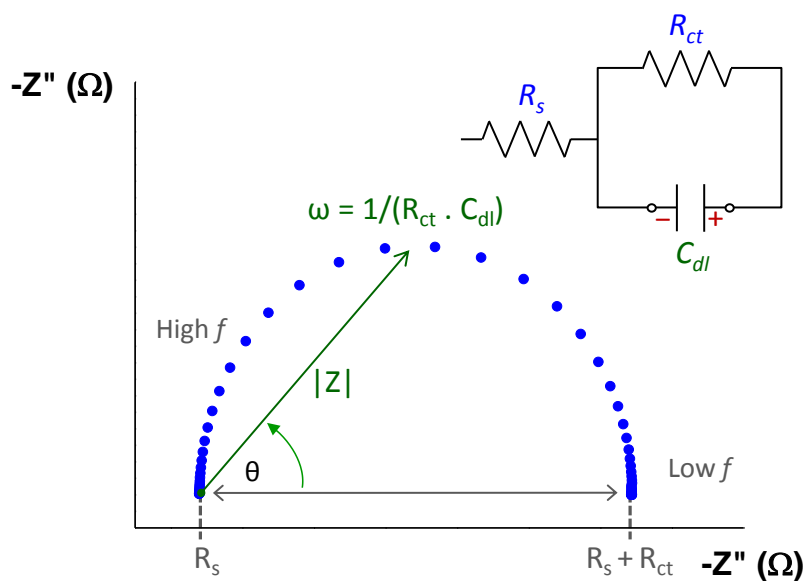
Figure 1.24: Nyquist plot including impedance vector and equivalent circuit diagram inset. (Reproduced from [283])

This plot is indicative of the capacitive and inductive character of the electrochemical cell as well as providing insight into the mechanisms of the reaction taking place. The R_S can be found by reading the real axis (Z') value at the high frequency intercept, near the origin of the plot. At the other end of the real axis (low f) the intercept is the sum of the

R_{ct} and the R_s. The diameter of the semicircle is therefore equal to the charge transfer resistance. In EIS, when the system is perturbed it relaxes to a new steady state. This relaxation takes an amount of time, known as the time constant. In Nyquist diagrams, each semicircle plot is characteristic of a single time constant. A disadvantage to this diagram is that the frequency cannot be determined from the plot; therefore, the AC frequency of selected data points should be indicated.

1.6.6.2 Bode Plot

Bode plots show the frequency-dependence of the impedance of the system. The bode modulus represents the impedance magnitude (or the real or imaginary components of the impedance) as a function of frequency. The bode phase represents the phase shifts discussed in section 1.6 again as a function of frequency. Both the logarithm of the absolute impedance, |Z| and the phase shift, φ, are plotted against the logarithm of the excitation frequency on a shared x-axis, see Figure 1.25.
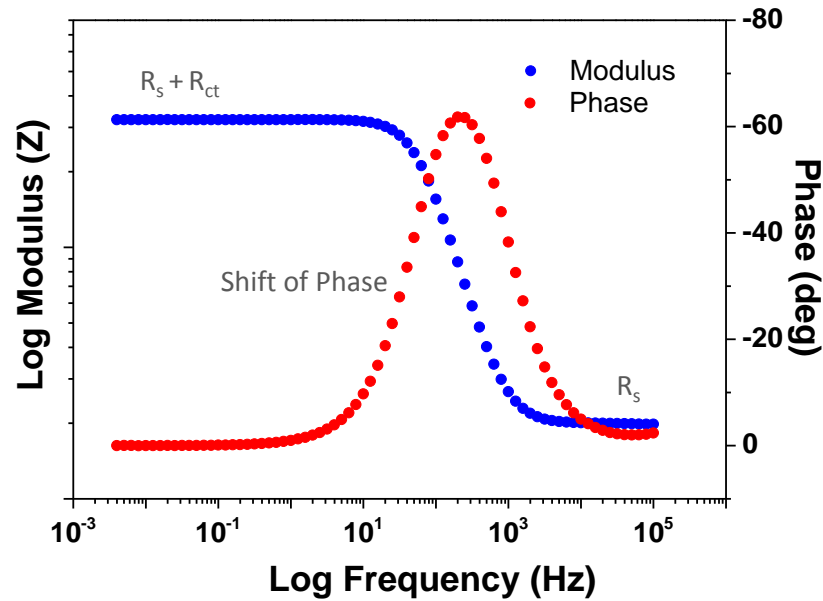
Figure 1.25: Bode Plots including impedance modulus and phase angle vs. log of frequency.

1.7 Introduction to Impedimetric Biosensors

A biosensor is "a device which uses a living organism or biological molecules, especially enzymes or antibodies, to detect the presence of chemicals." An electrochemical biosensor is composed of an electrochemical transducer (impedimetric, in this case), a biological recognition element and an electronic system, Figure 1.26. Briefly, the analyte in the electrochemical cell interacts with the biorecognition element and is converted to a measurable signal by the transduction system. The signal is then converted into a readout or display.
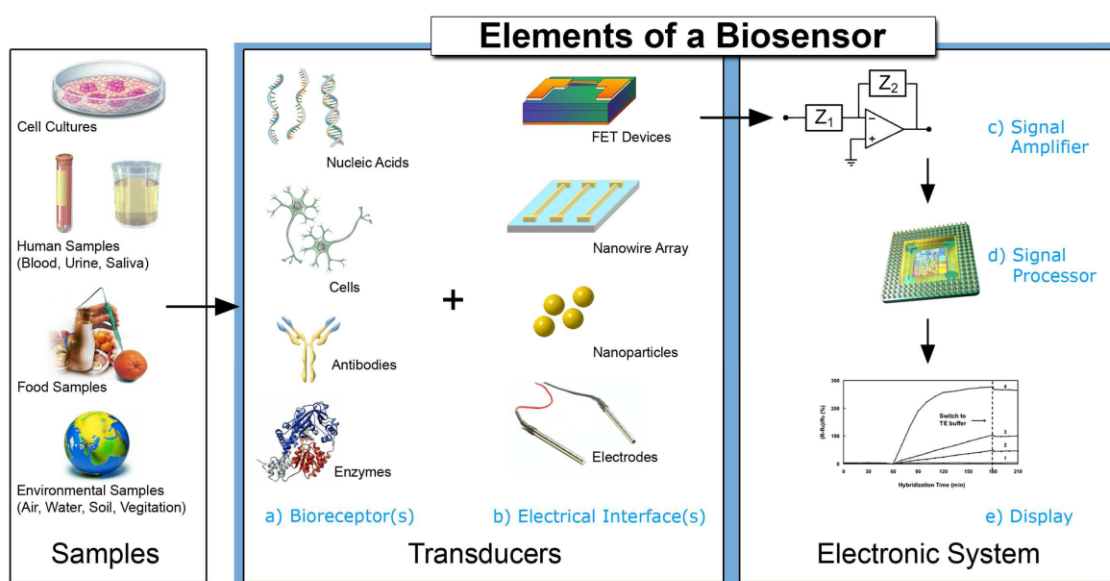
Figure 1.26: The elements of a biosensor, (reproduced from [284]).

Impedimetric biosensors are based on electrochemical impedance spectroscopy (EIS), discussed in the last section. It is used to measure intrinsic properties of a surface or a process that affects the resistive and the capacitive behaviour of an electrochemical system, such as, binding of analyte to the biorecognition molecules at the electrode surface. In other words, EIS can monitor electrode modifications, layer formation on electrode surfaces and binding kinetics between molecules such as DNAs, receptors, antibodies, antigens, proteins, ions, etc.

Impedimetric immunosensors have recently received particular attention since they possess a number of attractive characteristics associated with the use of electrochemical transducers, namely, low cost of electrode mass production, cost effective

instrumentation, the ability to be miniaturised and to be integrated into multi-array or microprocessor-controlled diagnostic tools and remote control of implanted sensor. Indeed, due to the above-mentioned characteristics, electrochemical impedance spectroscopy (EIS)-based sensors are considered as promising candidates for use at on-site applications. EIS biosensors can be classified as faradaic and non-faradaic biosensors.

1.7.1 Faradaic and Non-faradaic Impedance

The difference between faradaic and non-faradaic impedance spectroscopy is the presence and absence of a redox probe in the measurement solutions, respectively.[285]

The characteristics of a modified electrode can be investigated by employing a diffusing redox probe in the solution. As discussed in section 1.4, a redox probe, such as an iron or cobalt complex, is oxidised or reduced on the surface depending on the applied potential. A change in the interfacial properties of the electrode, e.g. from adsorption of biomolecules to the surface, will result in a more resistive behaviour (higher impedance) at the electrode. This is due to steric or electrostatic blocking of the redox ions whose motion between the electrolyte and the electrode constitutes the faradaic current. When the supply of ions does not meet the demand created by the potential, the resistance increases and the cell is then said to be polarised at that electrode. This is known as the faradaic impedance of the electrode.

Alternatively, the capacitive or dielectric features of the interface can be analytically measured in the absence of a redox probe, known as non-faradaic impedance.[286, 287] Electrode interfacial changes, via modification with biomolecules, will lead to a displacement of water ions from the electrode surface. This is detectable from the associated change in the electrode surface capacitance and, consequently, the impedance. The non-faradaic approach can be sensitive, although it is unpredictable in terms of the associated capacitive changes upon target analyte binding. Since these non-faradaic EIS based biosensors do not require an additional redox agent to improve their sensitivity they can be used in label-free point of care diagnostics. However, this technique can be less sensitive and non-specific binding can lead to false positive results.

1.7.2 Biorecognition Elements

Chemical biosensors are based on the presence of a biological recognition element which form a critical part of the biosensing devices. Normally, in order to create an efficient biosensing platform, the biological receptors are immobilised onto the electrode surface to form the biorecognition layer. The process is crucial to the senor development as the chosen biomolecules have to be able to maintain their structure, their function and their biological activity after immobilisation, and most importantly need to be stable during the use.

There are many methods to immobilise a biological recognition layer on to the substrate which depend on a number of factors, but mainly, it needs to be compatible with the electrode surface and material, the bio-receptor (capture molecule) and the analyte of interest (the target). EIS provides direct detection of the interaction between these biorecognition elements, measuring the change of impedance, and provide a non-destructive means for the characterisation of the electrical properties at biological interfaces. To this end, the EIS-based methods have been extensively employed to study protein binding at a surface, cell growth, bacterial growth, DNA hybridisation, and most commonly, the antigen–antibody reaction.

1.7.2.1 *Antibody-Antigen Based Sensors*

Antibody-antigen based biosensors are constructed by immobilising antibodies onto an electrode surface, then measuring the impedimetric response following antigen attachment. The binding of the antibody-antigen complex results in formation of an insulating layer on the electrode surface, producing a change in electrical properties over a range of frequencies. Antibodies are the most widely reported biological recognition element due to their high affinity, versatility, and commercial availability. The subsequent antigens can be a range of biomolecules including bacteria, cells, viruses or other proteins, which have an affinity to the antibody. Antibody-Antigen based sensors are also known as immunosensors.

Immunosensor sensitivity is strongly dependant on the amount of antibody immobilised on the electrode, i.e. the number of potential antigen binding sites; therefore the immobilisation chemistry plays an important role in the formation of these sensors. There

are many way to attach antibodies to a metallic surface, including polymer electrodeposition,[288-290] spontaneous adsorption,[291] self-assembled monolayers (SAM)[292] or by molecularly imprinted polymers.[293-295] Immunosensors could potentially be used to detect and selectively quantify any chemical compound by only changing the specific antibody that is employed.[296] Subsequently, they are very useful in widespread applications such as medical diagnostics and environmental monitoring, which will be discussed in the next section.

1.7.2.2 Enzyme-Based Sensors

In an enzyme-based biosensor, enzymes are immobilised onto the electrode surface through physical adsorption, covalent attachment, entrapment or cross-linking techniques. The specific binding capabilities and catalytic activity of enzymes make them popular recognition elements. EIS is employed to monitor changes of the interfacial properties of electrodes upon immobilisation of enzymes and to characterise biocatalytic processes at the enzyme-modified electrodes.[297] A detectable electroactive signal can be obtained in several ways: (i) the enzyme converts the analyte into a detectable product; (ii) the analyte activates or inhibits the enzyme; and (iii) interactions with analytes produce measurable modifications to the enzyme properties. The catalytic activity of enzymes allows lower limits of detection compared to common binding techniques. However, the stability of the enzyme limits the biosensor's lifetime. Enzymatic impedimetric sensors are commonly used to detect glucose,[298, 299] hydrogen peroxide,[300, 301] and urea.[302, 303]

1.7.2.3 Cell-Based Sensors

Cell-based impedimetric sensors involve the use of bacterial, prokaryotic, eukaryotic and mammalian cells for sensing and cell monitoring.[304] In particular for impedance spectroscopy, assays involve cell–cell or cell–analyte interactions. Living cells are excellent electrical insulators at low signal frequencies, therefore culturing cells onto electrodes, in turn, causes a change in the electrode impedance.[305]

Cell-based sensing systems are relatively easy and inexpensive to prepare and they tend to be stable to environmental changes (temperature and pH).[306] Though cell-based

biosensors are not as sensitive to environmental changes as molecular-based sensors; one of their main advantages is that they provide functional information, i.e. the physiological effect of a stimulus on a living system. For example, they can be used to study the functional characterisations of pharmaceutical compounds on a given physiological system, and can continuously monitor living cells to study cellular physiological action when subjected to stimulus.[307] Moreover, impedimetric cell-based methods deliver fast response times, have long-term use and enable label-free *in vivo* monitoring.[308, 309]

Impedimetric cell-based biosensors have been used for pharmaceutical evaluation of drugs, pathogens, and toxicants,[307] environmental monitoring of bacteria and food pathogens, [310-313] and in biomedicine for cancer monitoring.[309, 314, 315]

1.7.2.4 *Aptamer-Based Sensors*

Aptamers are artificial single-stranded nucleic acids, RNA or single-stranded DNA oligonucleotides which bind selectively to a desired target with high affinity, including proteins small molecules, cells, viruses, bacteria, and amino acids. Aptamers can be synthesised at low cost by *in vitro* evolutionary selection (SELEX) and easily modified with different functional groups for various immobilisation strategies including SAM with thiols or silanes.[316, 317] Impedimetric aptasensors offer analysis of interfacial properties and provide high selectivity and label-free detection.

Aptamers have presented high specificity of binding affinity, good stabilisation, and long shelf life. Moreover, aptamers can reversibly capture and release their target protein.[318] Aptasensors are used for contaminant detection, drugs, pesticides and toxins, in food [319-321] and the environment,[322, 323] as well as in medical diagnostics.[324-326]

.

1.7.3 Applications of Impedimetric Immunosensors

Potential application areas for affinity-based biosensors include health care, food processing, environmental monitoring, and defence. Although aptamer-based and cell-based biosensors show potential for future development, antibodies are currently the most highly developed recognition elements for these devices. Due to the commercial success of immunosensors in the aforementioned areas, the range of analytes, sensitivity, selectivity, and reliability afforded by these methods appears sufficient to warrant continued use and development.[327] Impedimetric immunosensors in particular provide real-time, label-free detection of antigen–antibody binding, as described above. When an antibody, immobilised on an electrode, binds to an antigen to form a complex, the impedance will exhibit changes in the interfacial properties at the electrode/electrolyte interface. Particularly for Faradaic sensing, the binding of the antigen –antibody complex hinders the transfer of electrons between the redox solution and electrode, thereby increasing resistance and decreasing capacitance.[328] Moreover, EIS is non-destructive to these biological interactions. [286]

These sensors have attracted interest in recent years for applications in areas that require both a high selectivity, a high sensitivity and require point of care sensing, such as health and the environment.[329]

1.7.3.1 Human and Animal Health

Antibody-based immunoassays are widely used for the monitoring of cancer biomarkers such as human epidermal growth factor receptor-3 (HER-3), [330-333] epidermal growth factor receptor (EGFR),[334-337] and carcinoembryonic antigen (CEA),[338-342]

The human epidermal growth factor receptor (HER) family plays a key role in regulation of mammalian cell survival, proliferation, adhesion, and differentiation. HER proteins exists in normal human adult and fetal tissues; however, in a risk of cancer, the levels of HER will be increased.[331] HER-3 and HER-2 are overexpressed 20–30% in a range of tumour cells, i.e. in breast cancers. It is therefore one of the best characterised biomarkers to aid in therapeutic decision making for patients with breast cancer.[332]

Impedimetric immunological biosensors have been effectively used for identification of HER proteins. Canabaz *et al*. demonstrated the ultrasensitive quantification of HER-3 with a linear range of 0.2–1.4 pg/mL. They employed a gold electrode surface, layered with, hexanedithiol, gold nanoparticles, and cysteamine, respectively. Anti-HER-3 antibody was covalently attached to cysteamine by glutaraldehyde and used as a bioreceptor.[343] Soares *et al.* also demonstrated detection of HER-2 by direct immobilisation via covalent attachment to the electrode and immobilisation in multiple steps by bioaffinity.[333] They showed a limit of detection (LOD) of 0.88 ng/mL and 1.64 ng/mL for the two sensing platforms, which is comparable to the immunosensors reported in the literature.[344, 345] Other biomarkers include carcinoembryonic antigen (CEA), a preferred tumour marker to help predict outlook in patients with colorectal cancer. Hou *et al.* developed a complex sandwich-type impedimetric immunosensor on glassy carbon electrodes.[328] Whereas Tang *et al*. demonstrated a simple and sensitive label-free electrochemical immunoassay for detection of CEA using on gold nanoparticles and a nonconductive polymer film.[342]

Finally, another receptor that is overexpressed in tumour cells is the epidermal growth factor receptors (EGFR). In addition, it has been identified as a strong prognostic indicator for aggressive disease stages in several types of cancers.[346] The quantification of this receptor is, therefore, highly desired for cancer screening and effective prognosis. Eshafey *et al.* used Au electrodes modified with gold nanoparticles functionalised by cysteamine/ PDITC/protein G for the detection of biomarker EGFR. The immunosensor had a LOD as low as 0.34 pg/mL in PBS and 0.88 pg/mL in human plasma.[347]. Similarly, Asav *et al.* demonstrated detection of EGFR in artificial serum samples.[337] Sensing in serum samples further supports the potential use of these sensors for commercial applications in healthcare. A large amount of publications based on impedimetric immunosensors also exist for the detection of C-reactive protein (CRP); a widely accepted biomarker for cardiovascular disease [348-352] and inflammation, as well as for prostate-specific antigen (PSA), which is elevated in the presence of prostate cancer or other prostate disorders. [353-356]

The determination of human and animal viruses is also a large area for the development of impedimetric immunosensors. Viral infections are often asymptomatic or present generic symptoms which are hard to diagnose. Impedimetric sensors that detect the presence of viruses or their specific antibodies on-site would provide doctors and veterinarians with a rapid diagnosis tool, which saves time and money (refer to section 1.1.1). EIS immunosensors have been used to detect a number of viruses including influenza virus,[357, 358] Citrus Tristeza virus,[359] hepatitis C virus (HCV),[360, 361] dengue virus,[362-367] HIV,[368] herpes virus and rabies. However, only a handful of these publications report actual viral detection and even fewer report detection in real sera.

Fang *et al.* demonstrated the detection of antibodies specific to the dengue virus in human serum. They immobilised inactivated dengue virus onto a silane/glutaraldehyde modified interdigitated electrode surface as detection probe.[366] Results show direct and repeatable correlation between signal outputs with respect to serum concentrations. Subsequently, this immunosensor has the potential to be developed into a hand-held device for clinical POC screening or molecular diagnosis of dengue infection in the field. The opposite immunosensor design was presented by Cecchetto *et al.* in which antibodies to a dengue protein, anti-NS1, were used as the capture biomolecule for the detection of dengue protein biomarker NS1.[362] This approach is more useful clinically in that NS1 is secreted from infected cells unlike antibodies which can be present for a variety of reasons. Moreover, this sensing method has the potential to detect all four dengue virus serotypes. Three of the four of these glycoproteins were identified by Luna et al on one platform. They developed a biosystem immobilising Concanavalin A lectin on a gold electrode modified with a lipid monolayer, for the specific identification of glycoproteins present in the sera of infected patients contaminated with dengue serotypes 1, 2 and 3.[363] This study is very promising to POC sensor development as it can classify the type of dengue virus.

Influenza type A viruses are of most significance to public health due to their potential to cause an influenza pandemic. Since the outbreaks of human influenza A (H1N1) virus in 2009, and outbreaks of the highly contagious avian influenza (H5N1), there have been numerous recent publications employing impedimetric immunosensing of different viral

strains. Arya *et al.* developed a label free immunosensor for the detection of human influenza virus hemagglutinin (HA) specific antibody. A coiled-coil peptide with integrated HA-antibody specific peptide was employed as a molecular recognition element.[369] The modified electrode showed great specificity towards the HA-antibody, however all the analytes were prepared in buffer not real samples. Although promising, the authors have not demonstrated detection in clinical samples, to enable POC virus detection. On the other hand, Jarocka *et al.* also demonstrated detection avian influenza hemagglutinin specific antibodies (anti-H5 HA Ab) in chicken sera.[358] Not only do the authors demonstrate detection in serum samples, they are also able to distinguish between sera of non-vaccinated and vaccinated hens, against avian influenza. Moreover, they demonstrated a sensitivity of almost 10^4 times better than ELISA. This sensor is highly sensitive and specific and has potential for POC use as a device for antibody detection. Furthermore, Wicklein *et al.* developed an affinity biosensor which could successfully detect and distinguish between human (H1N1) and avian (H5N9) isolates.[370] This discrimination between phenotypes of influenza virus is very important for POC sensing so that the correct strain of virus is detected and to avoid false positives.

1.7.3.2 *Food security*

The analysis of foods to assess the presence of both biological (bacterial pathogens) and chemical contaminants is critical to ensure food safety and quality. Impedimetric immunosensors for food safety applications, in particular the detection of antibiotic residues in foods, is reviewed.

Ionescu *et al.* developed an immunosensor technology for the determination of trace amounts of ciprofloxacin antibiotic.[371] The technology was based on the immobilisation of anti-ciprofloxacin antibodies by chemical binding onto a poly(pyrrole-NHS) film electrogenerated on a solid gold substrate. The detection method presented was fast and easy as they employed ciprofloxacin as analyte and immobilised its specific antibody on the electrode surface as the surface receptor. The ciprofloxacin antibiotic was detected at a range of 1 μg/ml down to 10 pg/ml in PBS buffer solutions. Conzuelo *et al.* demonstrated immunosensing of sulfonamide and tetracycline antibiotics residues, but instead they showed detection in milk.[372] Moreover, the type of milk analysed did not affect the immunosensor response, showing that they do not get interference from the

milk proteins. They employ an o-ABA modified surface (similar to the modification used in this thesis) on disposable dual screen-printed carbon electrodes and covalently attach Protein G to immobilise capture antibodies for the antibiotics. This disposable immunosensor demonstrates the multiplexed determination of different antibiotics in milk samples. Although it required labels which are non-ideal for POC sensing, it does not require milk sample treatment, which is promising. Another antibiotic that needs to be controlled is the synthetic antibiotic chloramphenicol (CAP), which is widely used as an anti-microbial agent. Chullasat *et al.* applied their immunosensor to analyse CAP analyte in shrimp samples.[373] They use a thiourea SAM modified Au macroelectrode for the detection of ultra-trace amount of CAP. Gold nanoparticles coated with mercaptosuccinic acid (MSA) were adsorbed on the electrode and Anti-CAP antibodies were immobilised as the capture biomolecule. Nanoparticles were used to increase the surface area for attachment of the immobilised antibody and which led to a higher signal. This platform yielded detection of a wide linear range $(0.50 - 10) \times 10^{-16}$ M, and a very low determination limit of 1.0×10^{-16} M.

The quality of the impedimetric immunosensors for the detection of pathogenic bacteria, in food analysis, is quite poor. In particular the detection limits can be improved. Very few publications exhibited low detection limits with relatively short analyses times, in real samples. Impedimetric detection of bacterial whole cells is otherwise quite common, in particular for *E.coli* (O157:H7)[374-379]. For example, Varshney *et al.* developed an impedimetric sensor for rapid and specific detection of *E. coli* O157:H7 in ground beef samples, demonstrating an LOD of 8.0×10^5 CFU ml^{-1}.[377] Other bacterial pathogens have also been detected, including Staphylococcus aureus, [380-382] Salmonella in milk samples[383, 384] and Listeria monocytogenes.[385] Melamine, again, is another contaminant that has been employed for electrochemical detection, as reviewed by Li *et al.*[386]

1.7.3.3 *Environmental Applications*

Finally, to review environmental immunosensors, I focus on pesticide detection, particularly in crop or water supplies. Fenvalerate is a pyrethroid insecticide, highly toxic

for bees and fish. It is not listed as a mandatory detection substance, leading to the rise of fenvalerate residues in tea leaves. Wang *et al.* employed glassy carbon electrodes for the detection of fenvalerate in tea.[387] Fenvalerate monoclonal antibodies were immobilised on the electrode via crosslinking with gluteraldehyde for the detection of fenvalerate via an antigen-antibody immunoreaction. POC determination of insecticides like this are required, as they could contaminate the ecological environment and drinking water sources by entering through means of leaching, surface run-off and dry/wet deposition.

Atrazine is widely used herbicide for the control of annual grasses and broad-leaved weeds. [296] Atrazine residues contaminate crops, wells, and streams due to spills, spraying and run-off. Moreover, they have often been found in drinking water which is a threat for the public health. Many immunological-based assays have been developed for the sensitive detection of atrazine. Valera *et al*. developed an impedimetric immunosensor which employed Au/Cr interdigitated microelectrodes for the detection of atrazine in buffer. [388] Impedance experiments were carried out directly without a redox probe, measuring the specific binding of a non-labelled antibody with a coated antigen. The assay relies on the immunochemical competitive reaction between the pesticide and the immobilised antigen on interdigitated microelectrodes for a small amount of the specific antibody. Although very sensitive and selective, the process is complex and time consuming. This platform was again used as a single frequency impedimetric immunosensor for atrazine detection. [296] Another study, by Ionescu *et al.* used histidine-labelled anti-atrazine antibodies, on a polypyrrole modified gold electrode, to detect the immunoreaction of atrazine by affinity binding. [389] Alternatively, Helali *et al.* described the development of an impedimetric immunosensor, based on niobium/niobium oxide electrodes, for the detection of atrazine. In this study, electrodes were silanised in APTES ((3-Aminopropyl)triethoxysilane) and activated using gluteraldehyde which cross-linked to the Fab fragment K47H antibody capture for atrazine detection.[390] This protocol does not require complex procedures or labelled antibodies and provides results at the required sensitivity. Therefore, this pesticide biosensor can be employed for the easy and rapid monitoring of water in environment.

To this end, diagnostics methods must be simple, sensitive and able to detect multiple biomarkers that exist at low concentrations in biological fluids or samples. In recent years, the demand has grown for disposable devices that demonstrate fast response times, are user-friendly, cost-efficient, and suitable for mass production. Biosensor technologies offer the potential to fulfil these criteria through an interdisciplinary combination of approaches from nanotechnology, chemistry and biochemistry. However, biosensor devices need to be further developed and improved to face these new challenges to allow, for example, multiplex analysis of several biomarkers where arrays of sensors need to be developed on the same chip. In this context, impedimetric biosensing is a promising analytical method for sensitive and selective detection of biomolecules. Furthermore, the label-free detection that avoids the use of complex and expensive pretreatment processes and ease of miniaturisation makes the impedimetric biosensors more attractive for POC multiplex analysis of different targets.

1.8 Scope and Organisation of this Thesis

The aim of the work presented is to develop sensing devices at nanoscale for the highly sensitive detection of molecules of interest in agricultural, environmental and pharmaceutical fields. We focused on developing SERS and electrochemical based nanosensors, as previously described. The fundamental design characteristic was to develop sensitive sensors that don't require experienced personnel or a lot of sample pre-treatment for POC use. The literature sections discussed previously in this chapter highlighted the state of the art sensor designs, however, only a handful of them exhibited POC capabilities. This thesis presents a SERS sensor that has minimal sample preparation requirements and provides tremendous opportunities for food safety and security sectors. Furthermore, a label-free, compact and cost-efficient electrochemical sensor chip platform, is presented, that demonstrates the potential development of immunoassay-based POC devices for on-farm diagnosis and therapeutic monitoring in animal health applications.

Firstly, I present work undertaken to date in nanosensors development employing surface enhanced Raman Spectroscopy in terms of fabrication and sensing application and performances. A low-cost templating nanofabrication approach was developed for fabrication of flexible SERS substrates employing a nanostructured soda drink can. These substrates were applied to the detection of crystal violet and melamine, two molecules of interest in the food industry. These substrates provided very high sensitivity and analysis times were on the order of 10 minutes. Secondly, I will present the electroanalysis undertaken using fully integrated nanowire devices developed within the Nanotechnology Group. These sensor devices were applied, in chapter four, to the detection of neonicotinoids pesticides recently banned by the EU. These devices were extremely sensitive exhibiting limits of detection below the statutory maximum residual limit thresholds. Furthermore, these devices are challenged to the detection of viruses associated with the BRD in conjunction with other sensing mechanisms, and also employing a multiplexed sensing approach.

Finally, I will conclude by outlining the enhancement and the potential of these sensors for security and environmental applications. Further potential opportunities for these nanosensors will be presented in future work.

1.8.1 Chapter 2

This chapter describes the fabrication and characterisation of SERS sensors, made from an aluminium drinks can. This work shows the quantitative detection of crystal violet and other dye molecules, as well as the deection of glucose and the adulterant melamine in milk and infant formula.

1.8.2 Chapter 3

Chapter 3 demonstrates the SERS detection of neonicotinoid pesticides, which are an environmental concern. In this chapter, SERS simulations are analysed and all Raman and SERS peaks are assigned to their corresponding molecular vibrations. This chapter also sees the introduction of electrochemical sensing. SWV is used to detect nano-molar concentration of neonicotinoid pesticides.

1.8.3 Chapter 4

In this chapter I present the development of an impedimetric immunosensor for a label-free serological diagnosis of BVDV-1. The chapter details the design, surface chemistry and electrochemical co-detection of BVD virus and antibody in different media of increasing biological complexity (buffer/ diluted serum). Ultimately, the sensor was employed to discriminate between disease positive and disease negative serum samples from both transiently infected and persistently infected calves. The chapter explains the various issues experienced during the development of the biosensor, as well as the strategies adopted to overcome these impediments. This sensor technology is versatile, amenable to multiplexing, easily integrated to POC devices, and has the potential to detect a wide range of animal diseases, as seen in the next chapter.

1.8.4 Chapter 5

This chapter presents preliminary work on the detection of bovine *Fasciola hepatica* or more commonly, liver fluke. The nanoband sensors from chapter 4 were again used in these experiments. Recombinant cathepsin L1 protease (from Dublin City University) was employed as the capture molecule on the nanoband electrodes. This enzyme has an affinity to anti-Fasciola hepatica antibodies in serum. Subsequently, determination of multiple seropositive and seronegative samples was investigated for the presence of fluke anitbodies.

1.8.5 Chapter 6

During the fabrication of the EIS based biosensor, it was found that the application of a second sensing mechanism can strengthen the applicability of the sensor. FET potentiometric sensing is employed in conjunction with the EIS sensing on the same platform described in chapter 4. The performance of the immunosensor, with both sensing mechanisms, is assessed and characterised in this chapter by challenging it to detection of Bovine Parainfluenza-3 Virus (BPI3-V).

1.8.6 Chapter 7

This chapter summarises the findings of the thesis and discusses their impact on the research field of biosensors for security and environmental applications. It also discusses the potential future directions of this work.

1.9 References

1. Food Agriculture Organisation, The Future of Food and Agriculture – Trends and Challenges; United Nations Rome, **2017**.

2. Tomley, F.M.; Shirley, M.W., Livestock Infectious Diseases and Zoonoses; *Philosophical Transactions of the Royal Society B: Biological Sciences,* **2009**, 364, 2637-2642.

3. Dehove, A.; Commault, J.; Petitclerc, M.; Teissier, M.; Macé, J., Economic Analysis and Costing of Animal Health: A Literature Review of Methods and Importance; *Revue Scientifique et Technique (International Office of Epizootics),* **2012**, 31, 605-17, 591-604.

4. Fulton, R.W., Bovine Respiratory Disease Research (1983-2009); *Animal Health Research Reviews,* **2009**, 10, 131-9.

5. Snowder, G.; Van Vleck, L.D.; Cundiff, L.; Bennett, G., Bovine Respiratory Disease in Feedlot Cattle: Environmental, Genetic, and Economic Factors; *Journal of Animal Science,* **2006**, 84, 1999-2008.

6. Wilkinson, A., Future of Brd Research: An Animal Health Industry Perspective; *Animal Health Research Reviews,* **2009**, 10, 163-164.

7. Ridpath, J.F., Bovine Viral Diarrhea Virus: Global Status; *Veterinary Clinics of North America: Food Animal Practice,* **2010**, 26, 105-121.

8. Horwood, P.F.; Gravel, J.L.; Mahony, T.J., Identification of Two Distinct Bovine Parainfluenza Virus Type 3 Genotypes; *Journal of General Virology,* **2008**, 89, 1643-1648.

9. Atkinson, N., The Impact of Bse on the Uk Economy; available at *http://www.veterinaria.org/revistas/vetenfinf/bse/14Atkinson.html*, **1999**.

10. Griebel, P.; Hill, K.; Stookey, J., How Stress Alters Immune Responses During Respiratory Infection; *Animal Health Research Reviews,* **2014**, 15, 161-165.

11. Haanes, E.J.; Guimond, P.; Wardley, R., The Bovine Parainfluenza Virus Type-3 (Bpiv-3) Hemagglutinin/Neuraminidase Glycoprotein Expressed in Baculovirus Protects Calves against Experimental Bpiv-3 Challenge; *Vaccine,* **1997**, 15, 730-738.

12. Gunn, G.J.; Saatkamp, H.W.; Humphry, R.W.; Stott, A.W., Assessing Economic and Social Pressure for the Control of Bovine Viral Diarrhoea Virus; *Preventive Veterinary Medicine,* **2005**, 72, 149-162.

13. Food Agriculture Organisation, International Code of Conduct on the Distribution and Use of Pesticides [on Line]; United Nations: Rome, **2005**.

14. Clevo, W., Environmental and Human Costs of Commercial Agricultural Production in South Asia; *International Journal of Social Economics,* **2000**, 27, 816-846.

15. Lichtenberg, E.; Zimmerman, R., Adverse Health Experiences, Environmental Attitudes, and Pesticide Usage Behavior of Farm Operators; *Risk Analysis,* **1999**, 19, 283-294.

16. Damalas, C.A.; Eleftherohorinos, I.G., Pesticide Exposure, Safety Issues, and Risk Assessment Indicators; *International Journal of Environmental Research and Public Health,* **2011**, 8, 1402-1419.

17.   Mostafalou, S.; Abdollahi, M., Pesticides and Human Chronic Diseases: Evidences, Mechanisms, and Perspectives; *Toxicology and Applied Pharmacology,* **2013**, 268, 157-177.

18.   Jeyaratnam, J., Acute Pesticide Poisoning: A Major Global Health Problem; *World Health Statistics,* **1990**.

19.   Aktar, M.W.; Sengupta, D.; Chowdhury, A., Impact of Pesticides Use in Agriculture: Their Benefits and Hazards; *Interdisciplinary Toxicology,* **2009**, 2, 1-12.

20.   Cooper, J.; Dobson, H., The Benefits of Pesticides to Mankind and the Environment; *Crop Protection,* **2007**, 26, 1337-1348.

21.   Wilson, C.; Tisdell, C., Why Farmers Continue to Use Pesticides Despite Environmental, Health and Sustainability Costs; *Ecological Economics,* **2001**, 39, 449-462.

22.   Lomborg, B., The Skeptical Environmentalist: Measuring the Real State of the World; *Cambridge University Press Cambridge,* **2003;** Vol. 1.

23.   Food Agriculture Organisation, Declaration on World Food Security; World Food Summit: Rome, **1996**.

24.   Fsai Food and Safety Authority Ireland; https://www.fsai.ie/home.html (Accessed on: 21/01/2018),

25.   Gossner, C.M.-E.; Schlundt, J.; Ben Embarek, P.; Hird, S.; Lo-Fo-Wong, D.; Beltran, J.J.O.; Teoh, K.N.; Tritscher, A., The Melamine Incident: Implications for International Food and Feed Safety; *Environmental Health Perspectives,* **2009**, 117, 1803-1808.

26.   Chan, E.Y.Y.; Griffiths, S.M.; Chan, C.W., Public-Health Risks of Melamine in Milk Products; *The Lancet,* 372, 1444-1445.

27.   Qian, G.; Guo, X.; Guo, J.; Wu, J., China's Dairy Crisis: Impacts, Causes and Policy Implications for a Sustainable Dairy Industry; *International Journal of Sustainable Development & World Ecology,* **2011**, 18, 434-441.

28.   Fao, H.H.H., Assessment and Management of Seafood Safety and Quality; 92-5-104954-8; Daya Books: Food and Agriculture Organisation of the United Nations, **2003**.

29.   Sapkota, A.; Sapkota, A.R.; Kucharski, M.; Burke, J.; Mckenzie, S.; Walker, P.; Lawrence, R., Aquaculture Practices and Potential Human Health Risks: Current Knowledge and Future Priorities; *Environment International,* **2008**, 34, 1215-1226.

30.   Eggins, B.R., Chemical Sensors and Biosensors; *John Wiley & Sons,* **2008;** Vol. 28.

31.   Kong, J.; Chapline, M.G.; Dai, H., Functionalized Carbon Nanotubes for Molecular Hydrogen Sensors; *Advanced Materials,* **2001**, 13, 1384.

32.   Zheng, G.; Patolsky, F.; Cui, Y.; Wang, W.U.; Lieber, C.M., Multiplexed Electrical Detection of Cancer Markers with Nanowire Sensor Arrays; *Nature Biotechnology,* **2005**, 23, 1294-1301.

33.   Kuo, T.-C.; Sloan, L.A.; Sweedler, J.V.; Bohn, P.W., Manipulating Molecular Transport through Nanoporous Membranes by Control of Electrokinetic Flow: Effect of Surface Charge Density and Debye Length; *Langmuir,* **2001**, 17, 6298-6303.

34.   Barry, S.; Dawson, K.; Correa, E.; Goodacre, R.; O'riordan, A., Highly Sensitive Detection of Nitroaromatic Explosives at Discrete Nanowire Arrays; *Faraday Discussions,* **2013**, 164, 283-293.

35.   Dawson, K.; Baudequin, M.; Sassiat, N.; Quinn, A.J.; O'riordan, A., Electroanalysis at Discrete Arrays of Gold Nanowire Electrodes; *Electrochimica Acta,* **2013**, 101, 169-176.

36.   Alivisatos, A.P.; Gu, W.; Larabell, C., Quantum Dots as Cellular Probes; *Annual Review of Biomedical Engineering,* **2005**, 7, 55-76.

37.   Mcmahon, J.M.; Henzie, J.; Odom, T.W.; Schatz, G.C.; Gray, S.K., Tailoring the Sensing Capabilities of Nanohole Arrays in Gold Films with Rayleigh Anomaly-Surface Plasmon Polaritons; *Optics express,* **2007**, 15, 18119-18129.

38.   Lovera, P.; Jones, D.; Corbett, B.; O'riordan, A., Polarization Tunable Transmission through Plasmonic Arrays of Elliptical Nanopores; *Optics express,* **2012**, 20, 25325-25332.

39.   Watson, J.D.; Crick, F.H., Molecular Structure of Nucleic Acids; *Nature,* **1953**, 171, 737-738.

40.   Patolsky, F.; Zheng, G.; Lieber, C.M., Nanowire Sensors for Medicine and the Life Sciences; *Nanomedicine,* **2006**, 1, 51-65.

41.   Anker, J.N.; Hall, W.P.; Lyandres, O.; Shah, N.C.; Zhao, J.; Van Duyne, R.P., Biosensing with Plasmonic Nanosensors; *Nature Materials,* **2008**, 7, 442-53.

42.   Skoog, D.A.; West, D.M.; Holler, F.J.; Crouch, S., Fundamentals of Analytical Chemistry; *Nelson Education,* **2013**.

43.   Siesler, H.W.; Holland-Moritz, K., Infrared and Raman Spectroscopy of Polymers; *M. Dekker,* **1980**.

44.   Kalantar-Zadeh, K.; Fry, B., Nanotechnology-Enabled Sensors; *Springer Science & Business Media,* **2007**.

45.   Settle, F.A., Handbook of Instrumental Techniques for Analytical Chemistry; *Prentice Hall PTR,* **1997**.

46.   Socrates, G., Infrared and Raman Characteristic Group Frequencies: Tables and Charts; *John Wiley & Sons,* **2001**.

47.   Raman, C.V.; Krishnan, K.S., A New Type of Secondary Radiation (Reprinted from Nature, Vol 121, Pg 501-502, 1928); *Current Science,* **1998**, 74, 381-381.

48.   Biology/Physics-Origin of the Different Colors of Things. 2017; http://howthingswork.org/physicsbiology-what-gives-rise-to-the-different-colours-of-things/.

49.   Koningstein, J.A., Introduction to the Theory of the Raman Effect; *Springer Science & Business Media,* **2012**.

50.   Ferraro, J.A.; Nakamoto, K.; Brown, C., Introductory to Raman Spectroscopy; *Elsevier,* **2003**.

51.   Long, D.A., The Raman Effect: A Unified Treatment of the Theory of Raman Scattering by Molecules; *John Wiley & Sons,* **2002**.

52.   Laserna, J., Modern Techniques in Raman Spectroscopy; *John Wiley and Sons,* **1996**.

53.   Jablonski, A., Efficiency of Anti-Stokes Fluorescence in Dyes; *Nature,* **1933**, 131, 839.

54.   Le Ru, E.; Etchegoin, P., Principles of Surface-Enhanced Raman Spectroscopy: And Related Plasmonic Effects; *Elsevier,* **2008**.

55.   Long, D.A., Raman Spectroscopy; *McGraw-Hill New York,* **1977;** Vol. 206.

56.   Bell, D.C.; Meyer, S.; Orchowski, A.; Tayebati, P.; Benner, G., Aberration-Correction in a Monochromated and Energy Filtered Environment; *Microscopy and Microanalysis,* **2009**, 15, 1490-1491.

57.   Gardiner, D.J., Practical Raman Spectroscopy; *Spinger-Verlag,* **1989**.

58.   Raman Spectrometer; http://way2science.com/raman-spectroscopy-2/ (Accessed on: 30/07/2018),

59.   Fleischmann, M.; Hendra, P.J.; Mcquillan, A.J., Raman Spectra of Pyridine Adsorbed at a Silver Electrode; *Chemical Physics Letters,* **1974**, 26, 163-166.

60.   Jeanmaire, D.L.; Van Duyne, R.P., Surface Raman Spectroelectrochemistry: Part I. Heterocyclic, Aromatic, and Aliphatic Amines Adsorbed on the Anodized Silver Electrode; *Journal of Electroanalytical Chemistry and Interfacial Electrochemistry,* **1977**, 84, 1-20.

61.   Albrecht, M.G.; Creighton, J.A., Anomalously Intense Raman Spectra of Pyridine at a Silver Electrode; *Journal of the American Chemical Society,* **1977**, 99, 5215-5217.

62.   Moskovits, M., Surface-Enhanced Spectroscopy; *Reviews of Modern Physics,* **1985**, 57, 783-826.

63.   Otto, A.; Mrozek, I.; Grabhorn, H.; Akemann, W., Surface-Enhanced Raman Scattering; *Journal of Physics: Condensed Matter,* **1992**, 4, 1143.

64.   Stiles, P.L.; Dieringer, J.A.; Shah, N.C.; Duyne, R.P.V., Surface-Enhanced Raman Spectroscopy; *Annual Review of Analytical Chemistry,* **2008**, 1, 601-626.

65.   Gersten, J.I., The Effect of Surface Roughness on Surface Enhanced Raman Scattering; *The Journal of Chemical Physics,* **1980**, 72, 5779-5780.

66.   Gersten, J.; Nitzan, A., Electromagnetic Theory of Enhanced Raman Scattering by Molecules Adsorbed on Rough Surfaces; *The Journal of Chemical Physics,* **1980**, 73, 3023-3037.

67.   Hutter, E.; Fendler, J.H., Exploitation of Localized Surface Plasmon Resonance; *Advanced Materials,* **2004**, 16, 1685-1706.

68.   Qiu, T.; Zhang, W.; Chu, P.K., Recent Progress in Fabrication of Anisotropic Nanostructures for Surface- Enhanced Raman Spectroscopy; *Recent Patents on Nanotechnology,* **2009**, 3, 10-20.

69.   Weaver, M.J.; Zou, S.; Chan, H.Y.H., Peer Reviewed: The New Interfacial Ubiquity of Surface-Enhanced Raman Spectroscopy; *Analytical Chemistry,* **2000**, 72, 38 A-47 A.

70.   Camden, J.P.; Dieringer, J.A.; Wang, Y.; Masiello, D.J.; Marks, L.D.; Schatz, G.C.; Van Duyne, R.P., Probing the Structure of Single-Molecule Surface-Enhanced Raman Scattering Hot Spots; *Journal of the American Chemical Society,* **2008**, 130, 12616-12617.

71.   Etchegoin, P.G.; Le Ru, E.C., A Perspective on Single Molecule Sers: Current Status and Future Challenges; *Physical Chemistry Chemical Physics,* **2008**, 10, 6079-6089.

72.   Park, W.H.; Kim, Z.H., Charge Transfer Enhancement in the Sers of a Single Molecule; *Nano Letters,* **2010**, 10, 4040-4048.

73.   Silmeco Hot Spots: Raman Scattering (Sers) Phenomenon; http://www.silmeco.com/knowledge-base/hot-spots (Accessed on: 20/08/2014),

74.   Le Ru, E.C.; Blackie, E.; Meyer, M.; Etchegoin, P.G., Surface Enhanced Raman Scattering Enhancement Factors: A Comprehensive Study; *The Journal of Physical Chemistry C,* **2007**, 111, 13794-13803.

75.   Sun, M.; Wan, S.; Liu, Y.; Jia, Y.; Xu, H., Chemical Mechanism of Surface-Enhanced Resonance Raman Scattering Via Charge Transfer in Pyridine–Ag2 Complex; *Journal of Raman Spectroscopy,* **2008**, 39, 402-408.

76.   Kambhampati, P.; Child, C.; Foster, M.C.; Campion, A., On the Chemical Mechanism of Surface Enhanced Raman Scattering: Experiment and Theory; *The Journal of Chemical Physics,* **1998**, 108, 5013-5026.

77.   Ikeda, K.; Suzuki, S.; Uosaki, K., Enhancement of Sers Background through Charge Transfer Resonances on Single Crystal Gold Surfaces of Various Orientations; *Journal of the American Chemical Society,* **2013**, 135, 17387-17392.

78.   Campion, A.; Ivanecky Iii, J.; Child, C.; Foster, M., On the Mechanism of Chemical Enhancement in Surface-Enhanced Raman Scattering; *Journal of the American Chemical Society,* **1995**, 117, 11807-11808.

79.   Lombardi, J.R.; Birke, R.L.; Sanchez, L.A.; Bernard, I.; Sun, S.C., The Effect of Molecular Structure on Voltage Induced Shifts of Charge Transfer Excitation in Surface Enhanced Raman Scattering; *Chemical Physics Letters,* **1984**, 104, 240-247.

80.   Adrian, F.J., Charge Transfer Effects in Surface-Enhanced Raman Scatteringa; *The Journal of Chemical Physics,* **1982**, 77, 5302-5314.

81.   Schatz, G.C., Theoretical Studies of Surface Enhanced Raman Scattering; *Accounts of Chemical Research,* **1984**, 17, 370-376.

82.   Campion, A.; Kambhampati, P., Surface-Enhanced Raman Scattering; *Chemical Society Reviews,* **1998**, 27, 241-250.

83.   Maier, S.A.; Brongersma, M.L.; Kik, P.G.; Meltzer, S.; Requicha, A.A.; Atwater, H.A., Plasmonics—a Route to Nanoscale Optical Devices; *Advanced Materials,* **2001**, 13, 1501-1505.

84.   Grzelczak, M.; Pérez-Juste, J.; Mulvaney, P.; Liz-Marzán, L.M., Shape Control in Gold Nanoparticle Synthesis; *Chemical Society Reviews,* **2008**, 37, 1783-1791.

85.   Lee, S.J.; Guan, Z.; Xu, H.; Moskovits, M., Surface-Enhanced Raman Spectroscopy and Nanogeometry: The Plasmonic Origin of Sers; *The Journal of Physical Chemistry C,* **2007**, 111, 17985-17988.

86.   Banholzer, M.J.; Millstone, J.E.; Qin, L.; Mirkin, C.A., Rationally Designed Nanostructures for Surface-Enhanced Raman Spectroscopy; *Chemical Society Reviews,* **2008**, 37, 885-897.

87.   Bell, S.E.; Mccourt, M.R., Sers Enhancement by Aggregated Au Colloids: Effect of Particle Size; *Physical Chemistry Chemical Physics,* **2009**, 11, 7455-7462.

88.   Grzelczak, M.; Vermant, J.; Furst, E.M.; Liz-Marzán, L.M., Directed Self-Assembly of Nanoparticles; *ACS Nano,* **2010**, 4, 3591-3605.

89.   Zhu, S.; Fan, C.; Wang, J.; He, J.; Liang, E., Self-Assembled Ag Nanoparticles for Surface Enhanced Raman Scattering; *Optical Review,* **2013**, 20, 361-366.

90.   Zhang, L., Self-Assembly Ag Nanoparticle Monolayer Film as Sers Substrate for Pesticide Detection; *Applied Surface Science,* **2013**, 270, 292-294.

91.   Hepel, M.; Zhong, C.-J., Functional Nanoparticles for Bioanalysis, Nanomedicine, and Bioelectronic Devices Volume 2; *American Chemical Society*, 2012; Vol. 1113, p 0.

92.   Lee, S.J.; Morrill, A.R.; Moskovits, M., Hot Spots in Silver Nanowire Bundles for Surface-Enhanced Raman Spectroscopy; *Journal of the American Chemical Society,* **2006**, 128, 2200-2201.

93.   Tang, J.; Zhao, Q.; Zhang, N.; Man, S.-Q., Facile Fabrication of Large-Area and Uniform Silica Nanospheres Monolayer for Efficient Surface-Enhanced Raman Scattering; *Applied Surface Science,* **2014**, 308, 247-252.

94.   Li, W.; Camargo, P.H.C.; Lu, X.; Xia, Y., Dimers of Silver Nanospheres: Facile Synthesis and Their Use as Hot Spots for Surface-Enhanced Raman Scattering; *Nano Letters,* **2009**, 9, 485-490.

95.   Martín, A.; Pescaglini, A.; Schopf, C.; Scardaci, V.; Coull, R.; Byrne, L.; Iacopino, D., Surface-Enhanced Raman Scattering of 4-Aminobenzenethiol on Au Nanorod Ordered Arrays; *The Journal of Physical Chemistry C,* **2014**, 118, 13260-13267.

96.   Martin, A.; Wang, J.J.; Iacopino, D., Flexible Sers Active Substrates from Ordered Vertical Au Nanorod Arrays; *RSC Advances,* **2014**, 4, 20038-20043.

97.   Xie, Z.; Tao, J.; Lu, Y.; Lin, K.; Yan, J.; Wang, P.; Ming, H., Polymer Optical Fiber Sers Sensor with Gold Nanorods; *Optics Communications,* **2009**, 282, 439-442.

98.   Lovera, P.; Creedon, N.; Alatawi, H.; Mitchell, M.; Burke, M.; Quinn, A.J.; O'riordan, A., Low-Cost Silver Capped Polystyrene Nanotube Arrays as Super-Hydrophobic Substrates for Sers Applications; *Nanotechnology,* **2014**, 25, 175502.

99.   Walker, D.A.; Browne, K.P.; Kowalczyk, B.; Grzybowski, B.A., Self-Assembly of Nanotriangle Superlattices Facilitated by Repulsive Electrostatic Interactions; *Angewandte Chemie International Edition,* **2010**, 49, 6760-6763.

100.   Liu, Z.; Yang, Z.; Peng, B.; Cao, C.; Zhang, C.; You, H.; Xiong, Q.; Li, Z.; Fang, J., Highly Sensitive, Uniform, and Reproducible Surface-Enhanced Raman Spectroscopy from Hollow Au-Ag Alloy Nanourchins; *Advanced Materials,* **2014**, 26, 2431-2439.

101.   Yang, M.; Alvarez-Puebla, R.N.; Kim, H.-S.; Aldeanueva-Potel, P.; Liz-MarzáN, L.M.; Kotov, N.A., Sers-Active Gold Lace Nanoshells with Built-in Hotspots; *Nano Letters,* **2010**, 10, 4013-4019.

102.   Sun, Y.; Xia, Y., Shape-Controlled Synthesis of Gold and Silver Nanoparticles; *Science,* **2002**, 298, 2176-2179.

103.   Vigderman, L.; Zubarev, E.R., Starfruit-Shaped Gold Nanorods and Nanowires: Synthesis and Sers Characterization; *Langmuir,* **2012**, 28, 9034-9040.

104.   Liu, M.; Guyot-Sionnest, P., Mechanism of Silver(I)-Assisted Growth of Gold Nanorods and Bipyramids; *The Journal of Physical Chemistry B,* **2005**, 109, 22192-22200.

105.   Chen, J.; Mclellan, J.M.; Siekkinen, A.; Xiong, Y.; Li, Z.-Y.; Xia, Y., Facile Synthesis of Gold−Silver Nanocages with Controllable Pores on the Surface; *Journal of the American Chemical Society,* **2006**, 128, 14776-14777.

106.   Shiohara, A.; Langer, J.; Polavarapu, L.; Liz-Marzan, L.M., Solution Processed Polydimethylsiloxane/Gold Nanostar Flexible Substrates for Plasmonic Sensing; *Nanoscale,* **2014**, 6, 9817-9823.

107.   Ye, J.; Van Dorpe, P.; Van Roy, W.; Borghs, G.; Maes, G., Fabrication, Characterization, and Optical Properties of Gold Nanobowl Submonolayer Structures; *Langmuir,* **2009**, 25, 1822-1827.

108.   Kuttner, C.; Mayer, M.; Dulle, M.; Moscoso, A.; López-Romero, J.M.; Förster, S.; Fery, A.; Pérez-Juste, J.; Contreras-Cáceres, R., Seeded Growth Synthesis of Gold Nanotriangles: Size Control, Saxs Analysis, and Sers Performance; *ACS Applied Materials & Interfaces,* **2018**, 10, 11152-11163.

109.   Li, C.; Shuford, K.L.; Chen, M.; Lee, E.J.; Cho, S.O., A Facile Polyol Route to Uniform Gold Octahedra with Tailorable Size and Their Optical Properties; *ACS Nano,* **2008**, 2, 1760-1769.

110.   Khlebtsov, N.G.; Dykman, L.A., Optical Properties and Biomedical Applications of Plasmonic Nanoparticles; *Journal of Quantitative Spectroscopy and Radiative Transfer,* **2010**, 111, 1-35.

111.   Alvarez-Puebla, R.; Liz-Marzán, L.M.; García De Abajo, F.J., Light Concentration at the Nanometer Scale; *The Journal of Physical Chemistry Letters,* **2010**, 1, 2428-2434.

112.   Zhang, B.; Xu, P.; Xie, X.M.; Wei, H.; Li, Z.P.; Mack, N.H.; Han, X.J.; Xu, H.X.; Wang, H.L., Acid-Directed Synthesis of Sers-Active Hierarchical Assemblies of Silver Nanostructures; *Journal of Materials Chemistry,* **2011**, 21, 2495-2501.

113.   Aroca, R.; Alvarez-Puebla, R.; Pieczonka, N.; Sanchez-Cortez, S.; Garcia-Ramos, J., Surface-Enhanced Raman Scattering on Colloidal Nanostructures; *Advances in Colloid and Interface Science,* **2005**, 116, 45-61.

114.   Lee, P.C.; Meisel, D., Adsorption and Surface-Enhanced Raman of Dyes on Silver and Gold Sols; *The Journal of Physical Chemistry,* **1982**, 86, 3391-3395.

115.   Rivas, L.; Sanchez-Cortes, S.; García-Ramos, J.V.; Morcillo, G., Mixed Silver/Gold Colloids: A Study of Their Formation, Morphology, and Surface-Enhanced Raman Activity; *Langmuir,* **2000**, 16, 9722-9728.

116.   Habuchi, S.; Cotlet, M.; Gronheid, R.; Dirix, G.; Michiels, J.; Vanderleyden, J.; De Schryver, F.C.; Hofkens, J., Single-Molecule Surface Enhanced Resonance Raman Spectroscopy of the Enhanced Green Fluorescent Protein; *Journal of the American Chemical Society,* **2003**, 125, 8446-8447.

117.   Faulds, K.; Littleford, R.E.; Graham, D.; Dent, G.; Smith, W.E., Comparison of Surface-Enhanced Resonance Raman Scattering from Unaggregated and Aggregated Nanoparticles; *Analytical Chemistry,* **2004**, 76, 592-598.

118.   Yang, J.-K.; Kang, H.; Lee, H.; Jo, A.; Jeong, S.; Jeon, S.-J.; Kim, H.-I.; Lee, H.-Y.; Jeong, D.H.; Kim, J.-H., Single-Step and Rapid Growth of Silver Nanoshells as Sers-Active Nanostructures for Label-Free Detection of Pesticides; *ACS Applied Materials & Interfaces,* **2014**, 6, 12541-12549.

119.   Aroca, R.F.; Goulet, P.J.G.; Dos Santos, D.S.; Alvarez-Puebla, R.A.; Oliveira, O.N., Silver Nanowire Layer-by-Layer Films as Substrates for Surface-Enhanced Raman Scattering; *Analytical Chemistry,* **2005**, 77, 378-382.

120.   Freeman, R.G.; Grabar, K.C.; Allison, K.J.; Bright, R.M.; Davis, J.A.; Guthrie, A.P.; Hommer, M.B.; Jackson, M.A.; Smith, P.C.; Walter, D.G., Self-Assembled Metal Colloid Monolayers: An Approach to Sers Substrates; *Science,* **1995**, 267, 1629-1632.

121.   Wang, Z.; Pan, S.; Krauss, T.D.; Du, H.; Rothberg, L.J., The Structural Basis for Giant Enhancement Enabling Single-Molecule Raman Scattering; *Proceedings of the National Academy of Sciences,* **2003**, 100, 8638-8643.

122.   Fan, M.; Brolo, A.G., Silver Nanoparticles Self Assembly as Sers Substrates with near Single Molecule Detection Limit; *Physical Chemistry Chemical Physics,* **2009**, 11, 7381-7389.

123.   Yu, W.W.; White, I.M., A Simple Filter-Based Approach to Surface Enhanced Raman Spectroscopy for Trace Chemical Detection; *Analyst,* **2012**, 137, 1168-1173.

124.   Andrade, G.F.S.; Fan, M.; Brolo, A.G., Multilayer Silver Nanoparticles-Modified Optical Fiber Tip for High Performance Sers Remote Sensing; *Biosensors and Bioelectronics,* **2010**, 25, 2270-2275.

125.   Lucotti, A.; Zerbi, G., Fiber-Optic Sers Sensor with Optimized Geometry; *Sensors and Actuators B: Chemical,* **2007**, 121, 356-364.

126.   Xie, Z.G.; Tao, J.; Lu, Y.H.; Lin, K.Q.; Yan, J.; Wang, P.; Ming, H., Polymer Optical Fiber Sers Sensor with Gold Nanorods; *Optics Communications,* **2009**, 282, 439-442.

127.   Polavarapu, L.; La Porta, A.; Novikov, S.M.; Coronado-Puchau, M.; Liz-Marzan, L.M., Pen-on-Paper Approach toward the Design of Universal Surface Enhanced Raman Scattering Substrates; *Small,* **2014**, 10, 3065-3071.

128.   Lee, C.H.; Tian, L.; Singamaneni, S., Paper-Based Sers Swab for Rapid Trace Detection on Real-World Surfaces; *ACS Applied Materials & Interfaces,* **2010**, 2, 3429-3435.

129.   Chen, J.M.; Huang, Y.J.; Kannan, P.; Zhang, L.; Lin, Z.Y.; Zhang, J.W.; Chen, T.; Guo, L.H., Flexible and Adhesive Surface Enhance Raman Scattering Active Tape for Rapid Detection of Pesticide Residues in Fruits and Vegetables; *Analytical Chemistry,* **2016**, 88, 2149-2155.

130.   Kahl, M.; Voges, E.; Kostrewa, S.; Viets, C.; Hill, W., Periodically Structured Metallic Substrates for Sers; *Sensors and Actuators B: Chemical,* **1998**, 51, 285-291.

131.   Yu, Q.; Guan, P.; Qin, D.; Golden, G.; Wallace, P.M., Inverted Size-Dependence of Surface-Enhanced Raman Scattering on Gold Nanohole and Nanodisk Arrays; *Nano Letters,* **2008**, 8, 1923-1928.

132.   Krishnamoorthy, S.; Krishnan, S.; Thoniyot, P.; Low, H.Y., Inherently Reproducible Fabrication of Plasmonic Nanoparticle Arrays for Sers by Combining Nanoimprint and Copolymer Lithography; *ACS Applied Materials & Interfaces,* **2011**, 3, 1033-1040.

133.   Diebold, E.D.; Mack, N.H.; Doorn, S.K.; Mazur, E., Femtosecond Laser-Nanostructured Substrates for Surface-Enhanced Raman Scattering; *Langmuir,* **2009**, 25, 1790-1794.

134.   Hulteen, J.C.; Treichel, D.A.; Smith, M.T.; Duval, M.L.; Jensen, T.R.; Van Duyne, R.P., Nanosphere Lithography: Size-Tunable Silver Nanoparticle and Surface Cluster Arrays; *The Journal of Physical Chemistry B,* **1999**, 103, 3854-3863.

135.   Fan, M.; Andrade, G.F.S.; Brolo, A.G., A Review on the Fabrication of Substrates for Surface Enhanced Raman Spectroscopy and Their Applications in Analytical Chemistry; *Analytica Chimica Acta,* **2011**, 693, 7-25.

136.   Huebner, U.; Boucher, R.; Schneidewind, H.; Cialla, D.; Popp, J., Microfabricated Sers-Arrays with Sharp-Edged Metallic Nanostructures; *Microelectronic Engineering,* **2008**, 85, 1792-1794.

137.   Li, K.; Clime, L.; Cui, B.; Veres, T., Surface Enhanced Raman Scattering on Long-Range Ordered Noble-Metal Nanocrescent Arrays; *Nanotechnology,* **2008**, 19, 145305.

138.   Marquestaut, N.; Martin, A.; Talaga, D.; Servant, L.; Ravaine, S.; Reculusa, S.; Bassani, D.M.; Gillies, E.; Lagugné-Labarthet, F., Raman Enhancement of Azobenzene Monolayers on Substrates Prepared by Langmuir−Blodgett Deposition and Electron-Beam Lithography Techniques; *Langmuir,* **2008**, 24, 11313-11321.

139.   Huang, Z.; Meng, G.; Huang, Q.; Chen, B.; Zhu, C.; Zhang, Z., Large-Area Ag Nanorod Array Substrates for Sers: Aao Template-Assisted Fabrication, Functionalization, and Application in Detection Pcbs; *Journal of Raman Spectroscopy,* **2013**, 44, 240-246.

140.   Wang, Y.; Wang, Y.; Wang, H.; Cong, M.; Xu, W.; Xu, S., Surface-Enhanced Raman Scattering on a Hierarchical Structural Ag Nano-Crown Array in Different Detection Ways; *Physical Chemistry Chemical Physics,* **2015**, 17, 1173-1179.

141.   Hu, M.; Ou, F.S.; Wu, W.; Naumov, I.; Li, X.; Bratkovsky, A.M.; Williams, R.S.; Li, Z., Gold Nanofingers for Molecule Trapping and Detection; *Journal of the American Chemical Society,* **2010**, 132, 12820-12822.

142.   Gunnarsson, L.; Bjerneld, E.; Xu, H.; Petronis, S.; Kasemo, B.; Käll, M., Interparticle Coupling Effects in Nanofabricated Substrates for Surface-Enhanced Raman Scattering; *Applied Physics Letters,* **2001**, 78, 802-804.

143.   Kleinman, S.L.; Frontiera, R.R.; Henry, A.-I.; Dieringer, J.A.; Van Duyne, R.P., Creating, Characterizing, and Controlling Chemistry with Sers Hot Spots; *Physical Chemistry Chemical Physics,* **2013**, 15, 21-36.

144.   Martin, C.R., Nanomaterials: A Membrane-Based Synthetic Approach; *Science,* **1994**, 266, 1961-1966.

145.   Yao, J.L.; Pan, G.P.; Xue, K.H.; Wu, D.Y.; Ren, B.; Sun, D.M.; Tang, J.; Xu, X.; Tian, Z.Q., A Complementary Study of Surface-Enhanced Raman Scattering and Metal Nanorod Arrays; *Pure and Applied Chemistry,* **2000**, 72, 221.

146.   Du, Y.; Shi, L.; He, T.; Sun, X.; Mo, Y., Sers Enhancement Dependence on the Diameter and Aspect Ratio of Silver-Nanowire Array Fabricated by Anodic Aluminium Oxide Template; *Applied Surface Science,* **2008**, 255, 1901-1905.

147.   Ruan, C.; Eres, G.; Wang, W.; Zhang, Z.; Gu, B., Controlled Fabrication of Nanopillar Arrays as Active Substrates for Surface-Enhanced Raman Spectroscopy; *Langmuir,* **2007**, 23, 5757-5760.

148.   Dickey, M.D.; Weiss, E.A.; Smythe, E.J.; Chiechi, R.C.; Capasso, F.; Whitesides, G.M., Fabrication of Arrays of Metal and Metal Oxide Nanotubes by Shadow Evaporation; *ACS Nano,* **2008**, 2, 800-808.

149.   Batista, E.A.; Dos Santos, D.P.; Andrade, G.F.S.; Sant'ana, A.C.; Brolo, A.G.; Temperini, M.L.A., Using Polycarbonate Membranes as Templates for the Preparation of Au Nanostructures for Surface-Enhanced Raman Scattering; *Journal of Nanoscience and Nanotechnology,* **2009**, 9, 3233-3238.

150.   Penn, M.A.; Drake, D.M.; Driskell, J.D., Accelerated Surface-Enhanced Raman Spectroscopy (Sers)-Based Immunoassay on a Gold-Plated Membrane; *Analytical Chemistry,* **2013**, 85, 8609-8617.

151.   Wigginton, K.R.; Vikesland, P.J., Gold-Coated Polycarbonate Membrane Filter for Pathogen Concentration and Sers-Based Detection; *Analyst,* **2010**, 135, 1320-1326.

152.   Piao, L.; Park, S.; Lee, H.B.; Kim, K.; Kim, J.; Chung, T.D., Single Gold Microshell Tailored to Sensitive Surface Enhanced Raman Scattering Probe; *Analytical Chemistry,* **2010**, 82, 447-451.

153.   Wang, J.J.; Zhou, F.; Duan, G.T.; Li, Y.; Liu, G.Q.; Su, F.H.; Cai, W.P., A Controlled Ag-Au Bimetallic Nanoshelled Microsphere Array and Its Improved Surface-Enhanced Raman Scattering Effect; *RSC Advances,* **2014**, 4, 8758-8763.

154.   Zhao, Y.H.; Luo, W.Q.; Kanda, P.; Cheng, H.W.; Chen, Y.Y.; Wang, S.P.; Huan, S.Y., Silver Deposited Polystyrene (Ps) Microspheres for Surface-Enhanced Raman Spectroscopic-Encoding and Rapid Label-Free Detection of Melamine in Milk Powder; *Talanta,* **2013**, 113, 7-13.

155.   Yang, L.; Ma, L.; Chen, G.; Liu, J.; Tian, Z.-Q., Ultrasensitive Sers Detection of Tnt by Imprinting Molecular Recognition Using a New Type of Stable Substrate; *Chemistry – A European Journal,* **2010**, 16, 12683-12693.

156.   Xie, W.; Schlucker, S., Medical Applications of Surface-Enhanced Raman Scattering; *Physical Chemistry Chemical Physics,* **2013**, 15, 5329-5344.

157.   Grubisha, D.S.; Lipert, R.J.; Park, H.-Y.; Driskell, J.; Porter, M.D., Femtomolar Detection of Prostate-Specific Antigen: An Immunoassay Based on Surface-Enhanced Raman Scattering and Immunogold Labels; *Analytical Chemistry,* **2003**, 75, 5936-5943.

158.   Justin, L.A.; Jeremy, D.D.; Ralph, A.T.; Yiping, Z. Current Progress on Surface-Enhanced Raman Scattering Chemical/Biological Sensing. In Functional Nanoparticles for Bioanalysis, Nanomedicine, and Bioelectronic Devices Volume 2; *American Chemical Society:* 2012; Vol. 1113, Chapter 10, pp 235-272.

159.   Alak, A.M.; Vo-Dinh, T., Surface-Enhanced Raman Spectrometry of Organo Phosphorus Chemical Agents; *Analytical Chemistry,* **1987**, 59, 2149-2153.

160.   European Food Safety Authority, The 2010 European Union Report on Pesticide Residues in Food; *EFSA Journal,* **2013**, 11, 3130.

161.   Li, D.W.; Zhai, W.L.; Li, Y.T.; Long, Y.T., Recent Progress in Surface Enhanced Raman Spectroscopy for the Detection of Environmental Pollutants; *Microchimica Acta,* **2014**, 181, 23-43.

162.   Halvorson, R.A.; Vikesland, P.J., Surface-Enhanced Raman Spectroscopy (Sers) for Environmental Analyses; *Environmental Science & Technology,* **2010**, 44, 7749-7755.

163.   Pang, S.T.R.; Yang, T.X.; He, L.L., Review of Surface Enhanced Raman Spectroscopic (Sers) Detection of Synthetic Chemical Pesticides; *TrAC Trends in Analytical Chemistry,* **2016**, 85, 73-82.

164.   Hou, R.; Pang, S.; He, L., In Situ Sers Detection of Multi-Class Insecticides on Plant Surfaces; *Analytical Methods,* **2015**, 7, 6325-6330.

165.   Fan, Y.X.; Lai, K.Q.; Rasco, B.A.; Huang, Y.Q., Analyses of Phosmet Residues in Apples with Surface-Enhanced Raman Spectroscopy; *Food Control,* **2014**, 37, 153-157.

166.   Yang, J.K.; Kang, H.; Lee, H.; Jo, A.; Jeong, S.; Jeon, S.J.; Kim, H.I.; Lee, H.Y.; Jeong, D.H.; Kim, J.H.; Lee, Y.S., Single-Step and Rapid Growth of Silver Nanoshells as Sers-Active Nanostructures for Label-Free Detection of Pesticides; *ACS Applied Materials & Interfaces,* **2014**, 6, 12541-12549.

167.   Liu, B.; Zhou, P.; Liu, X.M.; Sun, X.; Li, H.; Lin, M.S., Detection of Pesticides in Fruits by Surface-Enhanced Raman Spectroscopy Coupled with Gold Nanostructures; *Food and Bioprocess Technology,* **2013**, 6, 710-718.

168.   Li, J.F.; Huang, Y.F.; Ding, Y.; Yang, Z.L.; Li, S.B.; Zhou, X.S.; Fan, F.R.; Zhang, W.; Zhou, Z.Y.; Wu, D.Y.; Ren, B.; Wang, Z.L.; Tian, Z.Q., Shell-Isolated Nanoparticle-Enhanced Raman Spectroscopy; *Nature,* **2010**, 464, 392-395.

169.   Lee, D.; Lee, S.; Seong, G.H.; Choo, J.; Lee, E.K.; Gweon, D.G.; Lee, S., Quantitative Analysis of Methyl Parathion Pesticides in a Polydimethylsiloxane Microfluidic Channel Using Confocal Surface-Enhanced Raman Spectroscopy; *Applied Spectroscopy,* **2006**, 60, 373-377.

170.   Wang, J.; Kong, L.T.; Guo, Z.; Xu, J.Y.; Liu, J.H., Synthesis of Novel Decorated One-Dimensional Gold Nanoparticle and Its Application in Ultrasensitive Detection of Insecticide; *Journal of Materials Chemistry,* **2010**, 20, 5271-5279.

171.   Yan, F.; Vo-Dinh, T., Surface-Enhanced Raman Scattering Detection of Chemical and Biological Agents Using a Portable Raman Integrated Tunable Sensor; *Sensors and Actuators B: Chemical,* **2007**, 121, 61-66.

172.   Fathi, F.; Lagugne-Labarthet, F.; Pedersen, D.B.; Kraatz, H.B., Studies of the Interaction of Two Organophosphonates with Nanostructured Silver Surfaces; *Analyst,* **2012**, 137, 4448-4453.

173.   Yazdi, S.H.; White, I.M., A Nanoporous Optofluidic Microsystem for Highly Sensitive and Repeatable Surface Enhanced Raman Spectroscopy Detection; *Biomicrofluidics,* **2012**, 6.

174.   Feng, S.L.; Hu, Y.X.; Ma, L.Y.; Lu, X.N., Development of Molecularly Imprinted Polymers-Surface-Enhanced Raman Spectroscopy/Colorimetric Dual Sensor for Determination of Chlorpyrifos in Apple Juice; *Sensors and Actuators B: Chemical,* **2017**, 241, 750-757.

175.   Kim, A.; Barcelo, S.J.; Li, Z.Y., Sers-Based Pesticide Detection by Using Nanofinger Sensors; *Nanotechnology,* **2015**, 26.

176.   Li, C.H.; Yang, C.; Xu, S.C.; Zhang, C.; Li, Z.; Liu, X.Y.; Jiang, S.Z.; Huo, Y.Y.; Liu, A.H.; Man, B.Y., Ag2o@Ag Core-Shell Structure on Pmma as Low-Cost and Ultra-Sensitive Flexible Surface-Enhanced Raman Scattering Substrate; *Journal of Alloys and Compounds,* **2017**, 695, 1677-1684.

177.   Costa, J.C.S.; Ando, R.A.; Sant'ana, A.C.; Rossi, L.M.; Santos, P.S.; Temperini, M.L.A.; Corio, P., High Performance Gold Nanorods and Silver Nanocubes in Surface-Enhanced Raman Spectroscopy of Pesticides; *Physical Chemistry Chemical Physics,* **2009**, 11, 7491-7498.

178.   Creedon, N.C.; Lovera, P.; Furey, A.; O'riordan, A., Transparent Polymer-Based Sers Substrates Templated by a Soda Can; *Sensors and Actuators B: Chemical,* **2018**, 259, 64-74.

179.   Canamares, M.V.; Feis, A., Surface-Enhanced Raman Spectra of the Neonicotinoid Pesticide Thiacloprid; *Journal of Raman Spectroscopy,* **2013**, 44, 1126-1135.

180.   Wijaya, W.; Pang, S.; Labuza, T.P.; He, L., Rapid Detection of Acetamiprid in Foods Using Surface-Enhanced Raman Spectroscopy (Sers); *Journal of Food Science,* **2014**, 79, T743-T747.

181.   Zaim, M.; Jambulingam, P., Global Insecticide Use for Vector-Borne Disease Control; World Health Organization: **2007**.

182.   Kozawa, K.; Aoyama, Y.; Mashimo, S.; Kimura, H., Toxicity and Actual Regulation of Organophosphate Pesticides; *Toxin Reviews,* **2009**, 28, 245-254.

183.   Rosenstock, L.; Keifer, M.; Daniell, W.E.; Mcconnell, R.; Claypoole, K.; Group, P.H.E.S., Chronic Central Nervous System Effects of Acute Organophosphate Pesticide Intoxication; *The Lancet,* **1991**, 338, 223-227.

184.   Eskenazi, B.; Bradman, A.; Castorina, R., Exposures of Children to Organophosphate Pesticides and Their Potential Adverse Health Effects; *Environmental Health Perspectives,* **1999**, 107, 409.

185.   Stephens, R.; Spurgeon, A.; Calvert, I.A.; Beach, J.; Levy, L.S.; Harrington, J.; Berry, H., Neuropsychological Effects of Long-Term Exposure to Organophosphates in Sheep Dip; *The Lancet,* **1995**, 345, 1135-1139.

186.   Fries, E.; Püttmann, W., Occurrence of Organophosphate Esters in Surface Water and Ground Water in Germany; *Journal of Environmental Monitoring,* **2001**, 3, 621-626.

187.   Karalliedde, L.; Eddleston, M.; Murray, V., The Global Picture of Organophosphate Insecticide Poisoning; *World Scientific,* **2001;** p 431-471.

188.   Banks, K.E.; Hunter, D.H.; Wachal, D.J., Chlorpyrifos in Surface Waters before and after a Federally Mandated Ban; *Environment International,* **2005**, 31, 351-356.

189.   Pogačnik, L.; Franko, M., Determination of Organophosphate and Carbamate Pesticides in Spiked Samples of Tap Water and Fruit Juices by a Biosensor with Photothermal Detection; *Biosensors and Bioelectronics,* **1999**, 14, 569-578.

190.   Liu, B.; Han, G.; Zhang, Z.; Liu, R.; Jiang, C.; Wang, S.; Han, M.-Y., Shell Thickness-Dependent Raman Enhancement for Rapid Identification and Detection of Pesticide Residues at Fruit Peels; *Analytical Chemistry,* **2012**, 84, 255-261.

191.   Elbert, A.; Haas, M.; Springer, B.; Thielert, W.; Nauen, R., Applied Aspects of Neonicotinoid Uses in Crop Protection; *Pest Management Science,* **2008**, 64, 1099-1105.

192.   Jeschke, P.; Nauen, R., Neonicotinoids—from Zero to Hero in Insecticide Chemistry; *Pest Management Science,* **2008**, 64, 1084-1098.

193.   Lee, J.K.; Ahn, K.C.; Park, O.S.; Kang, S.Y.; Hammock, B.D., Development of an Elisa for the Detection of the Residues of the Insecticide Imidacloprid in Agricultural and Environmental Samples; *Journal of Agricultural and Food Chemistry,* **2001**, 49, 2159-2167.

194.   Watanabe, E.; Baba, K.; Eun, H.; Miyake, S., Application of a Commercial Immunoassay to the Direct Determination of Insecticide Imidacloprid in Fruit Juices; *Food Chemistry,* **2007**, 102, 745-750.

195.   Ferrer, I.; Thurman, E.M.; Fernández-Alba, A.R., Quantitation and Accurate Mass Analysis of Pesticides in Vegetables by Lc/Tof-Ms; *Analytical Chemistry,* **2005**, 77, 2818-2825.

196.   Obana, H.; Okihashi, M.; Akutsu, K.; Kitagawa, Y.; Hori, S., Determination of Acetamiprid, Imidacloprid, and Nitenpyram Residues in Vegetables and Fruits by High-Performance Liquid Chromatography with Diode-Array Detection; *Journal of Agricultural and Food Chemistry,* **2002**, 50, 4464-4467.

197.   Liu, S.; Zheng, Z.; Wei, F.; Ren, Y.; Gui, W.; Wu, H.; Zhu, G., Simultaneous Determination of Seven Neonicotinoid Pesticide Residues in Food by Ultraperformance Liquid Chromatography Tandem Mass Spectrometry; *Journal of Agricultural and Food Chemistry,* **2010**, 58, 3271-3278.

198.   Aguera, A.; Almansa, E.; Malato, S.; Maldonado, M.; Fernandez-Alba, A., Evaluation of Photocatalytic Degradation of Imidacloprid in Industrial Water by Gc-Ms and Lc-Ms; *Analysis,* **1998**, 26, 245-251.

199.   Navalón, A.; González-Casado, A.; El-Khattabi, R.; Vilchez, J.L.; Fernández-Alba, A.R., Determination of Imidacloprid in Vegetable Samples by Gas Chromatography–Mass Spectrometry; *Analyst,* **1997**, 122, 579-581.

200.   Ding, X.; Zhang, W.; Cheng, D.; He, J.; Yang, K.-L., Oligopeptides Functionalized Surface Plasmon Resonance Biosensors for Detecting Thiacloprid and Imidacloprid; *Biosensors and Bioelectronics,* **2012**, 35, 271-276.

201.   VíLchez, J.L.; Valencia, M.C.; Navalón, A.; Molinero-Morales, B.; Capitán-Vallvey, L.F., Flow Injection Analysis of the Insecticide Imidacloprid in Water Samples with Photochemically Induced Fluorescence Detection; *Analytica Chimica Acta,* **2001**, 439, 299-305.

202.   Nauen, R.; Bretschneider, T., New Modes of Action of Insecticides; *Pesticide Outlook,* **2002**, 13, 241-245.

203.   Tomizawa, M.; Casida, J.E., Neonicotinoid Insecticide Toxicology: Mechanisms of Selective Action; *Annual Review of Pharmacology and Toxicology,* **2005**, 45, 247-268.

204.   Henry, M.; Beguin, M.; Requier, F.; Rollin, O.; Odoux, J.-F.; Aupinel, P.; Aptel, J.; Tchamitchian, S.; Decourtye, A., A Common Pesticide Decreases Foraging Success and Survival in Honey Bees; *Science,* **2012**, 336, 348-350.

205.   Whitehorn, P.R.; O'connor, S.; Wackers, F.L.; Goulson, D., Neonicotinoid Pesticide Reduces Bumble Bee Colony Growth and Queen Production; *Science,* **2012**, 336, 351-352.

206.   European Commission, Commission Implementing Regulation (Eu) No 485/2013 of 24 May 2013 Amending Implementing Regulation (Eu) No 540/2011, as Regards the Conditions of Approval of the Active Substances Clothianidin, Thiamethoxam and Imidacloprid, and Prohibiting the Use and Sale of Seeds Treated with Plant Protection Products Containing Those Active Substances; *Official Journal of the European Union,* **2013**, 139, 12-14.

207.   European Food Safety Authority, The 2014 European Union Report on Pesticide Residues in Food; *EFSA Journal,* **2016**, 14, e04611-n/a.

208.   Cao, X.L.; Hong, S.H.; Jiang, Z.J.; She, Y.X.; Wang, S.S.; Zhang, C.; Li, H.; Jin, F.; Jin, M.J.; Wang, J., Sers-Active Metal-Organic Frameworks with Embedded Gold Nanoparticles; *Analyst,* **2017**, 142, 2640-2647.

209.   Wijaya, W.; Pang, S.; Labuza, T.P.; He, L.L., Rapid Detection of Acetamiprid in Foods Using Surface-Enhanced Raman Spectroscopy (Sers); *Journal of Food Science,* **2014**, 79, T743-T747.

210.   Yang, T.X.; Zhao, B.; Hou, R.Y.; Zhang, Z.Y.; Kinchla, A.J.; Clark, J.M.; He, L.L., Evaluation of the Penetration of Multiple Classes of Pesticides in Fresh Produce Using Surface-Enhanced Raman Scattering Mapping; *Journal of Food Science,* **2016**, 81, T2891-T2901.

211.   Zhai, C.; Li, Y.Y.; Peng, Y.K.; Xu, T.F.; Dhakal, S.; Chao, K.L.; Qin, J.W. Research on Identification and Determination of Mixed Pesticides in Apples Using Surface Enhanced Raman Spectroscopy. In Sensing for Agriculture and Food Quality and Safety Vii; *Proc. SPIE* 2015; Vol. 9488.

212.   Zhai, C.; Peng, Y.K.; Li, Y.Y.; Chao, K.L., Extraction and Identification of Mixed Pesticides' Raman Signal and Establishment of Their Prediction Models; *Journal of Raman Spectroscopy,* **2017**, 48, 494-500.

213.   Zhang, H.; Kang, Y.; Liu, P.; Tao, X.; Pei, J.W.; Li, H.; Du, Y.P., Determination of Pesticides by Surface-Enhanced Raman Spectroscopy on Gold-Nanoparticle-Modified Polymethacrylate; *Analytical Letters,* **2016**, 49, 2268-2278.

214.   Moreira, A.a.G.; De Lima-Neto, P.; Caetano, E.W.S.; Barroso-Neto, I.L.; Freire, V.N., The Vibrational Properties of the Bee-Killer Imidacloprid Insecticide: A Molecular Description; *Spectrochimica Acta Part A: Molecular and Biomolecular Spectroscopy,* **2017**, 185, 245-255.

215.   Atanasov, P.A.; Nedyalkov, N.N.; Nikov, R.G.; Fukata, N.; Jevasuwan, W.; Subramani, T.; Hirsch, D.; Rauschenbach, B., Sers Analyses of Thiamethoxam Assisted by Ag Films and Nanostructures Produced by Laser Techniques; *Journal of Raman Spectroscopy,* **2018**, 49, 397-403.

216.   Zhang, F.; Zhang, Y.; Ni, H.; Ma, K.; Li, R., Experimental and Dft Studies on the Vibrational, Electronic Spectra and Nbo Analysis of Thiamethoxam; *Spectrochimica Acta Part A: Molecular and Biomolecular Spectroscopy,* **2014**, 118, 162-171.

217.   Breidbach, A.; Bouten, K.; Kröger, K.; Ulberth, F., Capabilities of Laboratories to Determine Melamine in Food—Results of an International Proficiency Test; *Analytical and Bioanalytical Chemistry,* **2010**, 396, 503-510.

218.   Craig, A.P.; Franca, A.S.; Irudayaraj, J. Surface-Enhanced Raman Spectroscopy Applied to Food Safety. In Annual Review of Food Science and Technology, Vol 4; *Doyle, M. P.; Klaenhammer, T. R.*, Eds.; 2013; Vol. 4, pp 369-380.

219.   Fan, C.; Hu, Z.Q.; Mustapha, A.; Lin, M.S., Rapid Detection of Food- and Waterborne Bacteria Using Surface-Enhanced Raman Spectroscopy Coupled with Silver Nanosubstrates; *Applied Microbiology and Biotechnology,* **2011**, 92, 1053-1061.

220.   Zhang, Y.; Huang, Y.; Zhai, F.; Du, R.; Liu, Y.; Lai, K., Analyses of Enrofloxacin, Furazolidone and Malachite Green in Fish Products with Surface-Enhanced Raman Spectroscopy; *Food Chemistry,* **2012**, 135, 845-850.

221.   Cialla, D.; Marz, A.; Bohme, R.; Theil, F.; Weber, K.; Schmitt, M.; Popp, J., Surface-Enhanced Raman Spectroscopy (Sers): Progress and Trends; *Analytical and Bioanalytical Chemistry,* **2012**, 403, 27-54.

222.   Granger, J.H.; Schlotter, N.E.; Crawford, A.C.; Porter, M.D., Prospects for Point-of-Care Pathogen Diagnostics Using Surface-Enhanced Raman Scattering (Sers); *Chemical Society Reviews,* **2016**, 45, 3865-3882.

223.   Jarvis, R.M.; Goodacre, R., Characterisation and Identification of Bacteria Using Sers; *Chemical Society Reviews,* **2008**, 37, 931-936.

224.   Srivastava, S.; Sinha, R.; Roy, D., Toxicological Effects of Malachite Green; *Aquatic Toxicology,* **2004**, 66, 319-329.

225.   Littlefield, N.A.; Blackwell, B.-N.; Hewitt, C.C.; Gaylor, D.W., Chronic Toxicity and Carcinogenicity Studies of Gentian Violet in Mice; *Toxicological Sciences,* **1985**, 5, 902-912.

226.   Wang, X.T.; Shi, W.S.; She, G.W.; Mu, L.X.; Lee, S.T., High-Performance Surface-Enhanced Raman Scattering Sensors Based on Ag Nanoparticles-Coated Si Nanowire Arrays for Quantitative Detection of Pesticides; *Applied Physics Letters,* **2010**, 96.

227.   Nie, S.; Emory, S.R., Probing Single Molecules and Single Nanoparticles by Surface-Enhanced Raman Scattering; *Science,* **1997**, 275, 1102-1106.

228.   He, L.L.; Kim, N.J.; Li, H.; Hu, Z.Q.; Lin, M.S., Use of a Fractal-Like Gold Nanostructure in Surface-Enhanced Raman Spectroscopy for Detection of Selected Food Contaminants; *Journal of Agricultural and Food Chemistry,* **2008**, 56, 9843-9847.

229.   Kneipp, K.; Wang, Y.; Kneipp, H.; Perelman, L.T.; Itzkan, I.; Dasari, R.R.; Feld, M.S., Single Molecule Detection Using Surface-Enhanced Raman Scattering (Sers); *Physical Review Letters,* **1997**, 78, 1667-1670.

230.   Kneipp, K.; Kneipp, H.; Itzkan, I.; Dasari, R.R.; Feld, M.S., Surface-Enhanced Non-Linear Raman Scattering at the Single-Molecule Level; *Chemical Physics,* **1999**, 247, 155-162.

231.   Michaels, A.M.; Nirmal, M.; Brus, L., Surface Enhanced Raman Spectroscopy of Individual Rhodamine 6g Molecules on Large Ag Nanocrystals; *Journal of the American Chemical Society,* **1999**, 121, 9932-9939.

232.   Chen, L.M.; Luo, L.B.; Chen, Z.H.; Zhang, M.L.; Zapien, J.A.; Lee, C.S.; Lee, S.T., Zno/Au Composite Nanoarrays as Substrates for Surface-Enhanced Raman Scattering Detection; *Journal of Physical Chemistry C,* **2010**, 114, 93-100.

233.   Zhang, X.F.; Zou, M.Q.; Qi, X.H.; Liu, F.; Zhu, X.H.; Zhao, B.H., Detection of Melamine in Liquid Milk Using Surface-Enhanced Raman Scattering Spectroscopy; *Journal of Raman Spectroscopy,* **2010**, 41, 1655-1660.

234.   Liu, Y.Y.; Zhang, Y.X.; Ding, H.L.; Xu, S.C.; Li, M.; Kong, F.Y.; Luo, Y.Y.; Li, G.H., Self-Assembly of Noble Metallic Spherical Aggregates from Monodisperse Nanoparticles: Their Synthesis and Pronounced Sers and Catalytic Properties; *Journal of Materials Chemistry A,* **2013**, 1, 3362-3371.

235.   Wen, Z.Q.; Li, G.Y.; Ren, D., Detection of Trace Melamine in Raw Materials Used for Protein Pharmaceutical Manufacturing Using Surface-Enhanced Raman Spectroscopy (Sers) with Gold Nanoparticles; *Applied Spectroscopy,* **2011**, 65, 514-521.

236.   Lee, S.Y.; Ganbold, E.-O.; Choo, J.; Joo, S.-W., Detection of Melamine in Powdered Milk Using Surface-Enhanced Raman Scattering with No Pretreatment; *Analytical Letters,* **2010**, 43, 2135-2141.

237.   Mecker, L.C.; Tyner, K.M.; Kauffman, J.F.; Arzhantsev, S.; Mans, D.J.; Gryniewicz-Ruzicka, C.M., Selective Melamine Detection in Multiple Sample Matrices with a Portable Raman Instrument Using Surface Enhanced Raman Spectroscopy-Active Gold Nanoparticles; *Analytica Chimica Acta,* **2012**, 733, 48-55.

238.   Giovannozzi, A.M.; Rolle, F.; Sega, M.; Abete, M.C.; Marchis, D.; Rossi, A.M., Rapid and Sensitive Detection of Melamine in Milk with Gold Nanoparticles by Surface Enhanced Raman Scattering; *Food Chemistry,* **2014**, 159, 250-256.

239.   Lou, T.T.; Wang, Y.Q.; Li, J.H.; Peng, H.L.; Xiong, H.; Chen, L.X., Rapid Detection of Melamine with 4-Mercaptopyridine-Modified Gold Nanoparticles by Surface-Enhanced Raman Scattering; *Analytical and Bioanalytical Chemistry,* **2011**, 401, 333-338.

240.   Yazgan, N.N.; Boyaci, I.H.; Topcu, A.; Tamer, U., Detection of Melamine in Milk by Surface-Enhanced Raman Spectroscopy Coupled with Magnetic and Raman-Labeled Nanoparticles; *Analytical and Bioanalytical Chemistry,* **2012**, 403, 2009-2017.

241.   Tang, J.Q.; Tian, C.; Zeng, C.Y.; Man, S.Q., Alkaline Silver Colloid for Surface Enhanced Raman Scattering and Application to Detection of Melamine Doped Milk; *Spectroscopy and Spectral Analysis,* **2013**, 33, 709-713.

242.   Betz, J.F.; Cheng, Y.; Rubloff, G.W., Direct Sers Detection of Contaminants in a Complex Mixture: Rapid, Single Step Screening for Melamine in Liquid Infant Formula; *Analyst,* **2012**, 137, 826-8.

243.   Chen, L.M.; Liu, Y.N., Surface-Enhanced Raman Detection of Melamine on Silver-Nanoparticle-Decorated Silver/Carbon Nanospheres: Effect of Metal Ions; *ACS Applied Materials & Interfaces,* **2011**, 3, 3091-3096.

244.   Li, J.M.; Ma, W.F.; Wei, C.; You, L.J.; Guo, J.; Hu, J.; Wang, C.C., Detecting Trace Melamine in Solution by Sers Using Ag Nanoparticle Coated Poly(Styrene-Co-Acrylic Acid) Nanospheres as Novel Active Substrates; *Langmuir,* **2011**, 27, 14539-14544.

245.   Ma, P.Y.; Liang, F.H.; Sun, Y.; Jin, Y.; Chen, Y.; Wang, X.H.; Zhang, H.Q.; Gao, D.J.; Song, D.Q., Rapid Determination of Melamine in Milk and Milk Powder by Surface-Enhanced Raman Spectroscopy and Using Cyclodextrin-Decorated Silver Nanoparticles; *Microchimica Acta,* **2013**, 180, 1173-1180.

246.   Peng, B.; Li, G.Y.; Li, D.H.; Dodson, S.; Zhang, Q.; Zhang, J.; Lee, Y.H.; Demir, H.V.; Ling, X.Y.; Xiong, Q.H., Vertically Aligned Gold Nanorod Monolayer on Arbitrary Substrates: Self-Assembly and Femtomolar Detection of Food Contaminants; *ACS Nano,* **2013**, 7, 5993-6000.

247.   Li, Y.L.; Zhao, X.J.; Zhang, P.P.; Ning, J.; Li, J.F.; Su, Z.Q.; Wei, G., A Facile Fabrication of Large-Scale Reduced Graphene Oxide-Silver Nanoparticle Hybrid Film as a Highly Active Surface-Enhanced Raman Scattering Substrate; *Journal of Materials Chemistry C,* **2015**, 3, 4126-4133.

248.   Kumar, S.V.; Huang, N.M.; Lim, H.N.; Zainy, M.; Harrison, I.; Chia, C.H., Preparation of Highly Water Dispersible Functional Graphene/Silver Nanocomposite for the Detection of Melamine; *Sensors and Actuators B: Chemical,* **2013**, 181, 885-893.

249.   Cheng, Y.; Dong, Y.Y., Screening Melamine Contaminant in Eggs with Portable Surface-Enhanced Raman Spectroscopy Based on Gold Nanosubstrate; *Food Control,* **2011**, 22, 685-689.

250.   Lin, M.; He, L.; Awika, J.; Yang, L.; Ledoux, D.R.; Li, H.; Mustapha, A., Detection of Melamine in Gluten, Chicken Feed, and Processed Foods Using Surface Enhanced Raman Spectroscopy and Hplc; *Journal of Food Science,* **2008**, 73, T129-T134.

251.   Kim, A.; Barcelo, S.J.; Williams, R.S.; Li, Z.Y., Melamine Sensing in Milk Products by Using Surface Enhanced Raman Scattering; *Analytical Chemistry,* **2012**, 84, 9303-9309.

252.   Alvarez-Puebla, R.; Liz-Marzan, L., Environmental Applications of Plasmon Assisted Raman Scattering; *Energy & Environmental Science,* **2010**, 3, 1011-1017.

253.   Wood, B.R.; Heraud, P.; Stojkovic, S.; Morrison, D.; Beardall, J.; Mcnaughton, D., A Portable Raman Acoustic Levitation Spectroscopic System for the Identification and Environmental Monitoring of Algal Cells; *Analytical Chemistry,* **2005**, 4955-4961.

254.   Zhou, H.; Yang, D.; Ivleva, N.P.; Mircescu, N.E.; Niessner, R.; Haisch, C., Sers Detection of Bacteria in Water by in Situ Coating with Ag Nanoparticles; *Analytical Chemistry,* **2014**, 86, 1525-1533.

255.   Zhang, X.; Young, M.A.; Lyandres, O.; Van Duyne, R.P., Rapid Detection of an Anthrax Biomarker by Surface-Enhanced Raman Spectroscopy; *Journal of the American Chemical Society,* **2005**, 127, 4484-4489.

256.   Zhang, X.; Zhao, J.; Whitney, A.V.; Elam, J.W.; Van Duyne, R.P., Ultrastable Substrates for Surface-Enhanced Raman Spectroscopy: Al2o3 Overlayers Fabricated by Atomic Layer Deposition Yield Improved Anthrax Biomarker Detection; *Journal of the American Chemical Society,* **2006**, 128, 10304-10309.

257.   Stiles, P.L.; Dieringer, J.A.; Shah, N.C.; Van Duyne, R.P., Surface-Enhanced Raman Spectroscopy; *Annual Review Analytical Chemistry,* **2008**, 1, 601-626.

258.   Porter, M.D.; Lipert, R.J.; Siperko, L.M.; Wang, G.; Narayanan, R., Sers as a Bioassay Platform: Fundamentals, Design, and Applications; *Chemical Society Reviews,* **2008**, 37, 1001-1011.

259.   U. S, D.; Fu, C.Y.; Soh, K.S.; Ramaswamy, B.; Kumar, A.; Olivo, M., Highly Sensitive Sers Detection of Cancer Proteins in Low Sample Volume Using Hollow Core Photonic Crystal Fiber; *Biosensors and Bioelectronics,* **2012**, 33, 293-298.

260.   Cao, Y.C.; Jin, R.; Mirkin, C.A., Nanoparticles with Raman Spectroscopic Fingerprints for DNA and Rna Detection; *Science,* **2002**, 297, 1536-1540.

261.   Lyandres, O.; Shah, N.C.; Yonzon, C.R.; Walsh, J.T.; Glucksberg, M.R.; Van Duyne, R.P., Real-Time Glucose Sensing by Surface-Enhanced Raman Spectroscopy in Bovine Plasma Facilitated by a Mixed Decanethiol/Mercaptohexanol Partition Layer; *Analytical Chemistry,* **2005**, 77, 6134-6139.

262.   Bard, A.J.; Faulkner, L.R.; Leddy, J.; Zoski, C.G., Electrochemical Methods: Fundamentals and Applications; *Wiley* New York, **1980;** Vol. 2.

263.   Marcus, R.A., Electron Transfer Reactions in Chemistry. Theory and Experiment; *Reviews of Modern Physics,* **1993**, 65, 599-610.

264.   Wang, X.; Tabakman, S.M.; Dai, H., Atomic Layer Deposition of Metal Oxides on Pristine and Functionalized Graphene; *Journal of the American chemical Society,* **2008**, 130, 8152-8153.

265.   Barker, A.L.; Gonsalves, M.; Macpherson, J.V.; Slevin, C.J.; Unwin, P.R., Scanning Electrochemical Microscopy: Beyond the Solid/Liquid Interface; *Analytica chimica acta,* **1999**, 385, 223-240.

266.   Franaszczuk, K.; Herrero, E.; Zelenay, P.; Wieckowski, A.; Wang, J.; Masel, R., A Comparison of Electrochemical and Gas-Phase Decomposition of Methanol on Platinum Surfaces; *The Journal of Physical Chemistry,* **1992**, 96, 8509-8516.

267.   Understanding the Specifications of Your Potentiostat; https://www.gamry.com/application-notes/instrumentation/understanding-specs-of-potentiostat/ (Accessed on: 12/03/2013),

268.   Polk, B.J.; Stelzenmuller, A.; Mijares, G.; Maccrehan, W.; Gaitan, M., Ag/Agcl Microelectrodes with Improved Stability for Microfluidics; *Sensors and Actuators B: Chemical,* **2006**, 114, 239-247.

269.   Zhou, J.; Ren, K.; Zheng, Y.; Su, J.; Zhao, Y.; Ryan, D.; Wu, H., Fabrication of a Microfluidic Ag/Agcl Reference Electrode and Its Application for Portable and Disposable Electrochemical Microchips; *Electrophoresis,* **2010**, 31, 3083-3089.

270.   Bond, A.M.; Lay, P.A., Cyclic Voltammetry at Microelectrodes in the Absence of Added Electrolyte Using a Platinum Quasi-Reference Electrode; *Journal of Electroanalytical Chemistry and Interfacial Electrochemistry,* **1986**, 199, 285-295.

271.   Ghilane, J.; Hapiot, P.; Bard, A.J., Metal/Polypyrrole Quasi-Reference Electrode for Voltammetry in Nonaqueous and Aqueous Solutions; *Analytical chemistry,* **2006**, 78, 6868-6872.

272.   Pletcher, D.; Greff, R.; Peat, R.; Peter, L.; Robinson, J., Instrumental Methods in Electrochemistry; *Elsevier,* **2001**.

273.   Harvey, D. Voltammetric Methods; https://chem.libretexts.org/Textbook_Maps/Analytical_Chemistry/Book%3A_Analytical_Chem

istry_2.0_(Harvey)/11_Electrochemical_Methods/11.4%3A_Voltammetric_Methods (Accessed on: 03/08/2018),

274.   Wahl, A.; Barry, S.; Dawson, K.; Machale, J.; Quinn, A.J.; O'riordan, A., Electroanalysis at Ultramicro and Nanoscale Electrodes: A Comparative Study; *Journal of The Electrochemical Society,* **2014**, 161, B3055-B3060.

275.   Arrigan, D.W.M., Nanoelectrodes, Nanoelectrode Arrays and Their Applications; *Analyst,* **2004**, 129, 1157-1165.

276.   Conyers, J.L.; White, H.S., Electrochemical Characterization of Electrodes with Submicrometer Dimensions; *Analytical Chemistry,* **2000**, 72, 4441-4446.

277.   Compton, R.G.; Wildgoose, G.G.; Rees, N.V.; Streeter, I.; Baron, R., Design, Fabrication, Characterisation and Application of Nanoelectrode Arrays; *Chemical Physics Letters,* **2008**, 459, 1-17.

278.   Kounaves, S.P., Handbook of Instrumental Techniques for Analytical Chemistry; *Prentice Hall PTR,* **1997;** p 709-726.

279.   Lee, C.S.; Kim, S.K.; Kim, M., Ion-Sensitive Field-Effect Transistor for Biological Sensing; *Sensors,* **2009**, 9, 7111-7131.

280.   Tsai, M.-Y.; Creedon, N.; Brightbill, E.; Pavlidis, S.; Brown, B.; Gray, D.W.; Shields, N.; Sayers, R.; Mooney, M.H.; O'riordan, A., Direct Correlation between Potentiometric and Impedance Biosensing of Antibody-Antigen Interactions Using an Integrated System; *Applied Physics Letters,* **2017**, 111, 073701.

281.   Madou, M.J.; Cubicciotti, R., Scaling Issues in Chemical and Biological Sensors; *Proceedings of the IEEE,* **2003**, 91, 830-838.

282.   Jorcin, J.-B.; Orazem, M.E.; Pébère, N.; Tribollet, B., Cpe Analysis by Local Electrochemical Impedance Spectroscopy; *Electrochimica Acta,* **2006**, 51, 1473-1479.

283.   Wang, Y.; Ye, Z.; Ying, Y., New Trends in Impedimetric Biosensors for the Detection of Foodborne Pathogenic Bacteria; *Sensors,* **2012**, 12, 3449-3471.

284.   Grieshaber, D.; Mackenzie, R.; Voeroes, J.; Reimhult, E., Electrochemical Biosensors-Sensor Principles and Architectures; *Sensors,* **2008**, 8, 1400-1458.

285.   Gautier, C.; Esnault, C.; Cougnon, C.; Pilard, J.-F.; Casse, N.; Chénais, B., Hybridization-Induced Interfacial Changes Detected by Non-Faradaic Impedimetric Measurements Compared to Faradaic Approach; *Journal of Electroanalytical Chemistry,* **2007**, 610, 227-233.

286.   Daniels, J.S.; Pourmand, N., Label-Free Impedance Biosensors: Opportunities and Challenges; *Electroanalysis,* **2007**, 19, 1239-1257.

287.   Berggren, C.; Bjarnason, B.; Johansson, G., Capacitive Biosensors; *Electroanalysis,* **2001**, 13, 173-180.

288.   Sargent, A.; Sadik, O.A., Monitoring Antibody–Antigen Reactions at Conducting Polymer-Based Immunosensors Using Impedance Spectroscopy; *Electrochimica acta,* **1999**, 44, 4667-4675.

289.	Ouerghi, O.; Touhami, A.; Jaffrezic-Renault, N.; Martelet, C.; Ouada, H.B.; Cosnier, S., Impedimetric Immunosensor Using Avidin–Biotin for Antibody Immobilization; *Bioelectrochemistry,* **2002**, 56, 131-133.

290.	Teles, F.R.R.; Fonseca, L.P., Applications of Polymers for Biomolecule Immobilization in Electrochemical Biosensors; *Materials Science and Engineering: C,* **2008**, 28, 1530-1543.

291.	Jie, M.; Ming, C.Y.; Jing, D.; Cheng, L.S.; Jun, F.; Xiang, C.Y., An Electrochemical Impedance Immunoanalytical Method for Detecting Immunological Interaction of Human Mammary Tumor Associated Glycoprotein and Its Monoclonal Antibody; *Electrochemistry communications,* **1999**, 1, 425-428.

292.	Danilowicz, C.; Manrique, J., A New Self-Assembled Modified Electrode for Competitive Immunoassay; *Electrochemistry Communications,* **1999**, 1, 22-25.

293.	Blanco-López, M.C.; Lobo-Castañón, M.J.; Miranda-Ordieres, A.J.; Tuñón-Blanco, P., Electrochemical Sensors Based on Molecularly Imprinted Polymers; *TrAC Trends in Analytical Chemistry,* **2004**, 23, 36-48.

294.	Kong, L.; Jiang, X.; Zeng, Y.; Zhou, T.; Shi, G., Molecularly Imprinted Sensor Based on Electropolmerized Poly(O-Phenylenediamine) Membranes at Reduced Graphene Oxide Modified Electrode for Imidacloprid Determination; *Sensors and Actuators B: Chemical,* **2013**, 185, 424-431.

295.	Turner, A.P.F., Molecularly Imprinted Sensors: Overview and Applications Foreword; **2012;** p XI-XII.

296.	Rodríguez, Á.; Valera, E.; Ramón-Azcón, J.; Sanchez, F.J.; Marco, M.P.; Castañer, L.M., Single Frequency Impedimetric Immunosensor for Atrazine Detection; *Sensors and Actuators B: Chemical,* **2008**, 129, 921-928.

297.	Katz, E.; Willner, I., Probing Biomolecular Interactions at Conductive and Semiconductive Surfaces by Impedance Spectroscopy: Routes to Impedimetric Immunosensors, DNA-Sensors, and Enzyme Biosensors; *Electroanalysis,* **2003**, 15, 913-947.

298.	Zane, D.; Appetecchi, G.B.; Bianchini, C.; Passerini, S.; Curulli, A., An Impedimetric Glucose Biosensor Based on Overoxidized Polypyrrole Thin Film; *Electroanalysis,* **2011**, 23, 1134-1141.

299.	Shervedani, R.K.; Mehrjardi, A.H.; Zamiri, N., A Novel Method for Glucose Determination Based on Electrochemical Impedance Spectroscopy Using Glucose Oxidase Self-Assembled Biosensor; *Bioelectrochemistry,* **2006**, 69, 201-208.

300.	Periasamy, A.P.; Ting, S.W.; Chen, S.M., Amperometric and Impedimetric H2o2 Biosensor Based on Horseradish Peroxidase Covalently Immobilized at Ruthenium Oxide Nanoparticles Modified Electrode; *International Journal of Electrochemical Science,* **2011**, 6, 2688-2709.

301.	Shamsipur, M.; Asgari, M.; Maragheh, M.G.; Moosavi-Movahedi, A.A., A Novel Impedimetric Nanobiosensor for Low Level Determination of Hydrogen Peroxide Based on Biocatalysis of Catalase; *Bioelectrochemistry,* **2012**, 83, 31-37.

302.	Mozaffari, S.A.; Rahmanian, R.; Abedi, M.; Amoli, H.S., Urea Impedimetric Biosensor Based on Reactive Rf Magnetron Sputtered Zinc Oxide Nanoporous Transducer; *Electrochimica Acta,* **2014**, 146, 538-547.

303.   Slaugther, G., A Gold Interdigitated Microelectrodes Fabricated on Polyhydroxybutyrate Substrate for the Determination of Urea Using Impedimetric Measurements; *Ieee Sensors Journal,* **2012**, 12, 821-826.

304.   Banerjee, P.; Bhunia, A.K., Mammalian Cell-Based Biosensors for Pathogens and Toxins; *Trends in Biotechnology,* **2009**, 27, 179-188.

305.   Pancrazio, J.; Whelan, J.; Borkholder, D.; Ma, W.; Stenger, D., Development and Application of Cell-Based Biosensors; *Annual Review of Biomedical Engineering,* **1999**, 27, 697-711.

306.   Raut, N.; O'connor, G.; Pasini, P.; Daunert, S., Engineered Cells as Biosensing Systems in Biomedical Analysis; *Analytical and Bioanalytical Chemistry,* **2012**, 402, 3147-3159.

307.   Hondroulis, E.; Liu, C.; Li, C.Z., Whole Cell Based Electrical Impedance Sensing Approach for a Rapid Nanotoxicity Assay; *Nanotechnology,* **2010**, 21.

308.   Bousse, L., Whole Cell Biosensors; *Sensors and Actuators B: Chemical,* **1996**, 34, 270-275.

309.   Liu, Q.; Wu, C.; Cai, H.; Hu, N.; Zhou, J.; Wang, P., Cell-Based Biosensors and Their Application in Biomedicine; *Chemical Reviews,* **2014**, 114, 6423-6461.

310.   Kim, Y.-H.; Park, J.-S.; Jung, H.-I., An Impedimetric Biosensor for Real-Time Monitoring of Bacterial Growth in a Microbial Fermentor; *Sensors and Actuators B: Chemical,* **2009**, 138, 270-277.

311.   Muñoz-Berbel, X.; Vigués, N.; Jenkins, A.T.A.; Mas, J.; Muñoz, F.J., Impedimetric Approach for Quantifying Low Bacteria Concentrations Based on the Changes Produced in the Electrode–Solution Interface During the Pre-Attachment Stage; *Biosensors and Bioelectronics,* **2008**, 23, 1540-1546.

312.   Qi, P.; Wan, Y.; Zhang, D., Impedimetric Biosensor Based on Cell-Mediated Bioimprinted Films for Bacterial Detection; *Biosensors and Bioelectronics,* **2013**, 39, 282-288.

313.   Yang, L.; Bashir, R., Electrical/Electrochemical Impedance for Rapid Detection of Foodborne Pathogenic Bacteria; *Biotechnology Advances,* **2008**, 26, 135-150.

314.   Hofmann, U.; Michaelis, S.; Winckler, T.; Wegener, J.; Feller, K.H., A Whole-Cell Biosensor as in Vitro Alternative to Skin Irritation Tests; *Biosensors & Bioelectronics,* **2013**, 39, 156-162.

315.   Liu, Q.J.; Yu, J.J.; Yu, H.; Xiao, L.D.; Wang, P.; Yang, M., In Apcmbe 2008: 7th Asian-Pacific Conference on Medical and Biological Engineering; Peng, Y.; Weng, X., Eds.; 2008; Vol. 19.

316.   Guarisco, M.; Gandolfi, D.; Guider, R.; Vanzetti, L.; Bartali, R.; Ghulinyan, M.; Cretich, M.; Chiari, M.; Bettotti, P.; Pavesi, L.; Pederzolli, C.; Pasquardini, L., A New Aptamer Immobilization Strategy for Protein Recognition; *Sensors and Actuators B: Chemical,* **2017**, 252, 222-231.

317.   Zhang, X.; Yadavalli, V.K., Surface Immobilization of DNA Aptamers for Biosensing and Protein Interaction Analysis; *Biosensors and Bioelectronics,* **2011**, 26, 3142-3147.

318.   Erdem, A.; Eksin, E.; Muti, M., Chitosan–Graphene Oxide Based Aptasensor for the Impedimetric Detection of Lysozyme; *Colloids and Surfaces B: Biointerfaces,* **2014**, 115, 205-211.

319.   Castillo, G.; Lamberti, I.; Mosiello, L.; Hianik, T., Impedimetric DNA Aptasensor for Sensitive Detection of Ochratoxin a in Food; *Electroanalysis,* **2012**, 24, 512-520.

320.   Labib, M.; Zamay, A.S.; Koloyskaya, O.S.; Reshetneva, I.T.; Zamay, G.S.; Kibbee, R.J.; Sattar, S.A.; Zamay, T.N.; Berezovski, M.V., Aptamer-Based Viability Impedimetric Sensor for Bacteria; *Analytical Chemistry,* **2012**, 84, 8966-8969.

321.   Bagheryan, Z.; Raoof, J.B.; Golabi, M.; Turner, A.P.F.; Beni, V., Diazonium-Based Impedimetric Aptasensor for the Rapid Label-Free Detection of Salmonella Typhimurium in Food Sample; *Biosensors & Bioelectronics,* **2016**, 80, 566-573.

322.   Rapini, R.; Marrazza, G., Electrochemical Aptasensors for Contaminants Detection in Food and Environment: Recent Advances; *Bioelectrochemistry,* **2017**, 118, 47-61.

323.   Sett, A.; Das, S.; Bora, U., Functional Nucleic-Acid-Based Sensors for Environmental Monitoring; *Applied Biochemistry and Biotechnology,* **2014**, 174, 1073-1091.

324.   Jarczewska, M.; Gorski, L.; Malinowska, E., Electrochemical Aptamer-Based Biosensors as Potential Tools for Clinical Diagnostics; *Analytical Methods,* **2016**, 8, 3861-3877.

325.   Jolly, P.; Formisano, N.; Tkac, J.; Kasak, P.; Frost, C.G.; Estrela, P., Label-Free Impedimetric Aptasensor with Antifouling Surface Chemistry: A Prostate Specific Antigen Case Study; *Sensors and Actuators B: Chemical,* **2015**, 209, 306-312.

326.   Labib, M.; Zamay, A.S.; Muharemagic, D.; Chechik, A.V.; Bell, J.C.; Berezoyski, M.V., Aptamer-Based Viability Impedimetric Sensor for Viruses; *Analytical Chemistry,* **2012**, 84, 1813-1816.

327.   Rogers, K.R., Principles of Affinity-Based Biosensors; *Molecular Biotechnology,* **2000**, 14, 109-129.

328.   Hou, L.; Cui, Y.; Xu, M.; Gao, Z.; Huang, J.; Tang, D., Graphene Oxide-Labeled Sandwich-Type Impedimetric Immunoassay with Sensitive Enhancement Based on Enzymatic 4-Chloro-1-Naphthol Oxidation; *Biosensors and Bioelectronics,* **2013**, 47, 149-156.

329.   Rahman, M.A.; Shiddiky, M.J.A.; Park, J.-S.; Shim, Y.-B., An Impedimetric Immunosensor for the Label-Free Detection of Bisphenol A; *Biosensors and Bioelectronics,* **2007**, 22, 2464-2470.

330.   Canbaz, M.C.; Sezginturk, M.K., Fabrication of a Highly Sensitive Disposable Immunosensor Based on Indium Tin Oxide Substrates for Cancer Biomarker Detection; *Analytical Biochemistry,* **2014**, 446, 9-18.

331.   Canbaz, M.C.; Simsek, C.S.; Sezginturk, M.K., Electrochemical Biosensor Based on Self-Assembled Monolayers Modified with Gold Nanoparticles for Detection of Her-3; *Analytica Chimica Acta,* **2014**, 814, 31-38.

332.   Chun, L.; Kim, S.E.; Cho, M.; Choe, W.S.; Nam, J.; Lee, D.W.; Lee, Y., Electrochemical Detection of Her2 Using Single Stranded DNA Aptamer Modified Gold Nanoparticles Electrode; *Sensors and Actuators B: Chemical,* **2013**, 186, 446-450.

333.	Soares, J.C.; Shimizu, F.M.; Soares, A.C.; Caseli, L.; Ferreira, J.; Oliveira, O.N., Supramolecular Control in Nanostructured Film Architectures for Detecting Breast Cancer; *ACS Applied Materials & Interfaces,* **2015**, 7, 11833-11841.

334.	Ali, M.A.; Mondal, K.; Jiao, Y.Y.; Oren, S.; Xu, Z.; Sharma, A.; Dong, L., Microfluidic Immuno-Biochip for Detection of Breast Cancer Biomarkers Using Hierarchical Composite of Porous Graphene and Titanium Dioxide Nanofibers; *ACS Applied Materials & Interfaces,* **2016**, 8, 20570-20582.

335.	Elshafey, R.; Tavares, A.C.; Siaj, M.; Zourob, M., Electrochemical Impedance Immunosensor Based on Gold Nanoparticles-Protein G for the Detection of Cancer Marker Epidermal Growth Factor Receptor in Human Plasma and Brain Tissue; *Biosensors & Bioelectronics,* **2013**, 50, 143-149.

336.	Elshafey, R.; Tlili, C.; Abulrob, A.; Tavares, A.C.; Zourob, M., Label-Free Impedimetric Immunosensor for Ultrasensitive Detection of Cancer Marker Murine Double Minute 2 in Brain Tissue; *Biosensors & Bioelectronics,* **2013**, 39, 220-225.

337.	Asav, E.; Sezgintürk, M.K., A Novel Impedimetric Disposable Immunosensor for Rapid Detection of a Potential Cancer Biomarker; *International Journal of Biological Macromolecules,* **2014**, 66, 273-280.

338.	Huang, K.J.; Niu, D.J.; Xie, W.Z.; Wang, W., A Disposable Electrochemical Immunosensor for Carcinoembryonic Antigen Based on Nano-Au/Multi-Walled Carbon Nanotubes-Chitosans Nanocomposite Film Modified Glassy Carbon Electrode; *Analytica Chimica Acta,* **2010**, 659, 102-108.

339.	Jeong, B.; Akter, R.; Han, O.H.; Rhee, C.K.; Rahman, M.A., Increased Electrocatalyzed Performance through Dendrimer-Encapsulated Gold Nanoparticles and Carbon Nanotube-Assisted Multiple Bienzymatic Labels: Highly Sensitive Electrochemical Immunosensor for Protein Detection; *Analytical Chemistry,* **2013**, 85, 1784-1791.

340.	Kong, F.Y.; Xu, M.T.; Xu, J.J.; Chen, H.Y., A Novel Lable-Free Electrochemical Immunosensor for Carcinoembryonic Antigen Based on Gold Nanoparticles-Thionine-Reduced Graphene Oxide Nanocomposite Film Modified Glassy Carbon Electrode; *Talanta,* **2011**, 85, 2620-2625.

341.	Tang, D.P.; Yuan, R.; Chai, Y.Q., Magnetic Core-Shell Fe3o4@Ag Nanoparticles Coated Carbon Paste Interface for Studies of Carcinoembryonic Antigen in Clinical Immunoassay; *Journal of Physical Chemistry B,* **2006**, 110, 11640-11646.

342.	Tang, H.; Chen, J.; Nie, L.; Kuang, Y.; Yao, S., A Label-Free Electrochemical Immunoassay for Carcinoembryonic Antigen (Cea) Based on Gold Nanoparticles (Aunps) and Nonconductive Polymer Film; *Biosensors and Bioelectronics,* **2007**, 22, 1061-1067.

343.	Canbaz, M.Ç.; Şimşek, Ç.S.; Sezgintürk, M.K., Electrochemical Biosensor Based on Self-Assembled Monolayers Modified with Gold Nanoparticles for Detection of Her-3; *Analytica Chimica Acta,* **2014**, 814, 31-38.

344.	Marques, R.C.B.; Viswanathan, S.; Nouws, H.P.A.; Delerue-Matos, C.; González-García, M.B., Electrochemical Immunosensor for the Analysis of the Breast Cancer Biomarker Her2 Ecd; *Talanta,* **2014**, 129, 594-599.

345.	Loo, L.; Capobianco, J.A.; Wu, W.; Gao, X.; Shih, W.Y.; Shih, W.-H.; Pourrezaei, K.; Robinson, M.K.; Adams, G.P., Highly Sensitive Detection of Her2 Extracellular Domain in the

Serum of Breast Cancer Patients by Piezoelectric Microcantilevers; *Analytical Chemistry,* **2011**, 83, 3392-3397.

346.   Arteaga, C.L., Epidermal Growth Factor Receptor Dependence in Human Tumors: More Than Just Expression?; *The Oncologist,* **2002**, 7, 31-39.

347.   Elshafey, R.; Tavares, A.C.; Siaj, M.; Zourob, M., Electrochemical Impedance Immunosensor Based on Gold Nanoparticles–Protein G for the Detection of Cancer Marker Epidermal Growth Factor Receptor in Human Plasma and Brain Tissue; *Biosensors and Bioelectronics,* **2013**, 50, 143-149.

348.   Bryan, T.; Luo, X.; Bueno, P.R.; Davis, J.J., An Optimised Electrochemical Biosensor for the Label-Free Detection of C-Reactive Protein in Blood; *Biosensors and Bioelectronics,* **2013**, 39, 94-98.

349.   Chen, X.J.; Wang, Y.Y.; Zhou, J.J.; Yan, W.; Li, X.H.; Zhu, J.J., Electrochemical Impedance Immunosensor Based on Three-Dimensionally Ordered Macroporous Gold Film; *Analytical Chemistry,* **2008**, 80, 2133-2140.

350.   Hennessey, H.; Afara, N.; Omanovic, S.; Padjen, A.L., Electrochemical Investigations of the Interaction of C-Reactive Protein (Crp) with a Crp Antibody Chemically Immobilized on a Gold Surface; *Analytica Chimica Acta,* **2009**, 643, 45-53.

351.   Johnson, A.; Song, Q.F.; Ferrigno, P.K.; Bueno, P.R.; Davis, J.J., Sensitive Affimer and Antibody Based Impedimetric Label-Free Assays for C-Reactive Protein; *Analytical Chemistry,* **2012**, 84, 6553-6560.

352.   Vermeeren, V.; Grieten, L.; Vanden Bon, N.; Bijnens, N.; Wenmackers, S.; Janssens, S.D.; Haenen, K.; Wagner, P.; Michiels, L., Impedimetric, Diamond-Based Immmunosensor for the Detection of C-Reactive Protein; *Sensors and Actuators B: Chemical,* **2011**, 157, 130-138.

353.   Hou, L.; Gao, Z.; Xu, M.; Cao, X.; Wu, X.; Chen, G.; Tang, D., Dnazyme-Functionalized Gold–Palladium Hybrid Nanostructures for Triple Signal Amplification of Impedimetric Immunosensor; *Biosensors and Bioelectronics,* **2014**, 54, 365-371.

354.   Akter, R.; Rahman, M.A.; Rhee, C.K., Amplified Electrochemical Detection of a Cancer Biomarker by Enhanced Precipitation Using Horseradish Peroxidase Attached on Carbon Nanotubes; *Analytical Chemistry,* **2012**, 84, 6407-6415.

355.   Fernandez-Sanchez, C.; Mcneil, C.J.; Rawson, K.; Nilsson, O., Disposable Noncompetitive Immunosensor for Free and Total Prostate-Specific Antigen Based on Capacitance Measurement; *Analytical Chemistry,* **2004**, 76, 5649-5656.

356.   Kavosi, B.; Salimi, A.; Hallaj, R.; Amani, K., A Highly Sensitive Prostate-Specific Antigen Immunosensor Based on Gold Nanoparticles/Pamam Dendrimer Loaded on Mwcnts/Chitosan/Ionic Liquid Nanocomposite; *Biosensors & Bioelectronics,* **2014**, 52, 20-28.

357.   Jarocka, U.; Sawicka, R.; Gora-Sochacka, A.; Sirko, A.; Zagorski-Ostoja, W.; Radecki, J.; Radecka, H., An Immunosensor Based on Antibody Binding Fragments Attached to Gold Nanoparticles for the Detection of Peptides Derived from Avian Influenza Hemagglutinin H5; *Sensors,* **2014**, 14, 15714-15728.

358.   Jarocka, U.; Sawicka, R.; Góra-Sochacka, A.; Sirko, A.; Zagórski-Ostoja, W.; Radecki, J.; Radecka, H., Electrochemical Immunosensor for Detection of Antibodies against Influenza a Virus H5n1 in Hen Serum; *Biosensors and Bioelectronics,* **2014**, 55, 301-306.

359.	Haji-Hashemi, H.; Norouzi, P.; Safarnejad, M.R.; Ganjali, M.R., Label-Free Electrochemical Immunosensor for Direct Detection of Citrus Tristeza Virus Using Modified Gold Electrode; *Sensors and Actuators B: Chemical,* **2017**, 244, 211-216.

360.	Singhal, C.; Ingle, A.; Chakraborty, D.; Krishna, P.N.A.; Pundir, C.S.; Narang, J., Impedimetric Genosensor for Detection of Hepatitis C Virus (Hcv1) DNA Using Viral Probe on Methylene Blue Doped Silica Nanoparticles; *International Journal of Biological Macromolecules,* **2017**, 98, 84-93.

361.	Park, J.Y.; Lee, Y.S.; Chang, B.Y.; Kim, B.H.; Jeon, S.; Park, S.M., Label-Free Impedimetric Sensor for a Ribonucleic Acid Oligomer Specific to Hepatitis C Virus at a Self-Assembled Monolayer-Covered Electrode; *Analytical Chemistry,* **2010**, 82, 8342-8348.

362.	Cecchetto, J.; Carvalho, F.C.; Santos, A.; Fernandes, F.C.B.; Bueno, P.R., An Impedimetric Biosensor to Test Neat Serum for Dengue Diagnosis; *Sensors and Actuators B: Chemical,* **2015**, 213, 150-154.

363.	Luna, D.M.N.; Oliveira, M.D.L.; Nogueira, M.L.; Andrade, C.a.S., Biosensor Based on Lectin and Lipid Membranes for Detection of Serum Glycoproteins in Infected Patients with Dengue; *Chemistry and Physics of Lipids,* **2014**, 180, 7-14.

364.	Sinawang, P.D.; Fajs, L.; Elouarzaki, K.; Nugraha, J.; Marks, R.S., Tempo-Based Immuno-Lateral Flow Quantitative Detection of Dengue Ns1 Protein; *Sensors and Actuators B: Chemical,* **2018**, 259, 354-363.

365.	Deng, J.J.; Toh, C.S., Impedimetric DNA Biosensor Based on a Nanoporous Alumina Membrane for the Detection of the Specific Oligonucleotide Sequence of Dengue Virus; *Sensors,* **2013**, 13, 7774-7785.

366.	Fang, X.Q.; Tan, O.K.; Tse, M.S.; Ooi, E.E., A Label-Free Immunosensor for Diagnosis of Dengue Infection with Simple Electrical Measurements; *Biosensors & Bioelectronics,* **2010**, 25, 1137-1142.

367.	Cecchetto, J.; Fernandes, F.C.B.; Lopes, R.; Bueno, P.R., The Capacitive Sensing of Ns1 Flavivirus Biomarker; *Biosensors & Bioelectronics,* **2017**, 87, 949-956.

368.	Hassen, W.M.; Chaix, C.; Abdelghani, A.; Bessueille, F.; Leonard, D.; Jaffrezic-Renault, N., An Impedimetric DNA Sensor Based on Functionalized Magnetic Nanoparticles for Hiv and Hbv Detection; *Sensors and Actuators B: Chemical,* **2008**, 134, 755-760.

369.	Arya, S.K.; Kongsuphol, P.; Wong, C.C.; Polla, L.J.; Park, M.K., Label Free Biosensor for Sensitive Human Influenza Virus Hemagglutinin Specific Antibody Detection Using Coiled-Coil Peptide Modified Microelectrode Array Based Platform; *Sensors and Actuators B: Chemical,* **2014**, 194, 127-133.

370.	Wicklein, B.; Del Burgo, M.Á.M.; Yuste, M.; Carregal-Romero, E.; Llobera, A.; Darder, M.; Aranda, P.; Ortín, J.; Del Real, G.; Fernández-Sánchez, C., Biomimetic Architectures for the Impedimetric Discrimination of Influenza Virus Phenotypes; *Advanced Functional Materials,* **2013**, 23, 254-262.

371.	Ionescu, R.E.; Jaffrezic-Renault, N.; Bouffier, L.; Gondran, C.; Cosnier, S.; Pinacho, D.G.; Marco, M.P.; Sánchez-Baeza, F.J.; Healy, T.; Martelet, C., Impedimetric Immunosensor for the Specific Label Free Detection of Ciprofloxacin Antibiotic; *Biosensors and Bioelectronics,* **2007**, 23, 549-555.

372.   Conzuelo, F.; Campuzano, S.; Gamella, M.; Pinacho, D.G.; Reviejo, A.J.; Marco, M.P.; Pingarrón, J.M., Integrated Disposable Electrochemical Immunosensors for the Simultaneous Determination of Sulfonamide and Tetracycline Antibiotics Residues in Milk; *Biosensors and Bioelectronics,* **2013**, 50, 100-105.

373.   Chullasat, K.; Kanatharana, P.; Limbut, W.; Numnuam, A.; Thavarungkul, P., Ultra Trace Analysis of Small Molecule by Label-Free Impedimetric Immunosensor Using Multilayer Modified Electrode; *Biosensors and Bioelectronics,* **2011**, 26, 4571-4578.

374.   Radke, S.A.; Alocilja, E.C., A High Density Microelectrode Array Biosensor for Detection of E-Coli O157 : H7; *Biosensors & Bioelectronics,* **2005**, 20, 1662-1667.

375.   Ruan, C.M.; Yang, L.J.; Li, Y.B., Immunobiosensor Chips for Detection of Escherichia Coli O157 : H7 Using Electrochemical Impedance Spectroscopy; *Analytical Chemistry,* **2002**, 74, 4814-4820.

376.   Sadik, O.A.; Aluoch, A.O.; Zhou, A.L., Status of Biomolecular Recognition Using Electrochemical Techniques; *Biosensors & Bioelectronics,* **2009**, 24, 2749-2765.

377.   Varshney, M.; Li, Y.B., Interdigitated Array Microelectrode Based Impedance Biosensor Coupled with Magnetic Nanoparticle-Antibody Conjugates for Detection of Escherichia Coli O157 : H7 in Food Samples; *Biosensors & Bioelectronics,* **2007**, 22, 2408-2414.

378.   Varshney, M.; Li, Y.B.; Srinivasan, B.; Tung, S., A Label-Free, Microfluidics and Interdigitated Array Microelectrode-Based Impedance Biosensor in Combination with Nanoparticles Immunoseparation for Detection of Escherichia Coli O157 : H7 in Food Samples; *Sensors and Actuators B: Chemical,* **2007**, 128, 99-107.

379.   Yang, L.J.; Li, Y.B.; Erf, G.F., Interdigitated Array Microelectrode-Based Electrochemical Impedance Immunosensor for Detection of Escherichia Coli O157 : H7; *Analytical Chemistry,* **2004**, 76, 1107-1113.

380.   Joung, C.K.; Kim, H.N.; Lim, M.C.; Jeon, T.J.; Kim, H.Y.; Kim, Y.R., A Nanoporous Membrane-Based Impedimetric Immunosensor for Label-Free Detection of Pathogenic Bacteria in Whole Milk; *Biosensors & Bioelectronics,* **2013**, 44, 210-215.

381.   Escamilla-Gomez, V.; Campuzano, S.; Pedrero, M.; Pingarron, J.M., Gold Screen-Printed-Based Impedimetric Immunobiosensors for Direct and Sensitive Escherichia Coli Quantisation; *Biosensors & Bioelectronics,* **2009**, 24, 3365-3371.

382.   Tan, F.; Leung, P.H.M.; Liu, Z.B.; Zhang, Y.; Xiao, L.D.; Ye, W.W.; Zhang, X.; Yi, L.; Yang, M., A Pdms Microfluidic Impedance Immunosensor for E. Coli O157:H7 and Staphylococcus Aureus Detection Via Antibody-Immobilized Nanoporous Membrane; *Sensors and Actuators B: Chemical,* **2011**, 159, 328-335.

383.   Dong, J.; Zhao, H.; Xu, M.R.; Ma, Q.; Ai, S.Y., A Label-Free Electrochemical Impedance Immunosensor Based on Aunps/Pamam-Mwcnt-Chi Nanocomposite Modified Glassy Carbon Electrode for Detection of Salmonella Typhimurium in Milk; *Food Chemistry,* **2013**, 141, 1980-1986.

384.   Su, X.L.; Li, Y.B., A Qcm Immunosensor for Salmonella Detection with Simultaneous Measurements of Resonant Frequency and Motional Resistance; *Biosensors & Bioelectronics,* **2005**, 21, 840-848.

385.   Wang, R.H.; Ruan, C.M.; Kanayeva, D.; Lassiter, K.; Li, Y.B., Tio2 Nanowire Bundle Microelectrode Based Impedance Immunosensor for Rapid and Sensitive Detection of Listeria Monocytogenes; *Nano Letters,* **2008**, 8, 2625-2631.

386.   Li, Y.; Xu, J.; Sun, C., Chemical Sensors and Biosensors for the Detection of Melamine; *RSC Advances,* **2015**, 5, 1125-1147.

387.   Wang, M.; Kang, H.; Xu, D.; Wang, C.; Liu, S.; Hu, X., Label-Free Impedimetric Immunosensor for Sensitive Detection of Fenvalerate in Tea; *Food Chemistry,* **2013**, 141, 84-90.

388.   Valera, E.; Ramón-Azcón, J.; Rodríguez, Á.; Castañer, L.M.; Sánchez, F.J.; Marco, M.P., Impedimetric Immunosensor for Atrazine Detection Using Interdigitated M-Electrodes (Idμe's); *Sensors and Actuators B: Chemical,* **2007**, 125, 526-537.

389.   Ionescu, R.E.; Gondran, C.; Bouffier, L.; Jaffrezic-Renault, N.; Martelet, C.; Cosnier, S., Label-Free Impedimetric Immunosensor for Sensitive Detection of Atrazine; *Electrochimica Acta,* **2010**, 55, 6228-6232.

390.   Helali, S.; Abdelghani, A.; Hafaiedh, I.; Martelet, C.; Prodromidis, M.I.; Albanis, T.; Jaffrezic-Renault, N., Functionalization of Niobium Electrodes for the Construction of Impedimetric Biosensors; *Materials Science and Engineering: C,* **2008**, 28, 826-830.

Chapter 2   **Transparent Polymer-based SERS**

Substrates Templated by a Soda Can

2.1 Introduction

In recent years, advances in nanotechnology and nanofabrication techniques have enabled significant enhancement in a variety of analytical sensor devices. These devices, employing electronic,[1-3] electrochemical and optical[4-6] detection methods, have provided highly qualitative and sensitive measurements. However, within the environmental and security sectors, highly sensitive sensing alone is not enough; rapid on-site molecular identification is also required. One approach that addresses these criteria is surface enhanced Raman spectroscopy (SERS)[7, 8] which provides both a spectral molecular fingerprint and allows for trace detection; with the potential for single molecule sensitivity.[9-14] SERS is thus emerging as a powerful technique for chemical, [15, 16] and biological sensing applications.[17] †

As discussed in chapter 1, SERS enhancement occurs at nanostructured plasmonic surfaces following illumination with monochromatic radiation and results from (i) an increase in local electromagnetic field strengths of localised surface plasmons (in nanogaps between metal clusters called "hot spots") and (ii) chemical resonant energy charge transfer.[18] For these processes to occur, substrates must be capable of supporting plasmonic modes (collective oscillations of metal electrons) and have a nanostructured rough surface with well-defined gaps in the region of 10- 100 nm between metallic clusters (to conserve momentum). To this end, fabrication of SERS substrates using top down approaches including: lithography techniques (Ebeam[19, 20] and nanoimprint[21] lithography's), laser etching,[22] film deposition (sputtering, metal evaporation, atomic layer deposition)[23, 24] and templating (using anodic aluminium oxide,[25] masks,[23] or molds)[26] as well as bottom up approaches including chemical synthesis,[27] colloid aggregation,[28] and self-assembly[29, 30] of metal nanoparticles,[31, 32] nanowires,[2, 26] nanospheres,[31, 33, 34] nanorods,[35-37] nanotubes,[25] nanotriangles,[38] nano-urchins,[39] and/or nanoshells[40] have been reported. While these approaches are elegant and are attractive in research environments for their reproducibility and large SERS enhancement, they are limited in that they can be expensive, time consuming, and require complex fabrication approaches which may have low throughput. Consequently, a critical challenge limiting

---

the uptake of SERS for commercial applications is the lack of scalable and low-cost fabrication approaches compatible with mass manufacturing.

To address this challenge, we have developed a templating approach employing "inherent" nanostructured aluminium (Al) masters (obtained from commercial soda drink cans) to template low-cost polymer replicates which are subsequently coated with a thin (30 nm) silver (Ag) layer. These transparent polymer substrates offer a number of advantages: (i) the simple manufacturing approach is scalable offering the potential for low-cost fabrication and thus widespread uptake and applicability. (ii) The fine metallic nanostructures provide SERS hot spots upon optical excitation. (iii) The substrates are transparent and thus are compatible with back excitation and collection allowing measurement in liquid environments to be undertaken. (iv) the flexible substrates may be easily integrated in-line or on-line adding to the suite of spectroscopic process analytical techniques used in smart manufacturing industry 4.0 approaches. (v) Finally, the sensor may be chemically modified to widen the range of molecules that may be detected.

To explore the versatility of our as-fabricated SERS substrates towards real world applications, e.g., environmental monitoring and food security, a variety of different target molecules were selected and analysed. Initially, 4-aminothiophenol (4-ABT) and crystal violet (CrV)[41] were chosen to characterise SERS and allow comparison with the published literature. Malachite green was also selected as this and other trimethyldiamine dyes are used indiscriminately as antimicrobials in aquaculture, despite the reports of causing serious toxic, carcinogenic and mutagenic effects in mammalian cells.[42, 43] Consequently, the presence of trimethyldiamines are now tightly controlled with minimum reside limits (MRL) set at 2 µg/L (2 ppb) in water.[44] Glucose was analysed by first capturing the molecule on a substrate pre-modified with a mixed thiol monolayer in a manner similar to that reported by the Van Duyne group.[45] Chemical structures for these compounds are illustrated in Figure 2.1. Melamine was selected as the final contaminant as it now requires regular monitoring due to its previous use to give a false appearance of high protein levels in milk.[46] Melamine MRLs are now set at 2.5 ppm for food products (including milk) and 1 ppm in infant formulae.[47] Current detection methods for melamine are laboratory based using high-end instrumentation. The dominant detection paradigm for melamine is chromatography, which requires complex sample pre-treatment to extract analytes and eliminate matrix effects. Pre-treatment can

106

take the form of liquid phase extraction employing a variety of polar solvents or a combination of liquid phase and solid phase micro-extraction for more complex matrices.[48-50] Following pre-treatment analysis is undertaken using liquid chromatography mass spectroscopy approaches.[51-53] These methods are expensive, time consuming and require dedicated laboratories with highly trained personnel. Other approaches, for example ELISA, are significantly faster, but suffer from poor specificity.[54, 55]
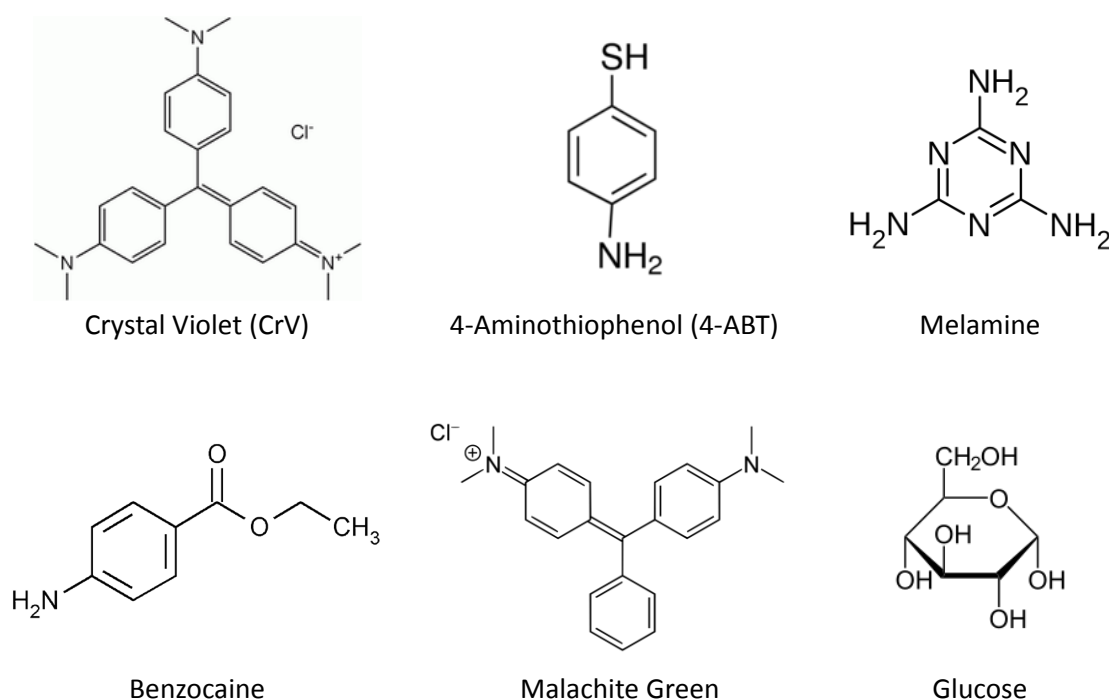
Figure 2.1: Chemical Structures for the compounds analysed in this chapter using SERS.

In this chapter, I discuss a new low-cost and rapid approach that permits robust, sensitive and selective detection for screening applications. I present the highly sensitive detection of crystal violet with a measured limit of detection of 204 ng/L (parts per trillion, equivalent to 5×10^{-10} M), well below the permitted MRL value. Detection of low concentrations of melamine (100 ppb) spiked into both milk and infant formula solutions were demonstrated, without the need for any sample pre-treatment. A drop-and-dry sampling technique was employed and an anaylsis time of 10 minutes was demonstrated. Finally, to benchmark these results, mass spectrometry was undertaken in collaboration with the Mass Spectrometry Research Centre in Cork Institute of Technology.

2.2 Experimental

2.2.1 Materials and Preparation of Standards

Polystyrene (PS), 4-aminothiophenol (97%), polyvinylidene fluoride (PVDF), crystal violet (<90% dye content), malachite green, benzocaine, 1-decanethiol, mercaptohexanol, glucose and melamine and analytical grade solvents were purchased from Sigma-Aldrich and used as received. Polydimethylsiloxane 184 silicon elastomer (PDMS) and curing agent were purchased from Sylgard®. PTFE syringe filters (0.45 μm) were purchased from Lab Unlimited. Full-fat milk and Aptamil® Follow on Milk infant formula were purchased from a local supermarket. 4-aminothiophenol (4-ABT), 1-decanethiol (DT) and mercaptohexanol (MH) were prepared by dissolving in ethanol. All standards of crystal violet (CrV), melamine, and glucose were prepared as required, using deionised water (18.2 MΩ.cm ELGA Pure Lab Ultra systems) and a serial dilution method employed to prepare standards in the desired concentration ranges. HPLC primary stock solutions of melamine were prepared in deionised water at a concentration of 10 ppm. Working standards were prepared in the range 0.1 ppm – 5.0 ppm using deionised water. For EIS-MS measurements, milk samples were diluted with deionised water (1:10) and passed through a 0.45 μm syringe filter to prevent blockage during infusion. Both melamine-spiked and unspiked milk samples were prepared in the same manner. All standard solutions were stored at room temperature (18 ºC).

2.2.2 Fabrication of the Polymer-based SERS Substrate

Substrates were fabricated as shown in the schematic below, Figure 2.2 (a). To prepare the aluminium template, the outer (printed side) of an Al soda can was sanded using fine (P120, ~125 μm particle size) and extra fine (P280, ~50 μm) grade sandpaper to remove the paint. The can was then polished with 6 μm and 1 μm alumina slurry, until it appeared shiny, to smoothen the deformities caused by sanding the Al. The Al preparation was finished by cutting the Al into 1 cm^2 squares, and immersing them into a chemical bath (5% NaOH, 2-3 minutes). The chemical wash dissolved the top layer of the aluminium surface and yielded a nano-sized random pattern on each of the square pieces. The wash also reduced inhomogeneous surface asperities and removed the sanding debris. The Al

squares were used to pattern several melted polymers, so they are referred to as "Al masters".

In this work three polymers were chosen for substrate fabrication and comparison: PVDF, PS and PDMS. Each polymer base was fabricated using separate processes. Pellets of polyvinylidene fluoride (PVDF) were placed on a microscope slide and heated at ~228°C on a hotplate until melted. A prepared Al master was then placed onto the melted droplet and pushed downward so the PVDF wetted the aluminium. The glass slide was then removed from the hotplate and allowed cool whereon the PVDF hardened and could be easily peeled from the Al, Figure 2.2 (b). The resulting polymer was yielded a flexible transparent substrate Figure 2.2 (c), employing the same nano-sized surface pattern as on the Al template. PS substrates were fabricated in a similar way to the PVDF above: Pellets of PS were mounted on a coverslip and heated at ~215 °C on a hotplate. A standard microscope slide was used to apply pressure to the pellets as they melted to obtain a flattened disc shape. The disc was then removed from the hotplate and as it cooled, it readily separated from the glass slide and cover slip. The prepared Al can was then templated with the melted polymer to obtain the nanostructured polymer. A different process was used to prepare and template the PDMS polymer. The Sylgard 184 Silicone Elastomer base and the curing agent were mixed in a 10:1 ratio in a plastic container. The polymer mixture was then degassed in a vacuum until no bubbles remained. The prepared aluminium pieces were then placed into the viscous polymer and heat cured at 60 ℃ for 1 hour. The aluminium pieces were cut out of the flexible polymer using a clean scalpel, and peeled from the polymer to yield a nanostructured PDMS surface.

Finally, to complete substrate fabrication, a thin silver layer (30 nm) was deposited onto the different polymer bases by thermal evaporation, at ~1.6 A under vacuum (3×10^{-7} mbar) using a Thin Film Deposition system (Edwards Autocore 500) within an MBraun glovebox. The thickness and the deposition rate were controlled *in situ* using a calibrated quartz microbalance. Control substrates were fabricated as above, where the Al master template was replaced with glass slides, to yield a smooth unpatterned surface.
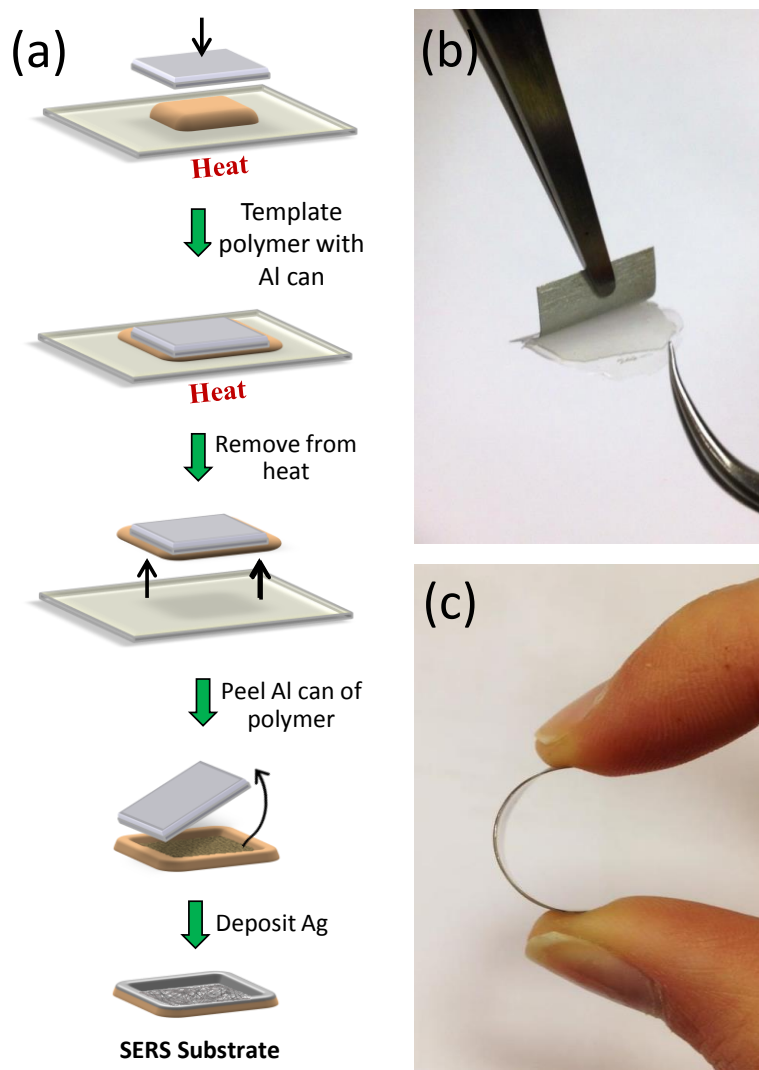
Figure 2.2: (a) Schematic outlining the fabrication of the Ag covered nanostructured PVDF SERS substrates. (b) Image of Aluminium easily peeling off the templated polymer. (c) Flexibility of PVDF

2.2.3 Structural Characterisation of SERS Substrates

The completed SERS substrates were characterised structurally using scanning electron microscopy (SEM). SEM analysis was undertaken to characterise and identify irregularities on the substrate surface after the fabrication procedure. SEM images were acquired using a calibrated field emission SEM (JSM-7500F, JEOL UK Ltd.) operating at beam voltages between 3 and 5 kV.

2.2.4 Raman Spectroscopic Characterisation of SERS Substrates

All Raman measurements were recorded using a Confocal Renishaw Raman Microscope equipped with a 514 nm Ar ion laser and analysed using Wire 3.0 computer software. The laser spot diameter was ~1 μm at the substrates surface and a laser power density of ~7×10^4 W/cm^2 was used. SERS spectra were obtained by measuring and averaging five different locations on pristine substrates. Data was collected using a 50x magnification (0.75 NA) objective microscope, with an acquisition time of 10 s, over an extended spectral range of 200 cm^{-1} to 2000 cm^{-1}. The spectrometer was equipped with a computer controlled motorised XYZ stage employed to focus and adjust the positioning of the sample on the silver surface. Subtraction of the baseline was performed on all spectra to eliminate background noise from the underlying polymer and the recorded spectra were imported into Origin® 7.4 (OriginLab) to facilitate data analysis.

2.2.5 Finite Element Method Simulations

Dr. Pierre Lovera undertook finite element method (FEM) simulations on the fabricated SERS substrates. The electromagnetic response of the nanostructure was simulated by the finite element method with a commercial software package (COMSOL Multiphysics with Wave Optics and CAD Import Modules). To construct a 3D image of the sample, the pixel value (pv) of the greyscale, 16 bit SEM micrograph was converted into height (h) with the following algorithm: if pv <15000, h=0 and if 15000≤ pv ≤65000, h=30*(pv-15000)/(50000). With this conversion, black areas with pixel values below 15000 corresponded to 0 nm and white areas with a pixel value of 65000 to 30 nm. This converted image was used as a parametric surface in COMSOL. The 3D geometry was then constructed by intersecting the parametric surface with blocks. This resulted in three domains, i.e. the Ag nanocluster with a PVDF substrate and an air superstrate. These domains were meshed with tetrahedral elements with a minimum size of 0.03 nm. A total volume of 100 x 100 x 150 nm^3 was chosen to keep the computational demand manageable for a 3.50 GHz, quad core, 16 GB RAM PC. The refractive index of air, PVDF and Ag were 1; 1.42 and 0.14, respectively. The value of Ag was obtained from Johnson and Christy for a wavelength of 514 nm.[56] A 5 nm perfectly matched layer was considered on all sides of the structures, as well as above the air superstrate and below

the PVDF substrate. A 514 nm plane wave E_{inc} with a power of 1 W (corresponding to an electromagnetic field magnitude of 3×10^7 V/m) and a polarisation along the Y axis was inputted and COMSOL solved for full field Etot. The enhancement factor G can be calculated as G= (Etot/Einc).

2.2.6 SERS Analysis

To explore the suitability of these substrates for highly sensitive measurements, a series of crystal violet standards ranging from 10^{-7} to 10^{-10} M were prepared in DI water and deposited via the drop/dry process on the substrates; depositing 50 µl of solution onto the substrate and allowing to air dry (10 minutes). All samples were thoroughly rinsed with DI water before Raman analysis to remove unadsorbed, clumped molecules that accumulated on the surface of the substrate during the drying process. 50 µL aliquots (10^{-6} M) of malachite green (in DI water), imidacloprid (in methanol and DI water), benzocaine (in DI water) and 4-ABT (in 97% ethanol) were also deposited and analysed in a similar manner.

2.2.6.1 *Glucose*

Glucose detection was undertaken using a similar method to Van Duyne *et al.*[45] A mixed decanethiol/ mercaptohexanol (DT/MH) functionalisation of the Ag surface was first undertaken to yield a mixed thiol self-assembled monolayer (SAM). Substrates were incubated in 1 mM DT for 45 minutes followed by incubation in 1 mM MH for 24 hours. A Raman analysis was undertaken at this point to obtain the SAM spectra. The substrate was then immersed into 10 mM of aqueous glucose solution for 6 hours, air dried and Raman analysis was undertaken.

2.2.6.2 *Melamine*

A series of 1 ppm Melamine standards were prepared in DI water, milk and infant formula. The same drop and dry method was employed for these experiments; depositing 50 µl of solution onto the substrate and allowing to air dry (10 minutes). Working solutions of infant formula were first prepared using manufacturer instructions, then diluted 1:10 with D.I. water. Working solutions of full-fat milk were similarly prepared

using a 1:10 dilution step. Melamine powder was dissolved using the appropriate volume of stock to yield a 10 ppm solution. The solution was sonicated for 10 minutes to ensure the melamine was fully dissolved. An un-spiked stock solution was used to dilute the 10 ppm milk/ infant formula standards to make 1 ppm standards. No further sample preparation was undertaken. All samples were thoroughly rinsed with DI water before Raman analysis to remove unadsorbed, clumped molecules that accumulated on the surface of the substrate during the drying process.

2.2.7 Direct Infusion MS/MS Analysis of Melamine

This work was carried out with partners in Cork Institute of Technology, Cork. As prepared melamine and full-fat milk 10 ppm stock solutions were diluted with appropriate volumes of working solutions to yield 0.5, 1, 1.5, 2, 3, 4, & 5 ppm solutions. Both melamine-spiked and unspiked milk samples were diluted with deionised water (1:10 dilution) and passed through a 0.45 µm syringe filter to prevent blockage during ESI infusion. Individual 500 µL glass syringes were then filled with these melamine standards followed by infusion into the ESI source of an Agilent 6340 series ion trap mass spectrometer (flow rate of 10 µL min^{-1}). The instrument was calibrated following the manufacturer guidelines and using Agilent ESI Tuning Mix (G2431A 100 ml acetonitrile solution for Ion-trap MS). For MS, a positive electrospray ionisation mode with nebulizer pressure at 103 kPa was employed. Nitrogen was used as the drying gas under a flow of 5 L min^{-1} and a temperature of 325 °C. Acquisition and analysis of data were performed with Agilent ChemStation LC and 6300 Series Trap Control (version 6.2). Library building and spectral matching were conducted using DataAnalysis™ and LibraryEditor™ software (Bruker Daltonik GmbH). ESI-MS conditions were initially optimised by directly infusing melamine standard (0.1 – 200 ppm) and varying the amplitude for both MS^2 and MS^3. The optimised conditions for the MS^2 fragmentation of precursor ion [m/z 127] was determined to have an amplitude of 0.5 and the optimised conditions for MS^3 fragmentation was determined to be an amplitude of 0.4.

2.3 Results and Discussion

2.3.1 Substrate Fabrication

2.3.1.1 Preparation of "soda" can

A polished soda can (cf. methods section) was used as a template on a melted pre-polymer generating a randomly nanostructured surface, illustrated schematically in Figure 2.2 (a). After the templating process, the cooled polymer was released from the glass support and the Al template easily peeled away to yield a flexible transparent polymer base, Figure 2.2 (b-c). Ag was then thermally deposited (30 nm) onto these nanopatterned polymer substrates to complete substrate fabrication. Fabrication of the Al master included removing the Al can's outer print using rough sandpaper. This process yielded micron-sized scratches across the Al master's surface. Substrates prepared with this type of Al master produced negligible Raman enhancement, as a result of the large surface roughness, and in turn, the lack of nano-sized hot spots. The introduction of polishing steps (alumina slurry polish, followed by a NaOH wash) smoothened the surface and greatly reduced the micron-sized scratches formed from the sanding, illustrated in Figure 2.3. Subsequently, this prepared Al master was used to template (or imprint) a melted polymer, in order to replicate the Al surface morphology. Once cooled, hardened, and the Al master removed, the polymer revealed a nano-patterned surface which produced a considerable SERS effect. Visual inspection of the fabricated SERS substrates displayed a uniform non-reflective surface. By contrast, un-templated "smooth" control substrates displayed a mirror finish following Ag deposition.
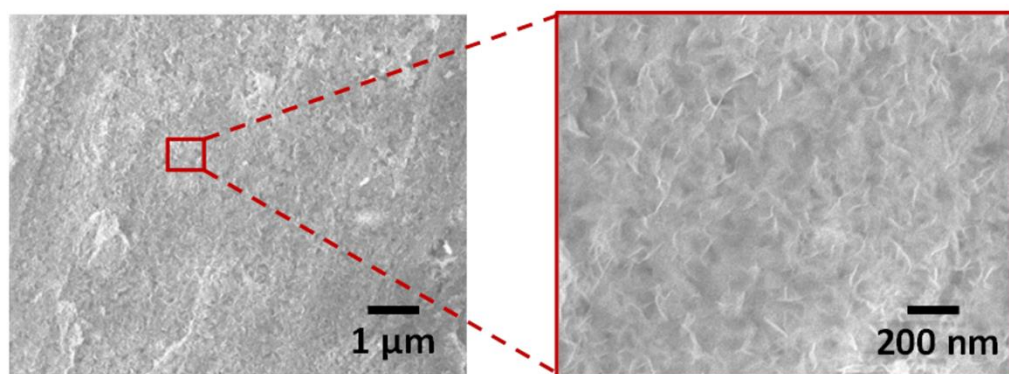
Figure 2.3: SEM of Al Master template after sanding and polishing steps.

2.3.1.2 *Analysis of alternative base polymers*

Three different polymers PVDF, PS and PDMS were assessed for fabrication of the SERS substrate. PDMS was chosen as it is a well-characterised material that is well known to replicate and template nanostructure surfaces.[57, 58] Similarly, PS has also been previously employed to template nanostructures[25] as it is known to form rigid homogenous surfaces. PVDF was selected as it is a known piezoelectric polymer.[59] SERS analysis was first undertaken on the bare Ag substrates, Figure 2.4, i.e. no molecule deposition. This allows the examination the Raman active modes of the three selected polymers. Then we employed both CrV and 4-ABT to compare and evaluate the SERS properties of each polymer substrate. Characteristic SERS spectra were obtained for both molecules from the three polymer substrates, see Figure 2.5.
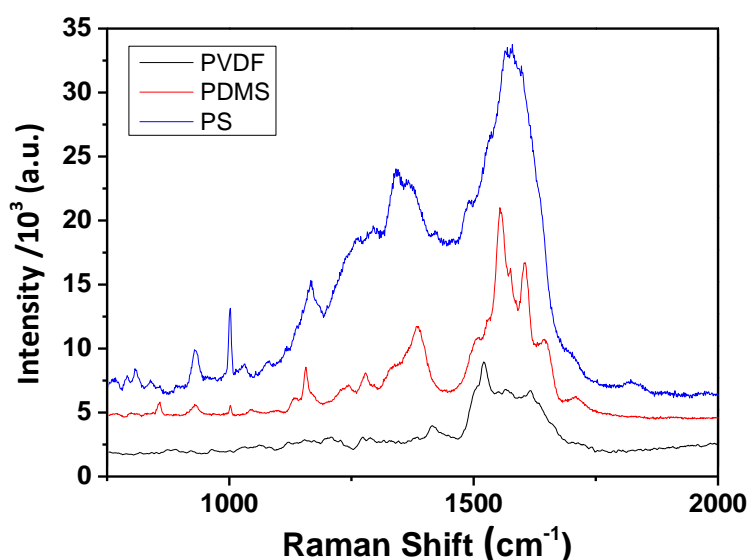
Figure 2.4: Comparison of bare polymer SERS spectra for PDMS, PS and PVDF substrates.

The SERS background spectra of the polymers (PVDF, PS and PDMS) are shown in Figure 2.4. The PS is more SERS active than the other two polymers. We predicted that this large polymer background signal would interfere with the SERS scattering from any deposited molecule on the substrate surface, hence quenching its signal. This prediction is supported by the SERS response observed for PS in Figure 2.5 (red spectra). Visually, all three polymers produced the same roughened Ag surface from the Al master; however the SERS responses were not equivalent. It was observed that the more SERS active the

actual polymer was, the more it interfered with the SERS response of the deposited molecule. The PDMS polymer exhibited high signal enhancement (blue spectra), similar to PVDF (green spectra), whereas the PS produced a considerably weaker signal (red spectra).
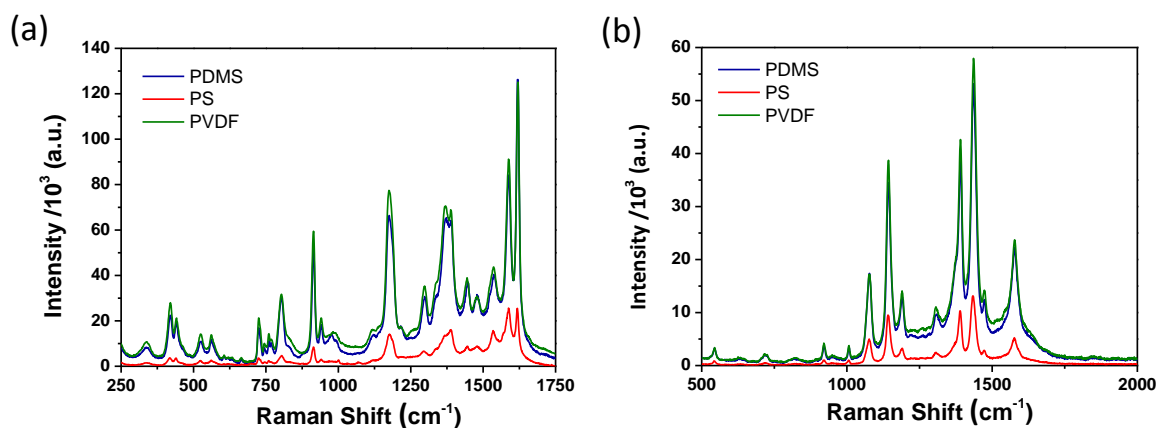
Figure 2.5: SERS spectra of (a) 10^{-6} M CrV and (b) 10^{-4} M 4-ABT. Comparison of Al templated polymers: PDMS, PS and PVDF, all with 30 nm Ag and 50µl drop of CrV solution. The SERS intensities were an average of 6 different measurements of laser power 7×10^4 W/cm².

To establish the optimum polymer for use in fabrication; characteristics of the polymer substrates were examined: The robustness of the resulting substrates was inspected and a scotch tape test was undertaken to confirm silver metal adhesion to the polymers. In this approach, scotch tape was stuck onto and peeled from the Ag coated nanostructured surfaces. The PDMS showed poor adherence of metal to its surface, resulting in the metal being easily rubbed off, damaging the substrate beyond use. The PDMS was disregarded for future fabrication. No degradation or removal of the Ag metal was observed for PVDF substrates and similarly, excellent adhesion of metal to the PS surface was seen. However the resulting SERS response of CrV and 4-ABT for the PS substrates, illustrated by the red spectra in Figure 2.5 (a and b), was considerably weaker compared to the other polymers tested. PS substrates were also rigid but fragile and easily shattered under stress. Consequently, PVDF was selected as it produced the best SERS surface for substrate fabrication and provided the largest intensity enhancement for both molecules.

2.3.1.3 Characterisation of PVDF substrate

Figure 2.6 shows a typical SEM micrograph of a portion of a fully prepared polymer substrate following Ag deposition. From SEM analysis the size distribution of the Ag nano-structures was estimated to be roughly 60 ± 20 nm while the gaps between the clusters were estimated to be on the order of 10 ± 5 nm (inset Figure 2.3 (b)) with the Ag nanostructures uniformly distributed over the entire polymer surface. These well-defined structures, comprising such small separations between clusters, are expected to deliver a high yield of hot-spots, making them very attractive and suitable for SERS sensing. To explore if these small gaps were sufficient to create electromagnetic hot spots and thus enable enhanced SERS response, experiments were undertaken.
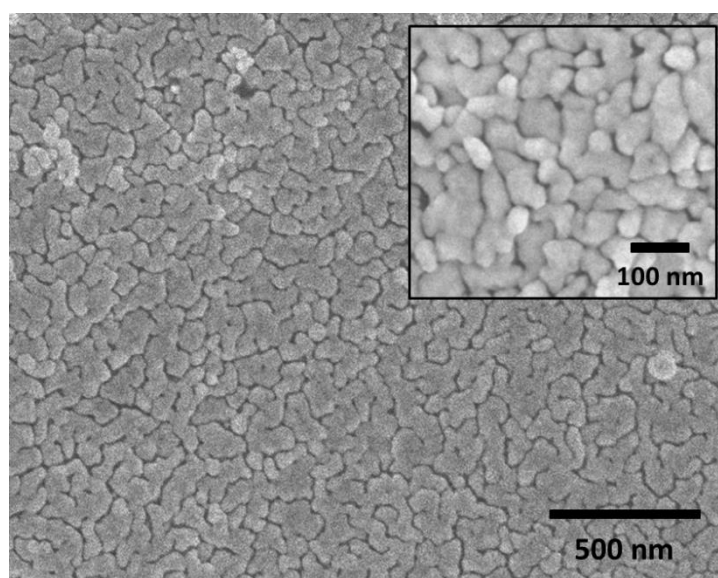
Figure 2.6: SEM image of a templated polymer (PVDF) substrate with 30 nm of Ag deposited over the surface. Inset: same substrates at a higher magnification

2.3.1.4 Using Aluminium master as a Substrate

Experiments were undertaken using the Al master as the substrate base, thereby eliminating the polymer step. Hence, Ag was deposited directly onto the polished Al surface. Figure 2.7 shows a comparison between the Al substrate (red spectrum) and a PVDF substrate (black spectrum). There was a slight SERS response from the nanostructured Ag on the Al metal; however the spectrum has significant differences when compared to the polymer substrate. We suspect that the presence of the aluminium under the thin silver layer is interfering with the SERS response. Although the correct

117

wavenumbers were maintained for the vibration modes of CrV on the Al substrate, there was a large amount of background noise in the spectrum. Weak signals were observed for the strongest CrV vibrations modes at 1620, 1386 and 915 cm^{-1} from the Al sample and a number of characteristic CrV peaks are not detected. We predict that, because the aluminium is not a plasmonic metal and is present in large quantities (approx. 1 mm) under the 30 nm silver layer, it is quenching the electromagnetic SERS effect from CrV, resulting in a reduced SERS response.
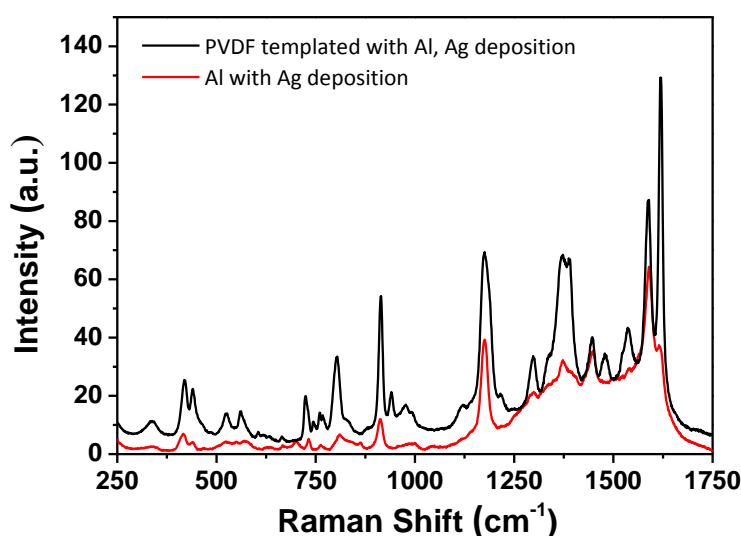
Figure 2.7: Spectra of 10^{-6} M CrV on (i) a silver coated Al template (red) and (ii) silver coated, Al templated PVDF substrates (black).

2.3.1.5 *Alternating Thickness of Silver Overlayer*

Further experiments assessing the effect of SERS responses with different silver thickness (10, 30 and 50 nm) on PVDF are shown, see Figure 2.8. The metal deposition technique is a slow process to allow the silver deposit uniformly on the surface of the nanostructured PVDF. SERS measurements of CrV and SEM analysis were used to investigate the different Ag film thicknesses. The spectra in Figure 2.8 were obtained by averaging 6 spectra from random locations on each substrate. SEM analysis of the 10 nm Ag substrates showed large separations between Ag clusters, due to the small amount of Ag deposited, leaving large areas of uncovered polymer and an absence of hotspot creation. As expected, the spectra obtained from different locations varied significantly and

produced very little SERS enhancement (see Figure 2.8 (a-b)). SEM analysis of the 50 nm Ag substrates showed an almost continuous film with a small number of separations visible. The corresponding spectra exhibited lower SERS enhancement compared to the 30 nm thick films, due to the lack of hot spots (see Figure 2.8 (c-d)). The 30 nm substrate SEM images revealed a homogeneous Ag layer across the nanostructured polymer surface, and the corresponding spectra exhibited excellent SERS responses, proving the optimum thickness for these substrates.
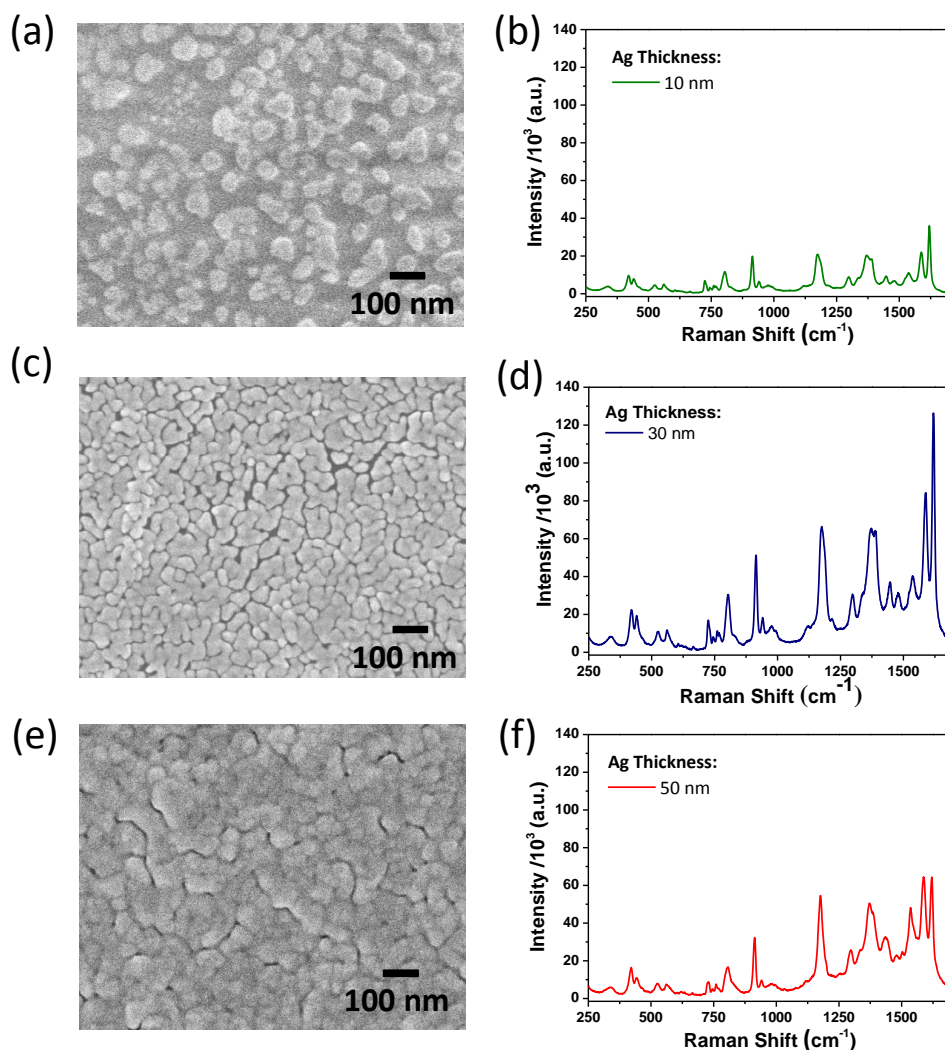
Figure 2.8: SEM images of Al templated PVDF substrates with (a) 10 nm Ag (c) 30 nm Ag and (e) 50 nm Ag; and (b,d,f) corresponding SERS spectra of 10^{-6} CrV on each substrate respectively.

2.3.2 Simulation Analysis

Concerning the 30 nm thick Ag deposited films, Figure 2.9 (a) shows a typical SEM image of a portion of a substrate. Dr. Pierre Lovera undertook these simulations. The dimensions of the Ag clusters were roughly 60 ± 20 nm while the separations between the clusters were estimated to be 10 ± 5 nm. Finite element method simulations were undertaken to explore if these metal-dielectric-metal nanogap structures were sufficient to produce localised significant electric field enhancements and consequently act as hotspots when illuminated with incident light (514 nm). A portion of a SEM image highlighted by the dashed box in Figure 2.3 (a) was imported and rendered in Comsol Multiphysics™ see Figure 2.9 (b). Figure 2.9 (c) shows the total electric field map 2 nm above the surface when the sample is illuminated with a light polarised along the y-axis. As can be seen, a very high electric field ($E \sim 10^8$ V/m) is concentrated on the edges of the Ag nanoclusters that are perpendicular to the axis of polarisation of the incident light
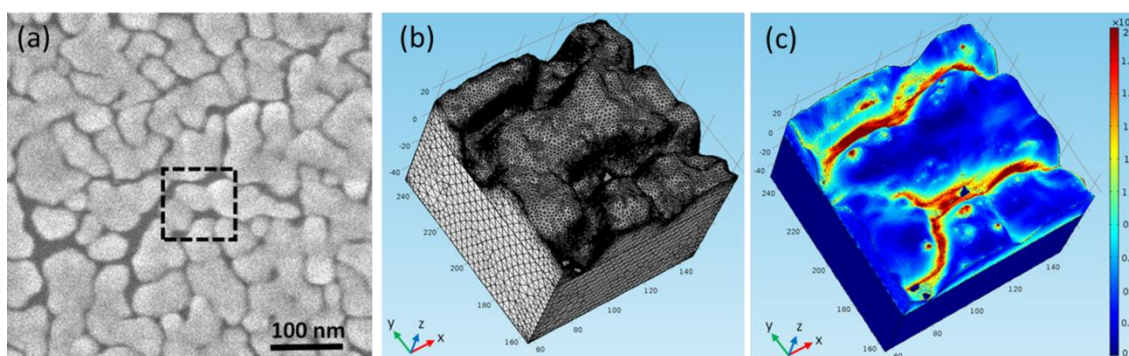
Figure 2.9: (a) SEM image obtained from a PVDF substrate coated with 30 nm Ag. (b) 3D geometry constructed by intersecting the parametric surface from the SEM image with blocks using COMSOL (c) FEM simulation showing highly localised electric field enhancements at the metal-dielectric-metal nanogap structures. To avoid possible artifacts at the interface metal/dielectric, the image shows the total electric field at a distance of 2 nm above the surface of the sample. (This work was undertaken by Pierre Lovera, Tyndall National Institute)

A cross section of the substrate, shown in Figure 2.10, demonstrates that the field enhancement is not confined to the surface of the nanoclusters but rather extends to the whole gap. This is characteristic of coupling of the individual localised surface plasmon modes of the adjacent nanoclusters. These simulations confirm that the substrates fabricated using the template technique should be sufficient to create nanogaps that will,

on illumination, create electromagnetic hot spots and that most of the SERS signal recorded from the sample will originate from molecules located in these nanogaps.
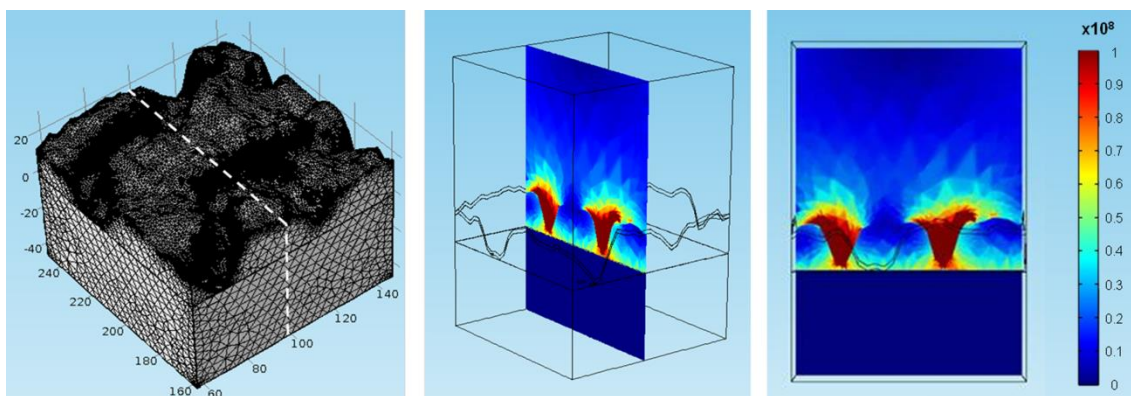
Figure 2.10: A cross section through the sample shows that the field enhancement is not confined to the surface of the nanoclusters but rather extends to the whole gap.

2.3.3 Spectroscopic Characterisation

2.3.3.1 Background Control Experiments

To validate the simulation model and confirm that the origin of the observed SERS responses arose from the metal-dielectric-metal nanogap structures, a number of control experiments were undertaken. Figure 2.11 (a) shows the front "top excitation" response for a 10^{-6} molar solution of CrV dropped and dried on a nanostructured silver coated PVDF substrate, and the corresponding control measurements: (i) smooth substrates prepared by depositing 30 nm of Ag onto smooth PVDF films, i.e., no templated nanostructures and (ii) Ag-coated nanostructured PVDF samples in the absence of CrV. No appreciable Raman signals were observed from the control experiments (black and green spectra, respectively).   By contrast, spectra recorded using Ag coated nanostructured PVDF substrates in the presence of CrV (blue spectrum) show a significant SERS response. This confirmed that the witnessed response was a SERS response and not a bulk Raman measurement arising from crystals potentially formed during the drying process. Such results strongly support the simulation model suggesting that the nanogap structures between nanostructured Ag clusters created hotspots for efficient SERS enhancement to occur.
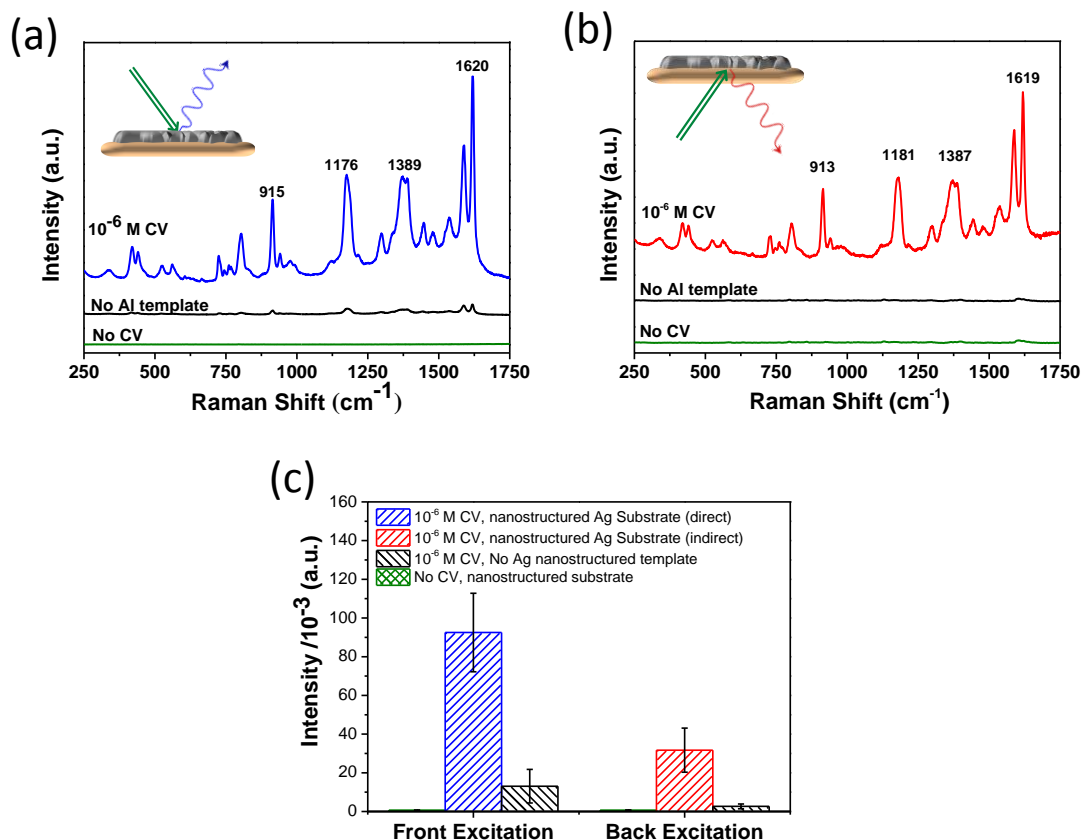
Figure 2.11: Front (a) and back (b) excited SERS spectra of 10^{-6} M CrV from substrate with 30 nm Ag, with the presence (blue) and absence (red) of the aluminium template. Raman spectrum of CrV in the absence of a deposited silver overlayer (green). (c) Chart illustrating the front and back excitation results for the control experiments

2.3.3.2 Raman Analysis of Crystal Violet

To examine the SERS effect further, the SERS spectral peaks were compared to those exhibited in the Raman spectrum from the bulk CrV material. The intensity of the SERS enhancements of particular Raman modes depends on the formation of, and interaction, between the silver surface and the adsorbed molecule.[18],[60]. The Raman spectrum of pure bulk crystal violet solid state illustrates the characteristic peaks of CrV, observed at 913, 1176, 1376 and 1618 cm^{-1} were in accordance with the reported values[12, 61]. These peaks were assigned in Table 1.

Normal Raman (cm^{-1}) CV powder	SERS 514 nm (cm^{-1})	Vibrations contributing to the Normal mode	Benzene Mode
1618	1620	-	8a
1586	1588	-	8a
1536	1538	$\nu(C_{ring}N) + \delta_s(CH_3)$	8b
1478	1478	$\delta_{as}(CH_3)$	19a
1444	1446	$\delta_{as}(CH_3)$	19b
1376	1389(d)	$\delta(CH) + \delta_s(CH_3) + \delta(CCC)_{ring}$	$\nu_{as}(\varphi\text{-}N)$
	1369(d)	$\nu_{as}(CC_{center}C) + \delta(CCC)_{ring} + \delta(CH)$	$\nu_{as}(\varphi\text{-}N)$
1302	1297	$\nu_{as}(CC_{center}C) + \delta(CCC)_{ring} + \delta(CH)$	-
1176	1175	$\nu_{as}(CC_{center}C)$	9a
940	941	$\rho_r(CH_3) + \nu(CN)$	1
913	915	$\delta(CC_{center}C)$	17a
804-810 broad	804	-	10a
761	759	$\nu_s(CC_{center}C) + \nu(CN)$	6a
724	724	$\nu(CN)$	4
561	561	$\gamma(CCC) + \delta(CNC) + \delta(CC_{center}C)$	6a
523	525	$\delta(CNC)$	16b
437(d)	440	$\delta(CNC)$	16a
419 (d)	419	$\delta(CNC) + \delta(CC_{center}C)$	16a
335	337	$\gamma(CNC) + \rho_r(CH_3)$	$\delta(\varphi\text{-}C\text{-}\varphi)$
206	208	$\tau(CH_3)$	Breathing $\nu(Ag\text{-}N)$

Table 1: Raman and SERS vibrational assignments [ν, stretching (s, symmetric; as, asymmetric); δ and γ, bending; τ, torsion ;} symbolises a doublet (d)]

Angeloni *et al.* demonstrated that aqueous solutions of CrV show a maximum absorption at 590 nm.[62] The Raman system used in these experiments, equipped with a 514 nm laser, theoretically could further increase the intensity of the Raman scattering due to resonance effects of the CrV molecule at this wavelength. Before qualitatively analysing the CrV detection, we employed a non-resonant molecule, 4-ABT, which does not exhibit any resonance Raman effect at 514 nm, to accurately estimate and compare the SERS capabilities of the substrate for both molecules, in the following section.

2.3.3.3 SERS Enhancement Factor

To evaluate the SERS capabilities of the substrate, we have estimated the enhancement factor (EF) based on experimental values of the Ag substrate by comparing the SERS and Raman intensities of the CrV vibrations at 1620, 1175 and 913 cm^{-1} from Figure 2.11 (a),

see Table 1. When considering these spectra, we calculated that there is approximately 10^6 fold enhancement in intensity. The EF values were calculated using the following equation:[63]

$$EF = \frac{I_{SERS} / N_{SURF}}{I_{NR} / N_{VOL}}$$

(Equation 2.1)

Where, I_{SERS} and I_{NR} are the intensities of the chosen vibrational bands (state above), from the SERS spectrum and the normal Raman spectrum, respectively. N_{SURF} represents the number of CrV molecules adsorbed to the SERS substrate that are illuminated by the laser spot (in the scattering volume), and N_{VOL} represent the number of CrV molecules illuminated by the laser in the bulk CrV powder. The number of CrV molecules in powder (N_{VOL}), illuminated by the laser spot, was calculated using the same method as Yoon *et al.*[64] We consider the laser as a cylinder with diameter ~0.836 μm (equation 2) and penetration depth ~20 μm into the bulk CrV.[25]

$$d_l = \frac{1.22\,\lambda}{NA} = 0.836\ \mu m$$

(Equation 2.2)

Where NA is the numerical aperture (0.75) of the 50x lens and λ is the wavelength of the laser (514 nm). Assuming that the volume of a cylinder represents the laser illumination volume ($\pi r^2 h = 1.097 \times 10^{-11}\ cm^3$) and using the density (1.19 g/cm^3), N_{VOL} is estimated as 1.93×10^{10} molecules.

To calculate N_{SURF}, the distribution of CrV molecules on the substrate surface must first be identified. Sasai *et al.* reported that Rhodamine 6G (R6G) molecule occupies an area of ~0.4 nm^2 when adsorbed in a perpendicular orientation on a surface.[65] The size of a CrV molecule is very similar to the size of R6G ~4 nm^2,[41] so we can assume that one CrV molecule occupies approximately 0.4 nm^2 on the silver surface. Taking into account the volume of CrV solution deposited onto the surface (50 μL) we estimate that this drop contains 3×10^{13} CrV molecules. We also calculated that the drop occupies a surface area of 0.164 cm^2; however, the surface area probed is larger than calculated due to its nanostructured roughness. A roughness factor of ~2 was evaluated from Atomic Force Microscope (AFM) measurements from Equation 2.3:

$$\frac{\text{image surface area}}{\text{image projected surface area}} = 2$$

(Equation 2.3)

Taking the surface roughness into account, the actual surface area available for adsorption is 0.328 cm^2. If all of the molecules present in the drop adsorb to the surface, due to the size of the CrV molecule, formation of a monolayer is not possible because an area of 0.328 cm^2 requires 8.2×10^{13} CrV molecules for full coverage. Subsequently, we assume a uniform distribution of CrV molecules on the substrate and therefore the number of molecules in the area occupied by the laser spot (5.51×10^{-9} cm^2) was estimated as 5.03×10^{5} molecules. The EF formula can therefore be written, based on Equation 2.1, as:

$$EF = \frac{I_{SERS} / 5.03\times10^{5}}{I_{NR} / 1.93\times10^{10}}$$

(Equation 2.4)

For the peak at ~1620 cm^2 the intensities for SERS and Raman are 126215 a.u. and 2008 a.u. respectively. Therefore we evaluate the enhancement factor for the vibration at 1620 cm^2 as 2.41×10^{6}. The vibrational band at 1175 cm^{-1} had an I_{SERS} value of 66016.6 cm^{-1} and an I_{NR} value of 1558 cm^{-1}. The vibrational band at 913 cm^{-1} had an I_{SERS} value of 51063.6 cm^{-1} and an I_{NR} value of 1433.29 cm^{-1}. The enhancement factors were calculated to be 1.62×10^{6} and 1.36×10^{6} respectively. Such enhancements compares well with the literature.[41, 66, 67] It should be noted that the measured enhancement corresponds to an average enhancement over the probed area (1 micron spot). Within this area, some hot spots have high enhancement while other ones have lower ones.

The enhancement factor for 4-ABT was calculated in a similar way: I_{SERS} and I_{NR} were selected from the Raman intensities at the peaks, 1620, 1175 and 913 cm^{-1}. N_{VOL} was calculated in the same way as for CrV because the same instrument and parameters were used, however taking into account the density and molecular weight of 4-ABT (1.18 g/L and 129.19 g/mol respectively), N_{VOL} was estimated as 6.23×10^{10} molecules. The calculation for N_{SURF} was slightly different as the 4-ABT was not prepared in an aqueous solution so the hydrophobicity of the surface is not a factor. When dropped onto the surface it forms a film over the entire surface (0.5 cm^2), as opposed to a spherical drop which was the case with the CrV. One 4-ABT molecule occupies an area of 0.2 nm^2 as reported by Kim *et al*. Theoretically 2.5×10^{14} 4-ABT molecules are needed to form a

monolayer over the silver surface, but taking the surface roughness of ~2 into account, the substrate needs 5×10^{14} molecules for full coverage. We used a concentration of 10^{-4} M 4-ABT and a volume of 50 μL on the 0.5 cm^2 substrate, which contains 3.011×10^{15} molecules, thus a monolayer was achieved on the surface. Correspondingly, N_{SURF} is calculated for a monolayer of laser spot area (5.49×10^{-9} cm^2) as 5.94×10^6 molecules. The enhancement factors therefore for peaks at 1437, 1391 and 1142 cm^{-1} were calculated as 2.77×10^6, 2.24×10^6 and 2.15×10^6 respectively, from Equation 2.1. With this procedure, the enhancement factor for 4-ABT can be calculated for any peak using the SERS and bare Raman spectra.

It was found that the SERS intensities and EF values for the non-resonant 4-ABT were similar to those of CrV, thus we consider the SERS substrate employed in this study to have excellent SERS properties for both resonant and non-resonant molecules.

2.3.4 Back Excitation SERS

A key advantage of the Ag coated PVDF substrates is that they are optically transparent in the visible spectrum which enables back excitation (though substrate) SERS measurements to be undertaken. Such a capability is important for many industrial in-line process analytical monitoring techniques (PAT) used in smart manufacturing 4.0 approaches. Back excitation SERS measurements, i.e. illumination and collection through the back facet of the substrate were described earlier, see Figure 2.11. A typical SERS spectrum using back excitation from 10^{-6} M CrV (red spectrum) is shown and exhibited characteristic spectral peaks at 914, 1176, 1376 and 1618 cm^{-1}. In the absence of CrV (green spectrum), there is a weak signal contribution from the PVDF, but it does not cause any significant SERS interferences, as expected from the front excitation experiments in Figure 2.5. Figure 2.11 (c) shows a direct comparison between the front and back excitation intensities for the peak at 1620 cm^{-1}. Although there was a threefold decrease in the measured intensity (compared with front excitation), since these spectra were acquired through a thick PVDF base, (3 mm) we believe that if thinner substrates were employed (by optimising the fabrication process further), reduced light scattering within the substrates would result in a larger measured SERS enhancements.

To explore back excitation further, a 50 µL droplet of CrV (10^{-6} M) was deposited onto a substrate and overlaid with a glass coverslip to form a fluid-type cell with a thickness of ~ 100 µm, see inset image of Figure 2.12 (b). If the molecule was simply dropped on the surface and allowed dry, due to the surface hydrophobicity, there would be very little wetting and we would observe localised pre-concentration of the target analyte on the Ag surface.[25, 68] In this case, we spread the droplet across the Ag surface using the cover slip, i.e. undertaking the SERS measurements through the back of the polymer with liquid on the metal surface. We believe that as the liquid dries, the CrV molecules can pre-concentrate in the remaining liquid, and that the slow the evaporation process allows the CrV molecules to adsorb more evenly across the entire surface. A number of SERS spectra were acquired (in the same position) through the polymer substrate over a 45-minute time frame. Figure 2.12 (a) shows a waterfall plot of CrV spectra. During these experiments, a SERS response was observed after 1 minute and, as expected, higher SERS signal intensities were observed with increasing time and eventually saturated. Figure 2.12 (b) illustrates a plot of peak area (913 cm^{-1} calculated using a Lorentzian function) vs. time; yielding a linear relation (R^2 of 0.98). We suggest that the increase in signal arises from the adsorption of the CrV molecules to the metal surface, as the droplet dries. The ability of these substrates to undertake SERS in liquid samples supports the suggestion that these transparent polymer substrates could find use in future in-line measurement applications required in PAT. This ability to undertake back excitation SERS could also open up other new remote sensing application areas if, for example, the substrates are integrated with optical emitters or at the end of optical fibres such enabling, e.g., *in-vivo* measurements or used for in-line measurement.
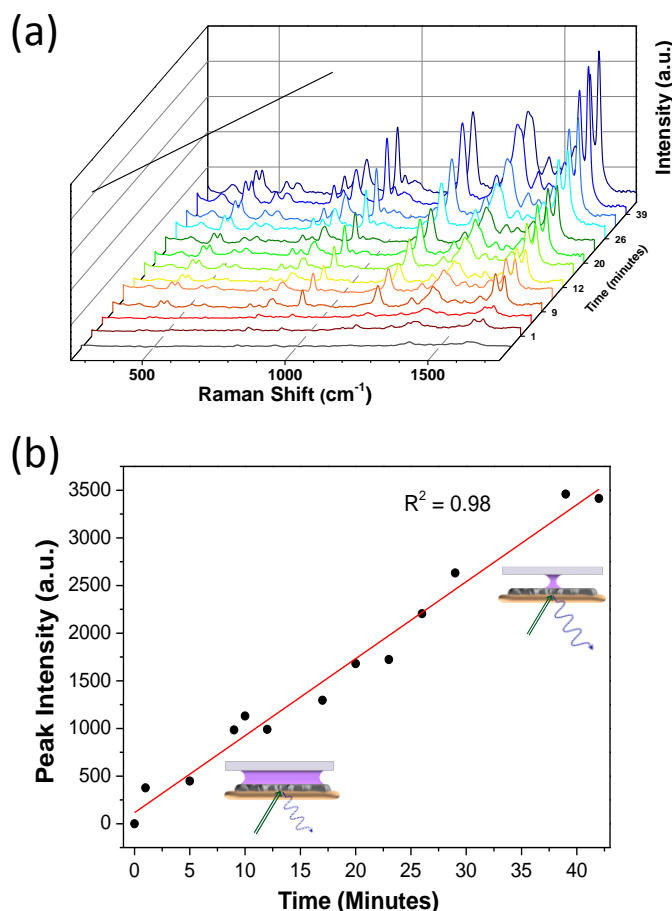
Figure 2.12: (a) Waterfall of SERS spectra recorded for 10^{-6} M CrV in solution in a single spot over 45 minutes (b) Graph showing the linear relationship between peak area (at 913 cm^{-1}) vs. droplet drying time.

2.3.5 SERS Quantitative Detection of Crystal Violet

To explore the suitability of these substrates for highly sensitive measurements, a series of CrV standards ranging from 10^{-7} to 10^{-10} M were prepared in DI water and deposited via the drop/dry process on the substrates. SERS spectra were obtained by measuring and averaging five different locations on pristine substrates. Data were collected using a 50x magnification (0.75 NA) objective microscope, with an acquisition time of 10 s, over a spectral range of 200 cm^{-1} to 2000 cm^{-1}. The averages of the five spectra for each concentration were plotted and typical spectra are presented in Figure 2.13 (a). As illustrated, all the characteristic CrV peaks are well defined even at such low concentrations (5 x 10^{-10}). The vibration peak at 915 was selected for calibration

measurements, the peak area for the averaged spectra for each standard was determined using a Lorentz function in Origin® 7.4 (OriginLab) and plotted versus log of concentration to obtain a quantitative calibration curve, see Figure 2.13 (b). Regression analysis was then undertaken Origin® 7.4 (OriginLab) and a correlation coefficient (R^2) of 0.9791 was determined with a measured limit of detection of 5 x 10^{-10} M. The results show that the SERS substrates permit rapid analysis times (~10 min from sample deposition). To evaluate the reproducibility and homogeneity of the substrates, Figure 2.13 (c) shows a waterfall graph for at 48 spectra (10^{-6} M CrV concentration) taken from 4 random locations in grids of 10 μm^2 (12 spectrum per grid) on a single substrate (north, south, east and west separated by 5 mm). The relative standard deviation for each of the peaks; 1620, 1587, 1174 and 913 cm^{-1}, were calculated as less than 15%.
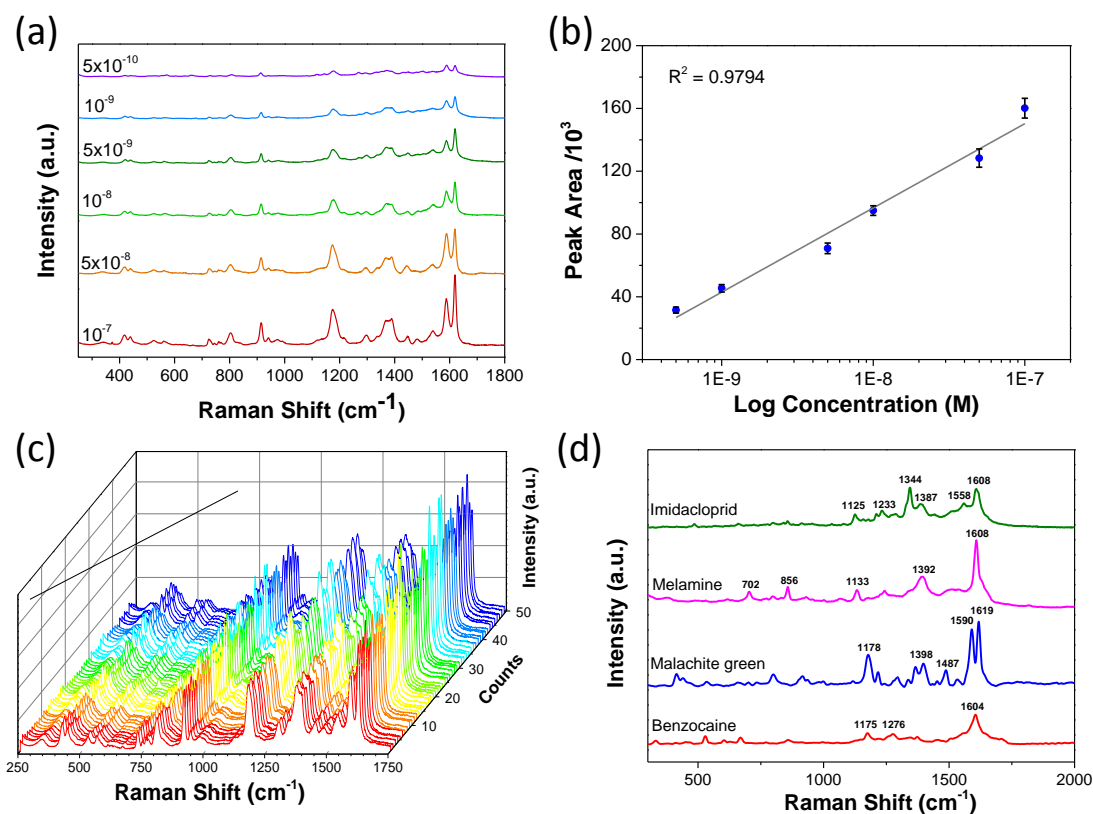
Figure 2.13: (a) SERS spectra recorded for different CrV concentrations ranging from 5 x 10^{-10} M to 1 x 10^{-7} M (204 pg/mL –40.8 ng/mL). (b) Graph showing semilog linear relationship between peak area (at 915 cm^{-1}, calculated using a Lorentzian function) and concentration of CrV (c) 48 separate SERS spectra (10^{-6} M CrV concentration) taken at 4 random locations on a single substrate (north south east and west separated by 5 mm) in grids of 10 μm^2 illustrating substrate surface homogeneity. (d) SERS spectra of four representative molecules: imidacloprid, melamine, malachite green and benzocaine.

2.3.6 Substrate Versatility and Stability

An essential characteristic of SERS substrates is maintaining their stability over time as well as in different media. To evaluate the versatility of the SERS substrate, various chemicals were analysed from different application fields; imidacloprid (neonicotinoid pesticide), melamine (previously used as a food adulterant), malachite green (agricultural antibiotic) and benzocaine (pharmaceutical molecule), see Figure 2.13 (d). The characteristic SERS peaks of all four molecules, in aqueous solution at a concentration of 10^{-6} M, are clearly resolved and correlate well to those reported in the literature. [36, 69-72] The stability of the PVDF polymer substrates was also assessed. PVDF has outstanding resistance to a wide range of chemical reagents as well as excellent heat stability; typical of fluorocarbon polymers. Regardless of this, experiments were carried out to test the polymer substrate's stability in various aqueous and organic solutions. Substrates were found to be stable following immersion in a wide range of acids (acetic, nitric, hydrochloric sulfuric and phosphoric acids) as well as most bases. They also upheld their integrity after prolonged exposure to both polar and non-polar solvents (methanol, ethanol, DMSO, toluene and hexane) for up to 20 minutes. However, a notable exception was that PVDF had low resistances to sodium hydroxide and acetone. Exposure to these solutions caused breakdown of the polymer base and deformation of the Ag surface.

2.3.6.1 Substrate Reusability

Another key quality in modern-day sensing platforms is the ability to reuse them. It was found that a single Al master can be re-used to template multiple PVDF SERS substrates. Following fabrication and characterisation of the PVDF substrates, a second PVDF replicate was cast using a previously used Al master and coated with 30 nm silver layer. Figure 2.14 (a) shows spectra from both the pristine and re-used Al master. Although there is a slight change in the intensity of the spectrum obtained from the second replicate sample, the close reproducibility of the data indicated that the templating procedure does not damage the aluminium and suggests that one Al master may be used multiple times. This is of significant advantage as the substrates could be re-used. Similar experiments were carried out where the substrate was cleaned and re-used. Substrates were also cleaned using a combination of a sonicated solvent wash (isopropanol and ethanol, 5 mins each) followed by exposure to UV-ozone (20 min at ambient pressure) and re-used

for analysis of 10^{-6} M CrV (at least four times) without any signal degradation, see Figure 2.14 (b). To avoid cross contamination and maintain a controlled experiment, the same volume and concentration of CrV was maintained and then characterised for comparison. The graph shows that the substrate itself can be re-used if required.
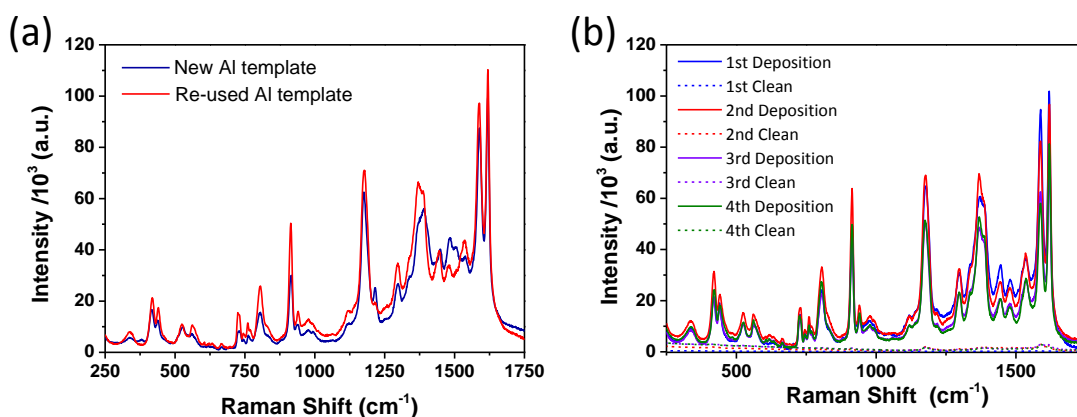
Figure 2.14: (a) SERS spectra showing the reproducibility of the substrates by demonstrating that the Al template can be reused after peeling of the polymer. (b) Showing that the SERS substrates can be re-used with minimal effect on the SERS response

2.3.6.2   SERS Detection of Glucose

The SERS substrates may also be applied to molecules, such as glucose, that have a poor binding affinity for the substrates Ag surface. In a manner similar to that reported by the Van Duyne group [45], a mixed self-assembled monolayer of mercaptohexanol and decanethiol was first employed to partition glucose from solution at a SERS sensor surface. The two thiols, having different length hydrocarbon chains, created "pockets" in the monolayer, shown schematically in Figure 2.15 (a), which promoted glucose partitioning to this modified surface via the formation of both Van Der Vaal and hydrogen bonding interactions. Figure 2.15 (b) shows a typical spectrum obtained for the as-deposited SAM layer (control sample, black spectrum) exhibiting a weak SERS response with peaks at 1122, 891 and 710 cm^{-1}. Following immersion in a 10 mMol glucose solution for 6 hours and air drying, a spectrum for the combined SAM / sequestered glucose layer was observed (dotted line spectrum). This spectrum contains vibrational peaks from both the SAM layer and glucose analyte.
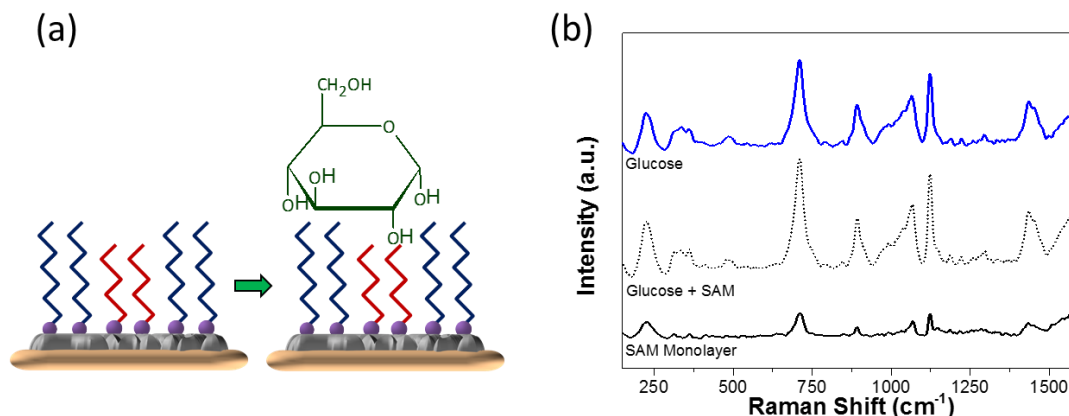
Figure 2.15: (a) Schematic showing partitioning of glucose at a mixed thiol surface and (b) SERS spectra of the mixed monolayer without (black line) and with (dotted line) glucose followed by background subtraction to show a glucose only spectrum (blue).

Finally, the glucose spectrum, obtained by subtracting the SAM spectrum from the combined glucose/SAM spectrum, is presented (blue spectrum). The resulting spectrum exhibited characteristic glucose peaks at 1434 1123, 1065, 912, 893, 710 and 542 cm^{-1}, which compare with both the literature and the characteristic Raman spectrum obtained from bulk glucose, see Figure 2.16.[73]
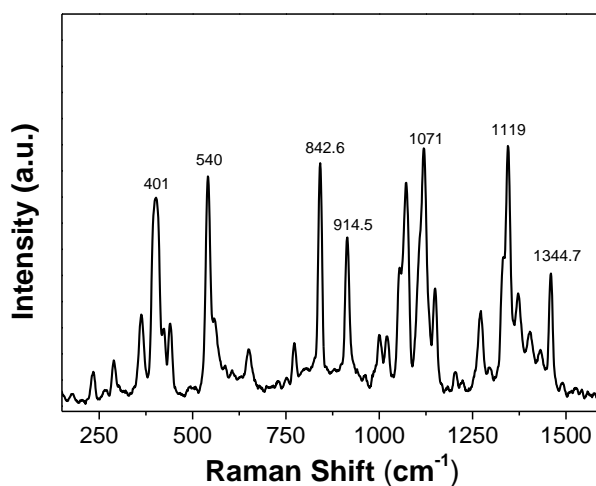
Figure 2.16: Bulk Raman spectrum recorded for pristine glucose powder on a glass slide. Characteristic vibration peaks are labelled.

2.3.6.3 SERS Detection of Melamine

Finally, a case study was undertaken to demonstrate the suitability of these substrates for real world applications, e.g. in food security. Melamine, a food adulterant, previously

used to falsify protein content in milk products in China[74, 75] and which is known to be difficult to detect was selected.[47] A typical SERS spectrum for 1 ppm melamine in deionised water is presented in Figure 2.17 (a). The characteristic peak observed at ~702 cm^{-1} in the SERS spectrum exists at 673 cm^{-1} in the Raman spectrum, and is attributed to the breathing mode and in plane deformation of the triazine ring,[76, 77] while the 855 cm^{-1} peak is attributed to the out of plane ring deformation.[78] Similar to the CrV spectrum, this shift can be attributed to melamine adsorption to the nanostructured Ag surface of the substrate. These peaks correspond well with reported values.[77]
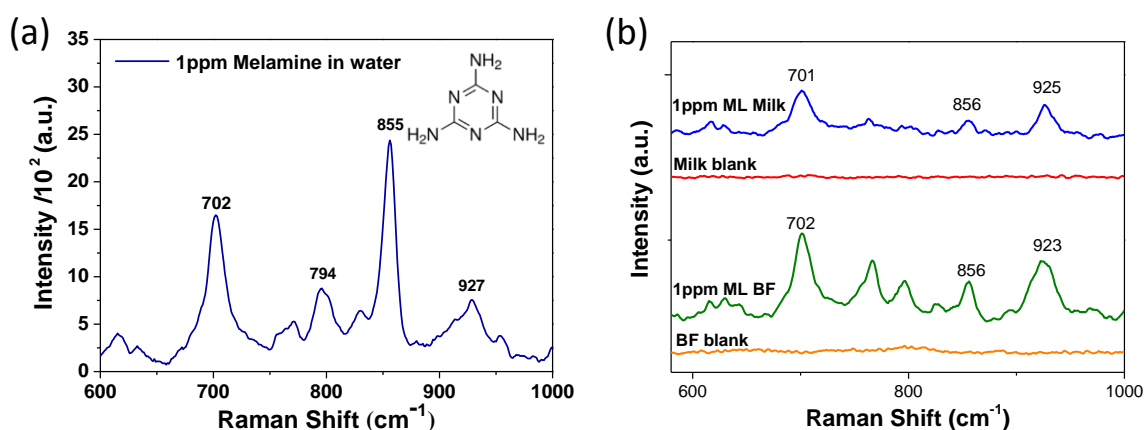
Figure 2.17: (a) SERS spectra of 1 ppm Melamine spiked in DI water (b) SERS spectra of 1 ppm Melamine spiked in (a) diluted whole milk and (b) infant formula, with no pre-treatment.

Figure 2.17 (b) shows spectra obtained from 1 ppm melamine-spiked into both milk and baby formula (diluted 1/100 as described in the experimental section). Control samples of diluted milk and baby formula were also analysed and the absence of SERS responses from these solutions showed that other large biomolecules (fats, proteins etc.) present in these solutions would not interfere with the melamine analysis By contrast, the melamine-spiked milk and baby formula samples exhibited characteristic melamine peaks, clearly distinguishable from the pristine solution spectra, confirming the presence of melamine even at very low concentrations, i.e., 1 ppm. A drop and dry approach was again adopted, the total analysis time was under 10 minutes and a LOD of 0.1 ppm was measured experimentally. These results suggest that these substrates may offer the possibility for the rapid detection of analytes in the field, with a limit of detection similar to gold standard laboratory-based techniques such as mass spectrometry.

2.3.6.4 *Analysis of Melamine with Mass Spectroscopy*

The SERS detection method was benchmarked against electrospray ionisation mass spectrometry (ESI-MS) in collaboration with the Cork Institute of Technology (CIT). The spiked melamine solutions were analysed with the MS, operated in single reaction monitoring positive mode, and the ion charge control function used to optimize both MS^2 and MS^3 fragmentation. Total ion count, MS^2 and MS^3 data were obtained.
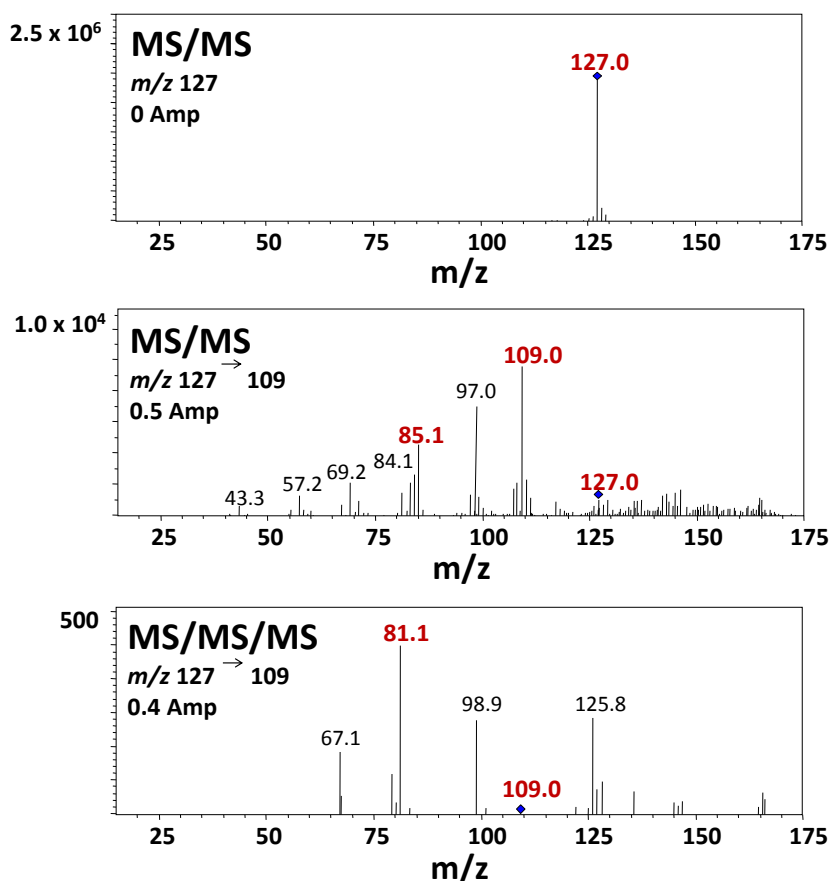
Figure 2.18: Mass spectra of melamine standard (0.1 ppm) spiked into deionised water and infused into the ESI source (heated) of an Agilent 6340 series ion trap mass spectrometer: (i) M^+H^+ precursor ion at m/z 127; (ii) MS^2 fragmentation of precursor ion at [m/z 127] to yield five predominant characteristic product ions at m/z 109, m/z 97, m/z 84, m/z 85 and m/z 69; (iii) MS^3 fragmentation of product ions at m/z 109 to yield the predominant product at m/z 81

Figure 2.18 shows MS^2 and MS^3 mass spectra obtained for the direct infusion of melamine standard (0.1 ppm) spiked into deionised water. Figure 2.19 shows MS^2 and MS^3 mass spectra obtained for the direct infusion of melamine standard (10 ppm) spiked in a diluted (1 in 10, DI) milk sample. MS^2 fragmentation of precursor ion at m/z 127 yielded five predominant characteristic product ions at m/z 109, 97, 84, 85 and 69 while

134

MS^3 fragmentation of product ions at m/z 109 yielded the predominant product at m/z 81. The spectra obtained for MS^2 and MS^3 for melamine correlated with spectra obtained in previously published studies.[79] In agreement with the SERS study, no trace of melamine was found in control pristine milk samples.
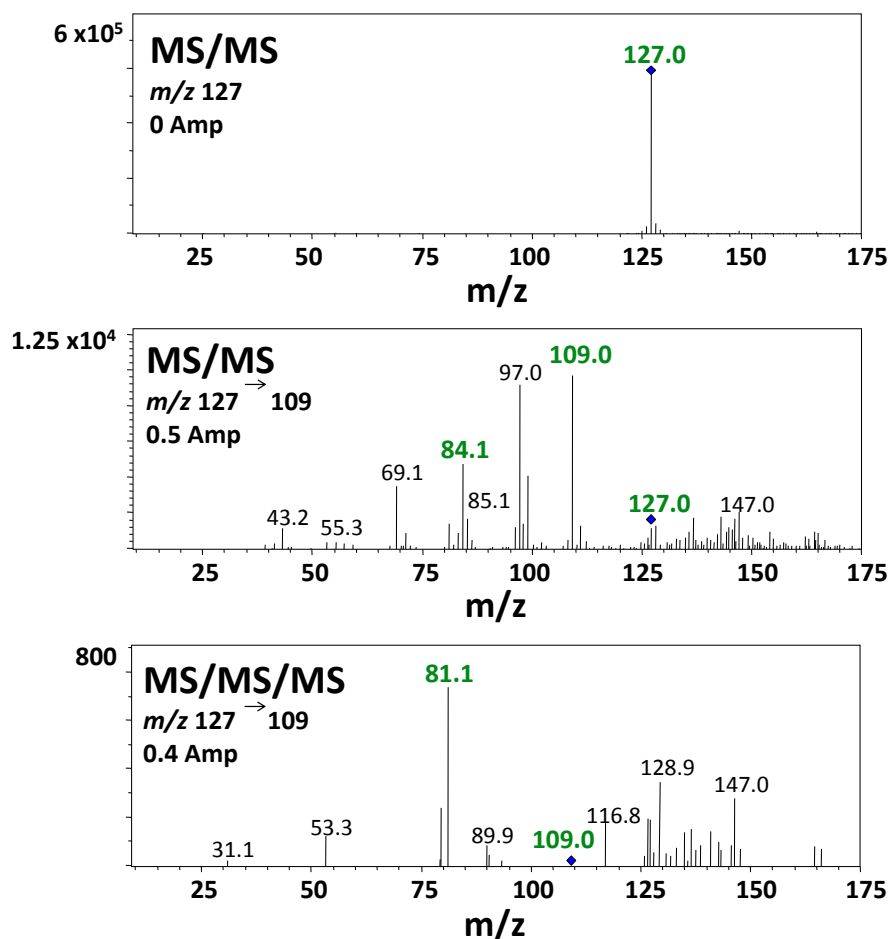
Figure 2.19: Mass spectra of melamine standard (10 ppm) spiked into 10% Milk sample and infused into the ESI source (heated) of an Agilent 6340 series ion trap mass spectrometer: (i) M$^+$H$^+$ precursor ion at m/z 127; (ii) MS^2 fragmentation of precursor ion at [m/z 127] to yield five predominant characteristic product ions at m/z 109, m/z 97, m/z 84, m/z 85 and m/z 69; (iii) MS^3 fragmentation of product ions at m/z 109 to yield the predominant product at m/z 81.

The SERS substrates exhibited a similar sensitivity to the ESI-MS data for melamine in water (LOD, 0.1 ppm) and for melamine detection in diluted milk samples (1 ppm). These results are very encouraging and demonstrate that our fabricated SERS substrates exhibit sensitivities comparable to the gold standard analytical technique. However, the ESI-MS samples did require the use of a syringe filter to remove any large interferences in the

milk including proteins and lipids that masked the melamine signal. SERS, on the other hand, had the ability to selectively detect melamine in spiked milk samples without complex sample pretreatment (due to the lack of a background signal). These results strongly support the assertation that SERS substrates offer the possibility for rapid and low-cost detection of target analytes in complex media, in remote settings.

2.4 Conclusion

In this chapter, we demonstrated the reproducible fabrication of a polymer based SERS substrate; nanostructured using a soda can as a template. The Ag coated PVDF exhibited strong SERS enhancement with good metal adhesion compared to PDMS and PS polymers. Simulations and control experiments confirmed that the Raman signal arose from the gaps ("hot spots") between the Ag clusters throughout the Ag layer. The substrates exhibited an enhancement factor of ~10^6 and that the signals observed with these substrates arose predominantly from an electromagnetic effect. The transparent substrates also permitted back excitation and collection through the substrate which corresponding spectra exhibiting clear and defined spectral SERS peaks. The versatility of the sensors was demonstrated by detection of a wide variety of analytes on pristine Ag surfaces. The sensors exhibited rapid, quantitative and high sensitivity, for example, 5 x 10^{-10} M (204 pg/mL) crystal violet detection in 10 minutes using a simple drop and dry method. We also show detection of glucose employing a chemically modified Ag surface bearing a pre-deposited SAM layer. Finally, we present the detection of trace amounts of melamine in complex media solution (milk and infant formula) and show the sensor sensitivity is comparable with commercial analytical instrumentation (MS-MS).

These transparent polymer substrates offer a number of advantages: (i) the simple manufacturing approach is scalable offering the potential for low-cost fabrication and thus widespread uptake and applicability. (ii) The fine metallic nanostructures provide SERS hot spots upon optical excitation. (iii) The substrates are transparent and thus are compatible with back excitation and collection allowing measurement in liquid environments to be undertaken. (iv) the flexible substrates may be easily integrated in-line or on-line adding to the suite of spectroscopic process analytical techniques. (v) Finally, the sensor may be chemically modified to widen the range of molecules that may be detected.

The SERS substrates described in this chapter show a substantial improvement in terms of cost and ease of fabrication as well as the SERS capability, compared to competitors in the literature, whom require the use of expensive, complex equipment and skilled personnel.

2.5 References

1.   Kong, J.; Chapline, M.G.; Dai, H., Functionalized Carbon Nanotubes for Molecular Hydrogen Sensors; *Advanced Materials,* **2001**, 13, 1384.

2.   Zheng, G.; Patolsky, F.; Cui, Y.; Wang, W.U.; Lieber, C.M., Multiplexed Electrical Detection of Cancer Markers with Nanowire Sensor Arrays; *Nature Biotechnology,* **2005**, 23, 1294-1301.

3.   Tarasov, A.; Gray, D.W.; Tsai, M.-Y.; Shields, N.; Montrose, A.; Creedon, N.; Lovera, P.; O'riordan, A.; Mooney, M.H.; Vogel, E.M., A Potentiometric Biosensor for Rapid on-Site Disease Diagnostics; *Biosensors and Bioelectronics,* **2016**, 79, 669-678.

4.   Alivisatos, A.P.; Gu, W.; Larabell, C., Quantum Dots as Cellular Probes; *Annual Review of Biomedical Engineering,* **2005**, 7, 55-76.

5.   Mcmahon, J.M.; Henzie, J.; Odom, T.W.; Schatz, G.C.; Gray, S.K., Tailoring the Sensing Capabilities of Nanohole Arrays in Gold Films with Rayleigh Anomaly-Surface Plasmon Polaritons; *Optics express,* **2007**, 15, 18119-18129.

6.   Lovera, P.; Jones, D.; Corbett, B.; O'riordan, A., Polarization Tunable Transmission through Plasmonic Arrays of Elliptical Nanopores; *Optics express,* **2012**, 20, 25325-25332.

7.   Albrecht, M.G.; Creighton, J.A., Anomalously Intense Raman Spectra of Pyridine at a Silver Electrode; *Journal of the American Chemical Society,* **1977**, 99, 5215-5217.

8.   Jeanmaire, D.L.; Van Duyne, R.P., Surface Raman Spectroelectrochemistry: Part I. Heterocyclic, Aromatic, and Aliphatic Amines Adsorbed on the Anodized Silver Electrode; *Journal of Electroanalytical Chemistry and Interfacial Electrochemistry,* **1977**, 84, 1-20.

9.   Botta, R.; Upender, G.; Sathyavathi, R.; Narayana Rao, D.; Bansal, C., Silver Nanoclusters Films for Single Molecule Detection Using Surface Enhanced Raman Scattering (Sers); *Materials Chemistry and Physics,* **2013**, 137, 699-703.

10.   Nie, S.; Emory, S.R., Probing Single Molecules and Single Nanoparticles by Surface-Enhanced Raman Scattering; *Science,* **1997**, 275, 1102-1106.

11.   Otto, A., Theory of First Layer and Single Molecule Surface Enhanced Raman Scattering (Sers); *Physica Status Solidi a-Applied Research,* **2001**, 188, 1455-1470.

12.   Kneipp, K.; Wang, Y.; Kneipp, H.; Perelman, L.T.; Itzkan, I.; Dasari, R.; Feld, M.S., Single Molecule Detection Using Surface-Enhanced Raman Scattering (Sers); *Physical Review Letters,* **1997**, 78, 1667-1670.

13.   Lombardi, J.R.; Birke, R.L.; Haran, G., Single Molecule Sers Spectral Blinking and Vibronic Coupling; *The Journal of Physical Chemistry C,* **2011**, 115, 4540-4545.

14.   Lim, D.-K.; Jeon, K.-S.; Kim, H.M.; Nam, J.-M.; Suh, Y.D., Nanogap-Engineerable Raman-Active Nanodumbbells for Single-Molecule Detection; *Nature Materials,* **2010**, 9, 60-67.

15.   Yang, L.; Ma, L.; Chen, G.; Liu, J.; Tian, Z.-Q., Ultrasensitive Sers Detection of Tnt by Imprinting Molecular Recognition Using a New Type of Stable Substrate; *Chemistry – A European Journal,* **2010**, 16, 12683-12693.

16.   Creedon, N.C.; Lovera, P.; Furey, A.; O'riordan, A., Transparent Polymer-Based Sers Substrates Templated by a Soda Can; *Sensors and Actuators B: Chemical,* **2018**, 259, 64-74.

17.   Xie, W.; Schlucker, S., Medical Applications of Surface-Enhanced Raman Scattering; *Physical Chemistry Chemical Physics,* **2013**, 15, 5329-5344.

18.   Stiles, P.; Dieringer, J.; Shah, N.; Van Duyne, R., Annual Review of Analytical Chemistry; **2008**.

19.   Kahl, M.; Voges, E.; Kostrewa, S.; Viets, C.; Hill, W., Periodically Structured Metallic Substrates for Sers; *Sensors and Actuators B: Chemical,* **1998**, 51, 285-291.

20.   Yu, Q.; Guan, P.; Qin, D.; Golden, G.; Wallace, P.M., Inverted Size-Dependence of Surface-Enhanced Raman Scattering on Gold Nanohole and Nanodisk Arrays; *Nano Letters,* **2008**, 8, 1923-1928.

21.   Krishnamoorthy, S.; Krishnan, S.; Thoniyot, P.; Low, H.Y., Inherently Reproducible Fabrication of Plasmonic Nanoparticle Arrays for Sers by Combining Nanoimprint and Copolymer Lithography; *ACS Applied Materials & Interfaces,* **2011**, 3, 1033-1040.

22.   Diebold, E.D.; Mack, N.H.; Doorn, S.K.; Mazur, E., Femtosecond Laser-Nanostructured Substrates for Surface-Enhanced Raman Scattering; *Langmuir,* **2009**, 25, 1790-1794.

23.   Hulteen, J.C.; Treichel, D.A.; Smith, M.T.; Duval, M.L.; Jensen, T.R.; Van Duyne, R.P., Nanosphere Lithography: Size-Tunable Silver Nanoparticle and Surface Cluster Arrays; *The Journal of Physical Chemistry B,* **1999**, 103, 3854-3863.

24.   Fan, M.; Andrade, G.F.S.; Brolo, A.G., A Review on the Fabrication of Substrates for Surface Enhanced Raman Spectroscopy and Their Applications in Analytical Chemistry; *Analytica Chimica Acta,* **2011**, 693, 7-25.

25.   Lovera, P.; Creedon, N.; Alatawi, H.; Mitchell, M.; Burke, M.; Quinn, A.J.; O'riordan, A., Low-Cost Silver Capped Polystyrene Nanotube Arrays as Super-Hydrophobic Substrates for Sers Applications; *Nanotechnology,* **2014**, 25, 175502.

26.   Lee, S.J.; Morrill, A.R.; Moskovits, M., Hot Spots in Silver Nanowire Bundles for Surface-Enhanced Raman Spectroscopy; *Journal of the American Chemical Society,* **2006**, 128, 2200-2201.

27.   Banholzer, M.J.; Millstone, J.E.; Qin, L.; Mirkin, C.A., Rationally Designed Nanostructures for Surface-Enhanced Raman Spectroscopy; *Chemical Society Reviews,* **2008**, 37, 885-897.

28.   Bell, S.E.; Mccourt, M.R., Sers Enhancement by Aggregated Au Colloids: Effect of Particle Size; *Physical Chemistry Chemical Physics,* **2009**, 11, 7455-7462.

29.   Grzelczak, M.; Vermant, J.; Furst, E.M.; Liz-Marzán, L.M., Directed Self-Assembly of Nanoparticles; *ACS Nano,* **2010**, 4, 3591-3605.

30.   Zhu, S.; Fan, C.; Wang, J.; He, J.; Liang, E., Self-Assembled Ag Nanoparticles for Surface Enhanced Raman Scattering; *Optical Review,* **2013**, 20, 361-366.

31.   Zhang, L., Self-Assembly Ag Nanoparticle Monolayer Film as Sers Substrate for Pesticide Detection; *Applied Surface Science,* **2013**, 270, 292-294.

32.   Hepel, M.; Zhong, C.-J., Functional Nanoparticles for Bioanalysis, Nanomedicine, and Bioelectronic Devices Volume 2; *American Chemical Society*, 2012; Vol. 1113, p 0.

33.   Tang, J.; Zhao, Q.; Zhang, N.; Man, S.-Q., Facile Fabrication of Large-Area and Uniform Silica Nanospheres Monolayer for Efficient Surface-Enhanced Raman Scattering; *Applied Surface Science,* **2014**, 308, 247-252.

34.   Li, W.; Camargo, P.H.C.; Lu, X.; Xia, Y., Dimers of Silver Nanospheres: Facile Synthesis and Their Use as Hot Spots for Surface-Enhanced Raman Scattering; *Nano Letters,* **2009**, 9, 485-490.

35.   Martín, A.; Pescaglini, A.; Schopf, C.; Scardaci, V.; Coull, R.; Byrne, L.; Iacopino, D., Surface-Enhanced Raman Scattering of 4-Aminobenzenethiol on Au Nanorod Ordered Arrays; *The Journal of Physical Chemistry C,* **2014**, 118, 13260-13267.

36.   Martin, A.; Wang, J.J.; Iacopino, D., Flexible Sers Active Substrates from Ordered Vertical Au Nanorod Arrays; *RSC Advances,* **2014**, 4, 20038-20043.

37.   Xie, Z.; Tao, J.; Lu, Y.; Lin, K.; Yan, J.; Wang, P.; Ming, H., Polymer Optical Fiber Sers Sensor with Gold Nanorods; *Optics Communications,* **2009**, 282, 439-442.

38.   Walker, D.A.; Browne, K.P.; Kowalczyk, B.; Grzybowski, B.A., Self-Assembly of Nanotriangle Superlattices Facilitated by Repulsive Electrostatic Interactions; *Angewandte Chemie International Edition,* **2010**, 49, 6760-6763.

39.   Liu, Z.; Yang, Z.; Peng, B.; Cao, C.; Zhang, C.; You, H.; Xiong, Q.; Li, Z.; Fang, J., Highly Sensitive, Uniform, and Reproducible Surface-Enhanced Raman Spectroscopy from Hollow Au-Ag Alloy Nanourchins; *Advanced Materials,* **2014**, 26, 2431-2439.

40.   Yang, M.; Alvarez-Puebla, R.N.; Kim, H.-S.; Aldeanueva-Potel, P.; Liz-MarzáN, L.M.; Kotov, N.A., Sers-Active Gold Lace Nanoshells with Built-in Hotspots; *Nano Letters,* **2010**, 10, 4013-4019.

41.   Kudelski, A., Raman Studies of Rhodamine 6g and Crystal Violet Sub-Monolayers on Electrochemically Roughened Silver Substrates: Do Dye Molecules Adsorb Preferentially on Highly Sers-Active Sites?; *Chemical Physics Letters,* **2005**, 414, 271-275.

42.   Srivastava, S.; Sinha, R.; Roy, D., Toxicological Effects of Malachite Green; *Aquatic Toxicology,* **2004**, 66, 319-329.

43.   Littlefield, N.A.; Blackwell, B.-N.; Hewitt, C.C.; Gaylor, D.W., Chronic Toxicity and Carcinogenicity Studies of Gentian Violet in Mice; *Toxicological Sciences,* **1985**, 5, 902-912.

44.   Commission, E., In Commission, E., Ed.; 2002; Vol. Commission Decision 2002/657/EC.

45.   Lyandres, O.; Shah, N.C.; Yonzon, C.R.; Walsh, J.T.; Glucksberg, M.R.; Van Duyne, R.P., Real-Time Glucose Sensing by Surface-Enhanced Raman Spectroscopy in Bovine Plasma Facilitated by a Mixed Decanethiol/Mercaptohexanol Partition Layer; *Analytical Chemistry,* **2005**, 77, 6134-6139.

46.   Chen, Z.; Yan, X., Simultaneous Determination of Melamine and 5-Hydroxymethylfurfural in Milk by Capillary Electrophoresis with Diode Array Detection; *Journal of Agricultural and Food Chemistry,* **2009**, 57, 8742-8747.

47.   Liu, Y.; Todd, E.E.D.; Zhang, Q.; Shi, J.-R.; Liu, X.-J., Recent Developments in the Detection of Melamine; *Journal of Zhejiang University. Science. B,* **2012**, 13, 525-532.

48.   Sun, H.; Wang, L.; Ai, L.; Liang, S.; Wu, H., A Sensitive and Validated Method for Determination of Melamine Residue in Liquid Milk by Reversed Phase High-Performance Liquid Chromatography with Solid-Phase Extraction; *Food Control,* **2010**, 21, 686-691.

49.   Xu, X.-M.; Ren, Y.-P.; Zhu, Y.; Cai, Z.-X.; Han, J.-L.; Huang, B.-F.; Zhu, Y., Direct Determination of Melamine in Dairy Products by Gas Chromatography/Mass Spectrometry with Coupled Column Separation; *Analytica Chimica Acta,* **2009**, 650, 39-43.

50.   Muñiz-Valencia, R.; Ceballos-Magaña, S.; Rosales-Martinez, D.; Gonzalo-Lumbreras, R.; Santos-Montes, A.; Cubedo-Fernandez-Trapiella, A.; Izquierdo-Hornillos, R., Method Development and Validation for Melamine and Its Derivatives in Rice Concentrates by Liquid Chromatography. Application to Animal Feed Samples; *Analytical and Bioanalytical Chemistry,* **2008**, 392, 523-531.

51.   Filazi, A.; Sireli, U.T.; Ekici, H.; Can, H.Y.; Karagoz, A., Determination of Melamine in Milk and Dairy Products by High Performance Liquid Chromatography; *Journal of Dairy Science,* **2012**, 95, 602-608.

52.   Liu, Y.; Todd, E.D.; Zhang, Q.; Shi, J.-R.; Liu, X.-J., Recent Developments in the Detection of Melamine; *Journal of Zhejiang University Science B,* **2012**, 13, 525-532.

53.   He, Q.; Liu, M.; Huang, L.; Yang, Y.; Liao, S., Determination of Melamine in Milk Powder and Milk by High Performance Liquid Chromatography; *Chinese Journal of Chromatography (Se Pu),* **2008**, 26, 752-754.

54.   Liu, J.; Zhong, Y.; Liu, J.; Zhang, H.; Xi, J.; Wang, J., An Enzyme Linked Immunosorbent Assay for the Determination of Cyromazine and Melamine Residues in Animal Muscle Tissues; *Food Control,* **2010**, 21, 1482-1487.

55.   Garber, E.a.E., Detection of Melamine Using Commercial Enzyme-Linked Immunosorbent Assay Technology; *Journal of Food Protection,* **2008**, 71, 590-594.

56.   Johnson, P.B.; Christy, R.-W., Optical Constants of the Noble Metals; *Physical review B,* **1972**, 6, 4370.

57.   Barrett, C.; Dawson, K.; O'mahony, C.; O'riordan, A., Development of Low Cost Rapid Fabrication of Sharp Polymer Microneedles for in Vivo Glucose Biosensing Applications; *ECS Journal of Solid State Science and Technology,* **2015**, 4, S3053-S3058.

58.   Singh, J.P.; Chu, H.; Abell, J.; Tripp, R.A.; Zhao, Y., Flexible and Mechanical Strain Resistant Large Area Sers Active Substrates; *Nanoscale,* **2012**, 4, 3410-3414.

59.   Cahill, P.; Nuallain, N.a.N.; Jackson, N.; Mathewson, A.; Karoumi, R.; Pakrashi, V., Energy Harvesting from Train-Induced Response in Bridges; *Journal of Bridge Engineering,* **2014**, 19, 04014034.

60.   Jiang, J.D.; Burstein, E.; Kobayashi, H., Resonant Raman Scattering by Crystal-Violet Molecules Adsorbed on a Smooth Gold Surface: Evidence for a Charge-Transfer Excitation; *Physical Review Letters,* **1986**, 57, 1793-1796.

61.   Canamares, M.V.; Chenal, C.; Birke, R.L.; Lombardi, J.R., Dft, Sers, and Single-Molecule Sers of Crystal Violet; *Journal of Physical Chemistry C,* **2008**, 112, 20295-20300.

62.   Angeloni, L.; Smulevich, G.; Marzocchi, M.P., Resonance Raman-Spectrum of Crystal Violet; *Journal of Raman Spectroscopy,* **1979**, 8, 305-310.

63.   Le Ru, E.C.; Blackie, E.; Meyer, M.; Etchegoin, P.G., Surface Enhanced Raman Scattering Enhancement Factors: A Comprehensive Study; *The Journal of Physical Chemistry C,* **2007**, 111, 13794-13803.

64.   Yoon, J.K.; Kim, K.; Shin, K.S., Raman Scattering of 4-Aminobenzenethiol Sandwiched between Au Nanoparticles and a Macroscopically Smooth Au Substrate: Effect of Size of Au Nanoparticles; *The Journal of Physical Chemistry C,* **2009**, 113, 1769-1774.

65.   Sasai, R.; Fujita, T.; Iyi, N.; Itoh, H.; Takagi, K., Aggregated Structures of Rhodamine 6g Intercalated in a Fluor-Taeniolite Thin Film; *Langmuir,* **2002**, 18, 6578-6583.

66.   Kleinman, S.L.; Ringe, E.; Valley, N.; Wustholz, K.L.; Phillips, E.; Scheidt, K.A.; Schatz, G.C.; Van Duyne, R.P., Single-Molecule Surface-Enhanced Raman Spectroscopy of Crystal Violet Isotopologues: Theory and Experiment; *Journal of the American Chemical Society,* **2011**, 133, 4115-4122.

67.   Chadha, R.; Maiti, N.; Kapoor, S., Triplet and Sers Study of Crystal Violet in Presence of Metal Nanoparticles; *Chemical Physics Letters,* **2013**, 579, 68-72.

68.   Kim, Y.J.; Sun, X.; Jones, J.E.; Lin, M.; Yu, Q.; Li, H., Surface Modification of Sers Substrates with Plasma-Polymerized Trimethylsilane Nanocoating; *Applied Surface Science,* **2015**, 331, 346-352.

69.   Si, K.J.; Guo, P.; Shi, Q.; Cheng, W., Self-Assembled Nanocube-Based Plasmene Nanosheets as Soft Surface-Enhanced Raman Scattering Substrates toward Direct Quantitative Drug Identification on Surfaces; *Analytical Chemistry,* **2015**, 87, 5263-5269.

70.   Vega Canamares, M.; Feis, A., Surface-Enhanced Raman Spectra of the Neonicotinoid Pesticide Thiacloprid; *Journal of Raman Spectroscopy,* **2013**, 44, 1126-1135.

71.   Zhang, Y.; Huang, Y.; Zhai, F.; Du, R.; Liu, Y.; Lai, K., Analyses of Enrofloxacin, Furazolidone and Malachite Green in Fish Products with Surface-Enhanced Raman Spectroscopy; *Food Chemistry,* **2012**, 135, 845-850.

72.   Qiu, C.; Maingi, A.T.; Jiang, C.Y., Surface-Enhanced Raman Scattering Detection of Melamine Via Silver Nanostructures; *Abstracts of Papers of the American Chemical Society,* **2011**, 241.

73.   Söderholm, S.; Roos, Y.H.; Meinander, N.; Hotokka, M., Raman Spectra of Fructose and Glucose in the Amorphous and Crystalline States; *Journal of Raman Spectroscopy,* **1999**, 30, 1009-1018.

74.   Chan, E.Y.Y.; Griffiths, S.M.; Chan, C.W., Public-Health Risks of Melamine in Milk Products; *The Lancet,* 372, 1444-1445.

75.   Ingelfinger , J.R., Melamine and the Global Implications of Food Contamination; *New England Journal of Medicine,* **2008**, 359, 2745-2748.

76.   Lin, M.; He, L.; Awika, J.; Yang, L.; Ledoux, D.R.; Li, H.; Mustapha, A., Detection of Melamine in Gluten, Chicken Feed, and Processed Foods Using Surface Enhanced Raman Spectroscopy and Hplc; *Journal of Food Science,* **2008**, 73, T129-T134.

77.   Koglin, E.; Kip, B.J.; Meier, R.J., Adsorption and Displacement of Melamine at the Ag/Electrolyte Interface Probed by Surface-Enhanced Raman Microprobe Spectroscopy; *The Journal of Physical Chemistry,* **1996**, 100, 5078-5089.

78.   Mircescu, N.E.; Oltean, M.; Chis, V.; Leopold, N., Ftir, Ft-Raman, Sers and Dft Study on Melamine; *Vibrational Spectroscopy,* **2012**, 62, 165-171.

79.   Yang, S.; Ding, J.; Zheng, J.; Hu, B.; Li, J.; Chen, H.; Zhou, Z.; Qiao, X., Detection of Melamine in Milk Products by Surface Desorption Atmospheric Pressure Chemical Ionization Mass Spectrometry; *Analytical Chemistry,* **2009**, 81, 2426-2436.

Chapter 3   **Spectro-electrochemical detection of Neonicotinoid Insecticides**

3.1 Introduction

The need for pest control in intensive agriculture systems has driven the growth of insecticide use within the agri-sector. In this regard, neonicotinoids are a relatively powerful class of insecticide, and since the introduction of imidacloprid in 1991; they have been the fastest-growing class of insecticides in modern crop protection,[1] representing almost 17% of the global insecticide market.[2] Neonicotinoids target the nicotinic acetylcholine receptors in insects[3] and are extremely effective against herbivorous insects, while having perceived low toxicity to mammals, birds and fish.[4] This led to their widespread uptake for use on a variety of crops.[1]

However, recently, significant concerns have been raised about their suspected environmental impact on the global pollinator population, including honey bees, bumble bees and solitary bees. It is claimed that neonicotinoids affect the homing capacity of honey bees and their reproductive ability resulting in colony collapse disorder.[5,6] Another emerging concern is that human exposure to these pesticides may increase prevalence of cancers,[7,8] respiratory diseases,[9,10] and damage to the reproductive system, nervous system and liver.[11,12] Children are particularly at risk.[13] Consequently, this class of insecticides has now become the subject of a world-wide debate.[14,15] The most widely used neonicotinoid imidacloprid, followed by clothianidin, are routinely spread on the major crops (cereals, corn, cotton and sugar beet).[1] Due to their high water solubility, 510 mg/L and 0.33 mg/L, respectively, they are easily spread on the pollen of flowering crops and are readily absorbed into soil and other plant via their roots or leaves.[16] Imidacloprid, containing a nitro substitution, is the most toxic with an LD50 (median lethal dose) of 4-18 ng/bee. The LD50 for clothianidin and thiamethoxam reported a similar level of toxicity to imidacloprid with values of between 5 and 30 ng/bee.[17-20]

The European Food Safety Authority (EFSA), recognising the potential threat caused by neonicotinoids, enforced a temporary ban by the European Union (Dec 2013).[21] Currently the maximum allowable residue limits of neonicotinoids are between 0.01 to 3 mg/kg for many fruits and vegetables.[22,23] Ecological and human health risk assessments for select

---

† This work has been submitted in full as "Neonicotinoid Detection using Nano-electrochemistry and SERS" in *The Journal of Physical Chemistry C*, 2018.

neonicotinoids; Imidacloprid, Clothianidin and Thiamethoxam, were reviewed by the EFSA this year (2018). Their review in February 2018 stated that the use of neonicotinoid pesticides on outdoor crops presents a risk to wild bees and honeybees.[24] Consequently, in April, EU governments passed a near-total ban on the use of neonicotinoid pesticides on outdoor crops due to their impact on pollinators. Member State authorities endorsed the European Union to completely ban the outdoor uses of three active substances – clothianidin, imidacloprid, and thiamethoxam. Subsequently, to enforce this ban, easy-to-use and low maintenance sensor devices are required to enable rapid and reliable decentralised detection of these pesticides, in order to maintain environmental security.

Current techniques for the detection of neonicotinoids include both chemical and optical detection methods: ELISA,[25, 26] HPLC- or GC- mass spectrometry,[22, 27-30] surface plasmon resonance[31] and fluorescence spectroscopy.[32] While these techniques have the ability to detect insecticides at low concentrations, the associated instruments are complex, have a high cost of ownership and are not suited to remote field analysis. Gold nanowires are of particular interest for sensing due to their high chemical and thermal stability, excellent electrical conductivity and their particular suitability for electroanalysis.[33] In electrochemistry, nanoelectrodes have a number of advantages including low background charging; high current density due to enhanced mass transport; low depletion of target molecules; low supporting electrolyte concentrations and faster response times when compared to macroelectrodes.[34, 35] Concerning electroanalysis, voltammetry techniques have been shown to permit effective determination of neonicotinoids. The voltammetric signals observed for these compounds arise from the reduction of their nitro groups to amine groups.[36] Square wave voltammetry serves as a sensitive and fast technique to study this reduction response.

One key limitation of electrochemistry is that the technique does not provide any qualitative information on what compounds are present. Consequently, combining it with an optical technique, such as SERS, provides a characteristic molecular spectrum of the molecules of interest. SERS also allows for trace analyte detection and offers complementary information to that of electrochemical techniques. Raman spectroscopy studies the structural vibrations within the compounds of interest, providing a weak spectral molecular finger print of the molecule. These vibrational responses are greatly enhanced by depositing the analyte on a nanostructured metallic surface.[37-40] Moreover,

SERS provides high sensitivity, fast analysis time and little background interference from water molecules. However the variability across the SERS substrate suggests that quantification can be difficult; but is easily permitted by SWV. To this end, both techniques will complement each other's sensing capabilities, providing qualitative and quantitative data.

In this chapter we focus on the detection of the neonicotinoids, imidacloprid and clothianidin. We developed and characterised two different nanosensors; (i) the silver nanostructured polymer substrate for SERS characterisation, used in Chapter 2, and (ii) an array of four gold nanowires employing a square wave voltammetric technique. The ultra-sensitive detection of neonicotinoids, imidacloprid and clothianidin, were demonstrated in aqueous buffer solutions, employing the SWV technique. This detection was then verified using SERS. Combining SWV and SERS detection methods provides both physical (vibrational spectrum) and chemical (reduction) data for the insecticide solutions. Furthermore, both SWV and SERS can be adapted to portable devices.

3.2 Experimental

3.2.1 Materials and Reagents

Ferrocenemonocarboxylic acid (FcCOOH), phosphate buffer saline (PBS) tablets, PVDF, silver wire, imidacloprid and clothianidin were purchased from Sigma-Aldrich and used as received. Acetate buffer was purchased from Sierra Sensors, Germany. Deionised water (18.2 MΩ cm) from an ELGA Pure Lab Ultra system was used for the preparation of samples. Electrochemical measurements are undertaken in acetate buffer solution (pH 5) unless otherwise stated.

3.2.2 SERS Substrate Sensor Fabrication

Pellets of PVDF were placed on a microscope slide and melted on a hotplate at ~220°C. An aluminium master template was prepared as described in detail in Chapter 2. [41]

3.2.3 Electrode Fabrication

Gold nanowire array electrodes were fabricated using a hybrid electron beam photolithography process on a four inch diameter wafer silicon substrates bearing a 300 nm layer of thermally grown silicon dioxide (Si/SiO_2).[42, 43] Nanowire structures and alignment marks were patterned in an e-beam sensitive resist (ZEP 520 Nippon Zeon) using direct electron beam writing (JBX-6000FS, JEOL UK Ltd) and developed. The optimised parameters for this step were: 50 kV beam voltage; 100 pA beam current; and a beam dose of 120 μC cm^{-1}.Following resist development, Ti/Pt/Au (5/5/30 nm) layers were blanket deposited by evaporation (Temescal FC-2000 E-beam evaporator) and standard lift-off techniques were employed to remove un-patterned areas to yield stacked Ti/Pt/Au nanowire structures. Using the electron bean alignment marks, micron-sized interconnection tracks, half disk electrodes (~1.6 ×10^{-4} cm^2) and peripheral contact pads (~1.5 nm diameter) were overlaid onto the wafer using photolithography, metal deposition (Ti/Au 10/200 nm) and lift-off techniques. Both half disk electrodes have a gold surface layer, so in order to fabricate the platinum reference electrode, a second metal evaporation (Ti/Pt 10/90 nm) on one half disk electrode was performed. In this manner, one central half-disk electrode may be employed as a gold counter and the other as a platinum pseudo-reference electrode, respectively. A silicon nitride passivation layer

(500 nm) was then deposited by plasma-enhanced chemical vapour deposition (PECVD) onto the wafer surface in order to prevent electrochemical reactions between the electro active species on the electrode and the interconnection tracks. Photolithography and dry etching were then employed to create a window (40 μm × 100 μm) in the passivation layer above the nanowires to allow contact with solution. This process was optimised so that the interconnection remained covered by the passivation layer, ensuring exclusive contact between the nanowires and electrodes and the external electrolyte solution. The passivation layer was also removed over the counter and reference electrodes along with peripheral contact pads. Following fabrication, wafers are diced into 16 × 16 mm chips, such that each chip contains twelve individually contacted gold nanowire working electrode arrays, an integrated gold counter electrode and a platinum pseudo-reference electrode.
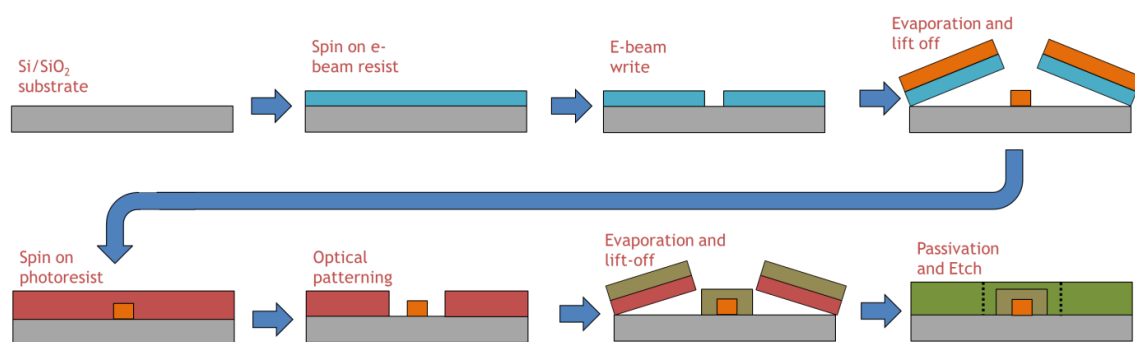
Figure 3.1: Schematic of hybrid e-beam lithography and optical lithography process used for nanowire fabrication.

3.2.4 Characterisation of the Sensors

3.2.4.1 Optical Characterisation

Optical micrographs were acquired using a calibrated microscope (Axioskop II, Carl Zeiss Ltd.) equipped with a charge-coupled detector camera (CCD; DEI-750, Optronics). Scanning electron microscopy analysis was undertaken to characterize the substrate surface after the fabrication procedure. Microscopy images were acquired using a calibrated field emission SEM (JSM-7500F, JEOL UK Ltd.) operating at beam voltages between 3 and 5 kV.

3.2.4.2 Raman Characterisation

All Raman measurements were recorded using a Confocal Renishaw Raman Microscope equipped with a 514 nm Ar ion laser and analysed using Wire 3.0 computer software. The laser spot diameter was ~1 μm at the substrate surface and a laser power density of ~7×10^4 W/cm^2 was used. SERS spectra collected using a 50x magnification (0.75 NA) objective microscope, with a data acquisition time of 10 s, over an extended spectral range of 200 cm^{-1} to 3500 cm^{-1}. The spectrometer was equipped with a computer controlled motorised XYZ stage employed to focus and adjust the positioning of the sample on the silver surface. Subtraction of the baseline was performed on all spectra to eliminate background noise from the underlying polymer and the recorded spectra were imported into Origin® 7.4 (OriginLab) to facilitate data analysis.

3.2.4.3 Simulation Computational Analysis

Computational analysis was undertaken by José Julio Gutiérrez Moreno (Materials Modelling for Devices Group, Tyndall National Institute). He performed ab initio calculations to find the equilibrium molecular structures. The Becke's three parameter Lee–Yang–Parr (B3LYP) [44] hybrid exchange-correlation functional along with triple-ζ valence with two sets of polarisation functions (TVZPP) basis set [45] were used as implemented in the Turbomole code.[46] The dispersion forces were corrected by the Grimme's DFT-D3 method.[47] Redundant internal coordinates were used for the geometry optimisation with an energy convergence criteria of less than 10^{-6} Hartree. [48] Force constant calculations were implemented to estimate the vibrational modes of the isolated imidacloprid and clothianidin molecules and harmonic vibrational frequencies were estimated by the analytical evaluation of second derivatives of the energy.[49, 50] A scaling factor of 0.9669 was applied to the fundamental vibrational frequencies to minimize the error due to the neglected enharmonic effects in the theoretical model. [51]

3.2.4.4 Electrochemical Characterisation

All electrochemical experiments were performed using a CHI660a Electrochemical Analyser and a Faraday Cage CHI200b (CH Instruments) connected to a PC. A three electrode electrochemical system was implemented; using an array of 4 gold nanowires (100 nm wide, separation 500 nm) as the working electrodes versus the on-chip platinum

pseudo-reference and gold counter electrodes. The cell was setup with a custom chip holder containing spring loaded gold pins to permit electrical contact to the working electrodes, and a sample well for the electrolyte solution, see Figure 3.2. To confirm electrode functionality cyclic voltammetry (CV) experiments were first undertaken in a 1 mM FcCOOH solution in 10 mM phosphate buffer saline solution (PBS, pH 7.4) purged in N_2 prior use to displace dissolved oxygen. CV measurements were carried out in the potential range -0.2 to 0.6 V at a scan rate of 100 mVs^{-1}.
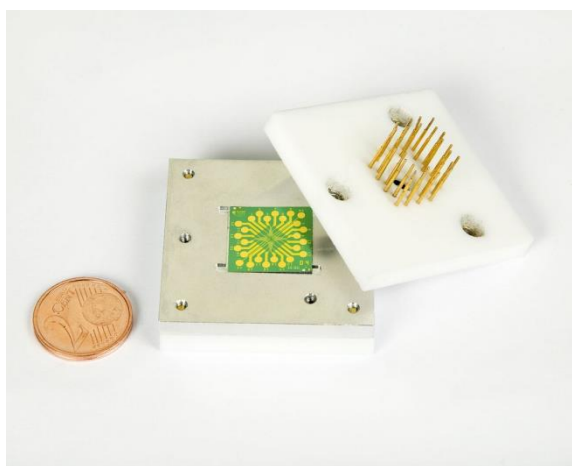
Figure 3.2: Image showing a fully fabricated chip mounted in the aluminium base of the custom-made chip holder.

3.2.5 Sensing of Neonicotinoids

3.2.5.1 Raman Analysis

Working solution of both clothianidin and imidacloprid were prepared in a methanol– DI water solution (1:1) and diluted to 1 ng/mL then deposited via the drop/dry process onto the SERS substrates; depositing 50 µl of solution onto the substrate and allowing to air dry (10 min). All samples were thoroughly rinsed with DI water before Raman analysis to remove unadsorbed, clumped molecules that accumulated on the surface of the substrate during the drying process. Bulk Raman spectra were also acquired for both molecules. All the wavenumbers stated in the discussion section are related to the Raman spectra, unless otherwise stated.

3.2.5.2 Electrochemical Analysis

SWV was performed by sweeping the potential from -0.2 V to -1.4 V in acetate buffer. All scans were performed using a frequency of 10 Hz, amplitude of 50 mV and a potential step of 4 mV. Blank SWV of acetate buffer (pH 5) were also obtained for the purpose of background subtraction. Imidacloprid and clothianidin stock solutions (in methanol– DI water, 1:1) were prepared at different concentrations, and were added sequentially to 90 µL AB in the cell using a serial addition approach. Five replicate SWV scans were undertaken for each addition. All experiments were performed at room temperature.

3.3 Results and Discussion

3.3.1 SERS Substrate Characterisation

SERS substrate characterisation, for these sensors, was explored in detail previously, in Chapter 2. [41] Figure 3.3 (a) shows a typical SEM micrograph of a portion of a SERS substrate used in this chapter. As expected, from SEM analysis, the size distribution of the Ag nano-structures was estimated to be roughly 60 ± 20 nm while the gaps between the clusters were estimated to be on the order of 10 ± 5 nm. These small separations between clusters are expected to deliver a high yield of electromagnetic hot-spots, making them very suitable for SERS sensing. Figure 3.3 (b) shows the SERS response of CrV on the fabricated sensors. All the characteristic peaks of CrV are well defined, indicating the presence of SERS hotspots on the surface.
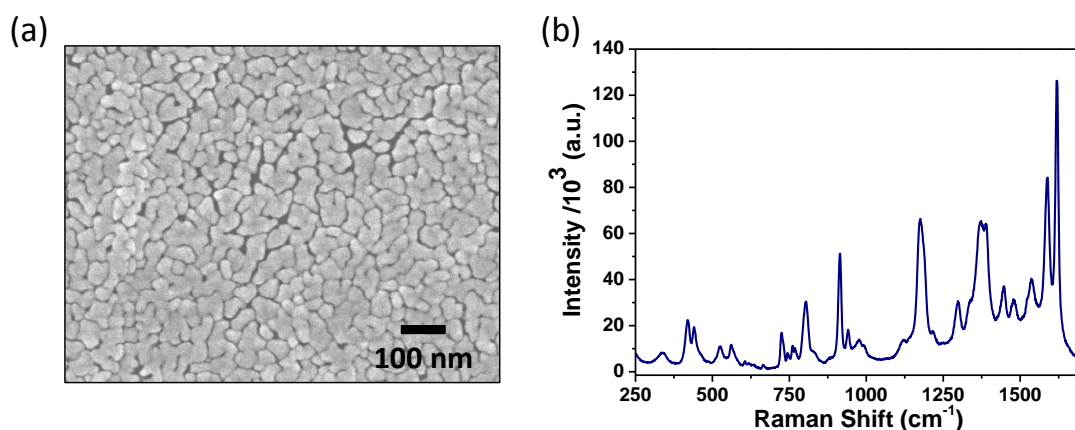
Figure 3.3: (a) SEM image of a portion of the fabricated SERS substrate silver surface and (b) SERS spectrum of 10^{-6} M crystal violet in water

3.3.2 Nanowire Electrochemical Characterisation

Nanowires were fabricated as described in the experimental section above. Each chip contains 12 gold working electrode arrays of 4 nanowires, along with single Pt reference and Au counter electrodes. The devices were characterised using optical microscopy. Figure 3.4 (a) shows an optical micrograph of the central chip region containing the 12 electrically isolated nanowire electrodes with the Au counter and Pt reference electrodes respectively. A more magnified image, Figure 3.4 (b), illustrates a fully fabricated and passivated four nanowire electrode array, separated by 500 nm. The width of the

passivation window (central dark rectangle) defined the exposed nanowire length at 45 µm for the nanowire arrays. This four nanowire array structure of Au working electrode was used throughout these experiments.
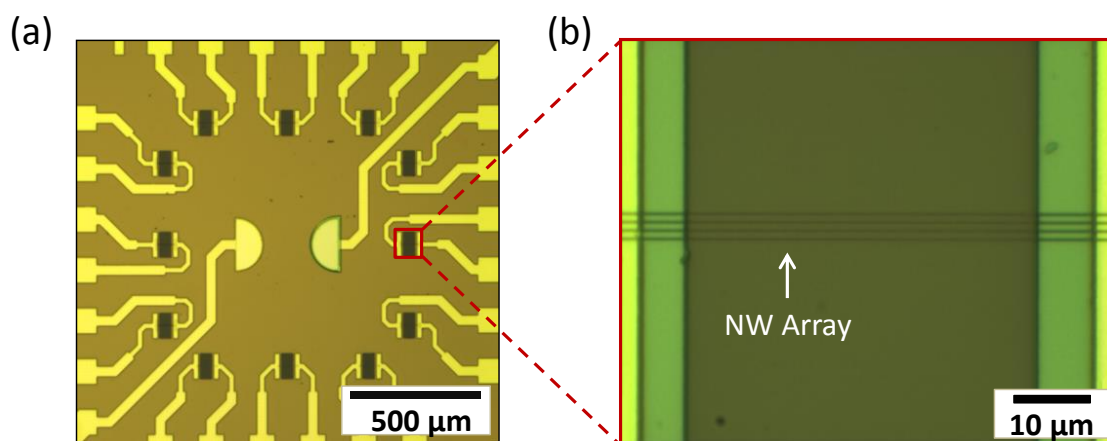
Figure 3.4: (a) Plan view of the central chip region which contains 12 individual nanowire (NW) sensors, with a gold half disk counter electrode (left) and a platinum half disk pseudo reference electrode (right) shown in the chip centre. (b) Higher magnification image of one nanowire sensor comprising a four nanowire array with both sides of the wire connected.

Nanowire electrodes were structurally characterised in detail previously, by Barry et al., using a combination of optical, electron and atomic force microscopy and electrically characterised using two point current voltage measurements.[52] Furthermore, cyclic voltammetry (CV) characterisation was performed by applying a potential range of −0.2 V to 0.6 V to the nanowire arrays in 1 mM FcCOOH in 10 mM PBS, pH 7.4, at 100 mV s^{-1}; see Figure 3.5 (a). The magnitude of the current (~2.5 nA) is typical of a nanoelectrode array and exhibits steady-state behaviour, as expected. [42] This confirms that the silicon nitride passivation layer has been removed to expose the gold nanowire array and successfully shields the rest of the chip from unwanted electrochemical reactions. Only chips that exhibit this current behaviour in FcCOOH were used for experiments; chips that demonstrated low or no electrochemical current were discarded and not used for further experiments. Figure 3.5 (b) shows a typical SWV of 1 mM FcCOOH in 10 mM PBS, pH 7.4 (frequency 10 Hz, amplitude 50 mV and a potential step 4 mV) displaying a current peak in the voltage range of 0.15 to 0.25 V vs. the on-chip Pt pseudo-reference electrode. This oxidation peak is in agreement with the CV data, and further validated the oxidation of FcCOOH is occurring at the electrodes.
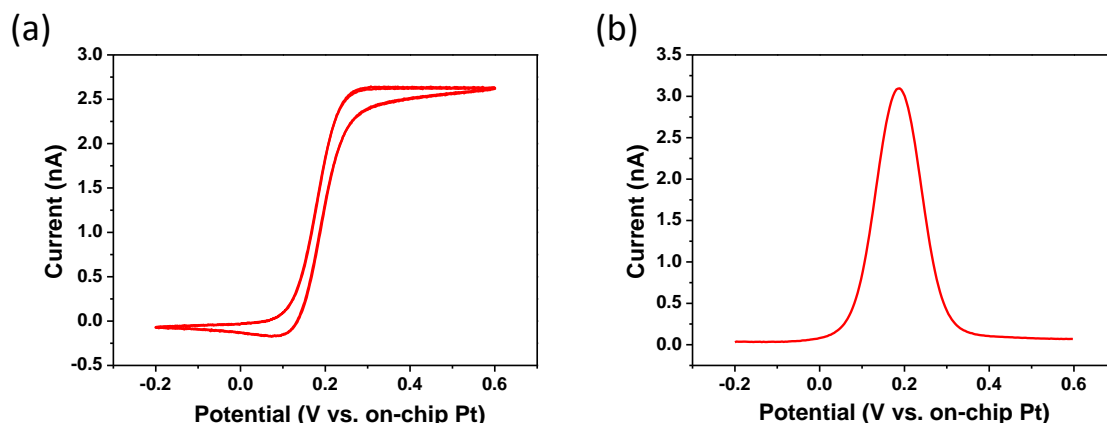
Figure 3.5: (a) CV and (b) SWV of 1 mM FcCOOH in 10 mM PBS, pH 7.4, at 100 mVs^{-1} vs. on-chip Pt pseudo-reference electrode; illustrating the steady-state behaviour of a 4x 100 nm nanowire electrode array separated by a distance of 500 nm.

3.3.3 Raman and SERS Characterisation of Neonicotinoids

Bulk Raman spectra were first acquired for both Clothianidin and imidacloprid pesticides. All the characteristic Raman peaks are well resolved from the bulk powder. All the Raman spectral modes for clothianidin and imidacloprid were assigned by comparison with hybrid Density Functional Theory (DFT) calculations, as described in material and methods section 3.2.4.3, and are listed in Table 3.1 and Table 3.2 below, respectively. Although imidacloprid and other neonicotinoids are widely published, [53-56] to our knowledge this is the first assignation of the Raman modes for Clothianidin.

3.3.3.1 Raman analysis of Clothianidin

Raman analysis on clothianidin bulk powder was first undertaken to observe if the molecule was Raman active. The Raman spectrum acquired for the bulk is illustrated in, Figure 3.6 (a), exhibiting all the characteristic peaks of the molecule. All the significant Raman spectral peaks were identified and assigned to their corresponding vibrational modes, detailed in Table 1. The assignations were achieved using a combination of direct visualisation of the DFT vibrational modes and by comparison to vibrations of similar molecules in the literature.[54, 57]

3.3.3.2 SERS analysis of Clothianidin

SERS for prepared clothianidin solutions were then investigated using the fabricated SERS substrates. Figure 3.6 (b) shows the SERS spectra for 10 ng/mL of clothianidin. The peaks are well resolved for the SERS measurement and the large characteristic peaks compare well to the bulk Raman spectrum, seen in Figure 3.6 (a). These SERS peaks were matched to their equivalent Raman vibrations, which were previously assigned, detailed in Table 1. We expect a shift in wavenumber for all the corresponding SERS peaks compared to the Raman spectrum. This is due to the adsorption of clothianidin to the SERS substrate Ag surface via the nitrogen's in the nitroguanidine structure. We believe that the largest shifts the SERS spectra will be observed at Raman vibrational frequencies relating to these nitroguanidine atoms. This is typical when employing surface enhanced Raman techniques.
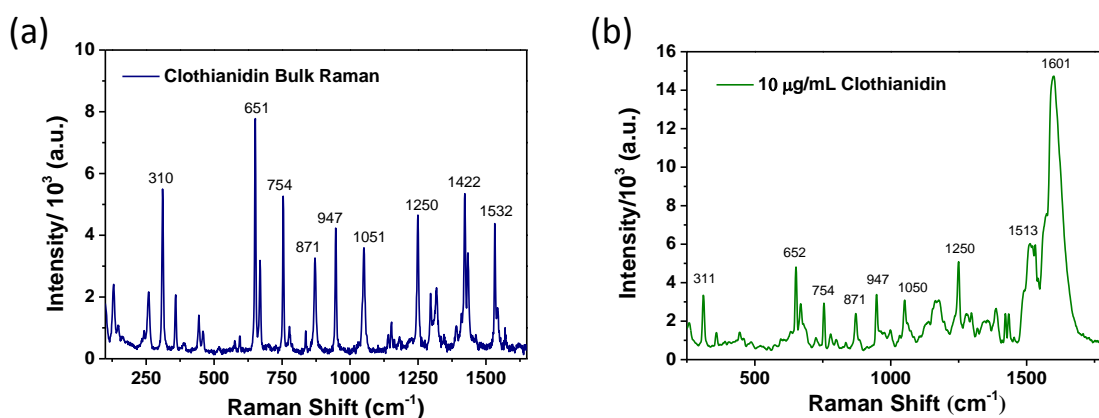
Figure 3.6: (a) Bulk Raman spectrum and (b) SERS spectrum (10 µg/mL) of clothianidin using fabricated silver coated PVDF substrates.

3.3.3.3 Vibrational Analysis of Clothianidin

Clothianidin consists of a chloro-thiazole ring linked by a carbon to a nitroguanidine structure. The structure of clothianidin with atomic numbering labels used in this study is given in Figure 3.7.

Raman	SERS (1ng)	DFT (scaled)	Vibrational Assignments
3086	-	3502.63	νN6-20
3013	-	3475.94	νN5C18
2983	-	3121.3	νC13-19
2952	-	3011.52	νC1016,H17 as
2936	-	2996.8	νC15C22 stretch
	-	2965.57	νC10H16,H17 sym
	-	2900.52	νC15C23,24 as
	-	2859.95	νC15C22,C23,24 sym
1570	1605.44	1669/1604	νN9O3O4 as; δN6H20; δN5H18
1532.18	1557.42	1517.25	νC11C13; νC10C11; δC13H19 (ip); δN5H18; νN7C14;
1433.75		1413.35	νN7C14; νC11C13; τC10H17,18
1422.27	1423.91	1403	δC15H21-23; δN6H20
1318.07	1335.62	1317	νN6N9; νN9O3,4 sym; δN8C12N5N6 ; δC5H18 (ip); ωC10H16 (oop)
1296	1304.89	1297	δC10C11C13; τC10H16,17 (oop); δC13H19
1248.83	1254.79	1237	τ C10H16,17 (oop); δC13H19 (ip); δN6H18; δC6H20
1152.94	1176.3	1148/1126	νC10C11; ρC10H16,17 (ip); δC13C11C10; νC11S2; νN6C12; δC13H19 (ip); νC13N7
1051.39	1047.63	1051.46	νHC15N8; νC10N5; δN5H18 (ip); τC10H16,17 (oop);
992	997.961	997.65	νN15N19; νN9O3O4 sym; ωC15H21-24; νC14S2Cl1 as; δN7C14C13H19
947.319	946.846	931.8	ρC10H16,17 (ip); δN5H18 (ip); νC15N8; δC10C11C13
871.121		867.64	ωC13H19 (oop)
754.219	758.308	750.01	ωN6N9O3O4
669		678	ωC12N5N6N8; ωC12N5C10C11; ρC10H16,17; νS2C11C14 as; ωC13H19
651.745	650.094	671.83	δN5C12C10H; ωN5H18 (oop); νS2C11C14 sym; νHN6N9O3; νN8C15
594	573.195	589	ωC10C11C13; ωHC13N7C14; ωC11C13N7C14; ωC13N7C14Cl1
577	556.784	545.78	ωN6H20; ωN5H18; ωS2C11C14; νC14Cl1
514	522.681	514	ωN6H20; ωN5H18
443	432.592	453	ωC11C13N7C14; ωH19C13N7C14S2; νC14Cl1; ωC12N5H18C10; δN6N9O3;
358.837	339.41	339.41	ρN9O3O4; ωC13N7C14Cl1; ωC14Cl1; ωHC10; δC12N6N9; ωC10C11S2; ωC12N5C10C11

310.554	310.513	292.69	δC12N6N9O4; δN6C12N8C15H; ωC12N5H18C10; δS2C14Cl1
259.539	237.97	237.97	ρC10H16,17; δS2C14Cl1; δN8C15H

Table 3.1: Assignments of the most intense experimental vibrational normal modes for clothianidin. The abbreviations are ν, stretching; ω, wagging; τ, twisting; ρ, rocking; δ, bending/scissoring; ip, in plane and oop, out of plane modes; sym and asym denote symmetric and asymmetric modes, respectively.
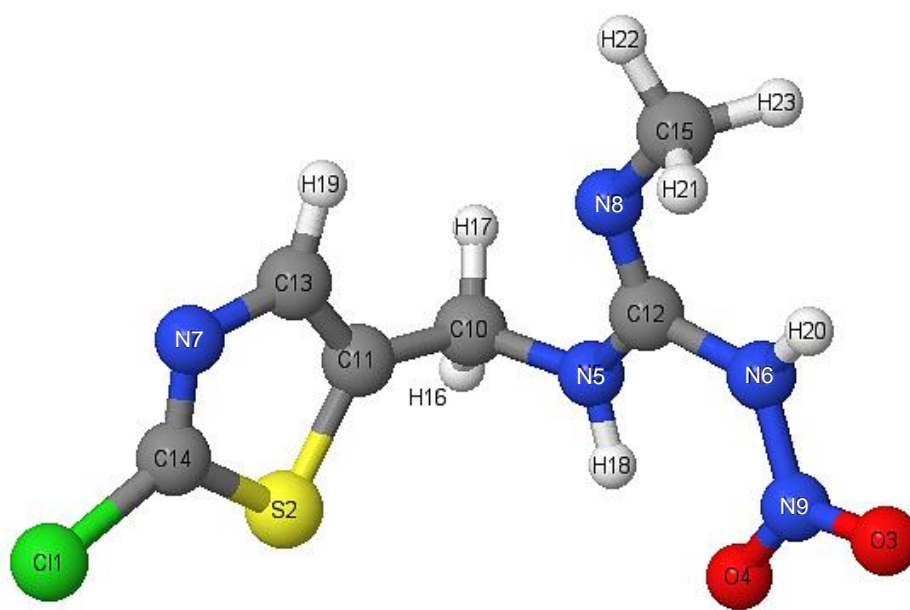
Figure 3.7: Structure of Clothianidin with atomic numbering.

3.3.3.3.1 C-H vibrations

To begin, all the CH vibrations in the molecule were assigned to their corresponding Raman band using the vibrations illustrated in the simulation. First the ring C13-H is discussed followed by the C10-H vibrations and finally the C15-H vibrations. All the single C-H stretching vibrations observed at an extended spectral range (~3000 - 3600 cm^{-1}) were assigned and are presented at the top of Table 3.1.

The Raman band at 3121 cm^{-1} was assigned as the only stretching vibration for the CH bond in the chlorothiazole ring, C13-H19. There are, however, several in-plane bending vibrations associated with C13-H, which were observed at 1532 cm^{-1}, 1296 cm^{-1}, 1248 cm^{-1} and 1152 cm^{-1}. The first mode was strongly coupled with C13-C11, C10 and N7-C14 stretching vibrations. The second and third were coupled with a C10-H twisting vibration, whereas the last mode was coupled with a C10-H rocking. The out of plane wagging modes for C13-H are observed at 871 cm^{-1} and 669 cm^{-1}.

The C10-H symmetric and asymmetric stretching modes are observed at 2965 cm^{-1} and 3011 cm^{-1}, respectively. The only C10H bending vibration was assigned at 1462 cm^{-1}. Alternatively, multiple out of plane twisting modes were found at 1422 cm^{-1}, 1296 cm^{-1}, 1248 cm^{-1} and 1051 cm^{-1}; including a C10H16 out of plane wagging at 1318 cm^{-1}. Finally Raman bands at 1152 cm^{-1}, 947 cm^{-1}, 669 cm^{-1} and 259 cm^{-1} can be assigned to the in-plane rocking of H16 and H17 with C10.

The C15-H symmetric and asymmetric stretching modes are observed at 2860 cm^{-1} and 2900 cm^{-1}, respectively. Raman peaks at 1422 cm^{-1} and 992 cm^{-1} were assigned to the in-plane bending and wagging modes of the CH$_3$ bonds, respectively.
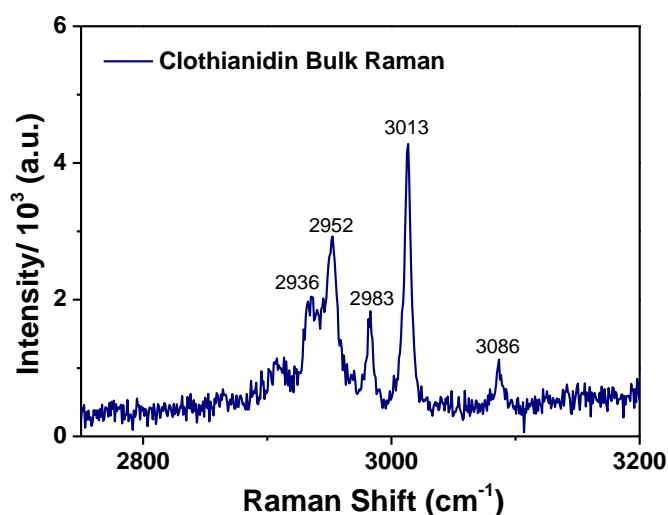
Figure 3.8: Raman spectrum for Clothianidin bulk powder at the higher wavenumber range.

3.3.3.3.2 Ring Vibrations

The chlorothiazole ring vibrations were examined next. First the stretching Raman vibrations were assigned, followed by the in-plane bending and out-of-plane wagging modes, and finally the C-Cl bond vibrations are discussed.

Strong ring C13-C11 and N7-C14 stretching modes are observed at 1532 cm^{-1} and 1433 cm^{-1} in the Raman spectrum, and are both coupled with a C10-C11 stretch. The C13-N7 stretching vibration is observed at 1152 cm^{-1} in Raman spectra. This band is also coupled with a C10-C11 stretch, as well as a C11-S2 stretch. A strong asymmetric stretch between C14-S2, Cl1 observed at the simulated value of 1029 cm^{-1}, was assigned to the 992 cm^{-1} band in the Raman spectrum, and coupled with a N7-C14 bending mode. Weak S2-C13, C11 symmetric and asymmetric stretching vibrations are observed at 651 cm^{-1} and 669

cm^{-1}, respectively. The former is coupled with C12N5C10H wagging out of plane vibrational mode. The observed band at 594 cm^{-1} in Raman spectrum is assigned to the out of plane wagging modes of the chlorothiazole ring, where C13 and C14 are vibrating out of plane in an opposite direction to N7. The other out-of-plane wagging modes were observed at 443 cm^{-1} and 358 cm^{-1}.

The vibrational modes for the C-Cl bond appeared at lower wavenumbers. The stretching vibration of C14-Cl1 was seen at 443 cm^{-1} in the Raman spectrum (432.6 cm-1 in the SERS), this is agreement with the literature data.[58] Raman peaks at 259 cm^{-1} and 358 cm^{-1} can be assigned to the weak bending and wagging mode of C-Cl, respectively. Both vibrations are strongly coupled with a C10-H rocking.

3.3.3.3.3 N-O, N-H and C-N Vibrations

Following assignations of the ring vibrations and CH modes, the peaks associated with the nitroguanidine structure were assigned. The N9-O symmetric and asymmetric stretching vibrations occur at 1318 cm^{-1} and 1570 cm^{-1}, respectively. The former, at 1318 cm^{-1} is coupled with weak stretching modes for N9-N6 and C12-N6, whereas the latter is coupled with the N-H bending of N6 and N5. These are two well resolved bands in both the Raman and SERS spectra, which compare well to the nitroalkane stretching reported in the literature.[58, 59] The wagging out of plane vibration of N9-O appears as the only observed band at 754 cm^{-1}; while the N9-O rocking occurs at 358 cm^{-1}, which is coupled with C12N6N9 bending in plane. The strong N9-N6 stretching appears at 992 cm^{-1}. The C12-N6 stretching mode is observed at 1152 cm^{-1}. The C12-N wagging vibrations occur at 669 cm^{-1} with C12 vibrating out of plane in opposite directions to the nitrogen atoms. Finally the C-N bending mode for this carbon is observed at 1318 cm^{-1}. Another C-N vibration witnessed was the N8-C15 stretching bands at 651 cm^{-1}, 947 cm^{-1} and 1051 cm^{-1} which are coupled with a strong in plane N5-C10, C12 bending; a N5-H bend and a N5-C10 stretch, respectively. The Raman band at 310 cm^{-1} shows the bending vibration from N5 through C12 to O4 (N5C12N6N9O4) and simultaneously a bending from N6 through to C15 (N6C12N8C15H). This band also reveals a N5-H18 wagging vibration. Similar bending and wagging vibrations are also seen at 443 cm^{-1}. The out of plane N-H wagging vibrations (N6H20 and N5H18) are observed at 651 cm^{-1}, 514 cm^{-1} and 577 cm^{-1}. The latter band is coupled with a weak ring wagging vibration

(C11S2C14), where C11 and C14 are vibrating out of plane. The in-plane N-H bending modes are observed at several higher wavenumbers; 1051, 1248, 1318, 1422, 1532 cm^{-1}.

3.3.3.4 *Raman and SERS analysis of Imidacloprid*

Following Clothianidin detection, solutions of imidacloprid were analysed using Raman and SERS. Figure 3.9 shows the bulk Raman spectrum for Imidacloprid and the SERS detection of a 10 ng/mL solution. The Raman spectrum was compared against the SERS data and the scaled simulated data. All vibration modes were assigned using a combination of the literature and the DFT simulated vibrations in Jmol [60-62]. Again, we expect that all the corresponding peaks identified in the SERS spectra will shift in wavenumber. This is due to the adsorption of imidacloprid to the SERS substrate Ag. Typically for molecules that containing a pyridine ring, the compound will attach to the metal surface via the N in the ring [63]. We expect that the largest shifts the SERS spectra will be observed with Raman vibrational frequencies relating to Ring 1.
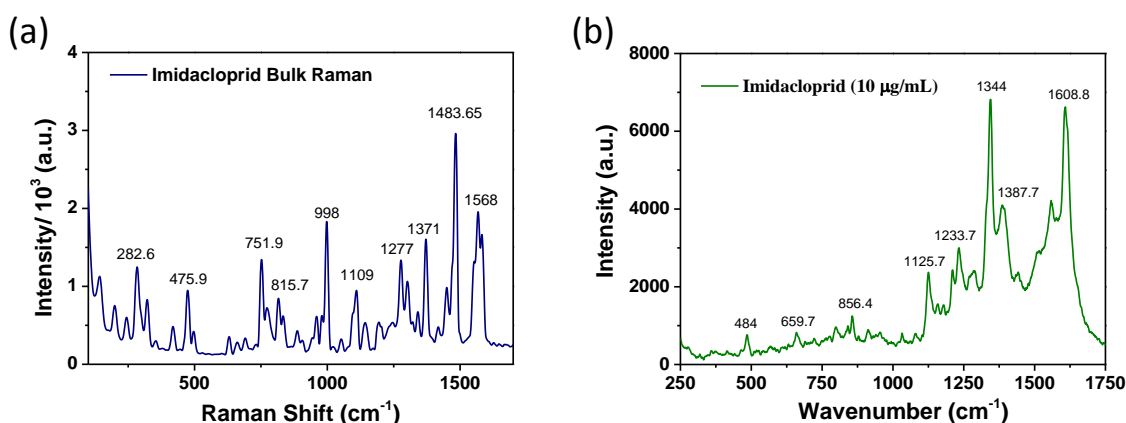
Figure 3.9: (a) Bulk Raman spectrum and (b) SERS spectrum (10 µg/mL) of imidacloprid using fabricated silver coated PVDF substrates.

3.3.3.5 *Vibrational Analysis of Imidacloprid*

The imidacloprid molecule consists of a chloropyridine ring linked with a carbon to an imidazole ring structure. For assignation purposes, we name these structures, ring 1 and ring 2, respectively. The structure of imidacloprid, with atomic numbering labels used in this study, is given in Figure 3.10.

Raman	SERS	DFT Scaled	Vibrational Assignments
-	-	3452.3	νN6-C24
-	-	3109.6	νC13,14 - H25,27 sym
-	-	3092.83	νC13,14 - H25,27 as
3051	-	3043.66	νC15-C26
2988	-	3008.08	νC10-H21
2970	-	2992.53	νC9-H19, C11-H23 as
2951	-	2982.53	νC9-H19, C11-H23 sym
2930	-	2933.884	νC11-H22
2900	-	2884.03	νC9-H18
-	-	2877.91	νC10-H20
1584.45	1607	1632/ 1606	νC12N4N5N6 as; δN6H24; νN7O2O3 as
1568.09	1568	1575/1547	CCC Stretching: νC13C14C15 as; νC17N8C16 as
1483.65	1464.07	1483.31	δC9H19,H18; δC11H23,H22
1451		1448.91	νC16C17C14 as; νC17N8; δHC14; δHC15; δHC16; δC10H20,H21
1371	1409	1376	νC16C17C14 sym; νC15N8C13 sym; ωC10H20H21
1302	1356.27	1320/1282	ωC9H19H18; ωC11H22H23; ωC10H20H21; δC14H25; νN7O2O3 sym
1277	1327	1279.75	νN7O2O3 sym; ωC9H1918; τC11H22H23; τC10H20H21; δHC15; δHC16
1241	1298.03	1253.77	Ring 1 stretching; τC10H20H21; ωC9H1918; ωC11H22H23; νC12N4N5N6 as; νN6N7
1195	1218	1217.61	τC9H18H19; τC11H22H23
1142	1190.94	1197	νC10C13; νC10C13C14C15 as; ωC10H20; ωC14H25; ωC15H26; ωC16H27;
1109	1162	1125.97	δH25C14C16H27; νC14C16;
998.43	987	1008.09	δC17C16N8; δC13C14C15
815	799	815.11	δC17C16N8, νC13C14C15C10 sym; νC17Cl1; ρC9H18H19; ρC11H23H24
751.931	740.628	768.22	O3O2N7N6 oop; Ring 2 breathing: [δN6N7C12, δC11N5C9]; ρC11H22H23; ρC9H18H19; δC10N4C13
691	677	683	C12N4N5N6 oop; ρC9C11-H sym; δC10N4; Ring 1 breathing: [δC10C14C15, νC17Cl1]
660	661	654	ωC12N4N5N6 oop; δC9C11N4; νC13C14C15; νC17Cl1; δC10N4C13
631	635	622	δN8C17C15; δC14C13C16; δC12N4C9C11

475.898	502.089	453	Ring 2 rocking: [ρC10N4C12N6 ρN6C12N4N5] δC13C10N4C12; νC17Cl1; ωC13C14C15; τN8C17C15;
320	320	306	ωN4C12N5; δN4C10C9 oop, δC12N5N16]; δC12N6N7O3
282.658	282.813	274	ρC10H20H21; ρC11H22H23; δC17Cl1
142.932	133.193	144.91	δN6N7O3; ρC11H22H23; ρC10C13N4

Table 3.2: Assignments of the most intense experimental vibrational normal modes for imidacloprid. The abbreviations are ν, stretching; ω, wagging; τ, twisting; ρ, rocking; δ, bending/scissoring; ip, in plane and oop, out of plane modes; sym and asym denote symmetric and asymmetric modes, respectively.
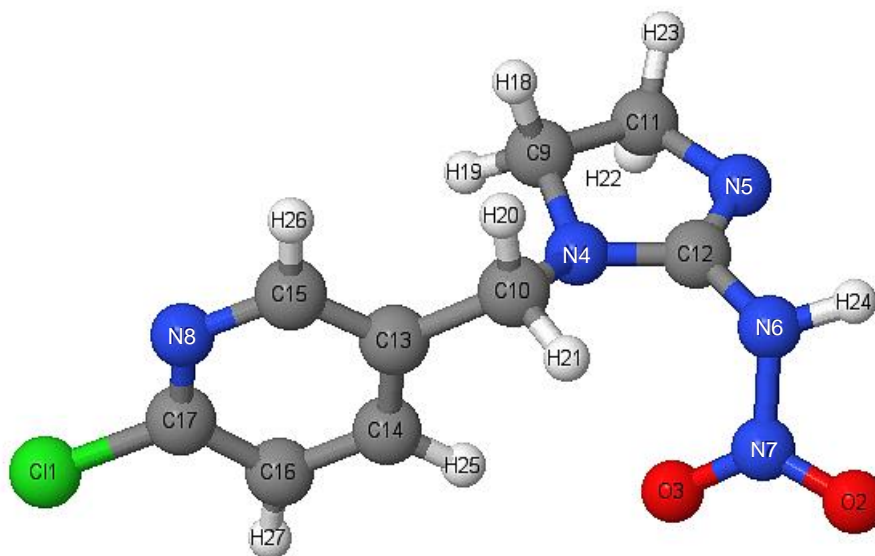
Figure 3.10: Structure of imidacloprid with atomic numbering.

3.3.3.5.1 C-H vibrations

To begin, all the CH vibrations were assigned to their corresponding Raman peaks. Firstly the C-H bonds in ring 1 are assigned, followed by C-H bonds adjoined in ring 2 (C9 and C11) and finally the C10-H vibrations were assigned.

There are 3 C-H bonds in the chloropyridine ring structure; C14, C15 and C16. Their stretching modes all vibrate as frequencies above ~3000 cm^{-1}, which is typical for C-H hetero-aromatic stretching vibrations.[64] These peaks are illustrated in the Raman spectrum of the extended spectral range for imidacloprid, in Figure 3.11. All these C-H stretching vibrations were assigned and are presented in at the beginning of Table 3.2.

There are several in-plane vibrations associated with the ring CH structures. The bending vibrations for C14H, C15H and C16H are observed at 1451 cm^{-1}, 1371 cm^{-1} and 1277 cm^{-1}, which were all coupled with stretching vibrations associated with Ring 1. Another band at 1109 cm^{-1} demonstrated the strong in-plane bending between the two hydrogens associated with C14 and C16 (H25 and H27). This band was also coupled with a C14-C16 stretching. The out of plane wagging modes for the pyridine ring C-H bonds are observed at 1142 cm^{-1} and coupled with a strong C13-C10 stretching mode.
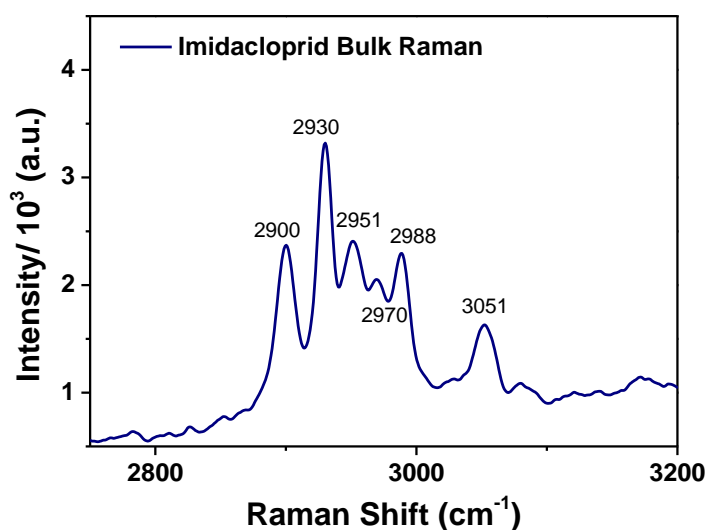
Figure 3.11: Raman spectrum for imidacloprid bulk powder at the higher wavenumber range.

The vibrational frequencies corresponding to C9H and C11H of ring 2 are also presented in Table 3.2. Briefly, the Raman bands observed at 2951 cm^{-1} and 2970 cm^{-1} are assigned to C9H and C11H symmetric and asymmetric stretching modes, respectively. The strong in plane bending vibration for C9-H and C11-H appears as the only observed band at 1484 cm^{-1}. No other C9H or C11H bending modes were seen in the simulated vibrations. The wagging out of plane vibrational mode of C9-H and C11-H was assigned as 1302 cm^{-1} in Raman spectra and was coupled with a C9-C11 weak stretching vibration. The other out of plane wagging modes were observed at 1277 cm^{-1} and 1241 cm^{-1}. The former band was coupled with CH bending vibrations in ring 1; and the latter band was strongly coupled with ring 1 stretching vibrations and weak asymmetric stretching in ring 2. The only twisting vibration for the C9-H and C11-H bonds was observed at 1195 cm^{-1}. Finally multiple C9-H and C11-H in-plane rocking modes were observed at 815 cm^{-1}, 751 cm^{-1},

691 cm^{-1} and 142 cm^{-1}. The first was coupled with a C10-C13 stretching mode and the other three bands were coupled with a C10-C13, N4 bending vibration.

The C10 symmetric stretching modes with H21 and H20 were observed at 3008 cm^{-1} and 2878 cm^{-1}, respectively in the simulated data. The only C10H bending vibration was assigned at 1451 cm^{-1} in the Raman spectrum. Multiple out of plane vibrational modes were observed for the C10-H20, H21 bonds in the Raman spectrum; including twisting vibrations at 1277 cm^{-1} and 1241 cm^{-1}, and wagging vibrations at 1371 cm^{-1}, 1302 cm^{-1} and 1142 cm^{-1}. Finally Raman band at 282 cm^{-1} was assigned to the in-plane rocking of H20 and H21 with C10.

3.3.3.5.2   Ring Vibrations

The vibrations for Ring 1 (chloropyridine) are studied first followed by the vibrations for ring 2 (imidazole). The 1568 cm^{-1} is one of the dominating Raman peaks and can be attributed to the pyridine ring stretching mode. In particular, this band represents the asymmetric stretching between C13 and C17 with their adjoining atoms (νC13C14C15 and νC17N8C16). Similarly, the band at 1451 cm^{-1} represents a C16-C17, C14 asymmetric stretching vibration and is coupled with a very weak C17-N8 stretch. A weak symmetric stretching at 1371 cm^{-1} was observed for C16 and C15 and their respective bonded atoms. The other ring stretching modes were observed at 1142 cm^{-1} and 815 cm^{-1}. The first band could be recognised as a ring breathing mode, but mainly consisted of an in-plane ring stretching from C13 to C14 and C15, with an asymmetric stretch to the out-of-ring C10. The second ring vibrations at 815 cm^{-1} contained a symmetric stretch from C13 to C14, C15 and C10; and a C17 ring bending with C16 and N8 which was coupled with a C17-Cl1 stretch. Some weak ring bending vibrations were observed at and 998 cm^{-1} and 691 cm^{-1}. The former band contains two bending modes C17-C16, N8, and C13- C14, C15, where by the C17 and C13 atoms are stationary. On the other hand, the latter band contains a C13-C14, C15 bend, whereby all the other ring atoms are vibrating with the bending mode, including a C17-Cl1 stretch. There is also weak ring vibration at 660 cm^{-1} consisting of a C13 bend with C14 and C15 coupled with a C17-Cl1 stretch and C10 bending with C13 and N4. Finally, the Raman peak at 631 cm^{-1} exhibited the strongest bending vibrations for the pyridine ring, specifically, the symmetric bending of C14 with C13/ C16 and N8 with C15/ C17 which was coupled with a weak ring 2 bending vibration,

C9-N4, C11. The Raman band at 476 cm^{-1} attributed to the only out of plane wagging of the pyridine ring, in particular, the C13 and C17 atoms are vibrating in the opposite direction to the other 4 atoms in the ring. This band is coupled with a C17Cl1 stretching and the bending of C10 with C13 and N4.

Raman vibrations associated with the C9 and C11 atoms of ring 2 were mostly discussed in the above "CH vibrations" section. Subsequently we assigned the remaining ring modes and also included vibrations involving the C12 carbon and its surrounding 3 nitrogen atoms. The C9-C11 stretching is observed at 982 cm^{-1}, in the simulated data. Due to the orientation of imidacloprid the majority of the imidazole ring modes were observed as out-of plane vibrations. However in-plane rocking and breathing modes were observed at 475 cm^{-1} and 751 cm^{-1}, respectively. The former involved rocking of the entire ring, in-plane, across the C10-N4-C12-N6 bond, while the atoms C10 and N6 remained stationary. The Raman band at 320 cm^{-1} was assigned as a ring wagging, mainly involving vibration of the N4-C12-N5 bond out-of-plane. A strong C12-N asymmetric stretching was observed at 1584 cm^{-1} in the Raman spectrum, which is one of the characteristic peaks for imidacloprid (1607 cm^{-1} in the SERS spectrum). A second weaker asymmetric stretching was seen at 1241 cm^{-1}. The common C12-N wagging vibrations were observed at 691 cm^{-1} and 660 cm^{-1}, whereby the C12 vibrated out-of-plane in opposite directions to the three surrounding nitrogen atoms. The latter band was coupled with the bending of C9 with N4 and C11.

3.3.3.5.3 N-O and C-N Vibrations

In this section, all the peaks associated with the nitro-structure were assigned; first the N7-O2, O3 modes were investigated, followed by the vibrations between N6-N7, and finally the N-H bond was studied. The N7-O symmetric and asymmetric stretching vibrations occur at 1302 cm^{-11} and 1584 cm^{-1}, respectively. The former is coupled with a weak N6-N7 stretch and the latter is coupled with the strong N6-H24 bending mode. These are two well resolved bands in both the Raman and SERS spectra, which compare well to the nitroalkane stretching reported in the literature.[64] A weak symmetric N-O stretching was also found at 1277 cm^{-1}. The out of plane wagging vibration of N7-O is observed at 751 cm^{-1}; while the bending vibration of N6N7O2O3 occurs at 142 cm^{-1}.

The N6-N7 stretching was observed at 1241 cm^{-1} in the Raman spectrum, with a second strong stretching vibration revealed at ~1050 cm^{-1} in the simulated data. A strong in-plane N6N7O2 bending mode was also observed at 443 cm^{-1} in the simulated data. The stretching vibration for N6-H24 was observed as highest mode in the simulated data, at 3452 cm^{-1}. The out of plane N-H wagging vibration for N6-H24 was observed at 631 cm^{-1} and a similar out of plane wagging vibration with N6-C12,H24 was identified at 691 cm^{-1}.

3.3.4 Electrochemical Pathway for Neonicotinoid Sensing

Following electrochemical characterisation, nanowire arrays were subjected to the detection of neonicotinoid pesticides. Electrochemical Imidacloprid detection is well documented in the literature,[65-68] whereas, to our knowledge, detection of Clothianidin has not been studied. Nanowire arrays were applied to the detection of both clothianidin and imidacloprid. The voltammetric reduction signals observed for these compounds arise from the reduction of NO$_2$ groups to NH$_2$ groups, via a two- step electro-reduction pathway, illustrated in Figure 3.12, which is well documented in the literature[67, 69-71]. Firstly, a nitro intermediate followed by a hydroxylamine intermediate are formed via a $4e^-/4H^+$ electron and proton transfer reaction. The hydroxylamine group is further reduced to an amine via a $2e^-/2H^+$ electron and proton transfer reaction.

Compared to CV, SWV is a very sensitive electrochemical method that permits fast scan rates, significantly reduces background noise and as such is suitable for remote electroanalysis. Combining this approach with the sensitivity of nanowire electrodes permits detection in simple acetate buffer thereby obviating the requirement for more complex mixed acid solutions such as Britton-Robinson buffer.[67, 72, 73] Guzvany *et al.* demonstrated previously that pH 4 to 9 is optimum for imidacloprid determination.[65] In fact, in alkaline medium the nitroguanidine functional group of imidacloprid undergoes alkaline hydrolysis.[74] Papp *et al.* showed later using linear sweep voltammetry (LSV) that the reduction peak of imidacloprid shifts towards anodic potential with increasing pH.[72] On this basis a pH of 5 was chosen for imidacloprid determination.
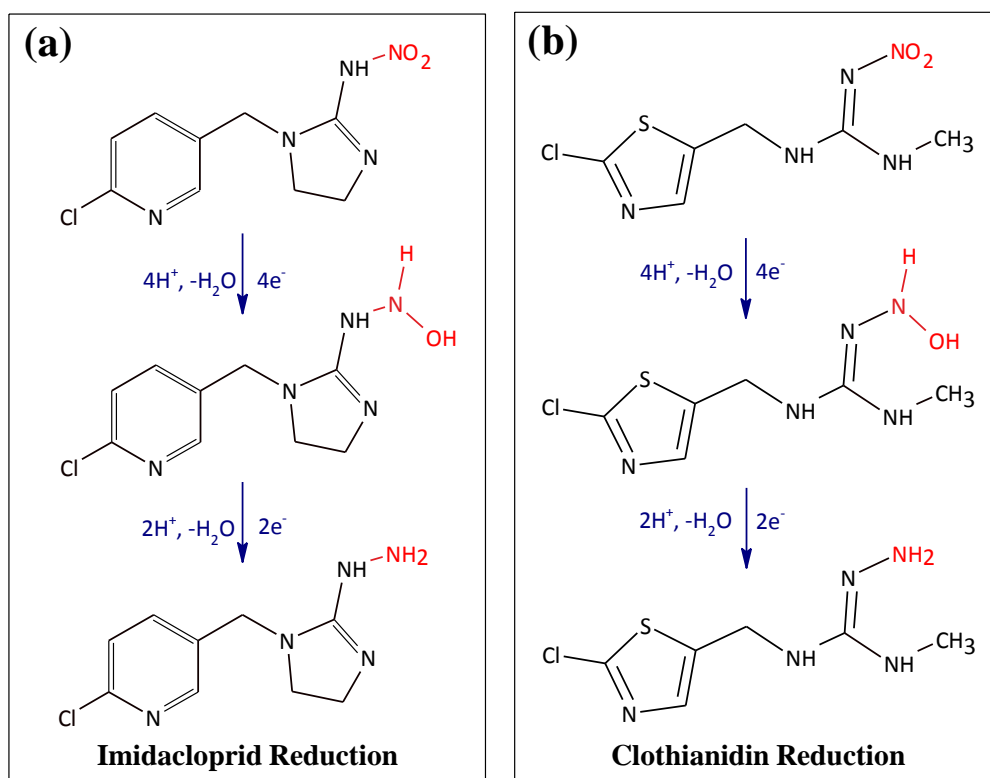
Figure 3.12: Reduction pathway of (a) Imidacloprid and (b) clothianidin pesticides.

3.3.5 Combined SERS and Electrochemical Sensing of Neonicotinoids

3.3.5.1 Detection of Clothianidin

Clothianidin solutions of 1 ng/mL were subjected to SERS analysis. The SERS spectrum of clothianidin is shown in Figure 3.13. Although the peaks are not well resolved at lower wavenumbers, there are large peaks at 946, 1176, 1335, 1557 and 1605 cm^{-1}, which correspond to the previously established characteristic peaks of clothianidin at 947, 1152, 1318, 1532 and 1570 cm^{-1} in the Raman spectrum. This demonstrated that clothianidin can be detected at lower concentrations by SERS using a simple drop and dry method. These tests can be easily performed using a portable Raman system.
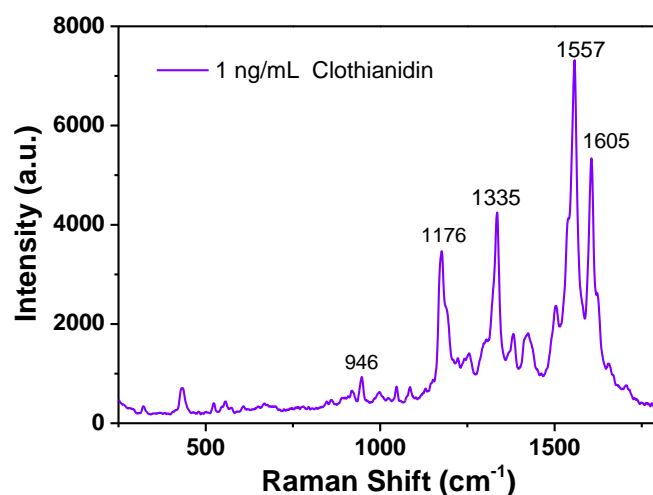
Figure 3.13: SERS detection of clothianidin at 1 ng/mL using the fabricated silver coated PVDF substrates.

Simultaneously the same solution was challenged to SWV detection to assess the reduction of molecule at a low concentration. Figure 3.14 (a) shows typical SWV following background subtraction for clothianidin in the concentration range of 0.88 nM – 378 nM (0.22 ng/mL – 94.57 ng/mL). The reduction peaks at -1.07 V and -1.18V represent the two-step reduction of the nitro group of imidacloprid; supporting the reduction mechanism for nitro group reduction. The first reduction is attributed to the four electron transfer of the nitro group to yield the corresponding hydroxylamine derivative. The second reduction wave ~-1.18V is attributed to the two electron transfer from the hydroxylamine to produce its amine derivative.[75, 76] To demonstrate the suitability of the nanowire arrays as sensors for clothianidin, calibration experiments were undertaken to examine the effects of increasing concentration on the SWV signals using a serial addition approach. Figure 3.14 (b) shows the calibration plot obtained by plotting the peak height at ~-1.07 V versus log of concentration. Each measurement was undertaken five times to monitor the stability and reproducibility of the electrodes and the error bars represent one standard deviation from the mean value of the five replicates. The measured detection limit for clothianidin was 0.22 ng/mL (0.88 nM) and a calibration coefficient of $R^2 = 0.984$ shows good linearity with increasing concentration in this concentration range.

Figure 3.14: (a) SWV of Clothianidin recorded at different concentrations in acetate buffer (pH 5) versus on-chip Pt pseudo reference electrode. (b) Calibration plot of peak current vs. log concentration of clothianidin solution. Error bars are included in clear data points.

3.3.5.2 Detection of Imidacloprid

In a similar manner, SERS measurements were undertaken on imidacloprid using the parameters described above for a 1 ng/mL solution. The SERS spectrum for imidacloprid is presented in Figure 3.15.
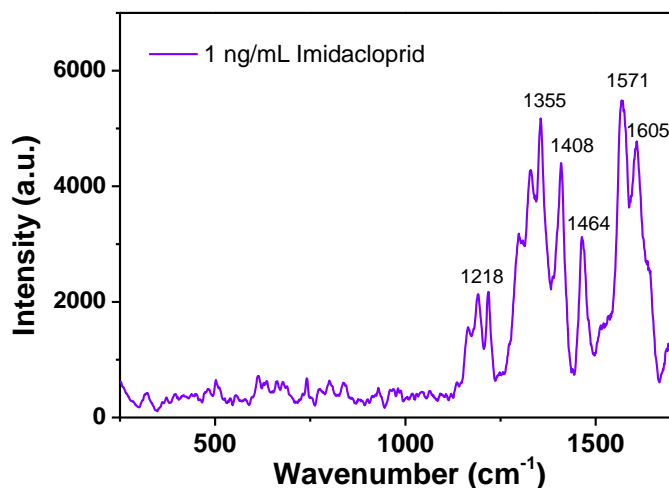
Figure 3.15: SERS detection of imidacloprid at 1 ng/mL using the fabricated silver coated PVDF substrates.

Again the peaks at high wavenumbers, which correspond to the characteristic peaks of the molecule, are well resolved. Bands at 1218, 1355, 1408, 1464, 1571 and 1605 cm^{-1}, labelled in Figure 3.15, represent similar peak in the Raman spectrum (refer back to

Figure 3.9 (a)). They are mainly attributed to the bending and wagging of the ring structures in imidacloprid. To further examine the 1 ng/mL pesticide solution, SWV was employed. We predicted that the reduction of the nitro-group would be well resolved, like for clothianidin. Figure 3.16 (a) shows the SWV of imidacloprid in the concentration range of 8 nM – 4.1 μM (2.15 ng/mL – 1.05 μg/mL) following background subtraction. The voltammogram shows the two reduction peaks representing the nitro-group reduction of imidacloprid with the peaks at ~ -1.05 and -1.2V being attributed to the first and second reduction steps, respectively. The quantitative determination of imidacloprid at gold electrodes is based on the linear relationship between peak current intensity (nA) and imidacloprid concentration. Figure 3.16 (b) shows the calibration plot obtained by plotting the peak current at approx. -1.2V versus log of concentration. Again, each measurement was undertaken five times to monitor the stability and reproducibility of the electrodes and the error bars represent one standard deviation from the mean value of the five replicates. The measured limit of detection was 2.14 ng/mL (8 nM) and a coefficient of $R^2 = 0.989$ shows good linearity with increasing concentration in this concentration range. This concentration range is lower than the lowest legal residue limit of ~10 ng/mL for food products.[77]
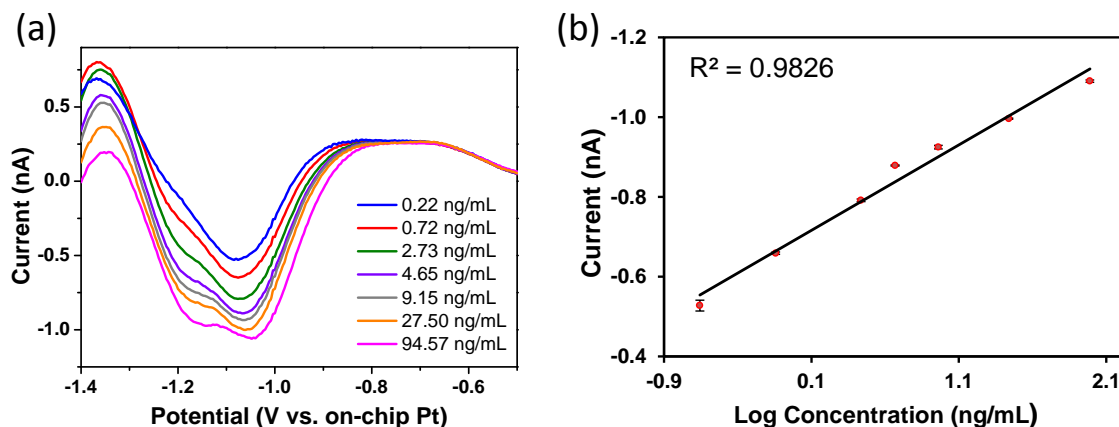

Figure 3.16: (a) SWV of Imidacloprid recorded at different concentrations in acetate buffer (pH 5) versus on-chip Pt pseudo reference electrode. (b) Calibration curve of peak current vs. log concentration of imidacloprid. Error bars are included in clear data points.

3.3.6 State of the art

The results for neonicotinoid detection obtained using our nanowire array devices were compared against those reported in the literature and typ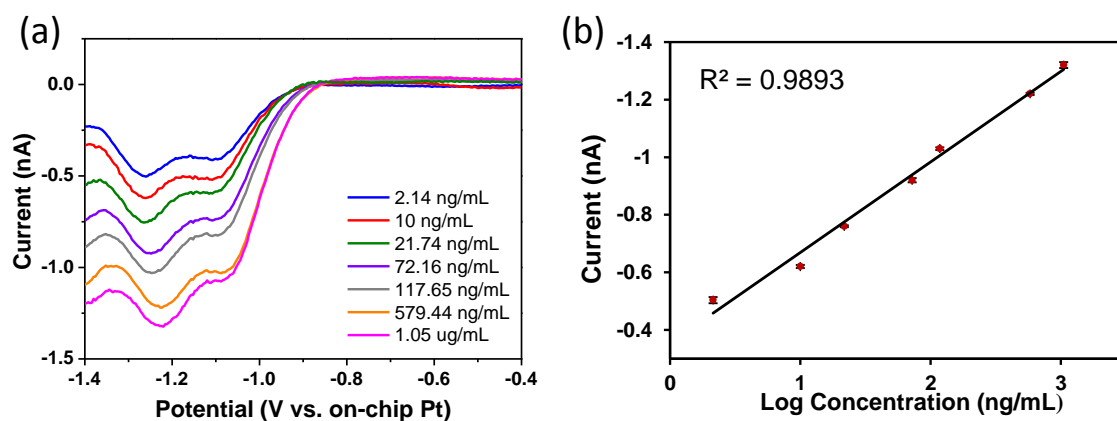ical values shown in Table 3.3. As can be seen the measured LOD was significantly better than solid state electrochemical measurements and on a par with results achieved using high-end laboratory instrumentation. The reproducibility of SWV combined with nanoelectrodes is a useful analytical tool and clearly demonstrates the viability of this approach to the selective detection of neonicotinoid species.

Detection method	Electrode Type/ Diameter	Neonicotinoid	Detected Linear Range	Ref
Differential-Pulse Voltammetry	Bismuth-Film Modified GCE	Clothianidin	6810 – 240300 nM	[78]
	Carbon paste electrode (d = 2 mm)	Imidacloprid	6700 – 117400 nM	[68]
	Hanging Mercury drop electrode	Imidacloprid	3910 – 4700 nM	[66]
	Nanosilver/SDS GCE (d = 3 mm)	Imidacloprid	500 – 3500 nM	[67]
	Hanging Mercury drop electrode	Imidacloprid	39 – 782.8 nM	[76]
Cyclic voltammetry	Glassy carbon Electrode (GCE)	Imidacloprid	10.9 –1956 µM	[65]
	Nanosilver/SDS GCE (d = 3 mm)	Imidacloprid	1000 – 7000 nM	[67]
	Reduced graphene oxide GCE (d = 3 mm)	Imidacloprid	750 – 70000 nM	[79]
Square wave Voltammetry	Silver-Amalgam Film Electrode	Clothianidin	6050 – 216600 nM	[73]
	Hanging Mercury drop electrode	Imidacloprid	20 – 500 nM	[75]
	Au nanowire electrode	**Imidacloprid**	**8 – 4100 nM**	**This work**
		Clothianidin	**0.88 – 378 nM**	
High performance liquid chromatography	-	Imidacloprid	290 – 23470 nM	[68]
	-	Imidacloprid	39 – 19560 nM	[80]
	-	Clothianidin	10 – 2000 nM	[81]
Enzyme-linked immunosorbent assays	-	Imidacloprid	20 – 490 nM	[25]
	-	Clothianidin	11 – 3080 nM	[82]
Gas Chromatography – Mass Spectroscopy	-	Clothianidin	40 – 16020 nM	[83]
Tandem Mass Spectrometry	-	Clothianidin	40 – 16020 nM	[84]

Table 3.3: Detection methods for clothianidin and imidacloprid in the literature compared with our results.

3.4 Conclusion

In this chapter, we employ the fabricated SERS subtraction for the environmental detection of neonicotinoid pesticides. Raman and SERS measurements were first undertaken, to ensure the compounds were Raman active. Following successful determination of both clothianidin and imidacloprid, vibrational analysis of the two compounds was undertaken, using a simulated model and algorithm designed by Julio Gutiérrez Moreno.

In this chapter we also present a hybrid electron beam photolithography technique that permits gold nanowire array electrodes, designed by Dr. Karen Dawson and Dr. Amelie Wahl.[33, 43, 52] These sensors offer the potential for enhancements in electroanalysis including: increased signal-to-noise ratio and increased sensitivity. Following this fabrication, clear and well defined characteristic reduction peaks of nitro groups from neonicotinoid insecticides were resolved using potential step SWV on gold nano-array electrodes. The gold nanowire electrodes permit LOD's of 0.22 mg/mL (0.88 nM) and 2.14 ng/mL (8 nM), for clothianidin and imidacloprid, respectively. The LOD's were simultaneously validated with SERS analysis on the prepared aqueous solutions, with the LOD being 1 ng/mL for both compounds. These detection limits are significantly higher than reported solid state electrochemical techniques and are on par with complex laboratory methods.

To our knowledge, this is the first demonstration of neonicotinoids detection on gold electrodes at the nanoscale which opens the door to future sensitive devices required for decentralised remote sensing of neonicotinoid insecticides. This is also the first SERS analysis and vibrational assignment of Clothianidin.

3.5 References

1.   Elbert, A.; Haas, M.; Springer, B.; Thielert, W.; Nauen, R., Applied Aspects of Neonicotinoid Uses in Crop Protection; *Pest Management Science,* **2008**, 64, 1099-1105.

2.   Jeschke, P.; Nauen, R., Neonicotinoids—from Zero to Hero in Insecticide Chemistry; *Pest Management Science,* **2008**, 64, 1084-1098.

3.   Nauen, R.; Bretschneider, T., New Modes of Action of Insecticides; *Pesticide Outlook,* **2002**, 13, 241-245.

4.   Tomizawa, M.; Casida, J.E., Neonicotinoid Insecticide Toxicology: Mechanisms of Selective Action; *Annual Review of Pharmacology and Toxicology,* **2005**, 45, 247-268.

5.   Henry, M.; Beguin, M.; Requier, F.; Rollin, O.; Odoux, J.-F.; Aupinel, P.; Aptel, J.; Tchamitchian, S.; Decourtye, A., A Common Pesticide Decreases Foraging Success and Survival in Honey Bees; *Science,* **2012**, 336, 348-350.

6.   Whitehorn, P.R.; O'connor, S.; Wackers, F.L.; Goulson, D., Neonicotinoid Pesticide Reduces Bumble Bee Colony Growth and Queen Production; *Science,* **2012**, 336, 351-352.

7.   Miligi, L.; Costantini, A.S.; Veraldi, A.; Benvenuti, A.; Will; Vineis, P., Cancer and Pesticides; *Annals of the New York Academy of Sciences,* **2006**, 1076, 366-377.

8.   Meinert, R.; Schüz, J.; Kaletsch, U.; Kaatsch, P.; Michaelis, J., Leukemia and Non-Hodgkin's Lymphoma in Childhood and Exposure to Pesticides: Results of a Register-Based Case-Control Study in Germany; *American Journal of Epidemiology,* **2000**, 151, 639-646.

9.   Betarbet, R.; Sherer, T.B.; Mackenzie, G.; Garcia-Osuna, M.; Panov, A.V.; Greenamyre, J.T., Chronic Systemic Pesticide Exposure Reproduces Features of Parkinson's Disease; *Nature Neuroscience,* **2000**, 3, 1301-1306.

10.   Salameh, P.; Baldi, I.; Brochard, P.; Raherison, C.; Saleh, B.A.; Salamon, R., Respiratory Symptoms in Children and Exposure to Pesticides; *European Respiratory Journal,* **2003**, 22, 507-512.

11.   Kimura-Kuroda, J.; Komuta, Y.; Kuroda, Y.; Hayashi, M.; Kawano, H., Nicotine-Like Effects of the Neonicotinoid Insecticides Acetamiprid and Imidacloprid on Cerebellar Neurons from Neonatal Rats; *PloS one,* **2012**, 7, e32432.

12.   Duzguner, V.; Erdogan, S., Acute Oxidant and Inflammatory Effects of Imidacloprid on the Mammalian Central Nervous System and Liver in Rats; *Pesticide Biochemistry and Physiology,* **2010**, 97, 13-18.

13.   Hanke, W.; Jurewicz, J., The Risk of Adverse Reproductive and Developmental Disorders Due to Occupational Pesticide Exposure: An Overview of Current Epidemiological Evidence; *International Journal of Occupational Medicine and Environmental Health,* **2004**, 17, 223-243.

14.   Blacquiere, T.; Smagghe, G.; Van Gestel, C.A.; Mommaerts, V., Neonicotinoids in Bees: A Review on Concentrations, Side-Effects and Risk Assessment; *Ecotoxicology,* **2012**, 21, 973-92.

15.   Wood, T.J.; Goulson, D., The Environmental Risks of Neonicotinoid Pesticides: A Review of the Evidence Post 2013; *Environmental Science and Pollution Research,* **2017**, 24, 17285-17325.

16.   Gupta, S.; Gajbhiye, V.T.; Kalpana; Agnihotri, N.P., Leaching Behavior of Imidacloprid Formulations in Soil; *Bulletin of Environmental Contamination and Toxicology,* **2002**, 68, 502-508.

17.   Iwasa, T.; Motoyama, N.; Ambrose, J.T.; Roe, R.M., Mechanism for the Differential Toxicity of Neonicotinoid Insecticides in the Honey Bee, Apis Mellifera; *Crop Protection,* **2004**, 23, 371-378.

18.   Cresswell, J.E., A Meta-Analysis of Experiments Testing the Effects of a Neonicotinoid Insecticide (Imidacloprid) on Honey Bees; *Ecotoxicology,* **2011**, 20, 149-157.

19.   Laurino, D.; Porporato, M.; Patetta, A.; Manino, A., Toxicity of Neonicotinoid Insecticides to Honey Bees: Laboratory Tests; *Bulletin of Insectology,* **2011**, 64, 107-113.

20.   Blacquière, T.; Smagghe, G.; Van Gestel, C.M.; Mommaerts, V., Neonicotinoids in Bees: A Review on Concentrations, Side-Effects and Risk Assessment; *Ecotoxicology,* **2012**, 21, 973-992.

21.   European Commission, Commission Implementing Regulation (Eu) No 485/2013 of 24 May 2013 Amending Implementing Regulation (Eu) No 540/2011, as Regards the Conditions of Approval of the Active Substances Clothianidin, Thiamethoxam and Imidacloprid, and Prohibiting the Use and Sale of Seeds Treated with Plant Protection Products Containing Those Active Substances; *Official Journal of the European Union,* **2013**, 139, 12-14.

22.   Ferrer, I.; Thurman, E.M.; Fernández-Alba, A.R., Quantitation and Accurate Mass Analysis of Pesticides in Vegetables by Lc/Tof-Ms; *Analytical Chemistry,* **2005**, 77, 2818-2825.

23.   European Food Safety Authority, The 2014 European Union Report on Pesticide Residues in Food; *EFSA Journal,* **2016**, 14, e04611-n/a.

24.   European Food Safety Authority, Peer Review of the Pesticide Risk Assessment for Bees for the Active Substance Clothianidin Considering the Uses as Seed Treatments and Granules; *EFSA Journal,* **2018**, 16, e05177.

25.   Lee, J.K.; Ahn, K.C.; Park, O.S.; Kang, S.Y.; Hammock, B.D., Development of an Elisa for the Detection of the Residues of the Insecticide Imidacloprid in Agricultural and Environmental Samples; *Journal of Agricultural and Food Chemistry,* **2001**, 49, 2159-2167.

26.   Watanabe, E.; Baba, K.; Eun, H.; Miyake, S., Application of a Commercial Immunoassay to the Direct Determination of Insecticide Imidacloprid in Fruit Juices; *Food Chemistry,* **2007**, 102, 745-750.

27.   Obana, H.; Okihashi, M.; Akutsu, K.; Kitagawa, Y.; Hori, S., Determination of Acetamiprid, Imidacloprid, and Nitenpyram Residues in Vegetables and Fruits by High-Performance Liquid Chromatography with Diode-Array Detection; *Journal of Agricultural and Food Chemistry,* **2002**, 50, 4464-4467.

28.   Liu, S.; Zheng, Z.; Wei, F.; Ren, Y.; Gui, W.; Wu, H.; Zhu, G., Simultaneous Determination of Seven Neonicotinoid Pesticide Residues in Food by Ultraperformance Liquid Chromatography Tandem Mass Spectrometry; *Journal of Agricultural and Food Chemistry,* **2010**, 58, 3271-3278.

29.   Aguera, A.; Almansa, E.; Malato, S.; Maldonado, M.; Fernandez-Alba, A., Evaluation of Photocatalytic Degradation of Imidacloprid in Industrial Water by Gc-Ms and Lc-Ms; *Analysis,* **1998**, 26, 245-251.

30.   Navalón, A.; González-Casado, A.; El-Khattabi, R.; Vilchez, J.L.; Fernández-Alba, A.R., Determination of Imidacloprid in Vegetable Samples by Gas Chromatography–Mass Spectrometry; *Analyst,* **1997**, 122, 579-581.

31.   Ding, X.; Zhang, W.; Cheng, D.; He, J.; Yang, K.-L., Oligopeptides Functionalized Surface Plasmon Resonance Biosensors for Detecting Thiacloprid and Imidacloprid; *Biosensors and Bioelectronics,* **2012**, 35, 271-276.

32.   VíLchez, J.L.; Valencia, M.C.; Navalón, A.; Molinero-Morales, B.; Capitán-Vallvey, L.F., Flow Injection Analysis of the Insecticide Imidacloprid in Water Samples with Photochemically Induced Fluorescence Detection; *Analytica Chimica Acta,* **2001**, 439, 299-305.

33.   Dawson, K.; Baudequin, M.; Sassiat, N.; Quinn, A.J.; O'riordan, A., Electroanalysis at Discrete Arrays of Gold Nanowire Electrodes; *Electrochimica Acta,* **2013**, 101, 169-176.

34.   Arrigan, D.W.M., Nanoelectrodes, Nanoelectrode Arrays and Their Applications; *Analyst,* **2004**, 129, 1157-1165.

35.   Compton, R.G.; Wildgoose, G.G.; Rees, N.V.; Streeter, I.; Baron, R., Design, Fabrication, Characterisation and Application of Nanoelectrode Arrays; *Chemical Physics Letters,* **2008**, 459, 1-17.

36.   Casida, J.E., Neonicotinoid Metabolism: Compounds, Substituents, Pathways, Enzymes, Organisms, and Relevance; *Journal of Agricultural and Food Chemistry,* **2011**, 59, 2923-2931.

37.   Albrecht, M.G.; Creighton, J.A., Anomalously Intense Raman Spectra of Pyridine at a Silver Electrode; *Journal of the American Chemical Society,* **1977**, 99, 5215-5217.

38.   Fleischmann, M.; Hendra, P.J.; Mcquillan, A.J., Raman Spectra of Pyridine Adsorbed at a Silver Electrode; *Chemical Physics Letters,* **1974**, 26, 163-166.

39.   Otto, A.; Mrozek, I.; Grabhorn, H.; Akemann, W., Surface-Enhanced Raman Scattering; *Journal of Physics: Condensed Matter,* **1992**, 4, 1143.

40.   Stiles, P.L.; Dieringer, J.A.; Shah, N.C.; Duyne, R.P.V., Surface-Enhanced Raman Spectroscopy; *Annual Review of Analytical Chemistry,* **2008**, 1, 601-626.

41.   Creedon, N.C.; Lovera, P.; Furey, A.; O'riordan, A., Transparent Polymer-Based Sers Substrates Templated by a Soda Can; *Sensors and Actuators B: Chemical,* **2018**, 259, 64-74.

42.   Dawson, K.; Baudequin, M.; Sassiat, N.; Quinn, A.J.; O'riordan, A., Electroanalysis at Discrete Arrays of Gold Nanowire Electrodes; *Electrochimica Acta,* **2013**, 101, 169-176.

43.   Wahl, A.; Dawson, K.; Machale, J.; Barry, S.; Quinn, A.; O'riordan, A., Gold Nanowire Electrodes in Array: Simulation Study and Experiments; *Faraday Discussions,* **2013**.

44.   Becke, A.D., Density-Functional Thermochemistry. Iii. The Role of Exact Exchange; *The Journal of chemical physics,* **1993**, 98, 5648-5652.

45.   Weigend, F.; Ahlrichs, R., Balanced Basis Sets of Split Valence, Triple Zeta Valence and Quadruple Zeta Valence Quality for H to Rn: Design and Assessment of Accuracy; *Physical Chemistry Chemical Physics,* **2005**, 7, 3297-3305.

46.   Pepin, J.F.; Riou, A.; Renault, T., Rapid and Sensitive Detection of Ostreid Herpesvirus 1 in Oyster Samples by Real-Time Pcr; *Journal of Virological Methods,* **2008**, 149, 269-276.

47.   Grimme, S., Semiempirical Gga-Type Density Functional Constructed with a Long-Range Dispersion Correction; *Journal of computational chemistry,* **2006**, 27, 1787-1799.

48.   Peng, C.; Ayala, P.Y.; Schlegel, H.B.; Frisch, M.J., Using Redundant Internal Coordinates to Optimize Equilibrium Geometries and Transition States; *Journal of Computational Chemistry,* **1996**, 17, 49-56.

49.   Deglmann, P.; Furche, F.; Ahlrichs, R., An Efficient Implementation of Second Analytical Derivatives for Density Functional Methods; *Chemical physics letters,* **2002**, 362, 511-518.

50.   Deglmann, P.; Furche, F., Efficient Characterization of Stationary Points on Potential Energy Surfaces; *The Journal of Chemical Physics,* **2002**, 117, 9535-9538.

51.   Merrick, J.P.; Moran, D.; Radom, L., An Evaluation of Harmonic Vibrational Frequency Scale Factors; *The Journal of Physical Chemistry A,* **2007**, 111, 11683-11700.

52.   Barry, S.; Dawson, K.; Correa, E.; Goodacre, R.; O'riordan, A., Highly Sensitive Detection of Nitroaromatic Explosives at Discrete Nanowire Arrays; *Faraday Discussions,* **2013**, 164, 283-293.

53.   Moreira, A.a.G.; De Lima-Neto, P.; Caetano, E.W.S.; Barroso-Neto, I.L.; Freire, V.N., The Vibrational Properties of the Bee-Killer Imidacloprid Insecticide: A Molecular Description; *Spectrochimica Acta Part A: Molecular and Biomolecular Spectroscopy,* **2017**, 185, 245-255.

54.   Zhang, F.; Zhang, Y.; Ni, H.; Ma, K.; Li, R., Experimental and Dft Studies on the Vibrational, Electronic Spectra and Nbo Analysis of Thiamethoxam; *Spectrochimica Acta Part A: Molecular and Biomolecular Spectroscopy,* **2014**, 118, 162-171.

55.   Cañamares, M.V.; Feis, A., Surface-Enhanced Raman Spectra of the Neonicotinoid Pesticide Thiacloprid; *Journal of Raman Spectroscopy,* **2013**, 44, 1126-1135.

56.   Hou, R.; Pang, S.; He, L., In Situ Sers Detection of Multi-Class Insecticides on Plant Surfaces; *Analytical Methods,* **2015**, 7, 6325-6330.

57.   Khaikin, L.S.; Grikina, O.E.; Lokshin, B.V.; Dyugaev, K.P.; Astakhov, A.M., Vibrational Spectra of 1,1,3,3-Tetramethyl-2-Nitroguanidine and Their Interpretation with the Use of Scaling of Quantum-Chemical Force Field; *Russian Chemical Bulletin,* **2008**, 57, 499-505.

58.   Socrates, G., Infrared and Raman Characteristic Group Frequencies: Tables and Charts; *John Wiley & Sons,* **2001**.

59.   Zhu, X.-M.; Zhang, S.-Q.; Zheng, X.; Phillips, D.L., Resonance Raman Study of Short-Time Photodissociation Dynamics of the Charge-Transfer Band Absorption of Nitrobenzene in Cyclohexane Solution; *The Journal of Physical Chemistry A,* **2005**, 109, 3086-3093.

60.   Markham, L.M.; Mayne, L.C.; Hudson, B.S.; Zgierski, M.Z., Resonance Raman Studies of Imidazole, Imidazolium, and Their Derivatives: The Effect of Deuterium Substitution; *The Journal of Physical Chemistry,* **1993**, 97, 10319-10325.

61.   Sundaraganesan, N.; Ilakiamani, S.; Anand, B.; Saleem, H.; Joshua, B.D., Ftir, Ft-Raman Spectra and Ab Initio Dft Vibrational Analysis of 2-Amino-5-Chloropyridine; *Spectrochimica Acta Part A: Molecular and Biomolecular Spectroscopy,* **2006**, 64, 586-594.

62.   Kumar, M.; Srivastava, M.; Yadav, R.A., Vibrational Studies of Benzene, Pyridine, Pyridine-N-Oxide and Their Cations; *Spectrochimica Acta Part A: Molecular and Biomolecular Spectroscopy,* **2013**, 111, 242-251.

63.   Chen, L.; Gao, Y.; Xu, H.; Wang, Z.; Li, Z.; Zhang, R.-Q., The Mechanism of N-Ag Bonding Determined Tunability of Surface-Enhanced Raman Scattering of Pyridine on Mag (M = Cu, Ag, Au) Diatomic Clusters; *Physical Chemistry Chemical Physics,* **2014**, 16, 20665-20671.

64.   Lin-Vien, D.; Colthup, N.B.; Fateley, W.G.; Grasselli, J.G., The Handbook of Infrared and Raman Characteristic Frequencies of Organic Molecules; *Elsevier,* **1991**.

65.   Guzsvány, V.J.; Gaál, F.F.; Bjelica, L.J.; Ökrész, S.N., Voltammetric Determination of Imidacloprid and Thiamethoxam; *Journal of the Serbian Chemical Society,* **2005**, 70, 735-743.

66.   Kashid, L.; Pawar, N., Voltammetric Behaviour of Imidacloprid and Its Electrochemical Mineralization Assessment by Differential Pulse Polarography; *International Journal of Scientific and Research Publications,* **2015**.

67.   Kumaravel, A.; Chandrasekaran, M., Electrochemical Determination of Imidacloprid Using Nanosilver Nafion®/Nanotio2 Nafion® Composite Modified Glassy Carbon Electrode; *Sensors and Actuators B: Chemical,* **2011**, 158, 319-326.

68.   Papp, Z.; Švancara, I.; Guzsvány, V.; Vytřas, K.; Gaál, F., Voltammetric Determination of Imidacloprid Insecticide in Selected Samples Using a Carbon Paste Electrode; *Microchimica Acta,* **2009**, 166, 169-175.

69.   Guzsvány, V.; Kádár, M.; Gaál, F.; Tóth, K.; Bjelica, L., Rapid Differential Pulse Polarographic Determination of Thiamethoxam in Commercial Formulations and Some Real Samples; *Microchimica Acta,* **2006**, 154, 321-328.

70.   Guziejewski, D.; Skrzypek, S.; Ciesielski, W., Application of Catalytic Hydrogen Evolution in the Presence of Neonicotinoid Insecticide Clothianidin; *Food Analytical Methods,* **2012**, 5, 373-380.

71.   Putek, M.; Guzsvány, V.; Tasić, B.; Zarębski, J.; Bobrowski, A., Renewable Silver-Amalgam Film Electrode for Rapid Square-Wave Voltammetric Determination of Thiamethoxam Insecticide in Selected Samples; *Electroanalysis,* **2012**, 24, 2258-2266.

72.   Papp, Z.; Guzsvány, V.; Svancara, I.; Vytras, K., Carbon Paste Electrodes for the Analysis of Some Agricultural Pollutants and Trace Metals; *Journal of Agricultural Science and Technology,* **2011**, 5, 85-92.

73.   Brycht, M.; Vajdle, O.; Zbiljić, J.; Papp, Z.; Guzsvány, V.; Skrzypek, S., Renewable Silver-Amalgam Film Electrode for Direct Cathodic Swv Determination of Clothianidin, Nitenpyram and Thiacloprid Neonicotinoid Insecticides Reducible in a Fairly Negative Potential Range; *International Journal of Electrochemical Science,* **2012**, 7.

74.   Zheng, W.; Liu, W., Kinetics and Mechanism of the Hydrolysis of Imidacloprid; *Pesticide Science,* **1999**, 55, 482-485.

75.   Guiberteau, A.; Galeano, T.; Mora, N.; Parrilla, P.; Salinas, F., Study and Determination of the Pesticide Imidacloprid by Square Wave Adsorptive Stripping Voltammetry; *Talanta,* **2001**, 53, 943-949.

76.   Navalón, A.; El-Khattabi, R.; González-Casado, A.; Vilchez, J., Differential-Pulse Polarographic Determination of the Insecticide Imidacloprid in Commercial Formulations; *Microchimica Acta,* **1999**, 130, 261-265.

77.   European Food Safety Authority, The 2011 European Union Report on Pesticide Residues in Food; *EFSA Journal 2014,* **2014**, 12, 3694.

78.   Guzsvány, V.; Papp, Z.; Zbiljić, J.; Vajdle, O.; Rodić, M., Bismuth Modified Carbon-Based Electrodes for the Determination of Selected Neonicotinoid Insecticides; *Molecules,* **2011**, 16, 4451.

79.   Kong, L.; Jiang, X.; Zeng, Y.; Zhou, T.; Shi, G., Molecularly Imprinted Sensor Based on Electropolmerized Poly(O-Phenylenediamine) Membranes at Reduced Graphene Oxide Modified Electrode for Imidacloprid Determination; *Sensors and Actuators B: Chemical,* **2013**, 185, 424-431.

80.   Obana, H.; Okihashi, M.; Akutsu, K.; Kitagawa, Y.; Hori, S., Determination of Neonicotinoid Pesticide Residues in Vegetables and Fruits with Solid Phase Extraction and Liquid Chromatography Mass Spectrometry; *Journal of Agricultural and Food Chemistry,* **2003**, 51, 2501-2505.

81.   Chen, M.-F.; Huang, J.-W.; Wong, S.-S.; Li, G.-C., Analysis of Insecticide Clothianidin and Its Metabolites in Rice by Liquid Chromatography with a Uv Detector; *Journal of Food and Drug Analysis,* **2005**, 13, 279-283.

82.   Li, M.; Sheng, E.; Cong, L.; Wang, M., Development of Immunoassays for Detecting Clothianidin Residue in Agricultural Products; *Journal of Agricultural and Food Chemistry,* **2013**, 61, 3619-3623.

83.   Li, L.; Jiang, G.; Liu, C.; Liang, H.; Sun, D.; Li, W., Clothianidin Dissipation in Tomato and Soil, and Distribution in Tomato Peel and Flesh; *Food Control,* **2012**, 25, 265-269.

84.   Kim, B.M.; Park, J.-S.; Choi, J.-H.; Abd El-Aty, A.M.; Na, T.W.; Shim, J.-H., Residual Determination of Clothianidin and Its Metabolites in Three Minor Crops Via Tandem Mass Spectrometry; *Food Chemistry,* **2012**, 131, 1546-1551.

Chapter 4   Bovine Viral Diarrhoea virus (BVDV) and antibody (BVDAb) detection in serum

4.1 Introduction

Bovine viral diarrhoea is a disease that is endemic in many countries worldwide. The causative agent, Bovine viral diarrhoea virus (BVDV), is a pestivirus. Viral infection results in reduced animal welfare, arising from immunosuppression, which has a significant economic cost for farmers through a combination of, e.g., aborted foetuses and greatly reduced milk production.[1-3] Its impact on animal health and the economics of livestock production has led to a number of European countries embarking on eradication schemes.[4, 5] Currently, Norway, Sweden, Denmark and Switzerland, have achieved BVDV eradication,[6-10] whilst the Republic of Ireland is close to eradication following five years of a compulsory testing programme and removal of persistently infected (PI) animals. Persistent infections in cattle occur when a foetus is exposed to BVDV *in utero* and subsequently develop an immunotolerance to the virus.[11] These PI cattle shed virus throughout their lives,[12] therefore in regions where BVDV is endemic, detection of virus and PI individuals is the method of choice to achieve eradication. [13, 14] In countries where prevalence was lower, serological screening to detect exposure to BVDV is the preferred choice. [15-17] For rapid progress to be made within an eradication programme, highly specific and sensitive assays are required. Moreover, the ability to be able to detect and identify both BVD virus and antibodies expressed by an animal to this virus is essential.[18]

Currently, there are a number of methods for diagnosing both persistent and transient BVDV infections including, several different types of enzyme-linked immunosorbent assays (ELISA),[19, 20] polymerase chain reaction (PCR) assays,[21, 22] and virus isolation techniques.[23, 24] The majority of these assays are laboratory-based techniques. As such, they often require postal submission of samples and subsequent reporting of results to both veterinarian and farmers. For example, the BVD national eradication scheme in the Republic of Ireland involves the collection of ear tissue samples from young calves by farmers using modified national identifier tags and submission of those samples by post to a designated laboratory for testing.[14] Both ELISA and PCR antigen detection

---

†This work has been submitted as "Bovine Viral Diarrhoea virus (BVDV) and antibody (BVDAb) detection in serum" in *Biosensors and Bioelectronics*, 2018

techniques have been employed throughout the scheme with the aim of identifying virus positive and potentially PI cattle.[3] While the individual techniques are relatively quick to perform on receipt of samples to the laboratory (90 to 180 minutes), delivery of samples, laboratory logistics, and reporting of results can delay PI detection, isolation and removal at farm level. The knock on effect of this is further unnecessary viral spread within a herd.

A number of 'in-field' tests for detection of BVDV have been described including; an immunochromatographic test, [25] rapid PCR test, [26] and ELISA-based method by IDEXX (SNAP, IDEXX Laboratories, Inc., Liebefeld, Switzerland). Each of the tests, however, are subject to constraints (i.e., long assay time, logistics of sample preparation and cost) which preclude their use from whole herd screening and incorporation into eradication schemes. More importantly, these tests focus on a single target, either BVD virus or antibody, (not both) meaning that two separate tests are required per animal adding cost to any disease eradication/surveillance scheme. An economical diagnostic device capable of rapid and sensitive detection of BVD (virus and antibody) in under 30 minutes still remains elusive.   In   this   regard,   we   aimed   to   investigate   application   of nanoelectrochemical-based sensor technology to potentially deliver rapid and early identification of a disease state on-farm.

Electrochemical biosensors constitute a promising group of sensing devices suitable for remote viral detection.[27-29] They permit high sensitivity, short analysis times, affordability, miniaturised platforms, with low sample consumption and the possibility for multiplexed measurements in complex samples.[30] Electrochemical biosensors can be classified based on the electrical property they measure and incude; amperometry, potentiometry and impedance spectroscopy (EIS). Of these, EIS represents a powerful method for the detection of target analytes at a functionalised sensor surface *via* an immunochemical interaction in a label-free manner.[31] EIS uses a periodic AC voltage amplitude applied to an electrode where a change of measured impedance at the electrode can be correlated to the amount of an analyte binding to the surface and thus provides a rapid and label-free method for disease detection.

In this chapter, we present the development of a new silicon chip impedimetric immunosensor device based on nanoband electrodes and demonstrate co-detection of both BVD antibodies and BVD virus in bovine serum. The chip comprises six individually addressable gold nanoband sensors as well as a gold counter and platinum pseudo-reference electrodes. Sensor chips were also designed with a MicroSD style edge connector to external electronic circuitry while also permitting simple removal and replacement of different chips essential for in-field analysis. The highly miniaturised nature of these electrodes provide a number of advantages, when compared to larger micro and macro electrodes, including: steady-state behaviour (particularly beneficial for EIS); low charge transfer resistance; high current density due to enhanced mass transport; low depletion of target molecules; low supporting electrolyte concentrations; and faster response times.[32, 33] In this work, different surface chemistries were examined, to develop a stable, reproducible process of immobilising biomolecules onto the electrode surface. The performance of the immunosensors was then assessed and characterised by challenging it with detection of virus and antibody target analytes in different media of increasing biological complexity, *via*, (i) spiked buffer solutions, (ii) diluted serum and (iii) whole serum. Finally, the sensor was challenged to discriminate between disease positive and disease negative serum samples from both TI and PI calves. BVD assay time-to-result is typically ~20 minutes demonstrating the potential of these nanoband electrochemical immunosensors for use in future on-farm diagnostic applications.

4.2 Experimental

4.2.1 Materials and Preparation of Standards

Bovine Viral Diarrhoea virus 1 (BVDV1) monoclonal antibody (RAE0823), specific to the envelop glycoprotein Erns antigen was purchased from APHA Scientific, Weighbridge, UK. Recombinant Purified Bovine Viral Diarrhoea Virus1 Erns protein (BVDR16-R-10) was purchased from Alpha Diagnostic International. Serum samples from BVDV persistently infected BVDV negative, BVDAb seropositive and BVDAb seronegative animals were provided by Teagasc (Moorepark, Cork, Ireland). Bovine IgG, Anti-Bovine IgG (whole molecule) antibody produced in rabbit, esterified biotin and streptavidin protein from *Streptomyces avidinii* affinity were purchased from Sigma Aldrich. Acetate buffer (10 mM; pH 4) and ethanolamine-HCl (1mM) were obtained from Sierra Sensors GmbH (Germany). HBS-EP buffer was prepared by mixing 10 mM HEPES, 150 mM NaCl, 3mM EDTA and 0.005% Tween-20 in DI water and adjusted to pH to 7.4 with 5% sodium hydroxide solution. All other reagents were purchased from Sigma Aldrich unless otherwise stated and used as received. Deionised water (resistance 18.2 MΩ cm^{-1}) was obtained using an ELGA Pure Lab Ultra system.

4.2.2 Design and Fabrication of the Chip

Gold nanoband electrodes, interconnection tracks, peripheral contact pads and on-chip gold counter (CE) and platinum pseudo-reference (RE) electrodes were fabricated on wafer-scale silicon substrates. The chips were fabricated similarly to those described by Dawson [34]. However, in this work, a new design was implemented wherein an on-chip electrical pin-out was included to permit facile electrical connection to external electronics using a PCB mounted microSD port. In this manner, chips could be easily swapped in and out enabling rapid analysis of multiple samples. Nanoband electrodes were fabricated on four inch diameter wafer silicon substrates bearing a ~300 nm layer of thermally grown silicon dioxide. Nanoband electrodes and wafer level optical alignment marks were first fabricated using a combination of optical lithography, metal evaporation (Ti 5 nm /Au 50 nm Temescal FC-2000 E-beam evaporator) and lift-off techniques to yield well-defined, stacked metallic (Ti/Au) nanoband (700 nm width, 50 nm height, 80 μm length) structures. Each chip consisted of six nanoband working electrodes (WE)

spaced 800 μm apart. A second optical lithographic and metal deposition (Ti 10 nm/Au 100 nm) process, aligning to the as-deposited wafer level alignment marks, was then undertaken to define a MicroSD pinout, interconnection tracks as well as counter and reference electrodes (500 μm wide x 10 mm long). These large counter (CE) and platinum reference (RE) were fabricated parallel to the nanoband working electrodes to ensure that all electrodes were equidistant from the both the CE and RE, see Figure 6.1 (a) and (b). Finally, a third optical lithographic and metal deposition and lift-off processes were undertaken, in a similar manner, to define the pseudo reference platinum (Ti/Pt 10/90 nm) reference electrode. To complete device fabrication, a ~500 nm thick insulating layer silicon nitride (Si_3N_4) was then blanket deposited by PECVD. Photolithography and reactive ion etching were then employed to selectively open windows (45 μm x 100 μm) in the insulating layer directly over the nanowire electrodes, as well as the on-chip counter and pseudo-reference electrodes and above the peripheral contact pads (to permit electrical contact).

A custom-built cell was fabricated to permit analysis of small sample volumes (~50 μL). The cell consisted of a base and lid fabricated from polymethylmethacrylate (PMMA). The base was milled to mount and hold the chip. The lid was fabricated so as to contain a central low volume well (volume of 100μL), sealed with an O-Ring (Polymax Ltd.) to prevent leaking of an analyte solution across a chip surface. Kalrez® O-rings were used to prevent chemical degradation of the O-ring. The inner diameter of the O-ring was ~5 mm selected such that all electrodes were suitably covered by the analyte solution. The holder was specifically designed so that when screwed together, the microSD primary contact pads protruded out of the holder to allow connection with a PCB mounted microSD port), see Figure 6.1 (c).

189

4.2.3 Chip Characterisation

4.2.3.1 Optical Characterisation at Nanoband Electrodes

Prior to use, nanoband electrodes were optically imaged using a calibrated microscope (Axioskop II, Carl Zeiss Ltd.) equipped with a charge-coupled detector camera (CCD; DEI-750, Optronics).

4.2.3.2 Electrochemical Analysis at Nanoband Electrodes

Electrochemical experiments were carried out using an Autolab Potentiostat/ Galvanostat PGSTAT128N (Metrohm Ltd, Utrecht, The Netherlands) controlled by the Autolab NOVA software. All experiments employed a standard three-electrode cell configuration using a single gold nanowire as the working electrode, versus the on-chip gold counter and platinum pseudo-reference electrodes. Each sensor working electrode were characterised by Cyclic voltammetry (CV) and faradaic electrochemical impedance spectroscopy (EIS), in a 10 mM PBS solution (pH = 7.4) containing 1 mM FcCOOH. For CV, the potential was cycled from -200 mV to +600 mV versus the on-chip platinum pseudo-reference electrode at a scan rate of 100 mV/s. The impedance measurements were performed over the frequency range from 100 mHz to 100 kHz at equilibrium potential of the FcCOOH (200 mV). The amplitude of the alternating voltage was 5 mV. All experiments were performed at room temperature in a Faraday cage.

4.2.4 Procurement of Serum samples (Teagasc)

Serum samples from BVDV PI's and uninfected animals have been acquired, in Ireland since 2008. Samples were collected (under license from the Health Products Regulatory Authority, Ireland, project number AE19132) by jugular venipuncture in calves and coccygeal venipuncture in cattle over six months of age. All samples were archived at -80ºC and were subsequently made available to this study. Concerning viral analysis, BVDV infected individuals ranged in age from one week to four years, while BVDV negative individuals ranged from one week to 9 years of age. Sera used in this study for virus detection, were first assayed in a commercial analytical lab using both AnDiaTec BoVir real time PCR kit (Kornwestheim, Germany) (2008 and 2009 samples) and the IDEXX BVDV PI X2 Test (Maine, USA) (2010 to 2017 samples). Animals were

classified as a PI if tested positive for BVDV on at least two occasions separated by an interval of at least three weeks.

Concerning antibody detection, BVDAb seropositive and seronegative samples were available from a Teagasc research project investigating the persistence of BVD antibodies in calves post-colostrum feeding. Samples were collected from 60 dairy calves immediately after birth and prior to feeding of colostrum to provide seronegative samples (0 month calves). Unlike their human counterparts, calves are not born with wide-ranging immunity to common microbes and therefore provide a source of serum deficient in protective antibodies. Passive immunity is provided to calves via consumption of colostrum (the milk produced by the dam in the hours prior to calving). In that regard, further samples were collected at monthly intervals post-colostrum feeding (month 1, 2, 3 etc.). Depending on the BVD antibody content of the colostrum fed to calves, monthly samples may be seropositive or seronegative. Sera used in this study for Ab detection were first assayed in a commercial analytical lab using IDEXX BVDV p80 Ab Test (Maine, USA) and results used to assign BVD serostatus to all samples.

4.2.5 Electrode Modification

4.2.5.1 *Investigation of surface chemistries*

Two procedures for the preparation of the sensing surfaces were carried out; modification with self-assembled monolayers (SAM) and electrodeposited polymers were investigated. Firstly, a single thiol, mercaptododecanoic acid (MDA), and a mixed SAM of mercaptoundecanoic acid (MUA) and mercaptohexanol (MH), were examined on the gold electrode. Stock solutions of MDA (5 mM), MUA and MH were prepared in pure ethanol (100% proof). MUA and MH were mixed appropriately to obtain a ratio if 1:10, respectively. Adsorption of MDA alone, or the mixed MUH/MH solution was accomplished by dropping of 40 µL of the solution onto the electrode surface. The solution was allowed to incubate for 18 hours at room temperature in sealed ethanolic atmosphere. Prior to use, the electrodes were thoroughly rinsed with ethanol to remove any loosely bound thiols.

Two insulating polymers were examined for modification of the gold nanoband electrodes. The first polymer, o-Phenylenediamine (o-PD) was made up in 10 mM PBS

and 5 mM Na$_2$SO$_4$ to produce a 10 mM stock solution. o-PD is deposited on the electrodes using chronoamperometry (0.6 V) for 20 minutes to 1 hour, at room temperature. A biotin-streptavidin complex was employed to test the effectiveness of o-PD as a surface modification. The second insulating polymer was anthranilic acid or o-aminobenzoic acid (o-ABA). oABA deposition was investigated in an acidic buffer solution (10 mM acetate buffer, pH 4) and sulfuric acid (0.5 M H$_2$SO$_4$) at concentrations of 10 mM and 50 mM, respectively. They were electrodeposited onto the electrode using cyclic voltammetry; cycled 8 times in the applied potential range of 0 to 0.8V at a scan rate of 50 mV/s.

4.2.5.2 *Sensor Functionalisation for BVD Investigation*

All chemical and bio-modification steps were performed using the prefabricated chip holder and the PCB mounted microSD port to connect the chip to the external potentiostat. On-chip nanoband electrodes were first cleaned using a mixed solvent clean process (acetone, isopropyl alcohol and DI water) for 15 minutes and dried under a stream of nitrogen. CV was then employed for electropolymerisation of o-aminobenzoic acid (o-ABA, 50 mM in 0.5 M H$_2$SO$_4$) to create a carboxylic terminated polymer layer at the gold electrode surface, as described in the previous section. Following polymerisation, the electrodes were carefully rinsed with DI water to remove any remaining monomer solution. A fresh mixture of 1:1 EDC/NHS (75 mg/mL EDC and 11.5 mg/mL NHS) was deposited onto a chip for 20 min to activate the carboxylic acid (COOH) surface. Working electrodes were coated with capture biomolecules and allowed incubate for 1 hour at 4°C to allow covalent attachment to the electrode surface. Following this immobilisation, the electrodes were rinsed well with acetate buffer solution containing 0.1% Tween-20 (AB-T) and DI water to remove any unbound capture biomolecules. The un-reacted active sites were blocked by immersing in 1M ethanolamine HCl, pH 8.5 for 20 mins. Impedance measurement following this step were undertaken and considered as the "baseline" for the on-chip sensors.

To undertake analysis, as-modified electrodes were exposed to target solutions (BVD antibody or virus, buffer or serum, respectively) by spotting with 2 µL aliquots followed by incubation for 10 min at room temperature. Electrodes were again rinsed thoroughly with HBS-EP buffer and DI water to remove non-specifically bound target biomolecules prior to subsequent electrochemical measurement. Control experiments were undertaken,

at appropriately bio-modified electrodes, using serum samples known to be negative, i.e., extracted from 0 month healthy calves. In a similar manner, negative samples were spotted (2 µL) onto electrodes 1 and 2 while the test serum samples were spotted onto electrodes 3, 4 and 5, on the same chip. All data were fitted using an equivalent circuit and experimental data were background subtracted using the values for the ethanolamine baseline as defined.

4.2.5.3 Target BVD Antibody Detection

Electrodes were modified using with BVD Virus-1 Erns antigen as the capture biomolecule. A concentration of 100 µg/mL (acetate buffer, pH 4) was prepared, deposited and allowed incubate for 1 hour at 4°C. BVDAb detection was then investigated in solutions of increasing biological complexity. (i) BVDAb in HBS-EP buffer, prepared using BVD monoclonal antibody (RAE0823 as purchased stock sample) diluted into working solutions of varying dilution (1:10 to 1:1000, respectively) using HBS-EP buffer, (ii) BVD seropositive samples diluted with HBS-EP; in the range of 0.1% to 10% serum, and (iii) BVD seropositive and seronegative undiluted serum samples using three different serum samples from 1 month old calves along with their corresponding pre-colostral negative sample (0 month). The spotting technique, described above, was employed to test one negative (electrode 1 and 2) and one positive sample (electrodes 3-5) on the same chip. Further experiments were undertaken by pooling 3 seropositive (1 month) samples and 3 seronegative (0 month) samples employing the same spotting technique. All serum samples were incubated on an electrode for a total ~10 minutes.

4.2.5.4 Target BVD Virus Detection

Electrodes were modified using BVD monoclonal antibody, specific to Erns antigen, as the capture biomolecule (100 µg/mL, acetate buffer, pH 4); incubated for 1 hour at 4°C. Employing antibodies to detect the Erns protein requires minimal processing as Erns is secreted from infected cells during virus replication at an adequate concentration to be used for testing serum.[35, 36] BVDV detection was investigated again using three solutions of increasing biological complexity. (i) BVDV in HBS-EP buffer, prepared using target Erns viral antigen (as purchased stock sample) diluted into working solutions of varying

dilution (1:10 to 1:1000, respectively) using HBS-EP buffer, (ii) BVD virus positive and virus negative samples diluted with HBS-EP; in the range 0.1% to 10% serum, and (iii) BVD Virus positive (PIs) and virus negative control (0 month) undiluted sera samples. The spotting technique, described above, was again employed to test one negative (electrode 1 and 2) and one positive sample (electrodes 3-5) per chip for five different samples.

4.3 Results and Discussion

4.3.1 Optical Characterisation of Nanobands

Following fabrication, as described in the experimental section, devices were first characterised using optical microscopy. Figure 4.1 (a) show a photo of a typical sensor chip. Each chip contained six separate nanoband working electrodes and gold counter and platinum pseudo-reference electrodes. A microSD pinout was implemented to allow facile and rapid interconnection with external instrumentation. Visual inspection was undertaken to confirm correct alignment between the different fabrication steps. Fabrication yields were ~99%; chips that exhibited visual defects were discarded and not used for experimental purposes.
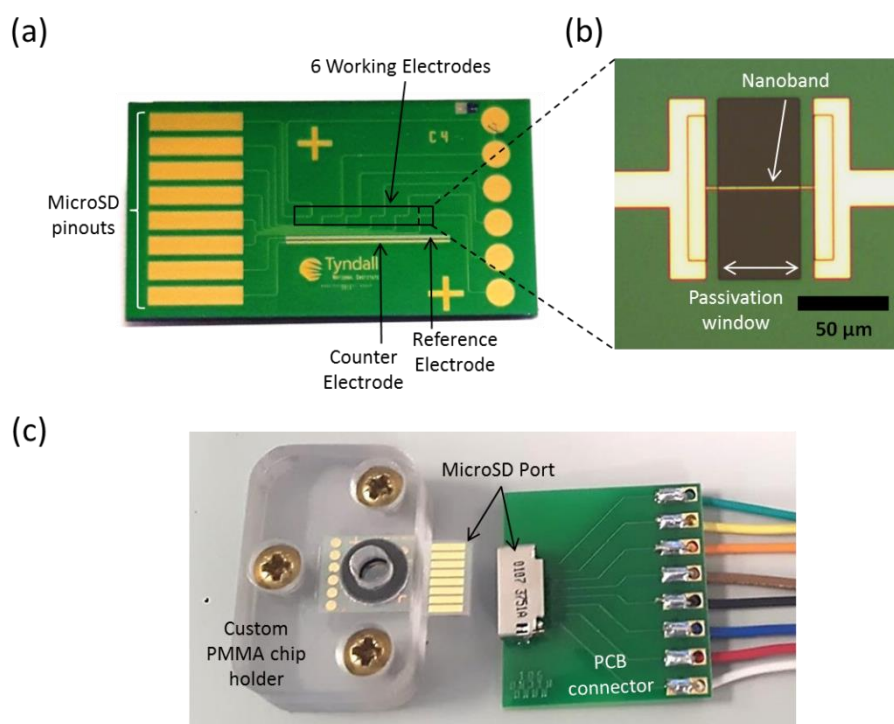

Figure 4.1: (a) Picture of fully integrated silicon sensor chip. (b) Optical micrograph of the single nanoband working electrode with dark passivation window. (c) Electrochemical setup with sensor chip and a PCB microSD connector

Figure 4.1 (b) shows an optical micrograph of a single fully passivated single nanoband electrode (700 nm in width). The width of the passivation window opening (central dark

rectangle) defined the exposed electrode length at 45 μm. Visual inspection was employed to confirm that the opening of the passivation windows were directly above a nanoband and not overlapping the interconnection metallisation. Openings in the passivation layer above the CE, RE and microSD pinout were also confirmed. Figure 6.1 (c) shows a sensor chip in a chip holder, prior to inserting the microSD pinout into a PCB mounted microSD connector. The well in the centre has a volume of ~100 μL, sealed onto the chip using an o-ring, and aligned over the on-chip sensor electrodes.

4.3.2 Potentiometric and Impedimetric Characterisation of Sensor Electrodes

To test electrochemical functionality, electrodes were first characterised using CV and electrochemical impedance spectroscopy, in presence of 1 mM FcCOOH redox probe. Figure 4.2 (a) shows a typical CV voltammogram obtained using a pristine nanoband electrode exhibiting a quasi-steady-state behaviour, as expected. [37, 38] This steady-state behaviour is ideal for EIS and helps to correct for drift in the system. The magnitude of the current (~1.6 nA) confirms that electrochemistry only occurs at a nanoband electrode and the passivation layer successfully prevents unwanted electrochemistry occurring at on-chip metallisation. Faradaic impedance spectroscopy was performed on pristine gold electrodes and a typical Nyquist plot (real Z' vs. imaginary Z'' impedance), is presented in Figure 4.2 (b). The FcCOOH redox probe was used to clearly show binding events occurring at an electrode interface, through a measured change in the impedance. The resistive and capacitive charges in the system can be interpreted from the Nyquist plot, by fitting the data with a Randles equivalent circuit (discussed in detail in Chapter 1, section 1.6.6). The double layer capacitance (C_{dl}) can be approximated by measuring the height of the semi-circle on the imaginary axis, Z''. The charge transfer resistance (R_{ct}) of impedimetric biosensors may be estimated by measuring the diameter of the semi-circle on the real axis, Z'. The W is negligible for our system and as a result, the change of surface properties on the sensing surface is mainly reflected through the change of R_{ct}. Therefore, the solution resistance (R_S), reflects the properties of the electrolyte solution that is not affected by electrode modifications. The R_{ct}, instead, reflects the transfer of electrons during redox reactions and can be used as a method to measure changes

occurring at the surface of the electrode. Hence, it is more suitable to present the hybridisation process as a modulation of R_{ct}.

The experimental data (blue dots) presented in Figure 4.2 (b) were fitted with an equivalent Randles circuit (Figure 4.2 (b) inset) modelled using the NOVA software. This fit data (solid line) overlays the experimental data (dots) extremely well, confirming the efficacy of the selected equivalent circuit components and defined values.
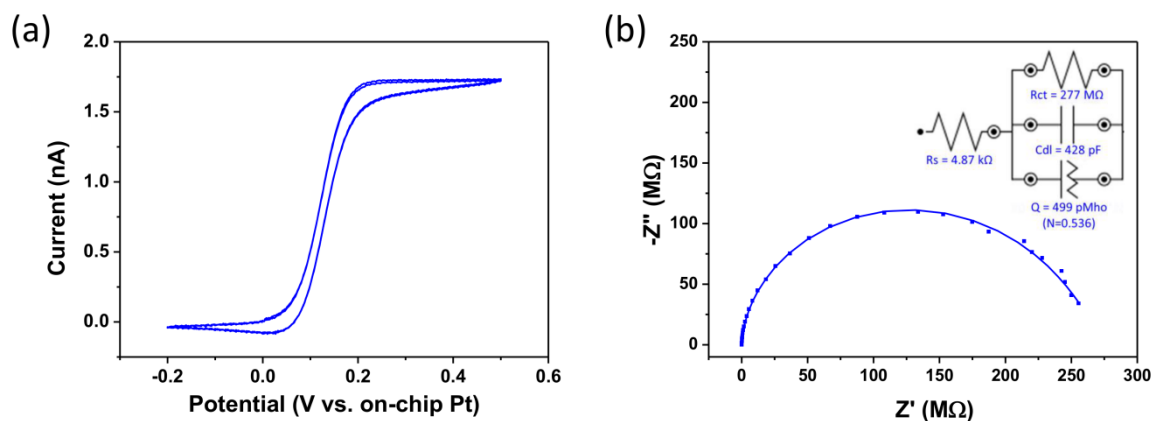

Figure 4.2: (a) Typical CV of a gold nanoband electrode obtained in 1 mM FcCOOH in 10 mM PBS, pH 7.4, in the potential range of -0.2 V to 0.5 V at 100 mV/s. (versus on-chip platinum RE). (b) Typical Nyquist plot for a clean gold electrode 0.1 mHz to 100 kHz; Inset: the applied equivalent electrical circuit.

4.3.3 Characterisation of the Biomodification Process

Surface chemistries for biomolecule immobilisation to electrode are numerous. In order to build a stable and reproducible immunosensor, two well-known electrode functionalisation processes were investigated; self-assembled monolayers (SAM) and electrodeposited polymers. Each step of the functionalisation was electrochemically characterised in ferrocene monocarboxylic acid to confirm the modification of the electrodes surface by following the changes in the access of the redox couple to the gold electrode. Some model immunoassay responses were also investigated.

4.3.3.1 Thiol modification

Thiols based self-assembled monolayers such as mercaptododecanoic acid (MDA) and mixed SAMs of mercaptoundecanoic acid (MUA) and mercaptohexanol (MH) (1:10)

were used to modify the gold nanoelectrodes. The CV and Nyquist data obtained following modification with MDA highlighted how the SAM depositions were neither reproducible nor homogenous and subsequently affecting the modification thereafter. However, the main issue with employing thiols is that they must be diluted with ethanol or other solvents which is not practical for use with our chip design. This is because solvent deposition on the silicon chips cannot be controlled and therefore can cover the entire chip surface, thereby modifying all the WE as well as altering the CE, RE and the gold contact pads. The ultimate aim for our sensor chips is to develop them for use in POC testing, of which, a key feature is the ability to independently modify the electrodes for different applications.

4.3.3.2 Polymer electrodeposition

In order to optimize the reproducibility of the modification, insulating polymers were studied, because of their ability to electropolymerise and thus, selectively functionalise electrodes.[39] Particular interest has been given to o-phenylenediamine (o-PD), generally used for the development of enzymatic biosensors as entrapping matrix;[40, 41] and o-aminobenzoic acid (o-ABA).[42, 43] The electrodeposition of o-PD onto the gold nanobands is shown in Figure 4.3, employing a model complex to investigate the functionality of the o-PD layer. Upon testing of several chips, it was observed that the deposited polymer adsorbs on all the electrodes neighbouring the selected electrode. Immunologic events were observed on the nanoband electrode, with an esterified biotin capture and a streptavidin target. CV plots and Nyquist plots obtained by EIS Figure 4.3 revealed a decrease in impedance from the o-PD to binding of the biotin. Subsequently, the impedance decreases with increasing concentration of the streptavidin. However, these experiments showed the poor stability of the o-PD as the layer integrity decreased with time. Degradation half period of about 5.4 hours in our working conditions were reported in the literature and can explain the important variability found between the electrodes. Moreover, o-PD would not be suitable long-term because selective deposition was not achievable.
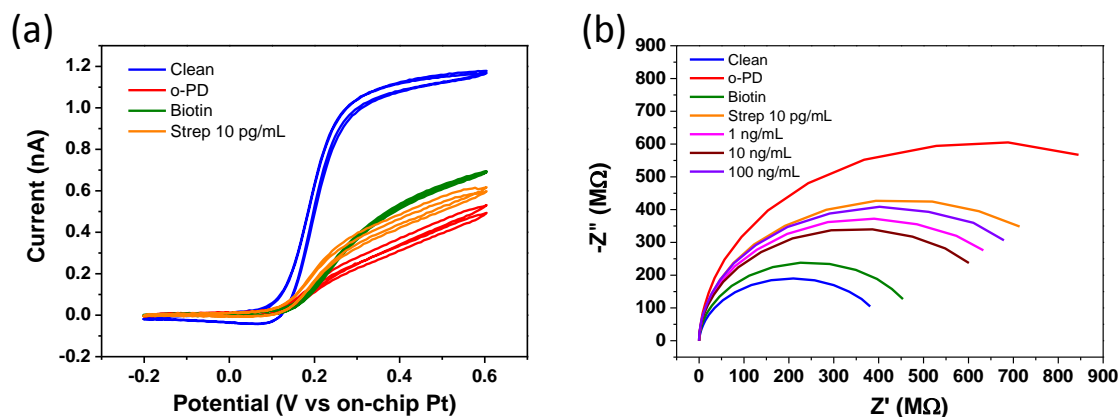
Figure 4.3: (a) CV's and (b) Nyquist plots of a single gold nanoband electrode (blue), modified with o-PD (red), and studying the immunologic detection of the model esterified biotin modified (green) and streptavidin 10 pg/mL (orange); 1 ng/mL (pink); 10 ng/mL (wine); 100 ng/mL (purple).

An alternative carboxyl functionalised polymer, capable of self-doping, o-aminobenzoic acid (o-ABA), was also assessed. This bio-compatible aniline polymer is emerging as a promising polyaniline derivative for biosensor applications. It electro-polymerises onto the sensor surface via the compound's amine groups, leaving carboxylic acid functional groups available on the sensor surface to enable bioconjugation , see Figure 4.4 (b). Carboxylic acids can easily crosslink to primary amines on proteins or other biomolecules, immobilising them to the sensor surface. A typical CV obtained for the electrodeposition of o-ABA on a nanoband is shown in Figure 4.4 (a). The first cycle of the electrodeposition displays an oxidative peak around 0.5 V corresponding to the formation of the polymer on the gold electrode. This peak disappears with subsequent scans and a small reversible peak around 0 V, characteristic of the doping-dedoping of the polymer, and a second dedoping peak at 0.3 V in the cathodic scan appear with increasing number of cycles. The emergence of these peaks confirms the electrodeposition of o-ABA on the gold surface.
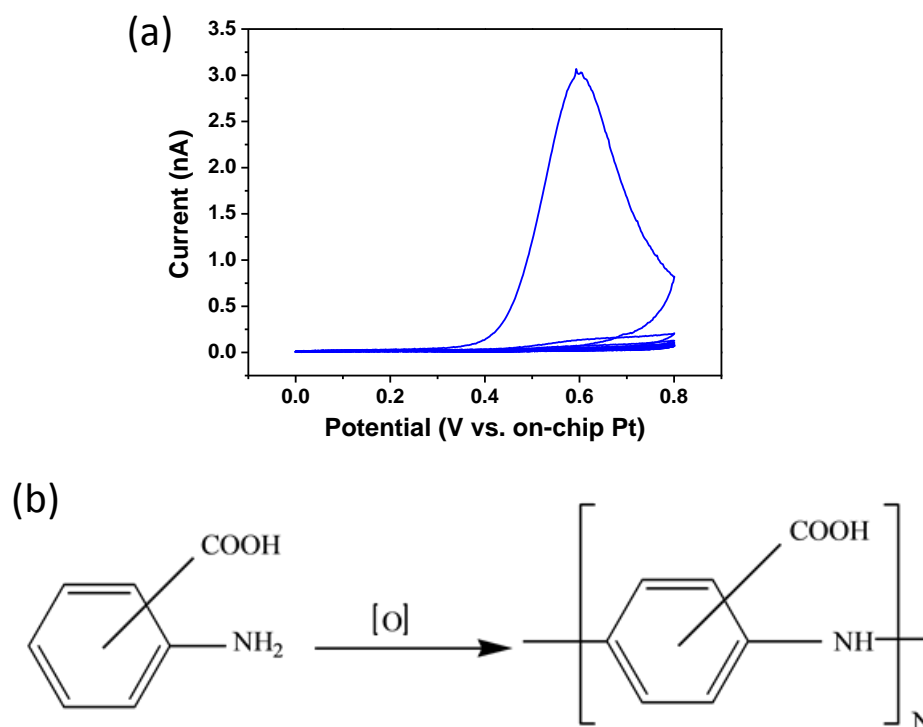
(a)

(b)

Figure 4.4: CV's for the electropolymerisation of o-aminobenzoic acid (o-ABA, 50 mM in 0.5 M H_2SO_4) at a gold microband electrode. The electrode was cycled 8 times in the applied potential range of 0 to 0.8V at a scan rate of 50 mV/s. (b) Electropolymerisation scheme for o-ABA.

Figure 4.5 shows the CV and Nyquist data for another well know antibody-antigen model system (IgG), to show the comparison of o-ABA electrodeposition in two media, acetate buffer (a and b) and sulphuric acid (c and d). The o-ABA deposition in sulfuric acid clearly shows a larger response, i.e. a measured increase in the impedance and a decrease in the CV current, for the antibody-antigen binding. All further electrochemical modifications in this thesis employ oABA electrodeposition in sulfuric acid as the "primer" layer.
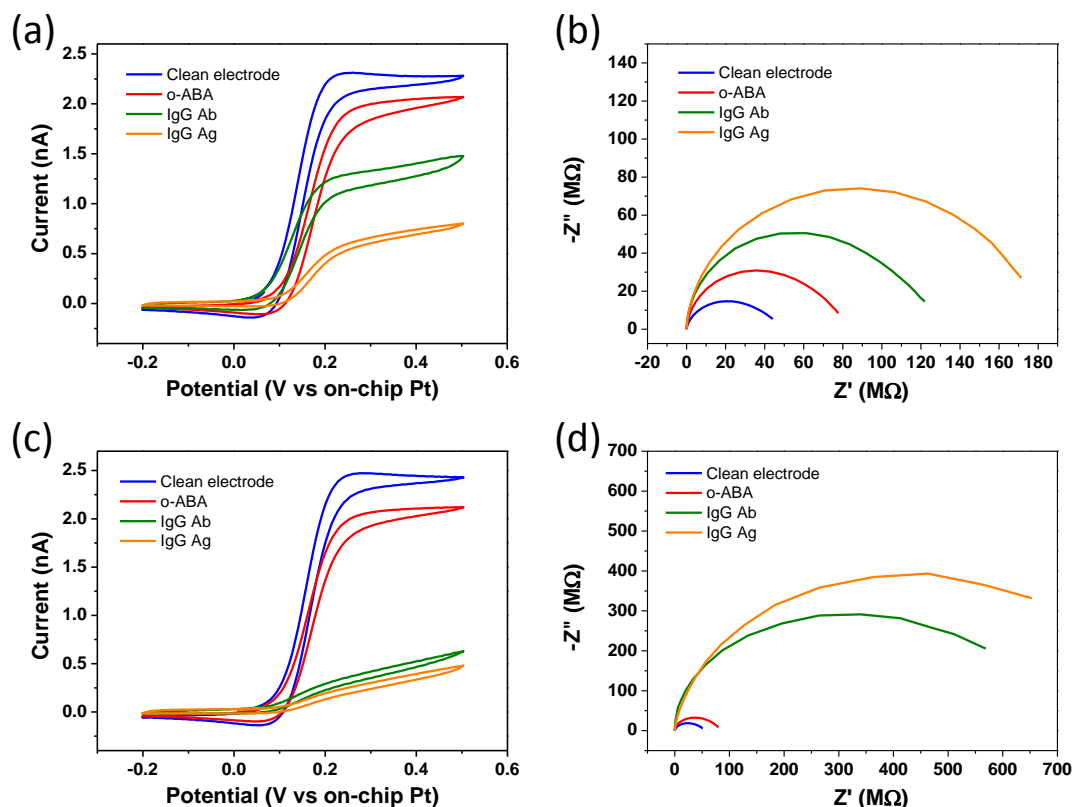
Figure 4.5: (a) CV's and (b) Nyquist plots for the deposition of 10 mM oABA in 10 mM acetate buffer pH 4 and subsequent binding of IgG Ab- Ag complex. (a) CV and (b) Nyquist plots for the deposition of 50 mM oABA in 0.5 M H₂SO₄ and subsequent binding of the same IgG Ab- Ag complex.

4.3.4 Detection of BVD in Buffer

4.3.4.1 Antibody Detection

Figure 4.6 shows the CV's at an electrode surface following modification and exposure to different concentrations of target antibody. As expected, the CV current magnitude decreases with increasing concentration due to layer build-up at the electrode–electrolyte interface. The layers are partially insulating and act to block FcCOOH redox ions from reaching the electrode surface, therefore decreasing electron transfer. The changes in current magnitude, however, are minimal and do not provide the necessary sensitivity required for POC experiments. Consequently, further CV experiments were not undertaken for this study.
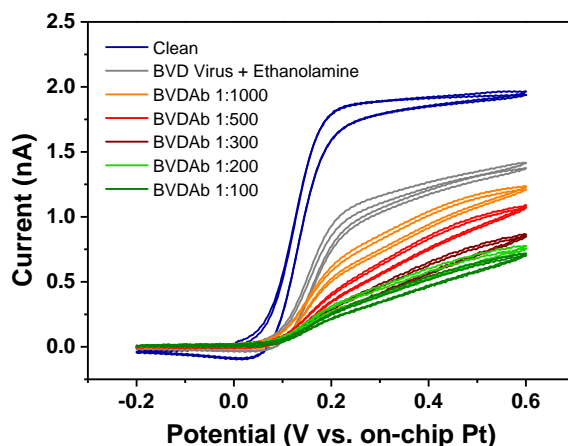
Figure 4.6: CV's obtained of o-ABA modified gold nanoband electrode with: BVD virus (100 µg/mL) modification, ethanolamine blocking and binding of BVD antibody in HBS-EP buffer; recorded in 10 mM PBS containing 1 mM FcCOOH.

By contrast to CV, EIS is measured at the formal potential of the redox probe (0.2 V, in this case); therefore the recorded data reveals other physical processes occurring following the biomolecule capture on the gold nanoband biosensor. The BVD Ab-virus complex can be considered as a coating film which provides a significant impedance response at the required sensitivity. A modified equivalent circuit, to account for the additional electrode bio-layers, was used to fit the results. This circuit is almost identical to the previous Randles fit except that an additional resistive and capacitive elements have been added. R1 and R2 both represent the charge transfer resistance, while C1 and C2 represent the double layer and coating capacitances respectively. All the capacitances shown in the equivalent electrical circuit are mathematically modelled using a constant phase element (CPE) in NOVA software; and represent all the frequency dependent electrochemical phenomena.

Figure 4.7 (b) shows the Nyquist diagrams, in the presence of 1 mM FcCOOH, measured an electrode surface following modification and exposure to different concentrations of target antibody. An increase in the semi-circle diameter i.e. increases of the charge transfer resistance (R_{ct}) and the global capacitance, was observed with increasing antibody concentration. This suggests that the antibodies bound to the immobilised E*rns* antigen, further block the electrode surface and subsequently restrict electron transfer. Figure 4.7 (c) shows that a semi-log linear relationship exists between the charge transfer

resistance across the band, and different dilutions of the stock antibody solution. The error bars represent n=3 replicates.
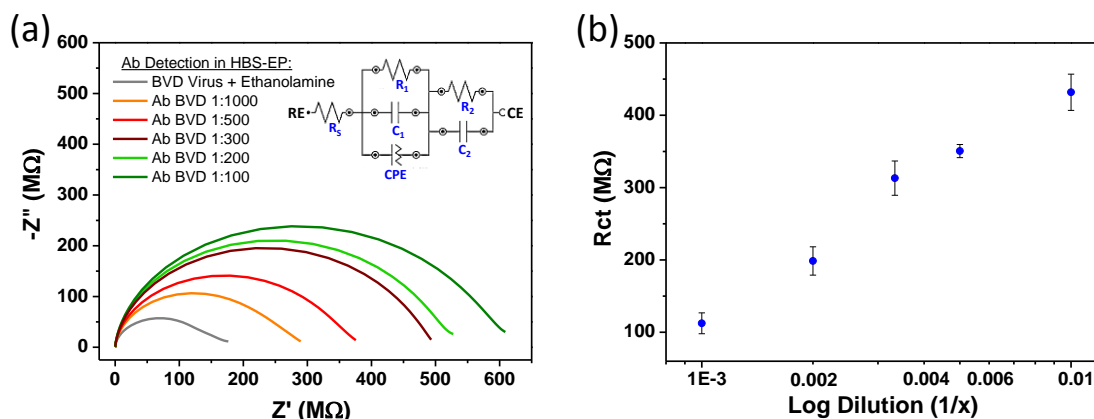

Figure 4.7: (a) Nyquist plots obtained of o-ABA modified gold nanoband electrode with: BVD virus (100 μg/mL) modification, ethanolamine blocking and binding of BVD antibody in HBS-EP buffer; recorded in 10 mM PBS containing 1 mM FcCOOH. (c) Semi-log relationship of the charge transfer resistance versus antibody dilution (error bars represent n=3 replicates) background subtracted using ethanolamine baseline.

4.3.4.2 Virus Detection

Figure 4.8 (a) shows the Nyquist diagrams, in the presence of 1mM FcCOOH, measured an electrode surface following modification and exposure to different concentration of viral protein in HBS-EP buffer ranging from 1 ng/mL to 10 µg/mL. A corresponding increase in measured R_{ct} (~200 MΩ to ~425 MΩ) was observed. This increase can be attributed to the virus binding as it acts as a kinetic barrier for electron transfer. These results also suggest that the antibody specificity/functionality is not hindered by its covalent attachment to an electrode. Figure 4.8 (b) shows the semi-log linear relationship between the R_{ct} sensor response and virus concentration thereby suggesting viral detection is possible with high sensitivity and a large dynamic range (1ng/mL to 10µg/mL). The error bars represent n=3 replicates.
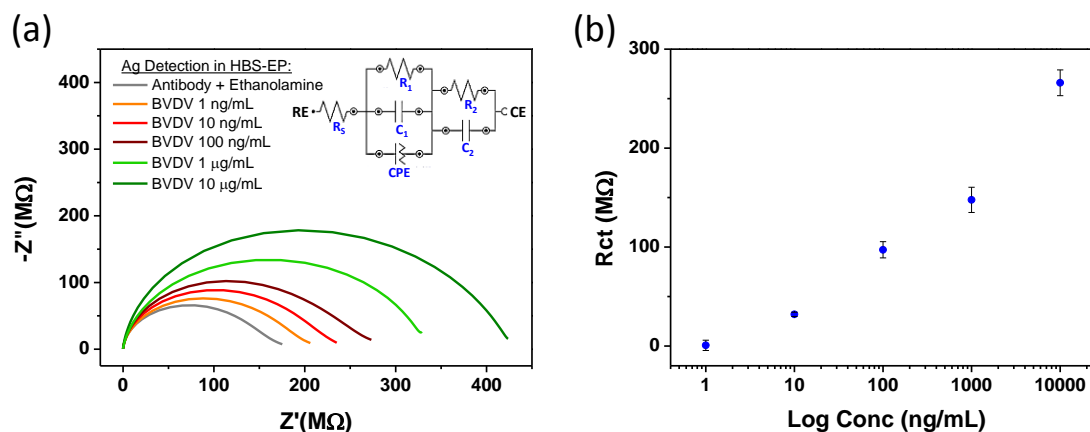
Figure 4.8: (a) Nyquist plots of 1 mM FcCOOH showing quantitative detection of recombinant BVDV1 Erns protein in HBS-EP buffer. (b) Semi-log relationship of the charge transfer resistance versus virus concentration (error bars represent n=3 replicates) background subtracted using ethanolamine baseline.

4.3.5 Detection in Diluted Serum

After successful detection of BVD antibodies and viruses in buffer, the immunosensor was applied to BVDV and BVDAb detection in diluted serum. These experiments were undertaken to examine the behaviour of the immunosensor in a more complex matrix, in order to identify and assess the amount of non-specific binding/adsorption and specificity in the presence of other non-specific proteins. To this end, (i) virus-modified sensors were applied to detection of BVD antibody in diluted bovine sera of known disease state i.e. BVDAb seropositive and seronegative samples. (ii) Reverse experiments were also undertaken where antibody-modified sensors were employed for the detection of BVDV in virus positive and virus negative sera samples.

4.3.5.1 Antibody detection in Diluted Serum

Figure 4.9 (a) shows the Nyquist diagrams, in the presence of 1 mM FcCOOH, of an electrode surface following modification and spotting of different dilutions of seropositive samples (0.1% to 10% serum). This dilution range was selected as it corresponds to the maximum dilution permitting the BVD Antibody detection with the ELISA (IDEXX) after 1h incubation of the positive infected serum sample. The Nyquist plot of the 0.1% dilution (orange plot) does not reveal any measurable increase in the

impedance ~140 MΩ versus the ethanolamine curve ~130 MΩ. Incubation with 0.5% serum sample lead to an increase in the impedance to ~200 Ω (red plot), thus an increase in double layer capacitance and charge transfer resistance. Analysis of 0.2%, 0.3%, 1%, 5% and 10% sera shows an incremental increase in the impedance as the concentration of the antibody increased; exhibiting a semi-log relationship similar to the buffer results in Figure 4.7, see Figure 4.9 (b). This is consistent with results presented in buffer and strongly agrees that the observed changes in the Nyquist spectra are attributed to the binding of BVD antibody to the modified electrode.

Figure 4.9: (a) Nyquist plots obtained of virus modified gold nanoband electrode when exposed to different concentration of antibody (dilute sera samples). (b) Semi-log relationship of the charge transfer resistance versus virus concentration (error bars represent n=6 replicates) background subtracted using ethanolami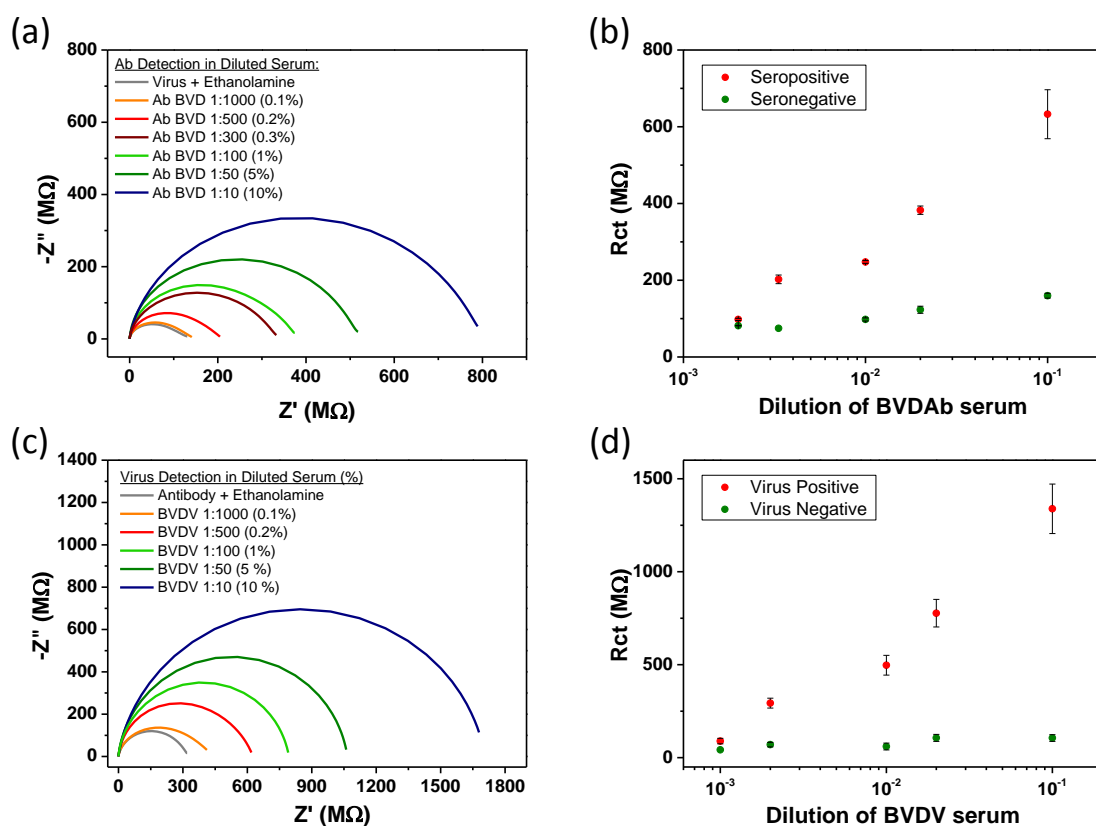ne baseline for positive and control samples. (c) Nyquist plots obtained of antibody modified gold nanoband electrode when exposed to different concentration of virus (dilute sera samples). (d) Semi-log relationship of the charge transfer resistance versus virus concentration (error bars represent n=6 replicates) background subtracted using ethanolamine baseline for positive and control samples.

To explore the specificity of the modified sensors against BVD antibodies and to assess the presence/degree of non-specific binding, control experiments were also undertaken using different electrodes on the same chips spotted with BVDAb seronegative samples. Following incubation, slight increases in the impedance (approximately 100 MΩ) versus the ethanolamine curve, were observed, arising from a slight reduction of electron transfer; see Figure 4.9 (b). Error bars represent 6 replicates. The corresponding raw data in Nyquist plots are presented in Figure 4.10 (a). This suggests a partial insulating layer was formed on the electrode, which may be attributed to nonspecific binding/adsorption by proteins present in the bovine serum. However, these data show that there is clear discrimination between BVD seropositive and seronegative bovine samples particularly at low dilution, i.e., 10% serum. This data strongly suggests that the sensors should be sufficiently sensitive and selective enough to discriminate between seropositive and seronegative in undiluted serum.

4.3.5.2 Virus Detection in Serum

In a similar manner, assays were undertaken to assess virus detection in diluted serum. Positive PI and virus negative control sera were spotted on different BVD antibody modified sensors on a chip. Figure 4.9 (c) shows the impedimetric response for BVD virus in 0.1 -10% diluted sera, measured for virus positive sera. The corresponding Nyquist data plots for virus negative sera are presented in Figure 4.10 (b). All Nyquist data were fit using the Randles-type circuit as described previously. An incremental increase in the impedance was observed, as the concentration of the virus is increased (decreasing dilution), which is consistent with results presented in buffer. The virus detection exhibits a larger impedance value (~600 – 1700 MΩ, Figure 4.9 (c)) compared to antibody detection (~200 – 800 MΩ, Figure 4.9 (b)), suggesting that binding of large BVD virus to the modified electrode sterically hinders the electron transfer. Figure 4.9 (d) shows a semi-log relationship between virus concentration and measured signal. Error bars represent 6 replicates. Control virus negative samples exhibited slight increases in the impedance when compared to the ethanolamine baseline. This data verifies that the virus positive response arose from the binding of BVD virus to the modified surface and demonstrates the potential for virus detection in undiluted serum.
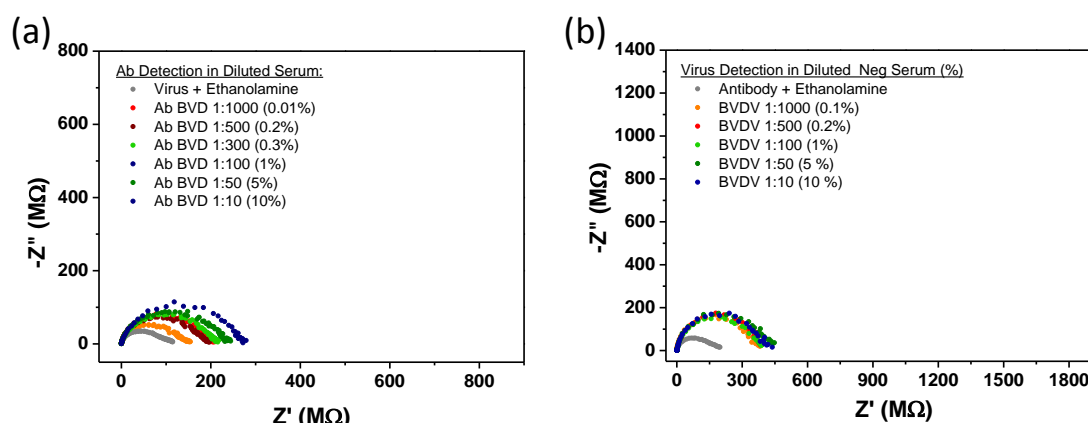
Figure 4.10: Nyquist plots, undertaken in 10 mM PBS containing 1 mM FcCOOH redox molecule, of o-ABA modified gold microband electrode with (a) BVD seronegative and (b) BVD virus negative controls in diluted bovine sera, background subtracted from their corresponding ethanolamine baseline (grey data). Plots are at the same scale as the target experiments for direct comparison.

4.3.6 Detection of BVD in Bovine Whole Serum Samples at MicroSD Devices

Following successful detection of BVD antibodies and viruses in diluted sera as described above, the immunosensors were applied to BVDV and BVDAb detection in whole (undiluted) serum. These experiments were then undertaken to assess suitability of the sensors for use as on-farm diagnostic applications. To this end, (i) virus-modified sensors were applied to the detection of BVDAb seropositive and seronegative samples; and (ii), antibody-modified sensors were applied to the detection of BVDV in PI calves (virus positive) and virus negative samples. The electrodes were again characterised using EIS and data fit as previously described.

4.3.6.1 Antibody detection in Serum:

A number of sensor chips were modified with virus (10 μg/mL) to test for BVDAb in pooled and unpooled seropositive and seronegative samples. A spotting technique was again employed to deposit multiple sera samples on separate electrodes on a chip. Typical EIS measurements for the detection of BVDAb in a single calf (No. 8954) obtained at time 0 month, and 1 month are presented in Figure 4.11 (a). Data from the seronegative sample produced an electrode impedance of ~350MΩ, a ~30 MΩ increase compared to

the baseline attributed to small amounts of non-specific binding (green plot). A significant increase in impedance was observed following incubation with a seropositive sample ~800 MΩ (red plot). This increase may be attributed to binding of the BVD antibodies present in the serum to the viral modified electrode surface. Figure 4.11 (b) shows experimental background subtracted R_{ct} EIS data in a bar chart format, obtained for a number of individual and pooled samples when undertaking BVDAb detection in seronegative and seropositive samples. Zero month samples (known to be seronegative) for an individual calf or pool are shown as dark green bars. These 0 month samples all exhibited very low impedance (<250 MΩ) for antibody detection, as expected. One month seronegative samples for two individual calves are presented as light green bars. The small difference in impedance values the zero and one month samples may be attributed to slight variation in the degree of non-specific adsorption and in electrode preparation. However, a clear increase in the electron-transfer resistance (>800 MΩ) red bars is observed between the negative controls and both individual and pooled seropositive samples, (time to results 15 minutes). These results strongly support the suitability of these sensors for use as on-farm diagnostic devices as the sensors can discriminate between seropositive and seronegative in undiluted blood serum.

4.3.6.2 Virus Detection in Serum:

A number of sensor chips, modified with monoclonal BVDAb (10 μg/mL), were employed to test for the presence of BVD virus in PI calf whole serum. In the same manner as previously discussed, a spotting technique was used to deposit PI serum and virus negative serum on electrodes 3-5 and 1-2, respectively. Nyquist plots, illustrating detection of BVDV positive serum (from PI calf 4334) and BVDV negative serum (from 0 month calf 8946) on the same microSD chip, are shown in Figure 4.11 (c). The deposition of BVDV negative serum 8946 shows an R_{ct} of ~600 MΩ, which increased slightly following the ethanolamine baseline ~350 MΩ, Figure 4.11 (c) green plot. As mentioned previously, this data suggest there is a small formation of a more insulating layer on the electrode which could be attributed to increasing nonspecific binding from protein in the bovine serum (like albumin) to the antibody modified electrode surface. On a separate electrode on the same chip, the target virus positive PI serum was immobilised and again, revealed a substantial R_{ct} value of ~1600 MΩ; an increase of ~1230 MΩ from the baseline, which compensates for the small amount of non-specific binding reported

from the negative serum samples. We suggest that this large increase in R_{ct} arises from the large virus molecules acting as a kinetic barrier to the transfer of electrons from the FcCOOH to the electrode, hence increasing the system resistance.
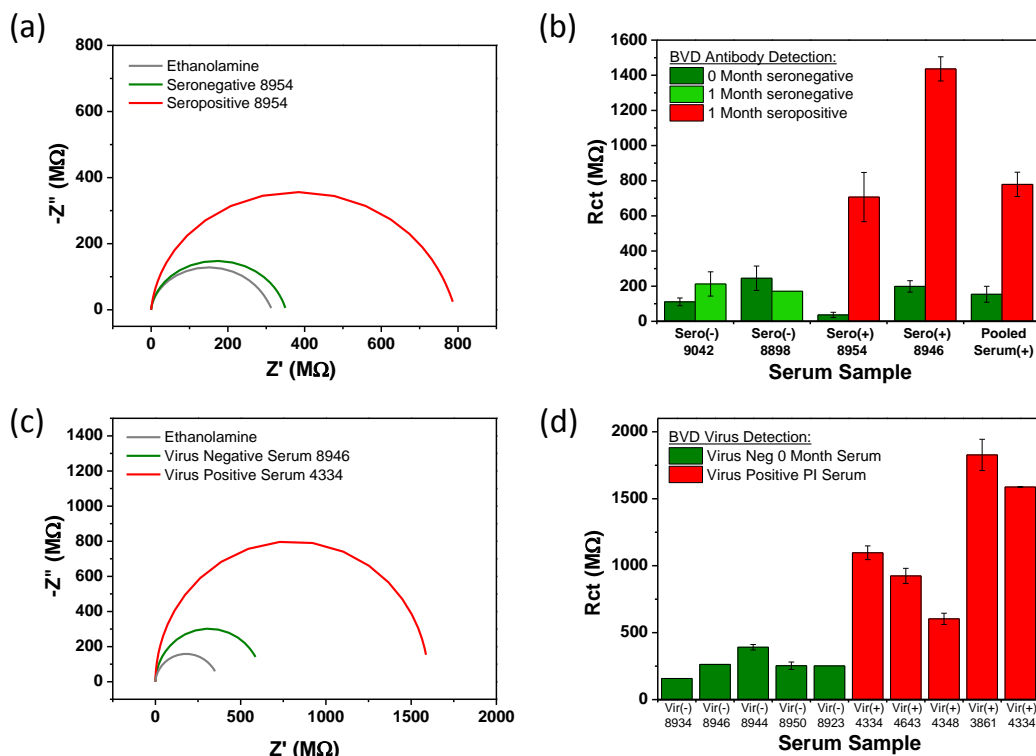
Figure 4.11: (a) Nyquist plots of seropositive and seronegative blood deposition on BVD virus (10 µg/mL) modified microelectrodes, in the presence of 10 mM PBS containing 1 mM FcCOOH. (b) Bar chart comparison of seropositive samples and their respective seronegative samples, background subtracted from their respective ethanolamine baselines. (c) Nyquist plots of a virus negative and virus positive PI serum, deposited on BVD antibody modified nanoband (measured in the presence of 1 mM FcCOOH). (d) Bar chart testing PI serum and virus negative serum samples, background subtracted from their respective ethanolamine baselines. \

In order to validate these findings, several more PI serum samples were tested for presence of virus and compared to virus negative serum samples. In total, five BVDV negative samples (green) and five BVDV positive PI samples (red) were examined and the R_{ct} value measured. The chart in Figure 4.11 (d) shows the background subtracted R_{ct} data for these assays. As expected the virus negative sera exhibited minor NSB binding to the electrode (<400 MΩ), whereas the target seropositive 1 month samples present a significant increase in the electron-transfer resistance (>800 MΩ). These results propose that there is successful serological binding of the BVDAb to the immobilised viral

protein. The results presented above, clearly demonstrate that the nanoband sensors have sufficient sensitivity and specificity for detection of both target antibody and virus detection in serum. The findings are of particular significance for on-farm POC applications where high sensitivity and specificity and low time-to-result, are required to permit early diagnostics by veterinarians.

4.3.7 Comparison to ELISA testing

All of the impedimetric results were compared with their respective ELISA measurements and are presented in Table 4.1. Ten chips were employed for the electrochemical detection of both BVDAb and BVDV. The use of a spotting technique permitted on-chip dual sensing capabilities, enabling the detection of a target biomolecule as well as a negative control experiment on the same chip. ELISA tests were performed using a commercial BVDV p80 Ab detection kit for the detection of specific antibodies directed to bovine viral diarrhea virus (IDEXX, UK). Briefly, the p80 modified ELISA plate of the kit was exposed to the serum samples diluted (10 %) in the commercial dilution solution. The conjugate was diluted (with the provided solution) and incubated in the plate for 30 min at room temperature. After washing, a chromogenic substrate was added for 20 min in dark room at room temperature. Finally, the reaction revealing the conjugate was stopped using the commercial stop solution and the absorbance value was read at 450 nm using an ELISA plate reader (DIASource, Belgium). The absorbance readings for each sample was analysed, and values less than 45 were considered BVD positive, whereas values greater than 45 were considered BVD negative. These readings were compared to the EIS data and revealed a 100% level of agreement between the ELISA and EIS results, illustrated in Table 4.1. The BVD negative results, EIS values <250 MΩ and ELISA's >45, are represented by green boxes. The BVD positive results, >250 MΩ EIS and <45 ELISA values are represented by red boxes.

BVD Target	Control (Electrode 1-2)				(Electrodes 3-5)				
	Calf ID/ Age		ELISA (IDEXX)	EIS (MΩ)	Calf ID/ Age		ELISA (IDEXX)	PCR	EIS (MΩ)
Antibody	8898	0 Month	96.78	245.21	8898	1 Month	88.85	-	17135
Ab pool	8928	0 Month	89.44	249.34	8976	1 Month	20.59	-	779.32
	8931		99.32		8978		8.58		
	8933		99.32		8980		5.38		
Virus	8934	0 Month	99.67	158.05	3861	PI calf	-	POS	1827.5
Virus	8938	0 Month	96.78	251.73	61491	PI calf	-	POS	1587.56
Virus	8944	0 Month	101.80	391.45	4643	PI calf	-	POS	923.71
Antibody	8946	0 Month	97.01	198.66	8946	1 Month	2.84	-	1436.20
Virus	8946	0 Month	97.01	263.18	4334	PI calf	-	POS	1096.61
Virus	8950	0 Month	100.86	252.83	4554	PI calf	-	POS	602.86
Antibody	8954	0 Month	95.12	363.76	8954	1 Month	6.86	-	707.15
Antibody	9042	0 Month	102.87	110.93	9042	1 Month	95.94	-	212.56

Table 4.1: EIS results obtained from the 10 nanoband senor chips in this study; and results obtained from the gold standard analytical laboratory technique, ELISA. Data constitutes detection of BVD antibody and virus on electrodes 1-2 (0 hour negative controls) and electrodes 3-5 on the microSD chips (1 month and PI calves).

4.4 Conclusions

In this chapter, we present new sensor chips that comprise six on-chip nanoband electrodes, integrated counter and pseudo reference electrode and a micro SD style pin-out connection to facilitate facile connection to external circuitry. The pin-out allows easy replacement of disposable biosensor chips in a final diagnostic device.

Biomolecules were immobilised at nanoband electrodes using an electrodeposited polymer anchor layer followed by EDC based covalent coupling of capture probe material to provide a robust bio-modification process that could withstand cleaning protocols without degradation. Appropriately modified sensors were challenged with their target analytes in three different media with increasing levels of biological complexity. In all cases, the sensors exhibited excellent specificity easily distinguishing between positive and negative samples while also exhibiting a semi-log linear dependency between concentration and increase in charge transfer resistance. Concerning whole serum, the sensors were benchmarked against and, in all cases, were in agreement with, commercial 'gold standard' laboratory results. These proof-of-concept studies in sera samples are very promising in that they show clear differentiation between BVD (antibody and virus) positive and negative sera samples. The nanoband sensors demonstrate the capability to detect both virus and antibodies in whole serum, which is an essential prerequisite for on-farm BVD serological screening and surveillance. The short measurement times ~20 minutes also satisfies the time requirements for on-farm analysis.

4.5 References

1.   Peterhans, E.; Schweizer, M., Bvdv: A Pestivirus Inducing Tolerance of the Innate Immune Response; *Biologicals,* **2013**, 41, 39-51.

2.   Richter, V.; Lebl, K.; Baumgartner, W.; Obritzhauser, W.; Käsbohrer, A.; Pinior, B., A Systematic Worldwide Review of the Direct Monetary Losses in Cattle Due to Bovine Viral Diarrhoea Virus Infection; *The Veterinary Journal,* **2017**, 220, 80-87.

3.   Graham, D.A.; Clegg, T.A.; O'sullivan, P.; More, S.J., Survival Time of Calves with Positive Bvd Virus Results Born During the Voluntary Phase of the Irish Eradication Programme; *Preventive Veterinary Medicine,* **2015**, 119, 123-133.

4.   Houe, H., Economic Impact of Bvdv Infection in Dairies; *Biologicals,* **2003**, 31, 137-143.

5.   Stott, A.W.; Humphry, R.W.; Gunn, G.J.; Higgins, I.; Hennessy, T.; O'flaherty, J.; Graham, D.A., Predicted Costs and Benefits of Eradicating Bvdv from Ireland; *Irish Veterinary Journal,* **2012**, 65, 12.

6.   Bitsch, V.; Hansen, K.E.L.; Rønsholt, L., Experiences from the Danish Programme for Eradication of Bovine Virus Diarrhoea (Bvd) 1994-1998 with Special Reference to Legislation and Causes of Infection; *Veterinary Microbiology,* **2000**, 77.

7.   Greiser-Wilke, I.; Grummer, B.; Moennig, V., Bovine Viral Diarrhoea Eradication and Control Programmes in Europe; *Biologicals,* **2003**, 31.

8.   Nyberg, O.; Østeras, O.; Plym Forshell, K. Eradication of Bvdv-Infection in Norwegian Cattle 1992-2003 - a Success Story. In Proceedings of the Second European Symposium on Bvdv Control; *Oporto:* Portugal, 2004.

9.   Presi, P.; Struchen, R.; Knight-Jones, T.; Scholl, S.; Heim, D., Bovine Viral Diarrhea (Bvd) Eradication in Switzerland--Experiences of the First Two Years; *Preventive Veterinary Medicine,* **2011**, 99.

10.   Ståhl, K.; Kampa, J.; Baule, C.; Isaksson, M.; Moreno-López, J.; Belák, S.; Alenius, S.; Lindberg, A., Molecular Epidemiology of Bovine Viral Diarrhoea During the Final Phase of the Swedish Bvd-Eradication Programme; *Preventive Veterinary Medicine,* **2005**, 72, 103-108.

11.   Mcclurkin, A.W.; Littledike, E.T.; Cutlip, R.C.; Frank, G.H.; Coria, M.F.; Bolin, S.R., Production of Cattle Immunotolerant to Bovine Viral Diarrhea Virus; *Canadian Journal of Comparative Medicine,* **1984**, 48, 156-161.

12.   Houe, H., Epidemiological Features and Economical Importance of Bovine Virus Diarrhoea Virus (Bvdv) Infections; *Veterinary Microbiology,* **1999**, 64, 89-107.

13.   Presi, P.; Heim, D., Bvd Eradication in Switzerland—a New Approach; *Veterinary Microbiology,* **2010**, 142, 137-142.

14.   Graham, D.A.; Lynch, M.; Coughlan, S.; Doherty, M.L.; Neill, R.; Sammin, D.; Flaherty, J., Development and Review of the Voluntary Phase of a National Bvd Eradication Programme in Ireland; *Veterinary Record,* **2014**, 174, 67.

15.   Lindberg, A.L.E.; Alenius, S., Principles for Eradication of Bovine Viral Diarrhoea Virus (Bvdv) Infections in Cattle Populations; *Veterinary Microbiology,* **1999**, 64, 197-222.

16.   Norström, M.; Jonsson, M.E.; Åkerstedt, J.; Whist, A.C.; Kristoffersen, A.B.; Sviland, S.; Hopp, P.; Wahlström, H., Estimation of the Probability of Freedom from Bovine Virus Diarrhoea Virus in Norway Using Scenario Tree Modelling; *Preventive Veterinary Medicine,* **2014**, 116, 37-46.

17.   Rossmanith, W.; Deinhofer, M.; Janacek, R.; Trampler, R.; Wilhelm, E., Voluntary and Compulsory Eradication of Bovine Viral Diarrhoea Virus in Lower Austria; *Veterinary Microbiology,* **2010**, 142, 143-149.

18.   Lanyon, S.R.; Hill, F.I.; Reichel, M.P.; Brownlie, J., Bovine Viral Diarrhoea: Pathogenesis and Diagnosis; *The Veterinary Journal,* **2014**, 199, 201-209.

19.   Kramps, J.A.; Maanen, C.V.; Wetering, G.V.D.; Stienstra, G.; Quak, S.; Brinkhof, J.; Rønsholt, L.; Nylin, B., A Simple, Rapid and Reliable Enzyme-Linked Immunosorbent Assay for the Detection of Bovine Virus Diarrhoea Virus (Bvdv) Specific Antibodies in Cattle Serum, Plasma and Bulk Milk; *Veterinary Microbiology,* **1999**, 64, 135-144.

20.   Howard, C.J.; Clarke, M.C.; Brownlie, J., An Enzyme-Linked Immunosorbent Assay (Elisa) for the Detection of Antibodies to Bovine Viral Diarrhoea Virus (Bvdv) in Cattle Sera; *Veterinary Microbiology,* **1985**, 10, 359-369.

21.   Belak, S.; Ballagi-Pordany, A. Bovine Viral Diarrhea Virus Infection: Rapid Diagnosis by the Polymerase Chain Reaction. In Ruminant Pestivirus Infections; *Springer:* 1991, pp 181-190.

22.   Letellier, C.; Kerkhofs, P., Real-Time Pcr for Simultaneous Detection and Genotyping of Bovine Viral Diarrhea Virus; *Journal of Virological Methods,* **2003**, 114, 21-27.

23.   Saliki, J.T.; Fulton, R.W.; Hull, S.R.; Dubovi, E.J., Microtiter Virus Isolation and Enzyme Immunoassays for Detection of Bovine Viral Diarrhea Virus in Cattle Serum; *Journal of Clinical Microbiology,* **1997**, 35, 803-807.

24.   Cornish, T.E.; Olphen, A.L.V.; Cavender, J.L.; Edwards, J.M.; Jaeger, P.T.; Vieyra, L.L.; Woodard, L.F.; Miller, D.R.; O'toole, D., Comparison of Ear Notch Immunohistochemistry, Ear Notch Antigen-Capture Elisa, and Buffy Coat Virus Isolation for Detection of Calves Persistently Infected with Bovine Viral Diarrhea Virus; *Journal of Veterinary Diagnostic Investigation,* **2005**, 17, 110-117.

25.   Kameyama, K.; Sakoda, Y.; Tamai, K.; Igarashi, H.; Tajima, M.; Mochizuki, T.; Namba, Y.; Kida, H., Development of an Immunochromatographic Test Kit for Rapid Detection of Bovine Viral Diarrhea Virus Antigen; *Journal of Virological Methods,* **2006**, 138, 140-146.

26.   Wakeley, P.R.; Errington, J.; Squirrell, D., Use of a Field-Enabled Nucleic Acid Extraction and Pcr Instrument to Detect Bvdv; *Veterinary Record,* **2010**, 166, 238.

27.   Pejcic, B.; Marco, R.D.; Parkinson, G., The Role of Biosensors in the Detection of Emerging Infectious Diseases; *Analyst,* **2006**, 131, 1079-1090.

28.   Kiilerich-Pedersen, K.; Daprà, J.; Cherré, S.; Rozlosnik, N., High Sensitivity Point-of-Care Device for Direct Virus Diagnostics; *Biosensors and Bioelectronics,* **2013**, 49, 374-379.

29.   Ciani, I.; Schulze, H.; Corrigan, D.K.; Henihan, G.; Giraud, G.; Terry, J.G.; Walton, A.J.; Pethig, R.; Ghazal, P.; Crain, J.; Campbell, C.J.; Bachmann, T.T.; Mount, A.R., Development of Immunosensors for Direct Detection of Three Wound Infection Biomarkers at Point of Care Using Electrochemical Impedance Spectroscopy; *Biosensors and Bioelectronics,* **2012**, 31, 413-418.

30.   Daniels, J.S.; Pourmand, N., Label-Free Impedance Biosensors: Opportunities and Challenges; *Electroanalysis,* **2007**, 19, 1239-1257.

31.   Chang, B.-Y.; Park, S.-M., Electrochemical Impedance Spectroscopy; *Annual Review of Analytical Chemistry,* **2010**, 3, 207-229.

32.   Arrigan, D.W.M., Nanoelectrodes, Nanoelectrode Arrays and Their Applications; *Analyst,* **2004**, 129, 1157-1165.

33.   Dawson, K.; Baudequin, M.; Sassiat, N.; Quinn, A.J.; O'riordan, A., Electroanalysis at Discrete Arrays of Gold Nanowire Electrodes; *Electrochimica Acta,* **2013**, 101, 169-176.

34.   Dawson, K.; Baudequin, M.; Sassiat, N.; Quinn, A.J.; O'riordan, A., Electroanalysis at Discrete Arrays of Gold Nanowire Electrodes; *Electrochimica Acta,* **2013**, 101, 169-176.

35.   Kuhne, S.; Schroeder, C.; Holmquist, G.; Wolf, G.; Horner, S.; Brem, G.; Ballagi, A., Detection of Bovine Viral Diarrhoea Virus Infected Cattle–Testing Tissue Samples Derived from Ear Tagging Using an Erns Capture Elisa; *Zoonoses and Public Health,* **2005**, 52, 272-277.

36.   Aberle, D.; Muhle-Goll, C.; Bürck, J.; Wolf, M.; Reißer, S.; Luy, B.; Wenzel, W.; Ulrich, A.S.; Meyers, G., Structure of the Membrane Anchor of Pestivirus Glycoprotein E(Rns), a Long Tilted Amphipathic Helix; *PLoS Pathogens,* **2014**, 10, e1003973.

37.   Wahl, A.; Barry, S.; Dawson, K.; Machale, J.; Quinn, A.J.; O'riordan, A., Electroanalysis at Ultramicro and Nanoscale Electrodes: A Comparative Study; *Journal of The Electrochemical Society,* **2014**, 161, B3055-B3060.

38.   Dawson, K.; Wahl, A.; Murphy, R.; O'riordan, A., Electroanalysis at Single Gold Nanowire Electrodes; *Journal of Physical Chemistry C,* **2012**, 116, 14665-14673.

39.   Malitesta, C.; Palmisano, F.; Torsi, L.; Zambonin, P.G., Glucose Fast-Response Amperometric Sensor Based on Glucose Oxidase Immobilized in an Electropolymerized Poly (O-Phenylenediamine) Film; *Analytical Chemistry,* **1990**, 62, 2735-2740.

40.   Garjonyte, R.; Malinauskas, A., Amperometric Glucose Biosensor Based on Glucose Oxidase Immobilized in Poly (O-Phenylenediamine) Layer; *Sensors and Actuators B: Chemical,* **1999**, 56, 85-92.

41.   Sassolas, A.; Blum, L.J.; Leca-Bouvier, B.D., Immobilization Strategies to Develop Enzymatic Biosensors; *Biotechnology Advances,* **2012**, 30, 489-511.

42.   Cosnier, S., Biomolecule Immobilization on Electrode Surfaces by Entrapment or Attachment to Electrochemically Polymerized Films. A Review; *Biosensors and Bioelectronics,* **1999**, 14, 443-456.

43.   Teles, F.R.R.; Fonseca, L.P., Applications of Polymers for Biomolecule Immobilization in Electrochemical Biosensors; *Materials Science and Engineering: C,* **2008**, 28, 1530-1543.

Chapter 5   **Label-free Impedimetric Immunosensing of Bovine Liver Fluke**

5.1 Introduction

The previous chapters introduced new sensor chips that employed a micro SD style pin-out connection for the detection of a virus associated with the bovine respiratory disease, bovine viral diarrhoea (BVD). The proof-of-concept studies, in the case of BVD detection, showed a clear differentiation between BVD positive and BVD negative sera samples for detection of both antibodies and viruses. In this chapter, the same sensor platform is employed and challenged to the detection of antibodies against Fasciola hepatica, or more commonly Liver Fluke.

Liver fluke disease (or fasciolosis) is a disease caused by a helminth flat worm parasite, *Fasciola hepatica,* affecting cattle and sheep globally.[1, 2] It is an ovoid shaped worm that colonises the liver of its host species. Grazing animals are infected through the ingestion of larvae (metacercariae) on contaminated grass. In cattle, liver fluke is most prevalent in Europe, with infection rates increasing because of the emergence of drug-resistant parasites and, possibly, as a result of climate change.[3] These infections are responsible for massive economic losses of ~€2.5 billion to livestock and food industries worldwide,[4-6] and is estimated to cost the Irish industry ~€90M, annually.[7] Similar to the other bovine diseases previously discussed, economic losses caused by liver fluke are mainly associated with a reduction in milk yields and meat production. Moreover the WHO have emphasised the serious and growing public health concern posed by foodborne trematode infections, which affect an estimated 40 million persons.[8] It is estimated that worldwide over 2.4 million humans are infected with *F. hepatica* and about 180 million, mainly in South America, are at risk of infection.[9, 10]. Therefore, there is an increased need to implement control measures against these infections, both in humans and animals.

Traditional diagnosis methods for *Fasciola* were based on faecal egg counts, or detection of the parasite's eggs in stool samples.[1] However these methods are reported to be unsatisfactory due to cases of low egg shedding.[11, 12] Current detection method includes the serological diagnosis in milk or serum by an ELISA. The majority of the ELISA described in the literature employ excretory-secretory (ES) antigens for the detection of anti-*Fasciola* antibodies.[13-18] Commercial ELISA's also exist as detection methods employing these ES antigens, including the Bio-X bovine F. hepatica ELISA kit[13] and the

219

Pourquier ELISA kit.[19, 17, 18] Furthermore, cathepsin L1 (cat L1), a major cysteine protease, has been widely recognised as a potential prospective diagnostic tool for *Fasciola* infections.[20] Robinson and Smith *et al.* have shown that the most predominant molecules secreted by *F. hepatica* parasites *in vitro* are cat L1 L-cysteine proteases and therefore function extracellularly. [21, 22] Biochemical and immunological studies indicate that, by the time the parasites have moved into the immunologically safe environment of the bile ducts, they become reliant solely on cathepsin L-proteases.[22, 23]

The reported literature presents the ELISA results for cat L1 affinity towards liver fluke antibodies. To our knowledge there are no electrochemical techniques used for the determination of the parasite, in the literature. Protease enzyme activity had to be explored electrochemically, for example as cancer biomarkers,[24] but they have not been employed as a capture biomolecule for the detection of liver fluke, previously. In this short chapter, proof of concept studies on the detection of anti-*Fasciola* antibodies in serum samples, are undertaken. A protease enzyme, cat L1 from University College Dublin, (UCD) was employed as the capture antigen on our electrodes and subsequently, the sensors were subjected to different groups of blood sera, of know serostatus.

5.2 Experimental

5.2.1 Materials and Preparation of Standards

Procathepsin L1 was expressed and purified by UCD.[20] Serum samples from *Fasciola hepatica* seronegative and seropositive animals were provided by Teagasc (Moorepark, Cork, Ireland). Anti-Bovine Albumin antibody produced in rabbit (B7276), was purchased from Sigma Aldrich. Acetate buffer (10 mM; pH 4) and ethanolamine-HCl (1mM) were obtained from Sierra Sensors GmbH (Germany). All other reagents were purchased from Sigma Aldrich unless otherwise stated and used as received. Deionised water (resistance 18.2 MΩ cm) was obtained using an ELGA Pure Lab Ultra system.

5.2.2 Fabrication and Characterisation of the Sensor Chip

5.2.2.1 Fabrication of Nanoband Electrodes

Gold nanoband, contact pads and on-chip gold counter and platinum pseudo-reference electrodes were fabricated using lithography processes as previously described in chapter 4 (section 4.4.2). The same connection with a PCB mounted microSD port was used in conjunction with the fabricated chip holders, for analysis.

5.2.2.2 Characterisation at Nanoband Electrodes

SEM analysis was undertaken following the electrodeposition of oABA, to examine the polymerisation on the electrode surface. SEM images were acquired using a calibrated field emission SEM (JSM-7500F, JEOL UK Ltd.) operating at beam voltages between 3 and 5 kV.

Electrochemical experiments were carried out using an Autolab Potentiostat/ Galvanostat PGSTAT128N (Metrohm Ltd, Utrecht, The Netherlands) controlled by the Autolab NOVA software. All experiments employed a standard three-electrode cell configuration using a single gold nanowire as the working electrode, versus the on-chip gold counter and platinum pseudo-reference electrodes.   Each sensor working electrode was characterised by CV and faradaic EIS, in a 10 mM PBS solution (pH = 7.4) containing 1 mM FcCOOH. For CV, the potential was cycled from -200 mV to +600 mV versus the

on-chip platinum pseudo reference electrode at a scan rate of 100 mV/s. The impedance measurements were performed over the frequency range from 100 mHz to 100 kHz at the equilibrium potential of the FcCOOH (200 mV). The amplitude of the alternating voltage was 5 mV. All experiments were performed at room temperature in a Faraday cage.

5.2.3 Target Liver Fluke Detection

The nanoband sensor was applied to the detection of anti-*Fasciola* antibodies in serum samples. Figure 5.1 illustrates a schematic of this modification process. On-chip nanoband electrodes were first cleaned using a mixed solvent clean process (acetone, isopropyl alcohol and DI water) for 15 minutes and dried under a stream of nitrogen. Cyclic voltammetry was then employed for electropolymerisation of o-aminobenzoic acid (o-ABA, 50 mM in 0.5 M H_2SO_4) to create a carboxylic terminated polymer layer at the gold electrode surface, as described in the previous chapter (section 4.2.5.3). The electrodeposition was performed using the prefabricated chip holder and the PCB mounted microSD port to connect the chip to the external potentiostat. A fresh NHS/EDC mixture was prepared in DI water and subsequently deposited onto the polymerised electrodes, for approximately 30 min, to activate the surface. Recombinant cat L1 enzyme protease was diluted in 10 mM sodium acetate buffer, pH 4.0 to a concentration of 10 µg/mL, and was deposited onto all the activated nanoband electrodes, for 1 hour, at 4°C. The unbound active-sites on the electrodes were then subsequently blocked with ethanolamine (1 M) for 20 minutes.

Fasciola hepatica seropositive and seronegative undiluted serum samples were then investigated. A spotting technique, was employed to test one negative (electrode 1 and 2) and one positive sample (electrodes 3-5) on the same chip. The samples were incubated on the electrodes for a 10 minutes, followed by thorough rinsing with HBS-EP buffer solution (contain Tween-20) to remove any un-bound antibodies.

A number of serum samples from different hosts were examined, all of which have corresponding ELISA results (undertaken by partners in Teagasc) determining whether the blood was seronegative or seropositive for anti-*Fasciola hepatica* antibodies.
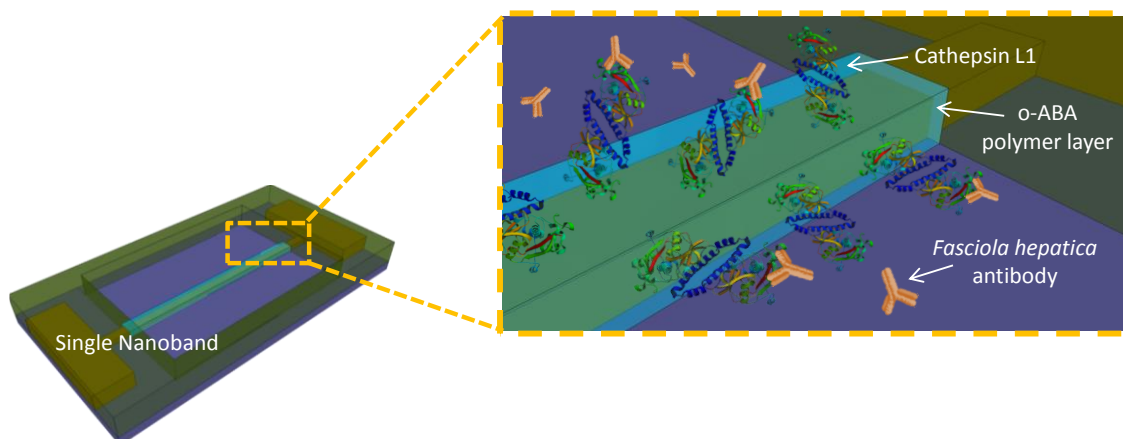
Figure 5.1: Schematic of the electrode surface modification for the detection of liver fluke antibodies (not to scale).

5.3 Results and Discussion

5.3.1 Electrode Characterisation

Figure 5.2 (a) shows a photograph of a sensor chip on the tip of a finger. The electrode are spaced out enough that their passivation window are visible to the human eye. As discussed, each chip contained six separate nanoband working electrodes and gold counter and platinum pseudo-reference electrodes. Following modification with oABA, SEM analysis was undertaken on the electrode to characterise the deposition of the oABA layer. Figure 5.2 (b) shows a typical SEM micrograph of clean gold nanoband electrode, whereas Figure 5.2 (c) portrays a nanoband electrode following electrodeposition of o-aminobenzoic acid. From SEM analysis, the polymer layer appears to be uniformly distributed over the entire electrode surface.
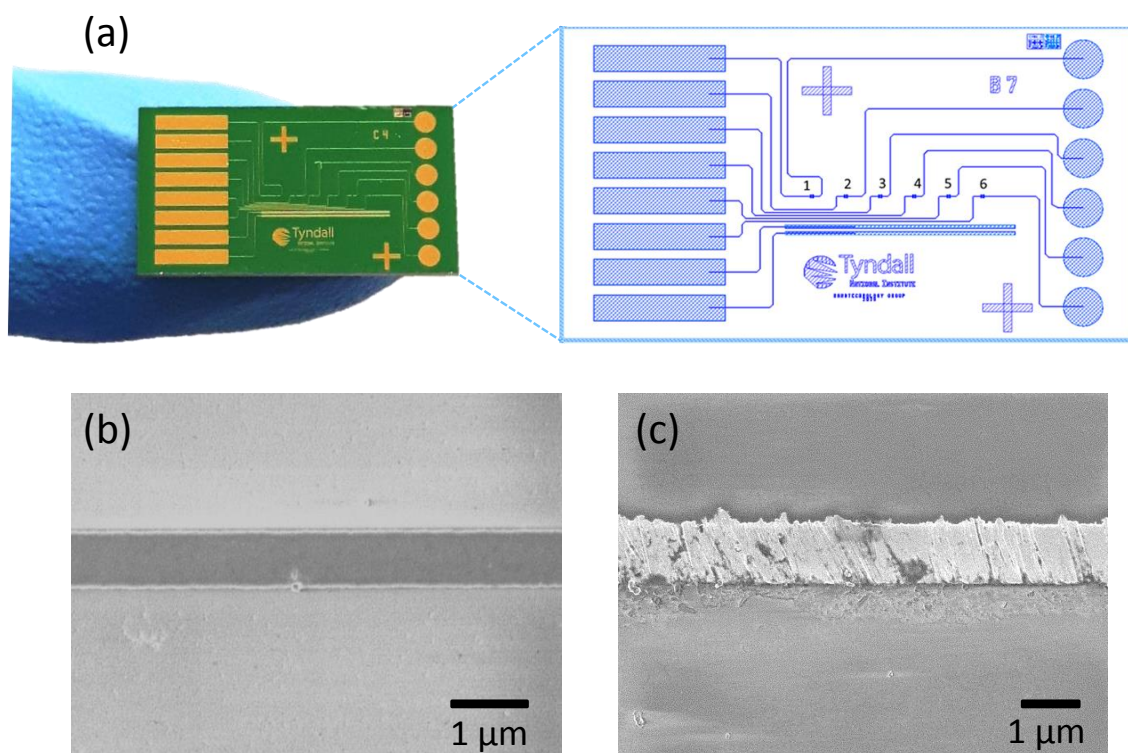

Figure 5.2: (a) Photograph of the micro-SD sensor chip and a schematic of the chip design layout with electrodes 1-6 labelled (right). (b) SEM image of a clean gold nanoband electrode (700 nm) and (c) SEM image of the nanoband following electropolymerisation with o-ABA.

The polymer layer covers the electrode enough for successful crosslinking to biomolecules. Also, there are slight gaps which are required to prevent a fully capacitive coating on the electrode and thus permit electron transfer.

5.3.2 Detection of Liver Fluke

A protein, cathepsin L1 was employed as the capture on the sensor to detect liver fluke antibodies present in bovine serum. A number of sensor chips, modified with cat L1 (10 µg/mL), were employed to test for the presence of fluke in calf whole serum. A spotting technique was used to deposit multiple fluke positive and negative sera samples on different on-chip electrodes. Typical EIS Nyquist plots for the detection of anti-Fasciola antibodies in seronegative (calf no.8954) obtained at time 0 month, and seropositive (calf no. 941) samples, are presented in Figure 5.3 (a) and (b), respectively. Both measurements were undertaken on separate electrodes on the same microSD chip.
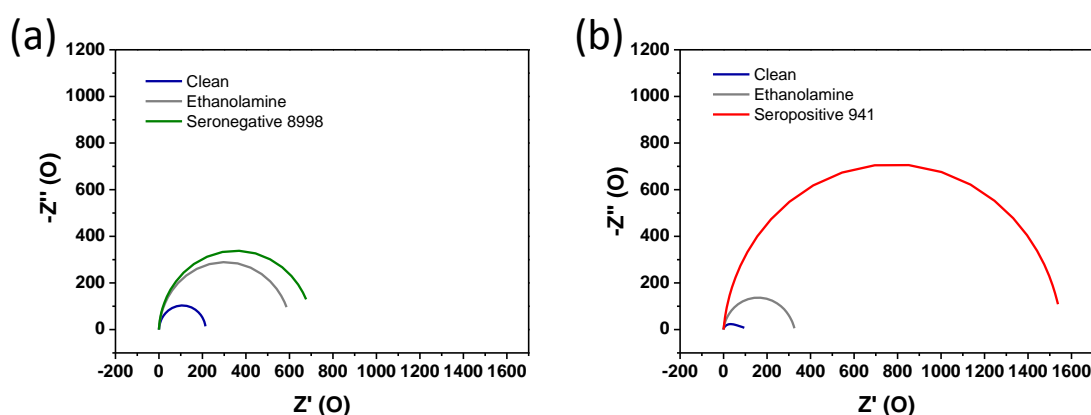

Figure 5.3: Nyquist plots for the detection of (a) a seronegative fluke sample and (b) a seropositive fluke sample.

Data from the seronegative sample produced an impedance of ~650 MΩ (R_{ct}), which increased slightly following the ethanolamine baseline of ~500 MΩ, see Figure 5.3 (a), green plot. This data suggest there is minimal non-specific binding from the serum samples. Moreover, judging from the baseline ethanolamine measurements, the cat L1 immobilisation appears to be blocking the electrode more than previously seen with BVD, in chapter 4. In these experiments, it is therefore crucial to background subtract the ethanolamine data from the target to ensure correct serostatus determination. The target

fluke seropositive sample revealed a substantial increase in the R_{ct} value (~1200 MΩ), following incubation when compared to the baseline (400 MΩ). We suggest that this large increase in R_{ct} arises from the binding of fluke antibodies to the cat L1 and thus act as a kinetic barrier to the transfer of electrons from the FcCOOH to the electrode, hence increasing the system resistance.

In order to validate these findings, several more seropositive and seronegative samples were analysed for the presence of liver fluke. Figure 5.4 shows a bar chart of experimental background subtracted Rct EIS data, obtained for a number of individual samples. All the samples were provided by Teagasc and were subjected to ELISA testing prior to analysis. The bars in Figure 5.4 have been colour coded corresponding to their ELISA results. Seronegative samples for individual calves are shown as green bars. These samples all exhibited very low impedance (<300 MΩ) for antibody detection, as expected. Calves that exhibited ELISA results that are considered "suspect" are presented as orange bars. These samples contain antibodies for fasciolosis at a level in which they cannot be determined positive or negative for the parasite infection. Briefly, ELISA testing has a scale by which they deem samples as positive or negative from their absorbance readings. The samples that fall close to the positive/negative border are the suspect samples. The impedance values for these samples lay between the positive and negative values. These samples may contain a small concentration of the fasciolosis antibodies, perhaps from the past infections, since antibodies may persist in the subject for years post treatment. The individual could also be newly infected, thus it is these samples that cause false positive or false negative results. The target seropositive samples, presented as red bars, show a significant increase in the electron-transfer resistance (>800 MΩ) at the electrode following deposition. Comparing this response to the seronegative response, the impedance increase can be attributed the attachments of anti-*Fasciola* antibodies to the cat L1 protein.

These results propose that there is successful serological binding of the fluke antibodies to the immobilised cat L1 protein, as experienced for the BVD samples in Chapter 4. Furthermore, the data supports the suitability of these sensors for use as on-farm diagnostic devices as the sensors can discriminate between seropositive and seronegative in undiluted blood serum with comparable ELISA results. Further work is however

needed, to improve sensitivity of the sensors and the inclusion of control electrodes are required, see Chapter 7.
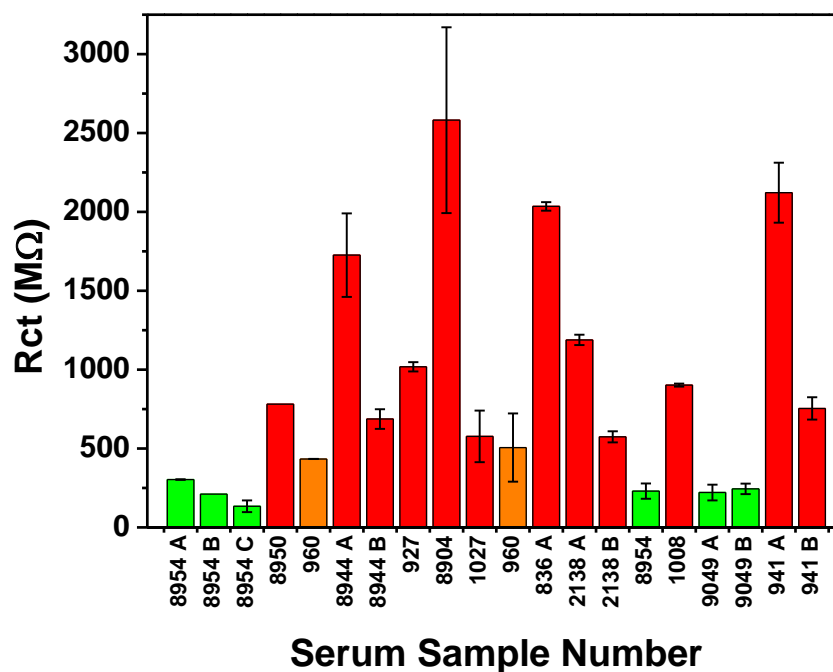

Figure 5.4: Bar chart testing seropositive and seronegative fluke samples, background subtracted from their respective ethanolamine baselines. Colours correspond to their equivalent ELISA readings, red – positive, green – negative and orange – unknown.

5.4 Conclusions

In this short chapter, I presented some of the preliminary proof of concept results obtained with the microSD sensing platform for the detection of a parasitic bovine liver fluke. A protease enzyme, cathepsin L1, produced by DCU was employed at the capture molecule for the detection of anti-*Fasciola* antibodies in serum samples. All serum samples employed in this study had previous ELISA testing undertaken by researchers in Teagasc. The serostatus observed from the EIS data was the same as for the ELISA testing, for a number of serum samples. To our knowledge this is the first electrochemical determination of the parasite, in the literature. For future experiments, the presence of the parasite anti-*Fasciola* antibodies will be explored in bovine milk samples as it requires little sample pre-treatment

5.5 References

1.   Boray, J., Flukes of Domestic Animals; *Elsevier,* Amsterdam, **1985;** Vol. B2.

2.   Tort, J.; Brindley, P.J.; Knox, D.; Wolfe, K.H.; Dalton, J.P., Proteinases and Associated Genes of Parasitic Helminths; *Advances in Parasitology,* **1999**, 43, 161-266.

3.   Stack, C.M.; Caffrey, C.R.; Donnelly, S.M.; Seshaadri, A.; Lowther, J.; Tort, J.F.; Collins, P.R.; Robinson, M.W.; Xu, W.; Mckerrow, J.H.; Craik, C.S.; Geiger, S.R.; Marion, R.; Brinen, L.S.; Dalton, J.P., Structural and Functional Relationships in the Virulence-Associated Cathepsin L Proteases of the Parasitic Liver Fluke, Fasciola Hepatica; *Journal of Biological Chemistry,* **2008**, 283, 9896-9908.

4.   Bisset, S.A., Helminth-Parasites of Economic Importance in Cattle in New-Zealand; *New Zealand Journal of Zoology,* **1994**, 21, 9-22.

5.   Sargison, N.D.; Scott, P.R., Diagnosis and Economic Consequences of Triclabendazole Resistance in Fasciola Hepatica in a Sheep Flock in South-East Scotland; *Veterinary Record,* **2011**, 168, 159-U22.

6.   Charlier, J.; Van Der Voort, M.; Kenyon, F.; Skuce, P.; Vercruysse, J., Chasing Helminths and Their Economic Impact on Farmed Ruminants; *Trends in Parasitology,* **2014**, 30, 361-367.

7.   Schweizer, G.; Braun, U.; Deplazes, P.; Torgerson, P.R., Estimating the Financial Losses Due to Bovine Fasciolosis in Switzerland; *Veterinary Record,* **2005**, 157, 188-193.

8.   Organization, W.H., Control of Foodborne Trematode Infections: Report of a Who Study Group; **1995**.

9.   Mas-Coma, S.; Bargues, M.D.; Valero, M.A., Fascioliasis and Other Plant-Borne Trematode Zoonoses; *International Journal for Parasitology,* **2005**, 35, 1255-1278.

10.   Mcmanus, D.P.; Dalton, J.P., Vaccines against the Zoonotic Trematodes Schistosoma Japonicum, Fasciola Hepatica and Fasciola Gigantica; *Parasitology,* **2007**, 133, S43-S61.

11.   Happich, F.; Boray, J., Quantitative Diagnosis of Chronic Fasciolosis. 1. Comparative Studies on Quantitative Faecal Examinations for Chronic Fasdola Hepatica in Sheep; *Australian Veterinary Journal,* **1969**, 45, 326-328.

12.   Mas-Coma, S.; Bargues, M.; Valero, M., Diagnosis of Human Fascioliasis by Stool and Blood Techniques: Update for the Present Global Scenario; *Parasitology,* **2014**, 141, 1918-1946.

13.   Salimi-Bejestani, M.R.; Mcgarry, J.W.; Felstead, S.; Ortiz, P.; Akca, A.; Williams, D.J.L., Development of an Antibody-Detection Elisa for Fasciola Hepatica and Its Evaluation against a Commercially Available Test; *Research in Veterinary Science,* **2005**, 78, 177-181.

14.   Anuracpreeda, P.; Wanichanon, C.; Chawengkirtikul, R.; Chaithirayanon, K.; Sobhon, P., Fasciola Gigantica: Immunodiagnosis of Fasciolosis by Detection of Circulating 28.5 Kda Tegumental Antigen; *Experimental Parasitology,* **2009**, 123, 334-340.

15.   Martinez, A.; Martinezcruz, M.S.; Martinez, F.J.; Gutierrez, P.N.; Hernandez, S., Detection of Antibodies to Fasciola Hepatica Excretory-Secretory Antigens in Experimentally Infected Goats by Enzyme Immunosorbent Assay; *Veterinary Parasitology,* **1996**, 62, 247-252.

16.	Arias, M.; Hillyer, G.V.; Sanchez-Andrade, R.; Suarez, J.L.; Pedreira, J.; Lomba, C.; Diaz, P.; Morrondo, P.; Diez-Banos, P.; Paz-Silva, A., A 2.9 Kda Fasciola Hepatica-Recombinant Protein Based Elisa Test for the Detection of Current-Ovine Fasciolosis Trickle Infected; *Veterinary Parasitology,* **2006**, 137, 67-73.

17.	Levieux, D.; Levieux, A.; Mage, C.; Garel, J.P., Immunological Detection of Chemotherapeutic Success in Bovine Fascioliasis Using the Specific Antigen-F2; *Veterinary Parasitology,* **1992**, 45, 81-88.

18.	Mezo, M.; Gonzalez-Warleta, M.; Castro-Hermida, J.A.; Muino, L.; Ubeira, F.M., Field Evaluation of the Mm3-Sero Elisa for Detection of Anti-Fasciola Igg Antibodies in Milk Samples from Individual Cows and Bulk Milk Tanks; *Parasitology International,* **2010**, 59, 610-615.

19.	Charlier, J.; De Meulemeester, L.; Claerebout, E.; Williams, D.; Vercruysse, J., Qualitative and Quantitative Evaluation of Coprological and Serological Techniques for the Diagnosis of Fasciolosis in Cattle; *Veterinary Parasitology,* **2008**, 153, 44-51.

20.	Collins, P.R.; Stack, C.M.; O'neill, S.M.; Doyle, S.; Ryan, T.; Brennan, G.P.; Mousley, A.; Stewart, M.; Maule, A.G.; Dalton, J.P.; Donnelly, S., Cathepsin L1, the Major Protease Involved in Liver Fluke (Fasciola Hepatica) Virulence; *Journal of Biological Chemistry,* **2004**, 279, 17038-17046.

21.	Smith, A.M.; Dowd, A.J.; Mcgonigle, S.; Keegan, P.S.; Brennan, G.; Trudgett, A.; Dalton, J.P., Purification of a Cathepsin L-Like Proteinase Secreted by Adult Fasciola Hepatica; *Molecular and Biochemical Parasitology,* **1993**, 62, 1-8.

22.	Robinson, M.W.; Tort, J.F.; Lowther, J.; Donnelly, S.M.; Wong, E.; Xu, W.; Stack, C.M.; Padula, M.; Herbert, B.; Dalton, J.P., Proteomics and Phylogenetic Analysis of the Cathepsin L Protease Family of the Helminth Pathogen Fasciola Hepatica: Expansion of a Repertoire of Virulence-Associated Factors; Molecular & Cellular Proteomics, 2008, 7, 1111-1123.

23.	Robinson, M.W.; Dalton, J.P.; Donnelly, S., Helminth Pathogen Cathepsin Proteases: It's a Family Affair; Trends in Biochemical Sciences, 2008, 33, 601-608.

24.	Swisher, L.Z.; Prior, A.M.; Shishido, S.; Nguyen, T.A.; Hua, D.H.; Li, J., Quantitative Electrochemical Detection of Cathepsin B Activity in Complex Tissue Lysates Using Enhanced Ac Voltammetry at Carbon Nanofiber Nanoelectrode Arrays; Biosensors and Bioelectronics, 2014, 56, 129-136.

Chapter 6   **Integrated   Impedimetric   and Potentiometric   Biosensing   of   BPI3-V   Antibody-Antigen Complex**

6.1 Introduction

In Chapter 4, the bovine viral diarrhoea virus, one of the viruses associated with bovine respiratory disease (BRD); the leading natural cause of death in the US and EU,[1-3] was introduced and discussed. Continuing the investigation on BRD, in this chapter, the bovine parainfluenza virus type 3 (BPIV-3) is presensted. BPI3-V is a member of the *Paramyxoviridae* family, genus *Respirovirus*, one of the largest and most rapidly growing groups of viruses causing significant human and veterinary disease. [4, 5] It is associated with the clinical condition known as 'shipping fever', in which the animal develops clinical signs after transport over long distances. To reiterate, these diseases have detrimental impacts on the cattle industry; decreasing on-farm efficiency and profitability through waste feed and increased veterinary costs. [6, 7] Furthermore, the demand for an increase in livestock production potentially increases virus development within herds. Although a few European countries have achieved total eradication, many countries have not initiated national schemes as they are deemed too cost-prohibitive and time-consuming.[8-10] This BPI3-V remains a major source of economic loss in the cattle industry, and again, early identification is essential to achieve disease control.[11]

Current detection methods are performed using Reverse Transcription Polymerase Chain Reaction (RT-PCR), immunohistochemistry or ELISA;[12-15] although these high-end analytical techniques are sensitive and reliable, they require dedicated laboratories, skilled personnel and long analysis times. Label-free immunosensors constitute a promising group of sensing devices that offer the potential to deliver rapid and early identification of animal disease state on-farm through the use of microfabrication techniques and biochemistry. They allow high sensitivity, short analysis times, affordability, miniaturised platforms with low sample consumption and the possibility for measurements in complex samples.[16, 17] Immunosensors measure the interaction of

---

[†] This work was published in part as "Direct correlation between potentiometric and impedance biosensing of antibody-antigen interactions using an integrated system." *Applied Physics Letters* **2017**, 111, 073701.

[†] This work has been prepared for publications as "Integrated Impedimetric and Potentiometric Biosensing of BPIV-3 Antibody-Antigen Complex" *Journal of Phys Chem* , in preparation

antibody-antigen complexes, and employ a transduction system to directly detect the immunochemical reaction and deliver a measurable signal.[18] The electrical transducer EIS, which demonstrated label-free sensing of BVD, in Chapter 4, is again employed in this chapter, but in combination with field effect transistor potentiometry.

Potentiometric and impedimetric sensors are both capable of label-free operation that can simplify sample preparation steps and enable on-site detection with shorter turnover times. Potentiometric sensors measure the potential change induced by biomolecule binding to the sensor surface, under DC operation, and directly translate this interaction into an electrical signal. The ion sensitive FET (ISFET) and extended gate FET (EGFET) are the most popular electrical sensors for immunosensing applications. [19-24] However, for these experiments, the EGFET design was preferred to an ISFET, because the presence of an extended gate separates the transducer from the sensing platform, providing a better configuration to allow parallel sensing with EIS and integration with the sensor chip platform. Alternatively, impedimetric sensors measure the current change in a system, which correlated to the amount of an analyte binding, through application of AC voltage amplitudes, against a DC bias. [25-28] This provides the resistive and capacitive properties of the sensor interface and can be correlated to the amount of biomolecule binding.[29] EIS measurements can be performed in the presence or absence of a redox probe; faradaic and non-faradaic respectively. Faradaic sensors measure the electron transfer between the redox molecules in solution and the electrode surface; whereas non-faradaic sensors directly measure the changes in capacitance, due to displacement of water and hydrated ions, at the electrode-electrolyte interface.[30] Potentiometric sensing is non-faradaic as FET sensors are not influenced by the presence of redox molecules. In general, for label-free EIS measurements it is expected that impedance changes will be most pronounced if the target is substantially larger than the probe or has significantly different properties. Whereas FETs rely on the interaction of external charges with carriers in a nearby semiconductor and thus exhibit enhanced sensitivity at low ionic strength.[17, 31] Combining both techniques, in turn, combines their advantages and provides data into the origins of the sensing signal while discovering similarities between both transducers. Furthermore, we can investigate the development of a hybrid biosensor through multiplexing and dual sensing experiments.

One of the challenges with combining both techniques with one physical sensor platform was choosing the suitable buffer solutions as salt concentration greatly affects the FET sensors. Again, whether, or not, to use a redox molecule was another challenge. In this chapter, experiments are undertaken in the presence and absence of redox probes, and also in different buffers, PBS and HBS-EP, at different salt concentrations. Furthermore, in the previous chapters non-specific binding (NSB) from the serum samples was not an issue as the deposited solutions were very specific and thorough rinsing steps were employed after each incubation. In this chapter, fish gelatin in introduced as a potential aid to reduce NSB. Fish Gelatin is a non-mammalian buffer solution that maximises the signal-to-noise ratio in immunoassays. It used to block non-specific binding sites, and because it is derived from the skin of cold water fish, it does not cross-react with mammalian antibodies which is ideal for these experiments. Additionally, low concentrations of Tween-20 present in the buffer solutions also prevent non-specific protein-protein interactions. The specific binding is usually more resistant to this detergent, but non-specifically bound proteins (week interactions) can be prevented from binding to the sensor surface. The combination of both Tween-20 and gelatin provides the best condition to decrease most of the non-specific binding. Different conditions, with and without, gelatin and Tween are investigated in this chapter.

Ultimately, we combine potentiometric FET-based sensing and electrochemical impedance techniques to undertake the label-free detection of antibody-antigen interactions on a shared sensor platform (previously used in Chapter 4). The sensor was first subjected to a trial immunoassay to investigate a well-documented model complex, the interaction between haptoglobin and anti-haptoglobin antibody in buffer, using both techniques. Following successful determination of haptoglobin, the non-specific binding properties of the sensor in serum were examined with the use of gelatin. Subsequently, the blocking functionality of gelatin on the nanobands was assessed using a second model complex (BSA/ anti-BSA Ab). Finally, the nanoband sensors were challenged to detection of bovine parainfluenza antibodies in a blood system using hemagglutinin-neuraminidase (HN) as the electrode modification capture protein; employing both sensing mechanisms. Assay times were typically ~20 minutes demonstrating the potential of these sensors for use in future portable devices required for on-farm diagnostic applications.

All the data in this chapter was undertaken in the Georgia Institute of Technology, Atlanta, USA, with project partners, namely Dr. Meng-Yen Tsai and Prof. Eric Vogel. The protein employed in our experiment was produced by partners in Queens University Belfast, namely, Dr. Darren Gray, Mr. Niall Shields and Dr Mark Mooney.

6.2 Experimental

6.2.1 Materials and Preparation of Standards

Bovine Parainfluenza Virus Type 3 (BPI3V) Hemagglutinin Neuraminidase (HN) was provided by Queens University Belfast. HN was produced using the baculovirus expression system using previously established protocols.[22] BPI3V positive and negative bovine serum samples were provided by Teagasc biobank (Moorepark, Ireland) and pooled before use. Blood samples taken from calves in Northern Ireland were processed to plasma[32] and screened for the presence of anti-BPI3V antibodies using the Svanovir PI3V-Ab ELISA. Bovine Serum Albumin 98% (A7906), Anti-Bovine Albumin antibody produced in rabbit (B7276), Haptoglobin from pooled human plasma (H3536) and rabbit anti-Haptoglobin antibody (Ab Hp, IgG fraction of antiserum) were purchased from Sigma Aldrich. Acetate buffer was prepared by titrating 200 mM sodium acetate into 200 mM acetic acid until pH 4.0 is reached; then the buffer is diluted to 10 mM with DI water. HBS-EP buffer was prepared by mixing 10 mM HEPES, 150 mM NaCl, 3 mM EDTA and 0.005% Tween-20 in DI water and adjusted to pH to 7.4 with 5% sodium hydroxide solution. All other reagents were purchased from Sigma Aldrich unless otherwise stated and used as received. Deionised water (resistance 18.2 MΩ cm) was obtained using an ELGA Pure Lab Ultra system.

6.2.2 Fabrication and Characterisation of the Sensor Chip

6.2.2.1 Fabrication of Nanoband Electrodes

Gold nanoband, contact pads and on-chip gold counter and platinum pseudo-reference electrodes were fabricated in Tyndall National Institute, using lithography processes as previously described in Chapter 4 (section 4.4.2). The same connection with a PCB mounted microSD port was used in conjunction with the fabricated chip holders, for analysis.

6.2.2.2 *Optical Characterisation at Nanoband Electrodes*

Chip characterisation was undertaken as outlined in Chapter 4 (section 4.2.3). They were examined optically using a calibrated microscope (Axioskop II, Carl Zeiss Ltd.) equipped with a charge-coupled detector camera (CCD; DEI-750, Optronics).

6.2.2.3 *Electrical Characterisation at Nanoband Electrodes*

The on-chip working electrode is common to both potentiometric (EGFET) and Impedimetric (EIS) sensing. Both sensing mechanisms were employed to compare model antibody-antigen interactions on a fully integrated biosensor chip. Electrochemical experiments were carried out using a Gamry Interface 1000™ potentiostat and controlled by the Gamery data software. All electrochemistry employed a standard three-electrode cell configuration using a single gold nanoband as the working electrode, versus the on-chip gold counter electrode and the on-chip platinum pseudo-reference electrode. Faradaic EIS was recorded in a frequency range of 100 mHz to 100 kHz at -0.45 mV, the equilibrium potential of the redox couple. The amplitude of the alternating voltage was 5 mV. All experiments were performed at room temperature in a Faraday cage.

The EGFET measurements were performed by Dr. Meng-Yen Tsai (GIT). A commercial n-MOSFET (VN0104, Supertex) was used as the transducer for EGFET biosensors, employing two-electrode system. In the two-terminal EGFET sensor, the Au nanoband electrode serves as the WE, i.e. the extended gate, which was electrically connected to the gate terminal of an n-MOSFET. This is exposed to the target analyte solution during the measurement. A flow-through reference electrode (Ag/AgCl; Microelectrodes Inc.) was placed into the chip holder well, close to the chip surface in order to gate the transistor through the liquid during the measurements and a DC voltage sweep is applied to the liquid. The electrical I-V measurements were performed using a semiconductor parameter analyser (Keithley 4200-SCS and HP 4145A). The resulting Id-Vref curve of the transistor will shift horizontally depending on the magnitude and the polarity of the change of surface potential on the Au sensing surface.

Most experiments were performed in a 10 mM HBS-EP solution (pH 7.4) containing 1 mM hexaammineruthenium (III) chloride as a redox molecule, unless otherwise stated. The oxidation and reduction of $[Ru(NH_3)_6]^{2+/3+}$ (RuHex) is achieved at negative potential

(-0.7 V to -0.1 V) which was preferred as it would not interfere with the positive voltage applied during the FET measurement.

6.2.3 Nanoband Sensor Modification

All chemical and bio modification steps were performed using the prefabricated chip holder and the PCB mounted microSD port to connect the chip to the external potentiostat. All on-chip nanoband electrodes employed in this chapter were solvent cleaned, polymerised with o-ABA (50 mM in 0.5 M H_2SO_4) and cross-linked using EDC/NHS to the capture biomolecule, as previously described in Chapter 4, (section 4.2.5.3).

6.2.3.1 Antibody Haptoglobin Detection

This haptoglobin Ab-Ag model complex assay was undertaken to assess the functionality of both sensing mechanisms. The chip was incubated in 10 µg/mL haptoglobin (from pooled human plasma) diluted with 10 mM acetate buffer, pH 4.0. The electrodes were subsequently blocked with ethanolamine and incubated with target Hp antibodies. Anti-haptoglobin target solutions were prepared using anti-Hp antibody (produced in rabbit as purchased stock sample) diluted with 10 mM PBS into working solutions of varying dilution (10 ng/mL to 100 µg/mL).

6.2.3.2 Assessment of non-specific binding – Fish Gelatin

The level of non-specific binding, from the serum samples was assessed by using fish gelatin as the capture probe using EIS only. Nanoband electrodes were first functionalised with oABA and EDC/NHS as detailed above; with fish gelatin as the capture molecule (1% solution, for 1 hour) to block the gold surface. There was no biomolecule deposition, i.e. no active sites. Ethanolamine (1 M) was deposited on the electrode for 20 minutes to block any remaining unbound EDC/ NHS sites. The gelatin-modified sensing surface was then exposed to four seronegative plasma samples (calf numbers 8891, 8892, 8898 and 8907) and two seropositive samples (calves 129 and 103). The serum was diluted with 1:16 HBS-EP buffer (10 mM) and incubated on the electrodes for 30 min contact time each. The EIS measurements were performed in buffer with 10 mM hexaammineruthenium (III) chloride in HBS-EP as the redox couple.

6.2.3.3 Antibody BSA Detection

This assay, employing BSA and Ab BSA, was undertaken to investigate the presence of gelatin blocking on a model antibody-antigen complex, using both sensing mechanisms again. Electrodes were modified using BSA proteins (50 ug/mL in acetate buffer, 30 mins), as the capture biomolecule through amine coupling using NHS/EDC. The protein was incubated for 1 hour at 4 °C. The electrode surface was blocked using 1% fish gelatin for 20 minutes, followed by the standard ethanolamine blocking (1 M in water, 20 mins). Anti-BSA detection was investigated in HBS-EP buffer, diluted into working solutions of varying dilution (100 pg/mL to 1 ug/mL). A 10 mM hexaammineruthenium (III) chloride in PBS was used as redox couple in HBS-EP, incubation for 20 mins.

6.2.3.4 Target Antibody BPI3-V Detection

Following the NSB testing, the sensor was subject to determination of BPI3-V antibodies in serum. An experimental control was also undertaken. To deposit the two capture biomolecules, a spotting technique was employed, allowing multiple detections within a single sample. Electrodes 1 and 3 were modified with 50 μg/ml Hemagglutinin Neuraminidase (HN) protein in acetate buffer, pH 4.0 (synthesised by QUB). Simultaneously, Ab BSA was spotted on to electrode 6, to use as a control electrode. Both biomolecules were incubated for 30 minutes at 4°C. Following these immobilisation steps, the electrodes were well rinsed with acetate buffer solution containing 0.1% Tween-20 (AB10-T) and DI water to remove any unbound proteins and the un-reacted active sites were blocked by immersing in 1% gelatin followed by 1M ethanolamine HCl, pH 8.5 for 20 mins. Finally, the modified electrodes were exposed to pooled BPI3V blood serum samples (antibody positive). Three seronegative dilutions (1:200 to 1:50) and three seropositive samples (1:300 to 1:50) were tested on the electrodes. All of the serum samples were diluted neat HBS-EP buffer (160 mM) at different concentrations, and incubated on the electrode for 20 minutes each. The electrodes were rinsed thoroughly with HBS-EP buffer and DI water to remove non-specifically bound target biomolecules prior to measurement.

The dual sensing experiments were carried out using the nanoband chip sensors with both sensing mechanisms. Firstly an EIS measurement was taken followed by a MOSFET scan

then a second EIS scan. This technique was used for every modification step on the electrode to evaluate if the MOSFET reader had any impact on the electrode.

6.3 Results and Discussion

6.3.1 EIS/ FET Functionality of Nanobands

Figure 6.1 shows a schematic of the nanoband sensor device, consisting of the two transducers for electrical measurements; EIS and FET. The gold nanoband surface can be chemically modified to achieve specific adsorption of certain biomolecules. Its surface potential (FET) and impedances (EIS) depend on the amount of biomolecule binding. To first assess functionality of employing this dual sensing method, the Au nanoband chip electrodes are employed as the shared active working electrodes for both EIS impedimetric and EGFET potentiometric techniques. This resulting fully integrated system, offers a direct comparison between both techniques, through analysis of the biomolecular binding events. Moreover the gold sensing surface allows the possibility of a direct comparison to commercial tools based on SPR, which also typically use a gold surface. Nanoband electrodes were of the same design as the arrays previously reported in Chapter 4 (700 nm width bands), see Figure 6.1 (b) Optical and electrical characterisation data for these electrodes used in this chapter bore no significant difference to those already presented.
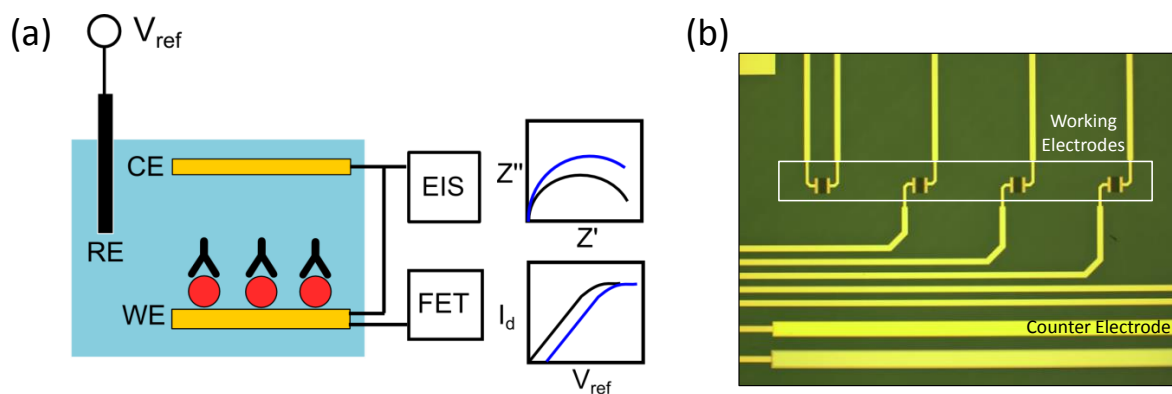

Figure 6.1: A scheme and an optical image of the integrated FET/EIS biosensor system. (a) The experimental setup of the integrated system. (b) An optical image of the biosensor chip used in chapter 4. (Image recreated from [33])

To test electrochemical functionality, electrodes were characterised using CV and EIS, in presence of 1 mM RuHex redox probe. Figure 6.2 (a), shows a typical CV voltammogram obtained using a pristine nanoband electrode exhibiting a quasi-steady-state behaviour, as expected.[34, 35] The magnitude of the current (~2.5 nA) confirms that electrochemistry

only occurs at the electrode and the passivation layer successfully prevents unwanted electrochemistry occurring at on-chip metallisation. Sensor devices that exhibited lower or no electrochemical current were discarded and not used for further experiments. Faradaic EIS was performed on pristine gold electrodes and a typical Nyquist plot presented in Figure 6.2 (b). The resistive and capacitive charges in the system were extracted from the Nyquist plot, by fitting the data with a Randles equivalent circuit, inset of Figure 6.2 (b). This circuit is limited to solution resistance, and charge transfer resistance in parallel with surface capacitance (Cdl). The experimental data (blue dots) presented in Figure 6.2 (b) were fitted with the equivalent circuit, modelled using the NOVA software. This fit data (solid line) overlays the experimental data (dots) extremely well, confirming the efficacy of the selected equivalent circuit components and defined values.
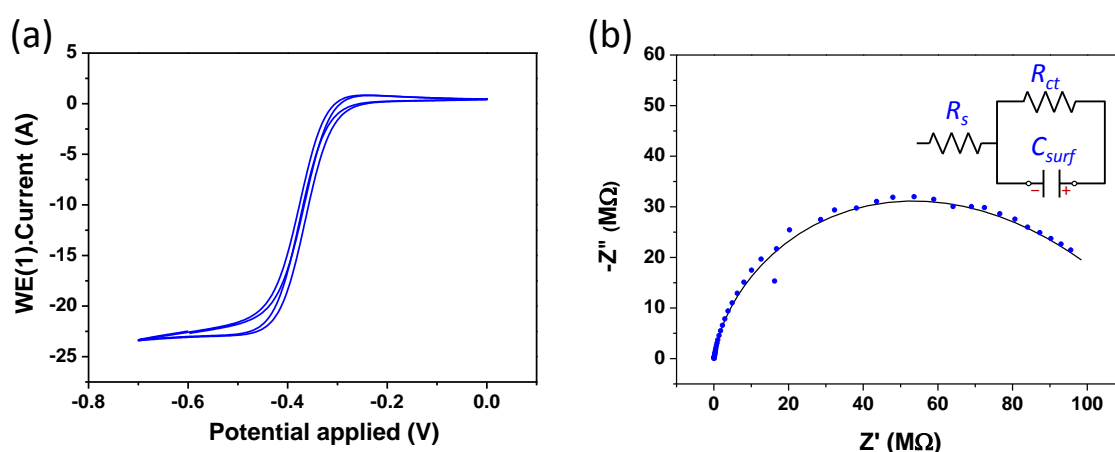

Figure 6.2: (a) CV for a clean gold nanoband electrode obtained in 1 mM $Ru(NH_3)_6$ (in 10 mM HBS-EP, pH 7.4), the potential was cycled from -0.7 V to -0.1 V, versus the on-chip platinum pseudo-reference electrode at a scan rate of 100 mV/s. (b) A Nyquist plot for the same electrode recorded at a frequency range of 100 mHz to 100 kHz at -0.45 mV (versus external Ag/AgCl RE, V_{ref}). The dots represent the experimental data, whereas the curved line represents the electrochemical circuit fit data (inset).

On a side note, as these experiments were undertaken in GIT, the instrumentation is different from the previous chapters. The faraday cage employed, in particular, was small and portable, and was not grounded. Hence, there is a small interference at 60 Hz in all the data, which is the standard frequency of the sockets in the United States. Following electrochemical characterisation, the nanoband chip was characterised using potentiometric extended-gate FET sensing, by Dr. Tsai. The commercial MOSFET was

used to read out the potential changes on the gold surface. The nanoband acts as the so-called "extended gate" of the MOSFET, and is electrically connected to the gate terminal. A reference electrode (Ag/AgCl) was immersed in the solution to gate the transistor through the RuHex solution. The resulting surface potential depends on the amount of charged molecules attached to the surface. A typical transfer curve was observed, of the liquid-gated EGFET in HBS-EP buffer. The drain current I_d can be modulated by sweeping the voltage at the reference electrode V_{ref}.[22]

6.3.2 Detection of Haptoglobin/ AbHp complex

To assess the functionality of the integrated EGFET potentiometric and EIS impedance biosensor system, the immunological detection of antibody Haptoglobin to its antigen, was first studied. Each modification step of the assay was characterised using EIS in only PBS, and both sensing mechanisms were employed to measure the antibody binding. A polymer modified single gold microband electrode was exposed to haptoglobin in acetate buffer as the capture molecule, and target anti-haptoglobin antibody was detected in PBS. No redox molecules were used in this experiment in order to direct compare the EIS and FET sensing, with little variability. EIS Nyquist plots in the absence of redox ions yield a large capacitive response, i.e. non-faradaic impedance. Therefore, to assess the potential binding of antibodies to the modified sensor surface, the EIS modulus plot was employed (total impedance vs. frequency); see Chapter 1 section 1.6.4.2, for more detail. Typically with EIS, the increases in charge transfer resistance and global capacitance of the nanoband are examined following biomolecule binding; hence in this case, an increase in the total impedance is expected. The potentiometric I-V curve and impedimetric modulus for the detection of antibody Hp are presented in Figure 6.3.

The EIS modulus data represented a response to the binding of different concentrations of Ab Hp is presented in Figure 6.3 (a). The total impedance ($|Z|$) increased with increasing anti-Hp concentration. This suggests that the Hp antibodies bound to the immobilised haptoglobin protein, changing the electrode interface and subsequently restricting access to the electrode surface. The solution resistance, R_s, arises from the finite conductance of the ions in bulk solution, and thus is generally not affected by binding. However, the capacitance between the metal electrode and ions in solution is

detectable, and can be modelled as a series combination of the surface modification capacitance and the double layer capacitance. This detectable response arises from the displacement of water ions from the electrode surface due to electrode interfacial changes following target binding. Furthermore, there is a semi-log linear relationship between the total impedance across the wire, and different dilutions of the stock antibody solution, shown in Figure 6.3 (b). This demonstrates that antibody detection is possible in the absence of a redox molecule, allowing for potential non-faradaic impedance studies.
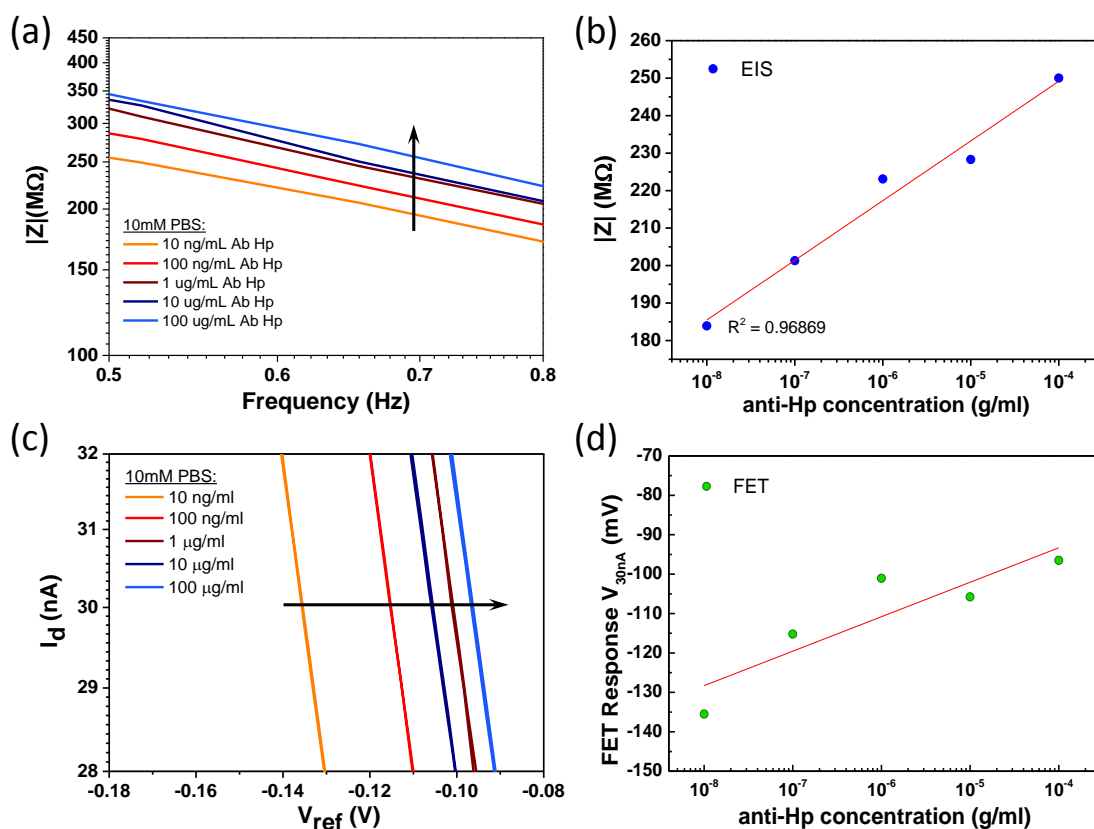

Figure 6.3: The responses for FET potentiometric and EIS impedance to anti-Hp concentrations on nanoband electrodes (a) Modulus data plots of impedance spectra measured with EIS and (b) the R_{ct} change in response to anti-BSA concentrations in logarithm scale. (c) The shift of I_d-V_{ref} curve measured with FET and (d) the FET signal (surface potential) in response to anti-BSA concentrations in logarithm scale

The potentiometric I_d-Vref measurement demonstrates the change of surface potential for the same binding events. Figure 6.3 (c) shows the transfer curve shifting horizontally to the right, i.e. in the positive direction, which indicates a negative charge on the surface. Figure 6.3 (d), in turn, shows the response of the active FET, i.e. the gate voltage required

to achieve a drain current of 10 nA, versus anti-Hp concentration in logarithm scale. The FET response for the nanoband exhibits a similar trend to the impedance modulus, validating that both sensing mechanisms are functional on the sensor chip. EIS measures the impedance of the biological layer, in the absence of a redox probe. The layer consists of an insulating oABA polymer film and the haptoglobin complex, which acts as a capacitor at the electrode-electrolyte interface. Field-effect devices are basically surface-charge measuring devices, i.e. they detect the charge in a capacitive way, and therefore they can principally measure the charge of adsorbed macromolecules (anti-Hp). Therefore both sensing mechanisms are detecting the capacitive response to the formation of the haptoglobin complex on the gold nanoband electrode.

6.3.3 Assessment of Non-specific Binding using Fish Gelatin

A fish gelatin was introduced to our experiments to investigate its use as an additional blocking agent to reduce any non-specific binding in serum samples. Electrodes were modified as normal, but employed a 1% fish gelatin solution as the capture molecule. This experiment aimed to saturate the sensor with BPI3-V seronegative samples to assess the level of NSB from the serum and also to test the functionality of employing the fish gelatin as a blocking agent. Moreover, HBS-EP buffer was used as the serum diluent which contained Tween-20. EIS only (not FET) was used as the sensing method to study this.

Figure 6.4 (a) shows the Nyquist plot for the immunoassay. The measured electrode resistance following the gelatin deposition ($\sim$250 MΩ) had increased compared to the clean electrode charge transfer resistance ($\sim$130 MΩ), as expected. The electrode was then blocked by ethanolamine and the R_{ct} increased further to $\sim$350 MΩ. The first negative sample was immobilised on the sensor and rinsed with 10 mM HBS-EP buffer. The resulting Nyquist plot R_{ct} value was measured as $\sim$700 MΩ. Subsequently, the second and third seronegative samples were tested (calves 8892 and 8898, respectively), and no change in the Nyquist plot was observed, i.e. R_{ct} remained at $\sim$700 MΩ. Although the fish gelatin did not remove all the NSB, it seemed to be limited. After the 3rd negative sample measurement, the electrode was washed with neat HBS-EP buffer (160 mM) and the 4th seronegative sample was deposited. Several impedance measurements were undertaken,

showing the Nyquist semi-circle had decreased back to ~350 MΩ, the ethanolamine baseline. This finding indicates that after the rinsing step in neat HBS-EP, the non-specifically bound proteins were removed from the electrode.
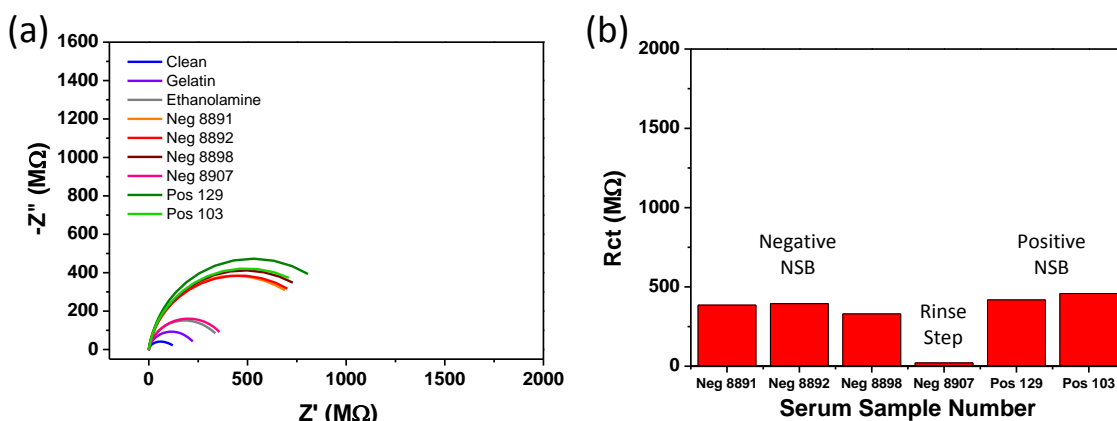

Figure 6.4: (a) Nyquist plots of o-ABA modified gold nanobands with 1% fish gelatin modification, ethanolamine blocking and binding of seronegative samples to assess NSB on the surface of the electrode. Data was recorded in 10 mM HSB-EP containing 1 mM Ru(NH$_3$)$_6$. (b) Plot demonstrating the level of NSB with increases in R$_{ct}$ at each deposition of seronegative blood samples, and subsequently the removal of the NSB following the thorough rinsing step.

Following the saturation of the electrode, the two seropositive samples were deposited onto the electrode, out of curiosity. There are no HN active sites on the electrode for the BPI3 antibodies to bind to, so there should be no observable difference in the impedance. The green data plots in Figure 6.4 (a) represent the seropositive samples deposited on the saturated electrode. The Nyquist semi-circle increased from the baseline at ~ 350 MΩ, to the same values as the seronegative samples (700 MΩ and 750 MΩ). As there are no HN binding sites, the impedance increase can therefore be attributed to the same non-specific binding witnessed for the negative samples.

Following the rinsing step in neat HBS-EP (160 mM), see Figure 6.4 (b), it appears that the weakly bound proteins which contributed to the NSB were removed from the electrode surface, due to higher concentration of the surfactant Tween-20 in the stock buffer (16 times more than serum samples diluent buffer). Although the gelatin does show slight reduction in NSB; its use alone does not provide the blocking required for the complex serum samples used in these experiments. The obvious outcome is to use neat HBS-EP buffer in all future serum dilutions in combination with the gelatin to ensure the

best blocking protocol. However, for FET sensing, solutions with a high ionic strength cause severe charge-screening effect by small inorganic counter ions present in the electrolyte solution. This results in uncharged layers and prevents measurements of immunospecies with field-effect devices. Therefore 1:16 diluted HBS-EP buffer had to be used for the dual sensing experiments. To this end, gelatin will be employed for the dual sensing experiments, but further testing with gelatin is also required, to ensure that it is practical to use on the electrode with the lower HBS-EP concentration.

6.3.4 Detection of BSA/ Antibody BSA

The gelatin blocking modification on the nanoband was investigated further using a second model complex, BSA/ anti-BSA, this time, employing both EIS and FET detection as well as the RuHex redox probe. As there are no other proteins present in the anti-BSA buffer solution, there will be no NBS interferences. Therefore, this experiment was undertaken to study the effect, if any, that gelatin had on the two sensing mechanisms; before undertaking dual sensing assays in complex serum samples. The potentiometric and EIS sensors' responses to the BSA versus anti-BSA system are shown in Figure 6.5. The I_d-V_{ref} curve of the transistor, Figure 6.5 (a), depicts the shift of potentiometric sensor in the positive direction in response to the increasing concentration of anti-BSA in the HBS-EP buffer, indicating that the anti-BSA (with an isoelectric point $4.8 - 5.2$) is negatively charged in the buffer.[36] Figure 6.5 (b) shows the change of surface potential measured by the FET sensor versus anti-BSA concentration in linear scale and logarithm scale (inset of Figure 6.5 (b)). The FET response data points (on the x-axis) represent the changes in surface potential on the electrode, due to the attachment of charged antibodies to the extended gate, i.e. the nanoband working electrode.
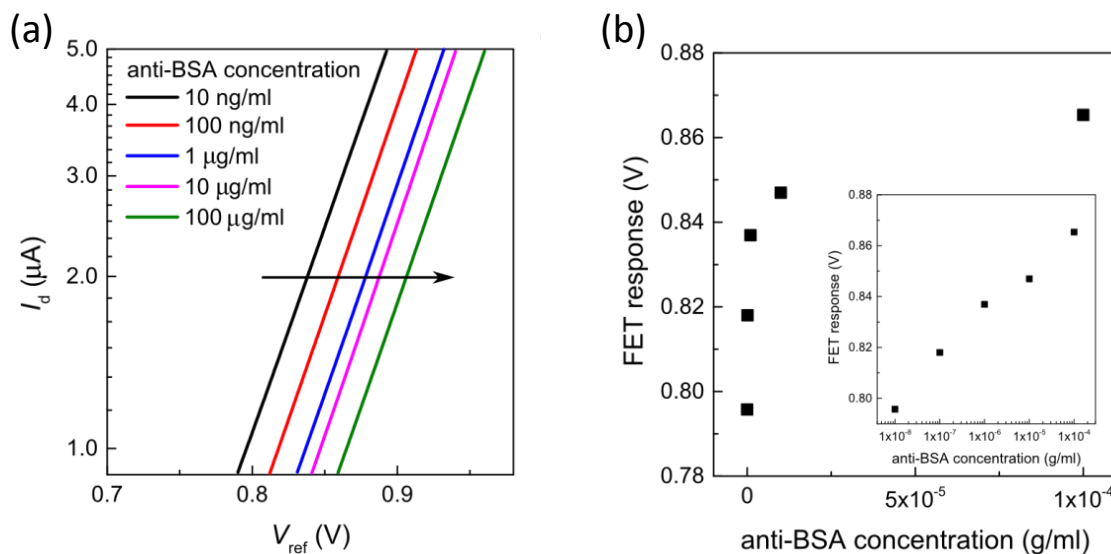
Figure 6.5: The responses of FET potentiometric and EIS impedance biosensors to anti-BSA concentrations. (a) The shift of I_d-V_{ref} curve measured with FET and (b) the FET response (surface potential) in response to anti-BSA concentrations in linear scale and logarithm scale (inset). (Image taken from [33])

Measuring the same binding event at the working electrode, the change of EIS sensor's impedance spectra with respect to anti-BSA concentration is presented in a Nyquist plot in Figure 6.6 (a). An increase in the semi-circle diameter i.e. increase in the resistance of the charge transfer between the electrode and the RuHex solution, as well as increased global capacitance, was observed with increasing antibody concentration, as expected. By fitting the impedance spectra with their equivalent circuit models, the values for R_{ct}, could be extracted. The R_{ct} values for each data plot in (a) is plot versus the log of the anti-BSA concentration, shown in Figure 6.6 (b). The charge transfer resistance, again, increases with increasing concentration of anti-BSA, suggesting binding of the antibodies to the available sites on the electrode. To conclude in this section, there were no major observed differences with the presence of fish gelatin, when compared to the haptoglobin assay results, thus the blocking does not interfere with the binding of Ab-Ag complexes.
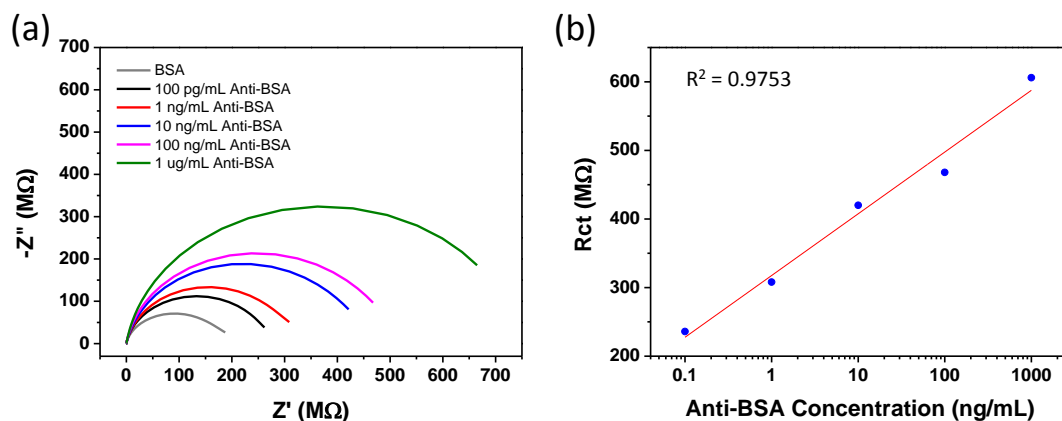
Figure 6.6: (a) Nyquist plots of impedance spectra measured with EIS and (b) the R_{ct} change in response to anti-BSA concentrations in linear scale and logarithm scale (inset) ; recorded in 10 mM HBS-EP containing 1 mM Ru(NH$_3$)$_6$.

6.3.5 Comparison between EIS and FET Model Responses

As outlined in the experimental section, the electrical measurements for BSA/aBSA were performed in buffer with 10 mM hexaammineruthenium (III) chloride in HBS-EP (10 mM), whereas for the Hp/aHp assay, measurements were undertaken in only PBS solution (10 mM). Hence, the total impedance value, from the EIS modulus, was used instead of the R_{ct} for the haptoglobin assay (section 6.3.2). The same semi-log relationship is observed for EIS responses, as for the FET surface potential responses. If the plots are overlaid, the trends for EIS and FET responses bare close resemblance for the haptoglobin and BSA immunoassays, Figure 6.7 (a) and (b) respectively. This suggests a correlation between surface potential and the impedance.

Dr. Meng-Yeng Tsai (GIT), revealed a correlation between surface potential of the FET and charge transfer resistance of EIS for this experiment, using the Butler-Volmer equation.[33] This equation predicts that R_{ct} is exponentially related to the change of surface potential (ΔV). For this nanoband biosensor, the surface potential changes results from the binding of charged biomolecules (anti-BSA) to the WE surface. Subsequently, Dr. Tsai demonstrated a high linearity for the relationship between R_{ct} (EIS) and the exponentiation of ΔV (FET) for the detection of the BSA/anti-BSA complex; confirming that both potentiometric and impedance biosensors are charge sensitive. EGFET sensors directly measure this surface potential change, which concurrently influences the

electrical current and impedance, by blocking the redox ions from reaching the electrode surface. This finding validates that not only does this dual sensing approach provide data from both sensing mechanisms but that the signal output from impedimetric biosensors can be linked to that of potentiometric biosensors.
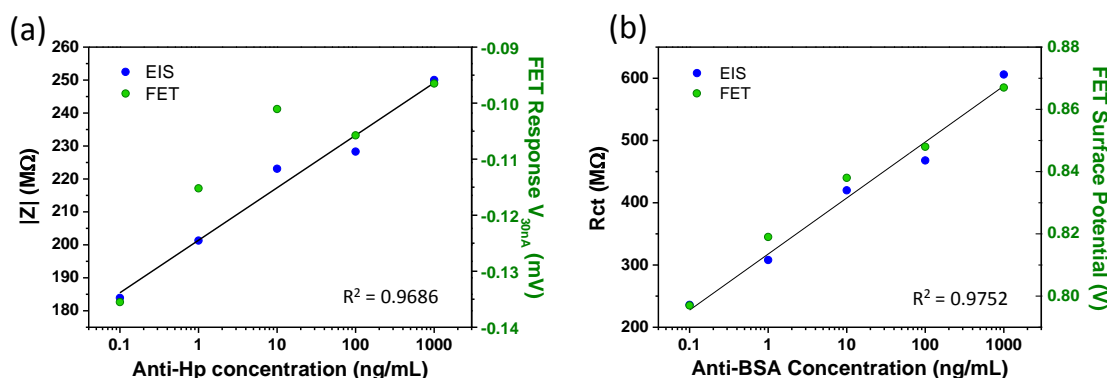

Figure 6.7: Comparison of the EIS R_{ct} change and the FET surface potential change in response to (a) anti-Hp antibody concentration and (b) anti-BSA antibody concentrations in logarithm scale.

This dual sensing approach can potentially be used eliminate false positives. The EGFET will measure surface potential (charge) whereas the EIS will measure the electrostatic repulsion or steric barriers (mass) inflicted on the electrode.

Similar to having a control experiment, the two techniques support each other when they are combined on the same active surface. In other words, to ensure an accurate result for the detection of a target analyte, both mechanisms must yield positive results or both must be negative. If the EIS displays a positive result and the FET is negative for a target then there is something influencing the EIS sensor, and vice versa. To get a false positive result with this dual sensing method, any ions or non-specific proteins which negatively influence the sensor would have to be the same size/mass as the target ions, as well as have the same charge. Furthermore, this establishes an important use for these dual sensors in POC sensing.

6.3.6 Detection of BPI3-V Antibodies

Based on the previously established model platform of Haptoglobin and BSA sensing using the combined potentiometric extended-gate sensing and electrochemical sensing, bovine parainfluenza virus type 3 (BPI3V) was investigated in animal blood against Haemagglutinin Neuraminidase (HN); chosen for its selectivity towards this virus. In addition to this, fish gelatin is employed to reduce the NSB attachment to the electrode, from the serum samples. On-farm serological sampling is time consuming and testing every individual sample is more costly for the farmer or veterinarian. Therefore to make these assays more feasible, practical and convenient, the seropositive and seronegative subsamples were pooled in composites of 10 and diluted in aliquots of 1:200, 1:100 and 1:50 serum to buffer (1:16 HBS-EP), prior to testing. To construct the immunoassay, the HN protein was covalently immobilised onto the gold electrode through the amide bond formed by the EDC-NHS coupling to the o-ABA polymer layer and the same electrode modification is employed as described previously. The electrodes were again characterised using EIS and FET.

The Nyquist spectrum of the layer-by-layer immunoassay and immunological detection of BPI3V is shown in Figure 6.8 (a). The cleaned gold microband electrode displays a semi-circle with an estimated charge transfer resistance around 30 MΩ. After electrodeposition of the o-ABA layer, the charge transfer resistance increases to 50 MΩ; this also indicates an increase in the global capacitance at the microband. These changes are attributed to the insulating polymer partially blocking the electrode and therefore limiting the electron transfer from RuHex to the gold electrode. The negative charges on the carboxylate terminated polymer can also induce an electrostatic repulsion of bulk RuHex ions. Covalent immobilisation of HN through EDC-NHS coupling reveals a slight increase in the impedance. This change can be attributed to the covalent immobilisation of HN at only the carboxylate activated sites of the polymer, therefore the accessible surface for the oxidation and reduction of the RuHex remains relatively constant, leading to a small decrease in the transfer of charged ions to the surface. After gelatin and ethanolamine steps, the resistance charge transfer further increases, suggesting that the remaining unbound active sites are blocked.
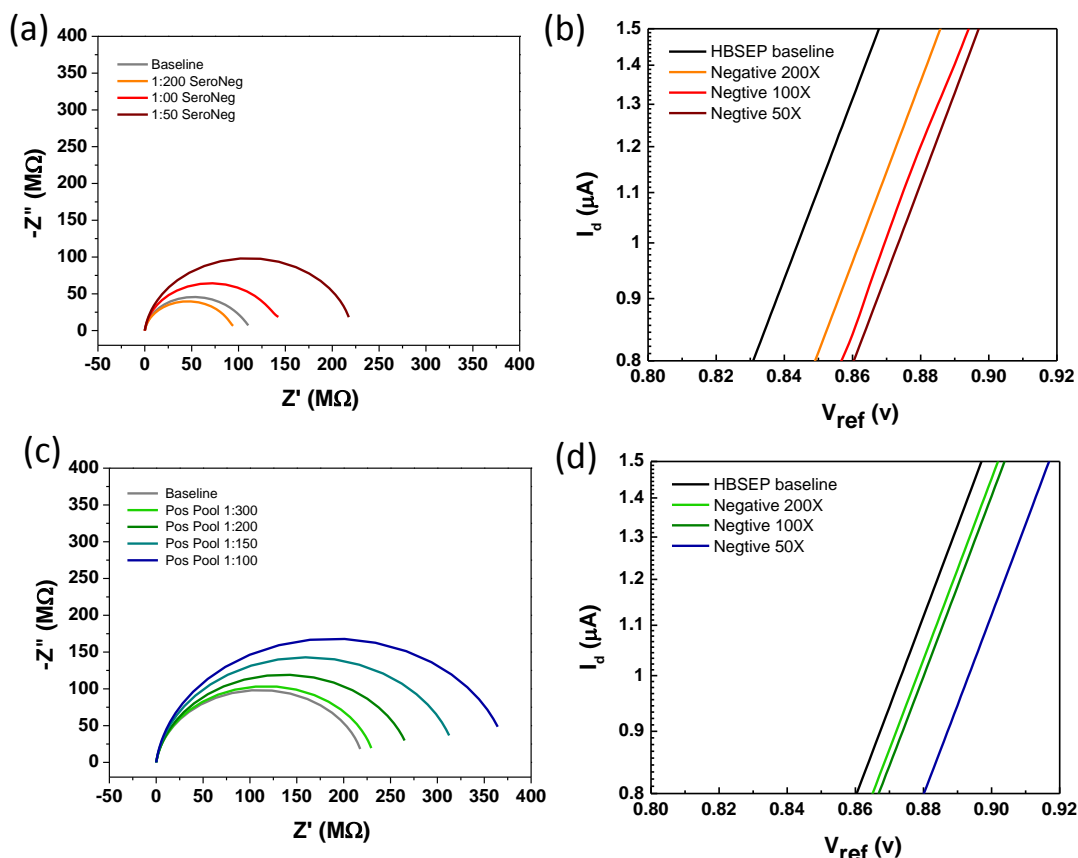
Figure 6.8: (a) Nyquist plots and (b) FET curves obtained from o-ABA modified gold nanoband electrode with: HN modification (50 μg/ml in pH 4), gelatin and ethanolamine blocking, and binding of BPI3V seronegative samples in HBS-EP buffer; recorded in 10 mM HBS-EP containing 1 mM Ru(NH$_3$)$_6$. (c) Nyquist and (c) IV curves for the same sensor surface, following deposition of the BPI3V seropositive samples.

The plots in Figure 6.8 (c), shows the Nyquist plot of the EIS impedance biosensors in response to several dilutions of positive BPIV3 plasma samples. The pooled serum samples were incubated for 10 minutes on the HN modified sensor, starting with the seronegative pooled samples. The measured impedance of ~90 MΩ for the 1:200 negative pooled samples had shown a decrease compared with the ethanolamine baseline of ~110 MΩ. This could be attributed to removal of some of the bulky blocking gelatin. The two lower dilutions (higher concentrations) of seronegative pooled serum, 1:100 and 1:50, unexpectedly presented increases in the measured impedance, ~140 MΩ and ~210 MΩ. Normally these increases would be attributed to binding of un-specific biomolecules to the sensor, as their values are minimal. The FET measurements following deposition of the seronegative samples, plot in Figure 6.8 (b), show the same trend. The FET data shift in the positive direction suggests binding to the sensor surface, therefore, there must

remain a slight NSB from the serum samples. These results suggest that the gelatin is not functional as a blocking agent on the nanoband electrode surface, when used with 1:16 diluted HBS-EP buffer.

As we have already discovered, when the charged HN protein attaches to the sensing surface, the subsequent BPI3-V antibody attachments cause the change of surface potential measured by the FET, as well as a change of the charge transfer resistance measured by EIS. The data plots, in Figure 6.8 (c), show the Nyquist EIS responses following electrode incubation with BPI3-V seropositive samples. Deposition of the 1:300 dilution of seropositive blood resulted in a slight increase in the impedance to ~230 MΩ. However, more significant increases in impedance were observed, reading ~ 260, 310 and 360 MΩ, following incubation with the three higher concentrations of seropositive BPIV3 pooled samples, 1:200, 1:150 and 1:100 dilutions, respectively. This is comparable to the results observed for the model immunoassays, indicating a decrease in charge transfer at the electrode (higher charge transfer resistance), which can be attributed to the HN/ BPIV3 complex forming on the sensor. Similarly, the I-V data in Figure 6.8 (d) shows the drain current FET readout from the same binding events on the electrode. The horizontal potential shifting to the right, i.e. in the positive direction, indicates that the BPI3-V antibodies are negatively charged on the surface.

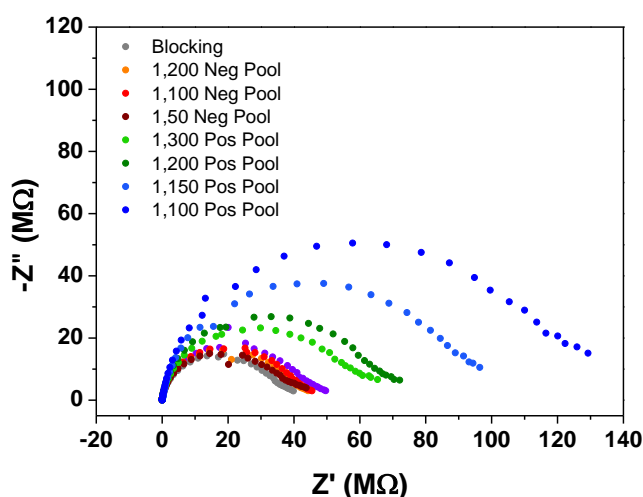**Figure 6.9**: Nyquist plots obtained from a nanoband electrode with Ab BSA modification (100 µg/ml in pH 4) and binding of pooled BPI3V seronegative and seropositive samples in HBS-EP buffer; recorded in 10 mM HBS-EP containing 1 mM Ru(NH$_3$)$_6$.

Another on-chip electrode (electrode 6) was prepared as a positive control to ensure the sensor is functional. Over 50% of bovine blood is made up of bovine serum albumin (BSA); commonly used in immunoassays as an effective blocking step. For these nanobands, we immobilise anti-BSA antibodies on the electrode and expect a binding to the surface from BSA, present in the serum samples. Following the fish gelatin/ethanolamine blocking steps, the measured impedance value was lower than usual ~40 MΩ. Deposition of the seronegative pool samples showed very slight increases in the measured impedance. However, upon deposition of the remaining seropositive samples the impedance increased sequentially to ~130 MΩ. The Nyquist data presented in Figure 6.9 was lower than expected but a still produced a trend comparable to that of the inverse experiments, BSA/ anti-BSA, in Figure 6.6.

Figure 6.10 shows a linear relationship between the exponentiation of surface potential change (measured by FET – green dots) and the charge transfer resistance (from EIS-black dots). Both sensors exhibit significant and very similar responses for detection of seropositive BPI3-V samples at different concentrations. The positive control, Ab BSA-coated electrode, also shows a positive response with increasing serum dilutions (red circles). This weaker response only suggests that the HN sensor has a stronger affinity to the BPI3-V antibodies, than the deposited anti-BSA does for albumin in serum. The linear relationship, again, confirms the correlation between potentiometric and impedimetric biosensors.
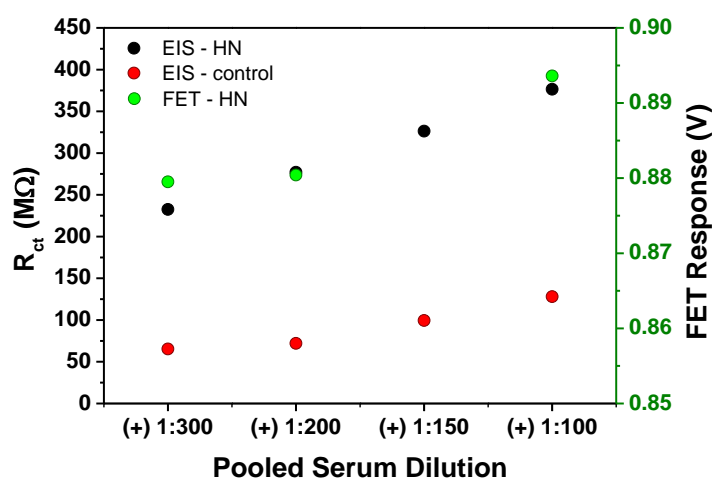

Figure 6.10: Linear relationship between the exponentiation of surface potential change (measured by FET) and the charge transfer resistance (from EIS) for the detection of seropositive BPI3-V samples.

SPR data was undertaken by QUB for these experiments, in the presence of gelatin, using neat HBS-EP buffer and 1:16 diluted HBS-EP buffer. The 1:16 diluted HBS-EP buffer was used for the nanoband sensor. Individual serum samples and pooled blood samples were both analysed using the SPR. HN modified sensors responded to seronegative and seropositive blood samples as expected, however the response was larger for the seropositive samples than for the seronegative samples. NSB causes a large contribution in the SPR results, however upon background subtraction, both seropositive and seronegative samples produced a similar performance to the immunoassay trend, see Figure 6.11. These results provide the initial insight of the non-specific binding behaviour on our EIS sensors. It was observed that the trends of all three techniques were comparable.
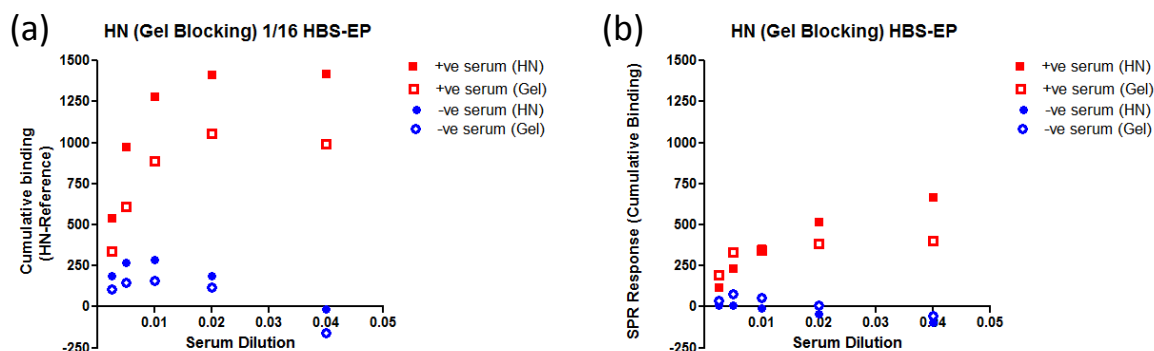
Figure 6.11: SPR data produced in GIT, by partners in QUB, for HN detection with and without gelatin.

6.3.7 Effect of two Sensing Techniques on one Electrode

As outlined in the experimental section (6.2.3.4), EIS measurements were undertaken first, followed by MOSFET scans, then a second set of EIS scans. This method was employed for all the modification steps. It was observed that the first set of EIS scans taken, for all the modification steps, presented a working immunoassay. The second set of EIS results, preceding the FET measurements, illustrated in Figure 6.12, demonstrated significant decreases in comparison to the first EIS scans. As the electrode was functional for the full experiment, and didn't break after the first MOSFET measurement; it is predicted that the reduced signal observed may be due to charges still present in the

electrode subsequent to the MOSFET scans. Further work is required to fully comprehend these observations.

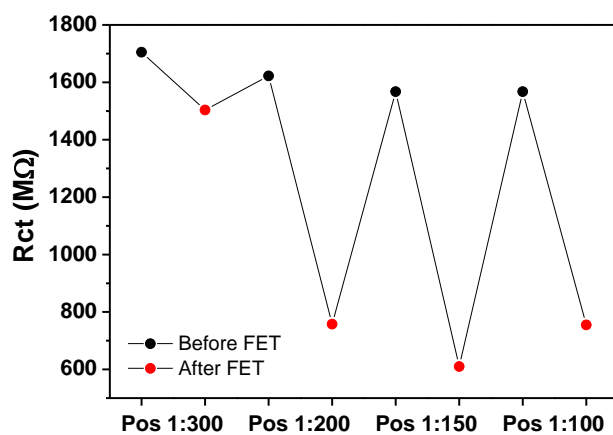**Figure 6.12:** Comparison between two sets of impedance values for the detection of three seropositive BPI3-V samples at different dilutions. The first scan (black dots) was taken prior to the FET scans and the second scans (red dots) were taken directly after the FET sans.

6.4 Conclusions

In this chapter, the work undertaken in Georgia Institute of Technology, with partners from GIT and Queens University Belfast, was presented. We combined potentiometric FET-based sensing and electrochemical impedance techniques to undertake the label-free detection of antibody-antigen interactions on a shared sensor platform. The modified nanoband chips presented in chapter 4, were used as the common WE platform. The dual sensing method was ultimately used to detect bovine parainfluenza antibodies in a complex blood system using Hemagglutinin-Neuraminidase (synthesised in Queens University Belfast).

The sensor was first subjected to a trial immunoassay to investigate the functionality of the dual sensing method. Successful demonstrations of the detection of Hp/ anti-Hp complex in PBS buffer only, established the sensor capabilities for use in faradaic and non-faradaic systems (i.e. presence and absence of a redox probe). Additionally, the FET and EIS data revealed comparable results for the model systems and a correlation between surface potential of the FET and charge transfer resistance of EIS, using the Butler-Volmer equation. This direct comparison sheds light on the fundamental origins of sensing signals produced by FET and EIS biosensors, as well as the correlation between the two.

Fish gelatin (1%) was also investigated, in this chapter, as an additional blocking step to minimise the NSB from serum samples. A test assay with gelatin modification, i.e. no active surface, was incubated in seronegative samples diluted with 1:16 HBS-EP buffer. Results revealed that although the gelatin does show slight reduction in NSB; its use alone does not provide the blocking required for the complex. The use of a neat HBS-EP rinsing buffer (160 mM) which has a higher concentration of the surfactant Tween-20, removed the weakly bound proteins that contributed to the NSB on the electrode. The presence of gelatin was further investigated using a second model complex (BSA/ anti-BSA Ab), which successfully demonstrated that gelatin does not interfere with the binding of Ab-Ag complexes.

The nanoband sensors were challenged to detection of BPI3-V antibodies in a blood serum samples using HN as the electrode modification capture protein; employing both sensing mechanisms. The HN protein from QUB performs well compared to SPR data. NSB remained an issue when samples were diluted in 1:16 HBS-EP buffer. SPR data show that this was significantly reduced with neat HBS-EP buffer (160 mM). Again, the relationship between signals from potentiometric and impedance sensors, ΔV and R_{ct}, respectively, agrees well with Butler-Volmer theory. The results further confirm the correlation between potentiometric and impedance sensors. Furthermore, with assay times of typically ~20 minutes, these findings suggest that the electrical sensor is a promising tool for use in future portable devices required for on-farm diagnostic applications.

6.5 References

1.   Snowder, G.; Van Vleck, L.D.; Cundiff, L.; Bennett, G., Bovine Respiratory Disease in Feedlot Cattle: Environmental, Genetic, and Economic Factors; *Journal of Animal Science,* **2006**, 84, 1999-2008.

2.   Ridpath, J.F., Bovine Viral Diarrhea Virus: Global Status; *Veterinary Clinics of North America: Food Animal Practice,* **2010**, 26, 105-121.

3.   Horwood, P.F.; Gravel, J.L.; Mahony, T.J., Identification of Two Distinct Bovine Parainfluenza Virus Type 3 Genotypes; *Journal of General Virology,* **2008**, 89, 1643-1648.

4.   Hall , C.B., Respiratory Syncytial Virus and Parainfluenza Virus; *New England Journal of Medicine,* **2001**, 344, 1917-1928.

5.   Henrickson, K.J., Parainfluenza Viruses; *Clinical Microbiology Reviews,* **2003**, 16, 242-264.

6.   Griebel, P.; Hill, K.; Stookey, J., How Stress Alters Immune Responses During Respiratory Infection; *Animal Health Research Reviews,* **2014**, 15, 161-165.

7.   Haanes, E.J.; Guimond, P.; Wardley, R., The Bovine Parainfluenza Virus Type-3 (Bpiv-3) Hemagglutinin/Neuraminidase Glycoprotein Expressed in Baculovirus Protects Calves against Experimental Bpiv-3 Challenge; *Vaccine,* **1997**, 15, 730-738.

8.   Presi, P.; Struchen, R.; Knight-Jones, T.; Scholl, S.; Heim, D., Bovine Viral Diarrhea (Bvd) Eradication in Switzerland--Experiences of the First Two Years; *Preventive Veterinary Medicine,* **2011**, 99.

9.   Nyberg, O.; Østeras, O.; Plym Forshell, K. Eradication of Bvdv-Infection in Norwegian Cattle 1992-2003 - a Success Story. In Proceedings of the Second European Symposium on Bvdv Control; *Oporto:* Portugal, 2004.

10.   Greiser-Wilke, I.; Grummer, B.; Moennig, V., Bovine Viral Diarrhoea Eradication and Control Programmes in Europe; *Biologicals,* **2003**, 31.

11.   Dehove, A.; Commault, J.; Petitclerc, M.; Teissier, M.; Macé, J., Economic Analysis and Costing of Animal Health: A Literature Review of Methods and Importance; *Revue Scientifique et Technique (International Office of Epizootics),* **2012**, 31, 605-17, 591-604.

12.   Thonur, L.; Maley, M.; Gilray, J.; Crook, T.; Laming, E.; Turnbull, D.; Nath, M.; Willoughby, K., One-Step Multiplex Real Time Rt-Pcr for the Detection of Bovine Respiratory Syncytial Virus, Bovine Herpesvirus 1 and Bovine Parainfluenza Virus 3; *BMC Veterinary Research,* **2012**, 8, 37.

13.   Horwood, P.F.; Mahony, T.J., Multiplex Real-Time Rt-Pcr Detection of Three Viruses Associated with the Bovine Respiratory Disease Complex; *Journal of Virological Methods,* **2011**, 171, 360-3.

14.   Dubovi, E.J., Laboratory Diagnosis of Bovine Viral Diarrhea Virus; *Biologicals,* **2013**, 41, 8-13.

15.   Lanyon, S.R.; Hill, F.I.; Reichel, M.P.; Brownlie, J., Bovine Viral Diarrhoea: Pathogenesis and Diagnosis; *The Veterinary Journal,* **2014**, 199, 201-209.

16. Vestergaard, M.D.; Kerman, K.; Tamiya, E., An Overview of Label-Free Electrochemical Protein Sensors; *Sensors (Basel, Switzerland),* **2007**, 7, 3442-3458.

17. Daniels, J.S.; Pourmand, N., Label-Free Impedance Biosensors: Opportunities and Challenges; *Electroanalysis,* **2007**, 19, 1239-1257.

18. Luppa, P.B.; Sokoll, L.J.; Chan, D.W., Immunosensors—Principles and Applications to Clinical Chemistry; *Clinica Chimica Acta,* **2001**, 314, 1-26.

19. Bergveld, P., Development of an Ion-Sensitive Solid-State Device for Neurophysiological Measurements; *IEEE Transactions on Biomedical Engineering,* **1970**, 17, 70-71.

20. Ozdemir, M.S.; Marczak, M.; Bohets, H.; Bonroy, K.; Roymans, D.; Stuyver, L.; Vanhoutte, K.; Pawlak, M.; Bakker, E., A Label-Free Potentiometric Sensor Principle for the Detection of Antibody–Antigen Interactions; *Analytical Chemistry,* **2013**, 85, 4770-4776.

21. Tarasov, A.; Tsai, M.-Y.; Flynn, E.M.; Joiner, C.A.; Taylor, R.C.; Vogel, E.M., Gold-Coated Graphene Field-Effect Transistors for Quantitative Analysis of Protein–Antibody Interactions; *2D Materials,* **2015**, 2, 044008.

22. Tarasov, A.; Gray, D.W.; Tsai, M.-Y.; Shields, N.; Montrose, A.; Creedon, N.; Lovera, P.; O'riordan, A.; Mooney, M.H.; Vogel, E.M., A Potentiometric Biosensor for Rapid on-Site Disease Diagnostics; *Biosensors and Bioelectronics,* **2016**, 79, 669-678.

23. Lee, C.-S.; Kim, S.K.; Kim, M., Ion-Sensitive Field-Effect Transistor for Biological Sensing; *Sensors (Basel, Switzerland),* **2009**, 9, 7111-7131.

24. Miao, Y.Q.; Guan, J.G.; Chen, J.R., Ion Sensitive Field Effect Transducer-Based Biosensors; *Biotechnology Advances,* **2003**, 21, 527-534.

25. Prodromidis, M.I., Impedimetric Immunosensors—a Review; *Electrochimica Acta,* **2010**, 55, 4227-4233.

26. Daniels, J.S.; Pourmand, N., Label-Free Impedance Biosensors: Opportunities and Challenges; *Electroanalysis,* **2007**, 19, 1239-1257.

27. Katz, E.; Willner, I., Probing Biomolecular Interactions at Conductive and Semiconductive Surfaces by Impedance Spectroscopy: Routes to Impedimetric Immunosensors, DNA-Sensors, and Enzyme Biosensors; *Electroanalysis,* **2003**, 15, 913-947.

28. Montrose, A.; Creedon, N.; Sayers, R.; Barry, S.; O'riordan, A., Novel Single Gold Nanowire-Based Electrochemical Immunosensor for Rapid Detection of Bovine Viral Diarrhoea Antibodies in Serum; *Journal of Biosensors & Bioelectronics,* **2015**, 6, 174.

29. Chang, B.-Y.; Park, S.-M., Electrochemical Impedance Spectroscopy; *Annual Review of Analytical Chemistry,* **2010**, 3, 207-229.

30. Berggren, C.; Bjarnason, B.; Johansson, G., Capacitive Biosensors; *Electroanalysis,* **2001**, 13, 173-180.

31. Poghossian, A.; Cherstvy, A.; Ingebrandt, S.; Offenhäusser, A.; Schöning, M.J., Possibilities and Limitations of Label-Free Detection of DNA Hybridization with Field-Effect-Based Devices; *Sensors and Actuators B: Chemical,* **2005**, 111-112, 470-480.

32.   Gray, D.W.; Welsh, M.D.; Doherty, S.; Mansoor, F.; Chevallier, O.P.; Elliott, C.T.; Mooney, M.H., Identification of Systemic Immune Response Markers through Metabolomic Profiling of Plasma from Calves Given an Intra-Nasally Delivered Respiratory Vaccine; *Veterinary Research,* **2015**, 46, 7.

33.   Tsai, M.-Y.; Creedon, N.; Brightbill, E.; Pavlidis, S.; Brown, B.; Gray, D.W.; Shields, N.; Sayers, R.; Mooney, M.H.; O'riordan, A., Direct Correlation between Potentiometric and Impedance Biosensing of Antibody-Antigen Interactions Using an Integrated System; *Applied Physics Letters,* **2017**, 111, 073701.

34.   Wahl, A.; Barry, S.; Dawson, K.; Machale, J.; Quinn, A.J.; O'riordan, A., Electroanalysis at Ultramicro and Nanoscale Electrodes: A Comparative Study; *Journal of The Electrochemical Society,* **2014**, 161, B3055-B3060.

35.   Dawson, K.; Wahl, A.; Murphy, R.; O'riordan, A., Electroanalysis at Single Gold Nanowire Electrodes; *Journal of Physical Chemistry C,* **2012**, 116, 14665-14673.

36.   Wang, C.; Wang, J.; Deng, L., Evaluating Interaction Forces between Bsa and Rabbit Anti-Bsa in Sulphathiazole Sodium, Tylosin and Levofloxacin Solution by Afm; *Nanoscale Research Letters,* **2011**, 6, 579.

Chapter 7　　**Summary, Conclusion and Future Work**

7.1 Summary

The original intent of this PhD work was to develop a commercially viable sensing platform that could be used at the point of care for applications in the agricultural and food industries. The intended devices were cost-effective, robust and highly reproducible sensing systems for effective determination of food contaminants and disease states. As outlined in the introduction chapter, there are a large number of sensing techniques and mechanisms that could be employed for these devices. SERS and EIS were selected as our two sensing methods as they both deliver sensitive and direct determination of analytes, and provide a non-destructive means for the characterisation of the sensor interfaces. To this end, two functional device platforms were developed, employing nanoscale sensing surfaces; (i) a SERS sensor and (ii) an electrochemical impedance sensor.

In Chapter 2, the simple fabrication of a polymer based SERS substrate was presented using a nanostructured soda can as a template. Simulations and control experiments confirmed that the Raman signal enhancement $\sim10^6$ arose from the gaps ("hot spots") between the Ag clusters occurring throughout the Ag layer and that the signals observed with these substrates arose predominantly from an electromagnetic effect. The transparent substrates also permitted back excitation and SERS detection through the substrate. The sensor demonstrated quantitative detection as well as a low LOD ($\sim$200 pg/mL) for the detection of dye molecule crystal violet. Versatility of the sensor performance was confirmed from the detection of trace amounts of melamine in milk and infant formula, as well as the detection of glucose via surface modification.

Chapter 3 focused on employing the SERS sensors in combination with electrochemical sensors for the environmental detection of neonicotinoid pesticides. Firstly, Raman and SERS analysis of two pesticides, imidacloprid and clothianidin, were performed to establish the characteristic vibrations of the molecules. All these vibration modes were subsequently assigned using a combination of the literature and the DFT simulated vibrations. A shift in wavenumber between the SERS and Raman spectra were observed, as expected, due to the adsorption of molecules to the substrate's silver surface. Gold nanowire array electrodes (4 x 100 nm) were fabricated on silicon chips using e-beam lithography, and applied to the detection of the neonicotinoids using square wave

voltammetry, alongside SERS determination. Well defined characteristic reduction peaks of nitro groups from neonicotinoid insecticides were resolved with SWV, permitting LOD's of ~1 ng/mL for both compounds, and were simultaneously validated with SERS analysis on the prepared aqueous solutions.

In Chapter 4, a new electrochemical sensor chip design was introduced, which comprised of six single on-chip nanoband electrodes, and a micro SD style pin-out connection. The objective was to modify the original chip design by increasing the inter-electrode spacing to permit independent modification of electrode and to facilitate easy connection to external circuitry via the new SD port. Moreover, the pin-out allows easy replacement of disposable biosensor chips in a final diagnostic device. Firstly, different surface chemistries were examined to develop a stable and reproducible method of immobilising biomolecules onto the electrode surface. The sensor performance was then assessed by challenging it with detection of virus and antibody target analytes in different media of increasing biological complexity, i.e. buffer and diluted serum samples. Ultimately, the sensor demonstrated co-detection of both BVD antibodies and BVD virus in whole bovine serum, using electrochemical impedance spectroscopy. The sensor also discriminated between disease positive and disease negative serum samples from both transiently and permanently infected calves. These detection capabilities in whole serum are an essential prerequisite for on-farm BVD serological screening and surveillance. BVD assay time-to-result was typically ~20 minutes, which also satisfies the time requirements for on-farm analysis.

Chapter 5 is a short chapter which focused on further development of applications for the microSD affinity sensors. Here, some of the preliminary results for the detection of a parasitic bovine liver fluke were presented. The selective detection of anti-*Fasciola* antibodies in serum samples was shown by employing a protease enzyme, cathepsin L1, as the immobilised capture biomolecule. Impedimetric investigation of several different serum samples revealed the same serostatus as ELISA data on the same samples.

In this chapter 6, a potentiometric FET-based sensing method (from Georgia Institute of Technology) was introduced in combination with electrochemical impedance spectroscopy. The objectives of this chapter were to employ the nanoband sensor chip, used in Chapter 4, as a shared platform for combined Label-free FET/EIS detection of

antibody-antigen interactions. The dual sensing method was used to detect bovine parainfluenza antibodies in a complex blood system using Hemagglutinin-Neuraminidase protein as the capture probe (synthesised by Queens University Belfast).

Furthermore, a correlation between surface potential of the FET and charge transfer resistance of EIS, was discovered. The blocking efficiency of the nanoband electrode was also assessed; using fish gelatin as an additional blocking step. The gelatin showed a slight reduction in NSB but it was found that the introduction of neat HBS-EP rinsing buffer (160 mM) containing the surfactant tween-20, worked more effectively in removing the weakly bound proteins that contributed to the NSB on the electrode.

To conclude, this thesis presents two sensing platforms that display POC capabilities for agri-food applications. The SERS substrate has a simple fabrication mechanism which exhibits a high enhancement factor, while providing a rapid analysis of a variety of analytes. The impedance sensor provides a simple and sensitive diagnosis of biomarkers in biological fluids at low concentrations. The re-design of the electrochemical sensor chips provided a platform in which multiplexed diagnostics could be performed and also allows the integration of micro-fluidics which will be discussed in the future work section. Furthermore, the label-free detection methods that were employed, avoids the use of expensive and time consuming pre-treatment processes and makes these sensor designs even more attractive for POC multiplexed analysis.

7.2 Future Work

During the course of this work, proof-of-concept immunosensors were developed for the detection of antibody-antigen complexes, whereby both biomolecules were employed as the capture probe. There is now a great opportunity to further exploit the capabilities of these devices. Furthermore, the sensors need to move out of proof-of-concept stages and towards development of viable commercial product. In order to achieve this, the sensitivity and selectivity of the sensors must be improved. Although the methods presented in this thesis are both sensitive and selective, employing interdigitated electrodes and microfluidic channels will create the standard of biosensor required for commercialisation.

The future experiments will be transferred from the nanoband sensor platforms onto interdigitated electrode arrays (IDE). The chip will remain the same with the SD pin-out but the 6 working electrodes will have an IDE design. By maintaining the inter-electrode separation at the nanoscale (~500 nm) reduces the solution impedance when one comb electrode is biased against a second. Using this approach, significantly smaller changes in impedance may be detected (due to the lower background) giving to up to 100 times increase in sensitivity compared to interdigitated microelectrodes. The nanoscale separation will also confine the electric field to within 200 nm of the surface of the interdigitated electrode, i.e. within the bio-molecular binding region, thus further increasing sensitivity.

A spotting technique was employed to independently modify nanoband electrodes for multiplexing applications in Chapters 4, 5 and 6. While this process is effective, it is not efficient and would be complicated to integrate into scalable processing techniques. The development of these sensors to become feasible products requires the introduction of a microfluidic mask, in order to facilitate the modification process so as to allow mass production. In addition, a microfluidic mask is necessary to enable a multichannel sensing platform. One positive control channel will be employed to confirm assay functionality, i.e. reducing false negatives, and one negative control will be used to correct for noise/drift and non-specific binding, thereby reducing false positives. This microfluidic sensor would also enable further collaboration with GIT and QUB, on the dual sensing EIS/FET platform. Preliminary work in developing polymer microfluidic moulds, for use

with the SD sensor chips, has been undertaken, see Figure 7.1. The initial mould designs were undertaken by Dr. Sean Barry, however have been updated since. Microfluidic technology seeks to improve analytical performance by integrating multiple processes in a single device as well as by increasing sensor reliability and sensitivity while reducing sample volume and analysis time.
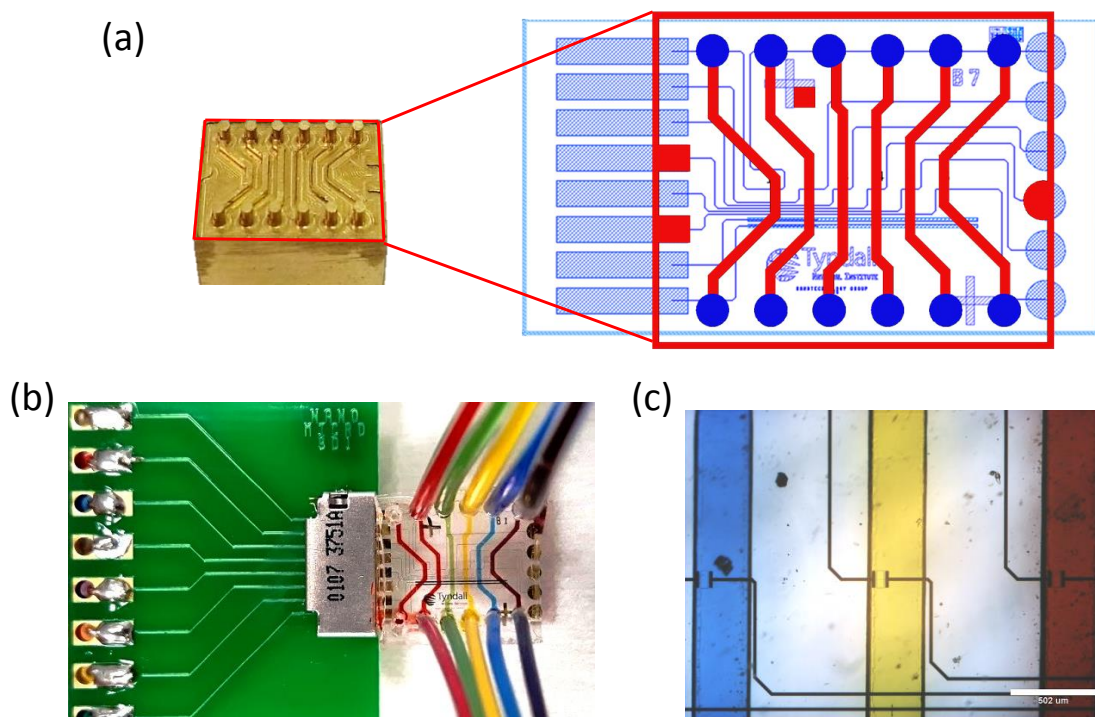

Figure 7.1: Initial designs for the microfluidic mould (a) the aluminium mould design (left) with schematic overlay of the chips (right), (b) PDMS bonded onto a sensor chip with 6 channels filled with different dyes and inserted into the microSD pin out. (c) Optical micrographs of the fluidic channels overlaying the electrodes.

These features are particularly suitable for immunoassay applications. Wet PDMS can be templated with the aluminium cast then heat cured to produce a PDMS microfluidic mould. This mould and the silicon chip are plasma cleaned to produce the required OH groups for surface binding. The mould is then aligned with alignment marks on the chips and both chip and mould are pushed together. Pressure is applied for several seconds to allow the binding to occur. The 6 micro-channels overlay the 6 electrodes and sections of both the counter and reference electrodes. The PDMS is aligned so that the chip's micro-SD connection pads are not blocked and can connect via the SD port. Holes at each end of the channel allow fluid to be pumped though for electrode functionalisation. Although we have produced the initial fluidic platform, electrode characterisation needs to be

undertaken and followed by assay development. Future work also needs to investigate the use of different polymers for fabrication, as PDMS is reported to allow adsorption of biomolecules. Moreover the PDMS moulds are being permanently bonded to the chips which reduce the potential applications for the sensors. Thus, reversible bonding would be a good asset for the sensor. The pumping mechanisms, i.e. by capillary force, injection or suction, needs to be assessed to reduce leakages in the mould. For example, a PMMA platform with built in channels could be a solution, whereby the chip would be placed into the platform and encompassed like a chip holder. The application of a microfluidic channel, coupled with coating the sensors with specific capture probe biomolecules and control molecules, will provide the necessary speed and specificity for further product development.

Additionally, more sensor experiments are required to improve sensor performance, particularly for bovine liver fluke detection. The preliminary detection of anti-*Fasciola* antibodies were presented in Chapter 5. These antibodies have the advantage of being present in the blood as early as two weeks post infection. This is far before the presence of eggs in the faeces (over two months), which is the current detection method on-farm. However, antibody detection tests are incapable of differentiating between the past and present infections, since antibodies may persist in the subject for years post treatment. Moreover, in fascioliasis, antigenemia concentration depletes and become undetectable in later phases of infection, so it is necessary to detect both the antibody and antigen for remote analysis. Hence for future work, we aim to develop a sensor that will detect both biomolecules in serum, employing the above mentioned microfluidic channels. Combining both tests on one sensor will increase the selectivity of the sensor for *Fasciola* detection, similar to the dual sensing discussed in the previous chapter, both results would have to be valid to ensure a trustworthy result.

Regarding the SERS work in Chapter 3, the next step is to co-localise the SERS and electrochemical sensing onto a single sensor to enable a dual sensing approach from both techniques. Further work would involve developing the connectivity of these devices, to utilise the cloud, and incorporate them into the Internet of Things network.

Appendices

A1. Abbreviations and Acronyms

4-ABT	4- Aminobenzenethiol
AAO	Anodic Alumina Oxide
Ab	Antibody
AFM	Atomic Force Microscopy
Ag/AgCl	Silver/Silver Chloride
Al	Aluminium
Au	Gold
BHV	Bovine Herpes Virus (Infectious Bovine Rhinotracheitis – IBR)
BPI3V	Bovine Parainfluenza 3 Viruse
BRD	Bovine Respiratory Disease
BRSV	Bovine Respiratory Syncytial Virus
BSA	Bovine Serum Albumin
BVD	Bovine Viral Diarrhoea
CAT L1	Cathepsin L1
CCD	Charge-Coupled Detector
CE	Counter Electrode
CM	Chemical Mechanism
CPE	Constant phase element
CrV	Crystal Violet
CV	Cyclic Voltammetry
DFT	Density functional theory
DI	Deionised
DNA	Deoxyribonucleic acid
DT	1-Decanethiol
EBL	Electron Beam Lithography
EDC	N-(3-Dimethylaminopropyl)-N′-ethylcarbodiimide hydrochloride
EF	Enhancement Factor
EFSA	European Food Safety Authority
EGFET	Extended gate field-effect transistor
EIS	Electrochemical impedance spectroscopy

ELISA	Enzyme-linked immunosorbent assay
EM	Electromagnetic Mechanism
FAO	Food and Agriculture Organisation
FcCOOH	Ferrocenemonocarboxylic Acid
FEM	Finite Element Method
FET	Field-effect transistor
gE	Glycoprotein E
H_2SO_4	Sulphuric acid
HN	Hemagglutinin neuraminidase
HOMO	Highest Occupied Molecular Orbital
Hp	Haptoglobin
ISFET	Ion-sensitive field-effect transistor
LOD	Limit of Detection
LSPR	Localised Surface Plasmon Resonance
LUMO	Lowest Unoccupied Molecular Orbital
MDA	16-Mercaptohexadecanoic acid
MG	Malachite Green
MH	Mercaptohexanol
MOFET	Metal–oxide–semiconductor field-effect transistor
MRL	Minimum Residue Limit
NaOH	Sodium Hydroxide
NHS	N-Hydroxysuccinimide
NP	Nanoparticle
NSB	Non-specific binding
NW	Nanowire
o-ABA	ortho-aminobenzoic acid
o-PD	ortho-phenelenediamine
OP	Organophosphate
PBS	Phosphate Buffered Saline
PCB	Printed Circuit Board
PDMS	Polydimethylsiloxane
PI	Persistently Infected
PMMA	Polymethylmethacrylate
POC	Point-of-care

PS	Polystyrene
Pt	Platinum
PTFE	Polytetrafluoroethylene
PVDF	Polyvinylidene Fluoride
RE	Reference electrode
SAM	Self-assembly monolayer
SEM	Scanning Electron Microscopy
SERS	Surface Enhanced Raman Scattering/ Spectroscopy
SiN	Silicon Nitride
SPR	Surface plasmon resonance
SWV	Square Wave Voltammetry
TI	Transiently Infected
WE	Working Electrode

A2. Peer Reviewed Publications

1. **Creedon, N**.; Lovera, P.; Furey, A.; O'Riordan, A. "Transparent polymer-based SERS substrates templated by a soda can" *Sensors and Actuators B: Chemical*, **2018**, 259, 64-74 (https://doi.org/10.1016/j.snb.2017.12.039)

2. Tsai, MG.; **Creedon, N.**; Brightbill, E.; Pavlidis, S.; Brown, B.; Gray, DW.; Shields, N.; Sayers. R.; Mooney, M.; O'Riordan, A.; Vogel, E. "Direct correlation between potentiometric and impedance biosensing of antibody-antigen interactions using an integrated system" *Applied Physics Letters*, **2017**, 111 (7), 073701 (https://doi.org/10.1063/1.4986190)

3. Tarasov, A.; Gray, DW.; Tsai, MG.; Shields, N.; Montrose, A.; **Creedon, N.**; O'Riordan, A.; Mooney, M.; Vogel, E. "A potentiometric biosensor for rapid on-site disease diagnostics" *Biosensors and Bioelectronics*, **2016**, 79, 669-678 (doi:10.1016/j.bios.2015.12.086)

4. Lovera, P.; **Creedon, N**.; O'Riordan, A. "Metal capped polystyrene nanotubes arrays as super-hydrophobic substrates for SERS applications" *SPIE Photonics Europe*, **2014**, 912908-912908-9 (doi:10.1117/12.2054443)

5. Lovera, P.; **Creedon, N**.; Alatawi, H.; O'Riordan, A. "Low-cost silver capped polystyrene nanotube arrays as super-hydrophobic substrates for SERS applications" *Nanotechnology*, **2014**, 25 (17), 175502 (doi:10.1088/0957-4484/25/17/175502)

A3. Publications in Submitted or in Preparation

1. **Creedon, N**.; Sayers, R.; Barry, S.; O'Sullivan, B.; Lovera, P.; O'Riordan, A. "Label-free impedimetric sensor for Bovine Viral Diarrhoea virus (BVDV) and antibody (BVDAb) detection in serum" – Submitted, *Biosensors and Bioelectronics,* 2018

2. **Creedon, N.**; Montrose, A.; O'Riordan, A. "Application of Gold Nanowire Electrodes for Spectro-electrochemical Detection of Neonicotinoid Insecticides" – Submitted, Sensors and Actuators B, 2018

3. **Creedon, N.**; Montrose, A.; Tsai, MG.; Tarasov A.; Gray, D.; Shields, N. ;Mooney, M.; Vogel, E.; O'Riordan, A. "Impedimetric and Potentiometric Dual Immunosensor for Rapid Detection of Bovine Parainfluenza 3 Virus" – In preparation

A4.   Conferences Attended

1. Agri-Tech Pitch, Tyndall Technology days, Cork, October 2017 "Smart sensing for agriculture, environment & security"   (Oral Pitching Presentation)

2. Powering the IOT Pitch, Tyndall Technology days, Dublin, October 2016 "Agri-Food smart sensor systems"   (Oral Pitching Presentation)

3. Innovation Arena Judging, National Ploughing Championship, "Nanosensor systems for on-farm disease diagnostics" Offaly, September 2016 (Oral Presentation)

4. Postgraduate Research Day, UCC, August 2016 "Fabrication of transparent Polymer-based Surface Enhanced Raman Spectroscopy (SERS) Sensors" (Oral Presentation)

5. Nanonet Ireland Conference, University of Limerick, October 2016 , "Rapid Electrochemical Detection of Bovine Viral Diarrhoea Disease in Serum" (Poster Presentation)

6. 29th World Buiatrics Congress, Dublin, July 2016. "Nanowire-based electrochemical detection of Bovine Viral Diarrhoea virus in serum" (Poster Presentation)

7. 68th Irish Universities Chemistry Research Colloquium, "Nanowire-based, Label-free Electrochemical Detection of Bovine Respiratory Disease Pathogens in Serum" UCC, June 2016 (Oral Presentation)

8. Conference of Analytical Sciences in Ireland, CASi - National Center for Sensor Research, Dublin City University, April 2016, "Soda Can Templated Flexible Polymer SERS Substrates for multiple sensing applications" (Oral and Poster Presentation)

9. Tyndall SAFE and ICT Conference, Tyndall Technology days, Cork, October 2014 "Electrochemical sensing of Neonicotinoid Pesticides" (Oral Pitching Presentation)

10. Second Food Integrity and Traceability Conference, Queens University Belfast, March 2014 "Low-cost SERS Substrates for Rapid Detection of Contaminants in Food Products" (Poster Presentation)

A5. Awards

1. Gold Medal Award, Most innovative Research Emerging from 3rd Level "Nanosensor systems for on-farm disease diagnostics" Innovation Arena, National Ploughing Championship, Offaly, September 2016

2. First Place, Best Presentation, "Soda Can Templated Flexible Polymer SERS Substrates for multiple sensing applications" CASi - National Center for Sensor Research, Dublin City University, April 2016

3. Second Place, Student Poster Competition "Rapid BVD Disease detection in Serum" Postgraduate Research Day, Tyndall, August 2015

4. Third Place, Poster Competition "AgriSense: Multichannel Disposable Sensors for Animal Health Disease Diagnostics" Second Food Integrity and Traceability Conference, Queens University Belfast, March 2014